Depth Dependent Damage in Heavy-Ion Irradiated Nickel

John Barry Whitley

August 1978

UWFDM-275

Ph.D. thesis.

Depth Dependent Damage in Heavy-Ion Irradiated Nickel

John Barry Whitley

Fusion Technology Institute
University of Wisconsin
1500 Engineering Drive
Madison, WI 53706

http://fti.neep.wisc.edu

August 1978

UWFDM-275

Ph.D. thesis.

DEPTH DEPENDENT DAMAGE IN
HEAVY-ION IRRADIATED NICKEL

BY

JOHN BARRY WHITLEY

A thesis submitted in partial fulfillment of the
requirements for the degree of

DOCTOR OF PHILOSOPHY
(Nuclear Engineering)
at the
UNIVERSITY OF WISCONSIN-MADISON
1978

ABSTRACT

DEPTH DEPENDENT DAMAGE IN HEAVY-ION IRRADIATED NICKEL

John Barry Whitley

Under the supervision of Professor Gerald L. Kulcinski

The irradiation of metals with high energy heavy-ions has become an important tool in the study of radiation damage in metals. The heavy-ion damage process is very complicated, however, and it cannot be completely utilized in the attempt to predict material response to high energy neutron bombardment until the peculiar features of these studies are better understood. In this investigation, specimens of high purity nickel were irradiated with high energy nickel, copper, aluminum and carbon ions under various irradiating conditions. The resultant damage microstructure was examined using a sample preparation technique in which the irradiated foils could be examined in a plane normal to the foil surface (i.e., in cross section). By using this technique, many of the unique features of the heavy ion damage process could be carefully studied, thereby giving valuable insight into defect clustering under changing irradiation conditions.

Void nucleation in these specimens was found to be very sensitive to hydrogen introduced into the samples prior to irradiation by anodic injection during electropolishing. Hydrogen doped specimens contained final void densities over two orders of magnitude greater than the void densities observed in thoroughly outgassed samples. However, the swelling values between these samples

differed by only a factor of 2 to 3. Since the hydrogen was outgassed at temperatures between 700 and 900°C, the hydrogen is believed to be trapped at interstitial impurities such as carbon prior to irradiation.

Samples were irradiated under similar conditions with 14 MeV nickel, 14 MeV copper, 8.1 MeV aluminum and 5 MeV carbon ions and the results compared. In all samples voids were observed at depths from 15 to 20% beyond the maximum predicted ion range. The variation in swelling from midrange to the peak of the damage region was significantly less than the variation in the displacement damage. This reduction in swelling rate was due to the higher dose rate in the end-of-range region. The mass of the irradiating ion had no noticeable effect on swelling, with the samples having similar swelling values at similar damage levels. None of the samples irradiated with copper, aluminum or carbon ions had any dramatic changes in the end-of-range void microstructure that could be attributed to an interaction with the implanted ions.

A series of samples were irradiated with 14 MeV nickel ions at fluences from 2×10^{15} to 1.4×10^{17} ions/cm^2 (peak damage 2 to 150 dpa). At a given damage level, void density increased with increasing depth, while void size and swelling decreased. At all depths, swelling was observed to saturate at about 3%, implying that the saturation level is independent of dose rate. The saturation dose did vary with depth, with the dose necessary for saturation increasing with depth. This saturation is believed to be related to the formation of a void superlattice which was observed in the highest dose sample.

After irradiation at 400°C, the depth dependent microstructure consisted of voids in the first micrometer, changing to a loop lattice structure in the next 2 micrometers, then ending with a region of voids. This behavior is an illustration of the temperature shift phenomenon, where an increasing dose rate has changed the observed structure from one of voids (indicative or a "high" irradiation temperature) to one of loops (indicative or a "low" irradiation temperature). A loop lattice was also observed after irradiation at 200°C. At both temperatures, the loop lattice spacing of 40 nm did not vary with depth.

Approved ______________________

ACKNOWLEDGEMENTS

In carrying out this research, the author is indebted to many different individuals for their guidance and support. In particular, this work was carried out under the supervision of Professor G.L. Kulcinski, and the author would like to express his appreciation for his continual guidance and encouragement. Special thanks are also due Professor P. Wilkes for his advice and assistance, and to Professor W.G. Wolfer, with whom the author had many stimulating and enlightening discussions.

The author would like to thank Dr. H.V. Smith, Jr., Dr. J. H. Billen, Dr. W.J. Weber, R.G. Lott, S.K. McLaurin, K.Y. Liou and C.A. O'Donnell for their assistance in the experimental work.

The author is grateful to the University of Wisconsin Nuclear Physics Group for the use of the tandem accelerator and its facilities.

This work was partially sponsored by the Department of Energy, Division of Magnetic Fusion Energy, Materials Branch, and by the University of Wisconsin Graduate School.

Finally, the author would like to dedicate this work to his wife, Janet, whose patience and support have made the obtaining of this degree possible.

TABLE OF CONTENTS

TABLE OF CONTENTS-Continued

LIST OF FIGURES

LIST OF FIGURES -continued

LIST OF FIGURES-Continued

LIST OF FIGURES-Continued

LIST OF FIGURES-Continued

LIST OF FIGURES-Continued

1. INTRODUCTION

A. History of Void Formation

In the early 1960's, it was generally believed by those involved in the study of radiation effects on the structural materials in Fast Breeder Reactors (FBR) that the primary materials problem would be embrittlement due to either internally generated helium from (n,α) reactions or from excessive radiation hardening. The emphasis of the materials research programs started shifting in 1967 when Cawthorne and Fulton (1) observed small cavities in neutron irradiated stainless steel using transmission electron microscopy (TEM). Since the total volume of the cavities they observed was greater than could be explained by gas filled bubbles resulting from nuclear reactions, Cawthorne and Fulton speculated that the cavities were the result of vacancy agglomeration. Later studies confirmed this hypothesis, and these three dimensional vacancy clusters containing less than equilibrium pressures of gas have been labeled voids.

Since their discovery, there have been many review articles (e.g., see references 2, 3) devoted to this subject and numerous conferences (4-16) include at least some discussion of void formation. The technological significance of void formation to advanced reactor development lies in the macroscopic swelling associated with the formation of voids. This swelling, which can reach values of 20% or greater, will require that proposed Liquid Metal Fast Breeder Reactors (LMFBR) be designed with excessively large coolant channels to accommodate the fuel cladding volume increase without blocking the channels. The swelling behavior of metals has also been found to be dependent both on neutron fluence and on temperature. This behavior could lead to bowing of the fuel assemblies due to the flux and temperature gradients in the reactor core. This bowing will require extra fuel restraint assemblies and will complicate maintenance considerably. Hence, any reactor design that is required to accommodate large structural swelling will be less compact, leading to a smaller breeding ratio. The economic cost of designing for a swelling value of 5% has been estimated by Huebotter and Bump (17) to be approximately one billion dollars (1970 $'s) for the period 1970-2020. As this economic penalty has become more evident, the amount of research in this area has increased dramatically.

Proposed Controlled Thermonuclear Reactors (CTR) first walls will be subjected to an even more energetic neutron flux and swelling problems are also expected in these materials. While the structural swelling of CTR first walls will not impact on the economics by lowering the breeding ratio, it will certainly complicate the design of a reliable structure. At this time, an acceptable solution of the void formation problem has not been found. The objective of this study was to better understand the radiation damage process by using a simulation technique.

B. Simulation Studies

A major obstacle to exhaustive studies of void formation during high energy neutron irradiation is the time required to achieve damage levels typical of proposed FBR's or Controlled Thermonuclear Reactors (CTR's). For example, an LMFBR component operating in a neutron flux of 6×10^{15} n/cm$^2 \cdot$s would accumulate a total fluence of 2×10^{23} n/cm^2 in 387 full power days, a fluence that would take almost 4-1/2 years to accumulate in the central position of EBR-II (17). When one considers that the actual neutron flux in the remainder of the core of EBR-II is lower than the central position, it is obvious that the time required to accumulate data and carry out proper screening and fundamental studies would reduce the usefulness of EBR-II.

Experimental devices capable of simulating the CTR radiation environment are extremely limited, with the total test volume available being only a few cubic centimeters and the neutron flux being so low that exposures equivalent to a year's operation in a CTR would take several years to achieve. If there is to be any hope of impacting reactors to be built in the near future, other experimental methods besides reactors have to be applied to the void swelling problem.

To overcome this time problem, various irradiation techniques besides neutrons were applied fairly quickly to void studies. The first use of ions to produce voids was by the Harwell group who irradiated nickel with 20 MeV carbon ions (18), followed quickly by the use of 5 MeV nickel and tantulum ions (19) and protons (20) in the United States. In these studies, a void and dislocation microstructure was formed which was similar to the microstructure observed after neutron irradiation. By the use of ions, and later the use of electrons at energies greater than 600 KeV, it has been possible to accumulate damage at rates from 10^2 to 10^5 times faster than occurs under neutron irradiation. A time compression of 10^4 will reduce a 14 year EBR-II irradiation down to one hour of accelerator time. It is also possible to more carefully control the experimental parameters, such as temperature and environment, in an ion target chamber than it is in a reactor core where access is difficult.

While the experimental time advantages of ion simulation are obvious, the actual correlation between these results and those from the neutron environment is not. Attempts to find a direct correlation between neutron irradiated and ion irradiated specimens have not been successful (21). To understand this discrepancy, the ion irradiation and the neutron irradiation damage mechanisms must be examined in detail. Of the several important parameters that are different between neutron irradiations and simulation studies, the first problem area that one might expect is that of time scaling. That is, what will be the overall effect of speeding up a process by a factor of 10^3 to 10^4? The present models, which will be discussed in Section II-D, predict that at a high dose rate, the final damage state will be indicative of a lower irradiation temperature. Simulation experiments also fail to produce the impurities which are generated by neutron interactions. These transmutations, especially the gaseous helium and hydrogen, are very important in the void nucleation stage. Simulation experiments attempt to study the effects of these impurities by either implanting the sample with the impurity before irradiation, or using the more realistic, but much more difficult process of injecting the impurity and irradiating simultaneously (133).

Another large difference between neutron and ion simulations is the energy of the primary recoil atom and the cascade density. Neutrons produce fairly isolated, high energy cascades; nickel ions produce a relatively large number of dense, lower energy cascades; carbon ions even lower energy cascades; and electrons produce no cascades, only isolated defects. Since both the amount of recombination and the amount of clustering of point defects that occurs in the cascade is strongly dependent on the point defect density, it is important that an understanding of the cascade details be achieved. The details of cascade formation will be discussed in Section II-B.

The final area of uncertainty in understanding ion simulation experiments lies in the overall effect of the limited damage region on point defect behavior. Heavy ions accelerated to energies of 50 MeV will only penetrate a metal target to depths of ~10 microns, leading to several problems. First, since point defects interact strongly with free surfaces, the microstructure observed in regions less than one micron (10^{-6}m) from the front surface may not be typical of a bulk material response to the irradiation. This problem can be overcome by the use of high energy (i.e., > 10 MeV) heavy ions which have ranges greater than this affected region. Secondly, since the damage region is physically confined by the undamaged region beyond the ion range and by the material around the ion beam spot, any swelling that occurs will generate internal stresses. These stresses are difficult to calculate since they are at least partially relieved by radiation creep, yet they are important in correctly determining the interaction energies of point defects with voids and dislocations.

The short ion range also means that the incident ion is stopped within the target material. If the incident ion is different from the target material, such as copper or carbon ions incident on nickel, then the region near the end of range will contain these impurity atoms. Since point defects are well known to interact with impurities, any analysis done in this region is always questionable. Even if the incident ion is the same as the target material, it still represents an excess interstitial atom, and may modify the delicate balance of vacancy and interstitial flow in this region. Finally, the short range of heavy ions excludes any type of mechanical property study, such as creep or embrittlement, and implies that heavy ion bombardment studies are useful primarily to study the microstructure changes that occur under irradiation.

C. Nickel as a Model Element for Radiation Damage Studies

There are several reasons nickel was chosen for this study. Nickel, as an alloying element, has been used more and more in recent years as attempts are made to push up the useful operating temperatures of structural materials while maintaining good mechanical toughness and corrosion resistance (22). Nickel has a high melting temperature (1453°C), a high solubility for most other metallic elements, serves to stabilize the face centered cubic (fcc) phase in certain alloys (such as the stainless steels), and also readily forms precipitates which serve to strengthen the matrix (23,24). Since either stainless steel or a high nickel alloy has been chosen for the near term breeder reactor, and quite possibly for the first fusion reactors, the importance of understanding the irradiation behavior of nickel and its alloys is obvious.

There are other reasons for choosing nickel besides its technological importance. A pure material was chosen both to simplify any theoretical application of the results and to lay the groundwork for future studies in nickel alloys. High purity nickel swells readily at relatively low damage levels, and the point defect properties (such as formation and migration energies) have been measured. Sufficient swelling data has been accumulated under many types of irradiations to allow some comparison of results, and Smith et al. (25) have developed a nickel ion source suitable for use on the U.W. tandem accelerator which will allow self-ion irradiations to be performed. Finally, the choice of nickel allows the application of a relatively new technique for preparation of the irradiated foils. This technique, which will be described in detail in Section IV-B, allows the examination of the damage region in a plane normal to the foil surface, that is, in cross section. This allows for both an increased amount of information from each irradiation and for a decrease in the experimental uncertainty of many parameters.

In this study, specimens of high purity nickel were irradiated with high energy nickel, copper, aluminum, and carbon ions and the resultant microstructure examined in cross-section. The effect of various sample pre-irradiation preparation techniques was studied, along with the effect of varying the irradiation temperature and the damage level. A computer code was written to calculate the point defect concentration profiles in an ion irradiated foil, and the results of these calculations are compared to the observed swelling profiles. A radiation enhanced diffusion model was applied to give the final concentration profile of impurities introduced when the irradiating ion was a species other than nickel.

II. THEORY OF VOID FORMATION .

A. Production of Point Defects

There are basically two different mechanisms by which neutron irradiation can affect a metal, namely by the introduction of impurities from transmutation reactions, and by the atoms being physically knocked out of their crystal lattice sites by neutron interactions (26-29). The calculation of the buildup of transmutation impurities during an irradiation is straightforward, and with a knowledge of the relevant cross sections, they can be applied to any given neutron spectrum (30). The calculation of the total number of displacements is more complicated, however, since the initial neutron interaction usually initiates a large cascade, producing many displacements. In an ion irradiation, the initial neutron interaction is replaced by an ion-atom scatter, with the scattered atom initiating cascades. Since the final damage state is dependent to some extent on the total number of atoms displaced, the procedure for calculating displacements will now be addressed in detail.

The accepted unit of radiation damage is the displacement per atom (dpa), which is equivalent, in theory, to the average number of times a lattice atom is energetically forced from its lattice site to an interstitial position during the irradiation. Note that this definition includes only those events that produce point defects, and does not include the events where an energetic atom collides and ejects another atom from its lattice site, but in the collision loses enough energy to become trapped in the ejected atom's site. These replacement events are not thought to be important in pure materials, but would be important if the irradiation was being carried out on an ordered alloy or other structured material.

The rate at which displacements are produced by an arbitrary flux of particles $\phi(E)$ is given by (31)

$$R_d = N \int_{E_{d/\Lambda}}^{\infty} \phi(E)\,dE \int_{E_d}^{\Lambda E} \sigma(E,T)\ \nu(T)\ dT \qquad 1$$

where N = atom number density of the target

$\sigma(E,T)$ = the differential cross section for an incoming particle of energy E to transfer energy T to a recoil atom

$\nu(T)$ = number of displacements caused by a recoil of energy T.

and $\Lambda = \dfrac{4M_1\ M_2}{(M_1+M_2)^2}$ where M_1 and M_2 are the masses of the incoming and target atoms respectively. The measurement of $\phi(E)$ and $\sigma(E,T)$ for the case of neutrons is relatively well understood and will not be discussed here. For the case of a heavy ion beam, or when calculating $\nu(T)$, the interaction involves an energetic, partially ionized projectile that is interacting with both the electronic and nuclear charge distributions within the target. In metals, the interactions with electrons do not result in displacements and only dissipate the ion energy, while the nuclear collisions are capable of generating vacancy-interstitial pairs. A precise description of the spatial distribution of point defects is an essential part of understanding the radiation damage process. Unfortunately, this is a many body problem, requiring detailed knowledge of the interaction potentials for both the incident ions and the target atoms. In the absence of such detailed knowledge, various semi-empirical formulations have been developed to calculate the damage. For heavy ion irradiations, they involve the following steps: 1) calculate the ion energy at a given depth into the target, 2) calculate the differential cross section to produce a recoil of energy T, 3) partition the recoil energy into electronic and nuclear energy losses, and 4) convert the nuclear energy losses into dpa.

The energy partition model developed by Lindhard, Scharff, and Schiott (32) (hereafter referred to as LSS) has proven the most useful in determining the energy loss for charged particles. This model assumes the electronic and nuclear energy loss mechanisms can be totally separated. Using a Thomas-Fermi model for the atom, and assuming an amorphous solid, LSS were able to develop an universal range theory that can describe, to a good approximation, the nuclear energy loss for many target-projectile combinations by a single curve. The dimensionless parameters used in this treatment are the reduced energy

$$\varepsilon = E/E_L \qquad 2$$

and the reduced range

$$\rho = R/R_L \qquad 3$$

where

$$E_L = Z_1Z_2e^2(M_1+M_2)/aM_2 \qquad 4$$

$$R_L = (M_1+M_2)^2/(4\pi a^2NM_1M_2) \qquad 5$$

$$a = 0.8853 \left(\frac{\hbar^2}{me^2}\right) \left(Z_1^{2/3} + Z_2^{2/3}\right)^{-1/2} \qquad 6$$

N = atomic density

M_1 = projectile mass

M_2 = target mass

Z_1 = projectile atomic number

Z_2 = target atomic number

R = range

and E = projectile energy

By assuming that the scattering occurs by a screened coulomb potential which was the screening length "a" (Eq. 5) as the only parameter, LSS obtain a universal differential cross section by a perturbation method, i.e.,

$$d\sigma = \pi a^2 \frac{dt}{2t^{3/2}} f(t^{1/2}) \qquad 7$$

where $t^{1/2} = \varepsilon \sin(\theta/2)$ and θ is the scattering angle in the center of mass coordinate system. For elastic collisions, $\sin^2(\theta/2) = T/T_m$, where T is the energy transferred to the PKA and T_m is the maximum energy of PKA possible from conservation of momentum. The scaling function $f(t^{1/2})$ was numerically calculated for a Thomas-Fermi potential by LSS and is shown in Figure 1a. An analytical approximation of $f(t^{1/2})$ by Winterbon et al. (33) gives

$$f(t^{1/2}) = \lambda t^{1/6} \, [1 + (2\lambda t^{2/3})^{2/3}]^{-3/2} \qquad 8$$

with $\lambda = 1.309$.

Using equations 2 and 3, the nuclear stopping power $(d\varepsilon/d\rho)_n$ can now be expressed dimensionlessly as

$$\left(\frac{d\varepsilon}{d\rho}\right)_n = \frac{R_L}{E_L} \left(\frac{dE}{dR}\right)_n \qquad 9$$

where

$$\left(\frac{dE}{dR}\right)_n = N \int_0^{T_m} T d\sigma \qquad 10$$

it can then be shown that

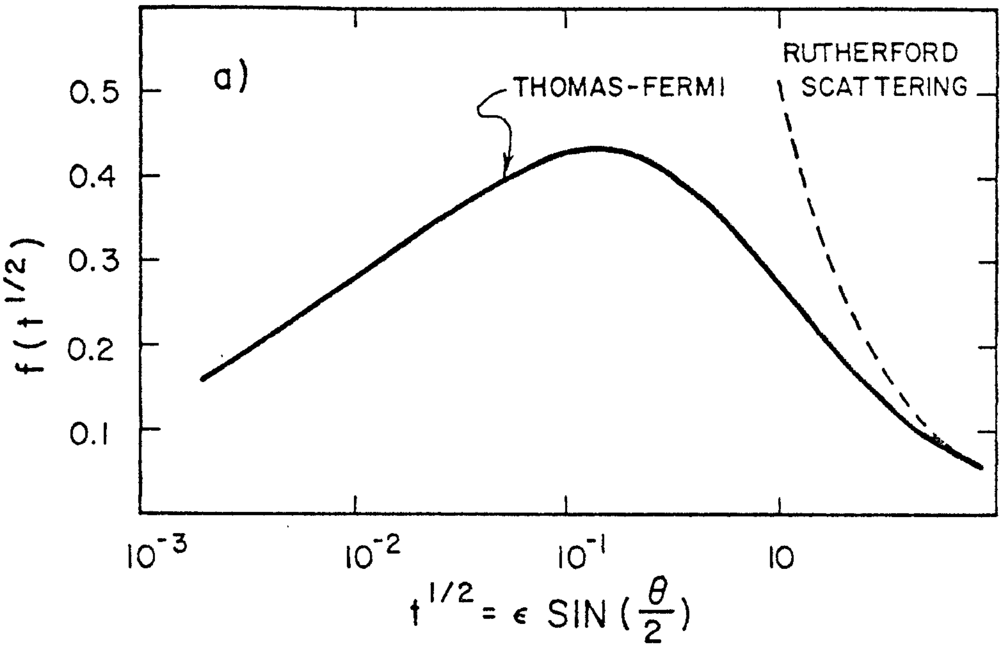

Figure 1a. Universal differential scattering cross section for elastic nuclear collisions based on a Thomas-Fermi type potential. At high values of $t^{1/2}$ it joins smoothly the Rutherford scattering.

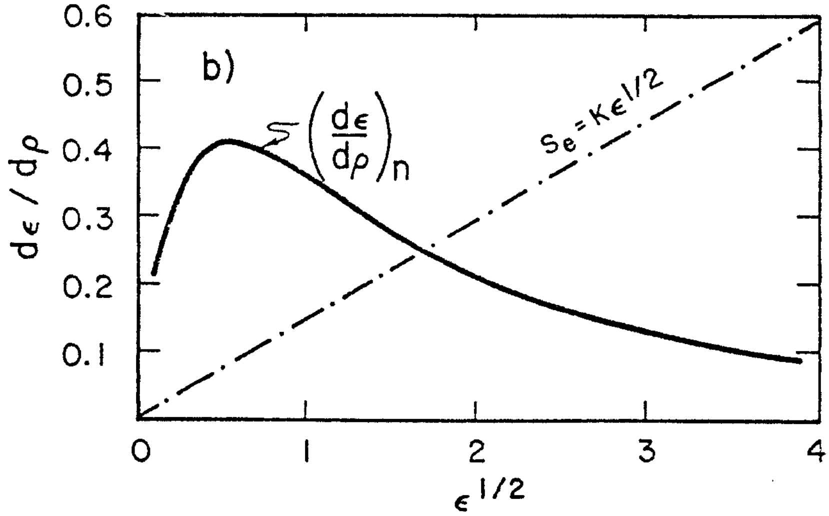

Figure 1b. The LSS result for the nuclear stopping cross section. The abscissa is proportional to the ion velocity. The full drawn curve is eq.11, and the dot/dash curve is the electronic stopping of eq. 12 with k = .15. (Ref. 32)

$$\left(\frac{d\varepsilon}{d\rho}\right)_n = \int_0^E dx\ f(x)/E \qquad 11$$

where $x = t^{1/2}$

Note that this treatment is only valid for energies great enough that the collision interaction can be described by a Thomas-Fermi potential. This condition is generally met if $\varepsilon > 0.01$ (34).

To find the electronic stopping power, LSS use the model developed in a previous paper (35) where the electronic stopping power is found to be directly proportional to the ion velocity. This treatment, which is valid only for ions of relatively low energy, first calculates the effective charge of the ion by modeling the electron stripping mechanism, and then calculates the energy lost in electron-ion collisions by assuming the target electrons are a uniform electron gas. Since electrons are bound Fermions and cannot receive arbitrary amounts of energy in a collision, only those electrons near the Fermi energy are included in the calculation. With these assumptions, the electronic loss is found to be of the form

$$\left(\frac{d\varepsilon}{d\rho}\right)_e = k\ \varepsilon^{1/2} \qquad 12$$

where k is given by Lindhard as

$$k = \xi_c \frac{0.0793\ Z_1^{1/2} Z_2^{1/2} (A_1+A_2)^{3/2}}{(Z_1^{2/3}+Z_2^{2/3})^{3/4}\ A_1^{3/2} A_2^{1/2}} \qquad 13$$

with $\xi_c \cong Z_1^{1/6}$

k is normally of the order of 0.1 to 0.2, and for nickel ions incident on a nickel target, k = 0.1605. Equation 10 is valid for ion velocities $v < v_o Z_1$ ($v_o = e^2/h$); that is, for ion energies (in MeV)

$$E_{lim} < 0.025\ M_1 Z_1^{4/3} \qquad 14$$

Typical curves for $\frac{d\varepsilon}{d\rho}$ are shown in Figure 1b. At high energies, electronic stopping is seen to dominate, while at low energies, nuclear stopping is larger. The approximate limits of validity of these curves for several ions incident on nickel are listed in Table 1.

TABLE 1

THE LIMITS OF VALIDITY OF LINDHARD THEORY FOR VARIOUS IONS INCIDENT ON NICKEL

Ion	E_{lower}(MeV)	E_{lim}(MeV)	a(nm)	E_L(keV)
H	2.8×10^{-5}	2.5×10^{-2}	1.46	2.80
He	6.05×10^{-5}	0.252	1.42	6.05
C	2.21×10^{-4}	3.27	1.32	22.1
Al	6.3×10^{-4}	20.6	1.22	63.0
Cl	9.32×10^{-4}	38.0	1.17	93.4
Ni	2.07×10^{-3}	123.	1.09	207
Cu	2.25×10^{-3}	140.	1.08	225
Ta	1.34×10^{-2}	1380.	0.906	1340

The ion energies can now be found as a function of pathlength by integrating the nuclear and electronic energy losses over the pathlength traveled. For most applications, the projected pathlength is more useful and can be found by a function given by LSS. Another important quantity is the amount of energy straggling in the beam. This term, which arises from the statistical nature of the energy loss mechanisms, is difficult to predict and is usually inferred from the range straggling data (19). An example of applying this particular method is that of Manning and Mueller (36). By using LSS energy partition theory, they obtain the following relationship for the nuclear energy loss S_D at the projected depth x:

$$S_D(x) = \int_x^\infty f(x') \; S_L[E_1(x'-x)] \; \frac{dR(x'-x)}{dx'} \, dx' \qquad 15$$

where $E_1(x)$ = average energy of an ion whose projected range is x

$S_D(x)$ = average energy deposited into displacements as the ion travels a projected distance dx

$RI(x)$ = total range of ion

with the total amount of energy to displacements being

$$S_L(E) = N \int_0^{T_M} T \, \eta(T) \, d\sigma \, (T) \qquad 16$$

Manning and Mueller assume a Gaussian range distribution given by

$$f(x) = \frac{1}{\sqrt{2\pi}\ \alpha_x} \exp\left(-\frac{(x-x_m)^2}{2\ \alpha_x^2}\right) \qquad 17$$

with α_x = RMS standard deviation in the projected range. The value of $d\sigma(T)$ is calculated from LSS theory (eq. 7), and $\eta(T)$, which is the fraction of PKA energy dissipated into displacements, is obtained from the representation of Lindhard (37):

$$\eta(T) = [1 + kg(\varepsilon)]^{-1} \qquad 18$$

with the numerical solution of $g(\varepsilon)$ fit by Robinson to (38)

$$g(\varepsilon) = \varepsilon + 0.40244\varepsilon^{3/4} + 3.4008\varepsilon^{1/6} \qquad 19$$

The quantity dR/dx relates the total range to the projected range and is evaluated by an interpolation technique.

Once the nuclear energy deposition is known, the number of displacements can be calculated using a modified Kinchen and Pease model of Torrens and Robinson (39) of the form

$$R_d = \frac{J}{N}\ \frac{\kappa\ S_D(x)}{2\ E_D} \qquad 20$$

where J is the ion flux. The form of Equation 18 was recommended by an IAEA task force as the standard for estimating the number of displacements during irradiation (40). κ is a factor termed the displacement efficiency, and is used to account for the displacement events that are not elastic. Computer calculations of Torrens and Robinson (39) have found that κ is usually of the order of 0.8. E_d is the mean displacement energy and can be visualized as the average energy that must be transferred to an atom to displace it from its site. In reality, E_d is strongly dependent on the crystallographic direction in which the atom is displaced, and the use of a single value for E_d is a spherical average of the saddle points in the potential barrier surrounding the equilibrium site. In most heavy ion experiments, however, the use of a single value for E_d probably does not lead to large errors since most displacements are caused by relatively high energy events which swamp much of the directional dependence. In nickel, the minimum displacement energy was found to be 24 eV (41), and for a first approximation, a multiplying factor of 5/3 is used to correct this threshold value for such things as directional dependence and spontaneous recombination events (42). This gives a mean displacement energy for nickel of 40 eV, which is consistent with other work on nickel (43). Note that in this treatment, E_d is assumed to be a constant. In reality, E_d may depend on the local defect concentration. For example, E_d in the region of a dense displacement cascade may be different than the value of an isolated displacement event.

A somewhat different approach to these damage calculations is taken by Brice (44). For the electronic stopping terms, he uses a three factor formula with the coefficients determined by fitting experimental range data. This procedure can be used successfully to much higher energies than the Lindhard treatment and is necessary for calculations involving relatively light ions such as carbon. Brice also calculates the energy transported by the energetic recoils. This code has been adopted for use on the U.W. computer system, and the result obtained for the case of 14 MeV nickel ion incident on nickel is shown in Figure 2. The 14 MeV ion has a predicted range of about 2.0 micrometers and the damage varies approximately a factor of 10 from the front surface to the peak region. The dip in the damage curve at the surface is due to the energy transport feature of the code. When the damage region is viewed in cross section, knowing the variation in damage level with depth is of critical importance in trying to fully understand the microstructure. The accuracy of the LSS treatment is discussed by Manning and Mueller, and they generally observed agreement with experimentally observed ranges to within approximately 20%. Other experiments using a variety of projectile - range combinations have shown agreement within 20%, (45) and for heavy ions transversing heavy metals, the agreement was usually within 10% (46). A recent review by Robinson, (47) however, questions the assumptions of LSS used in determining the electronic energy loss. Robinson believes the electronic

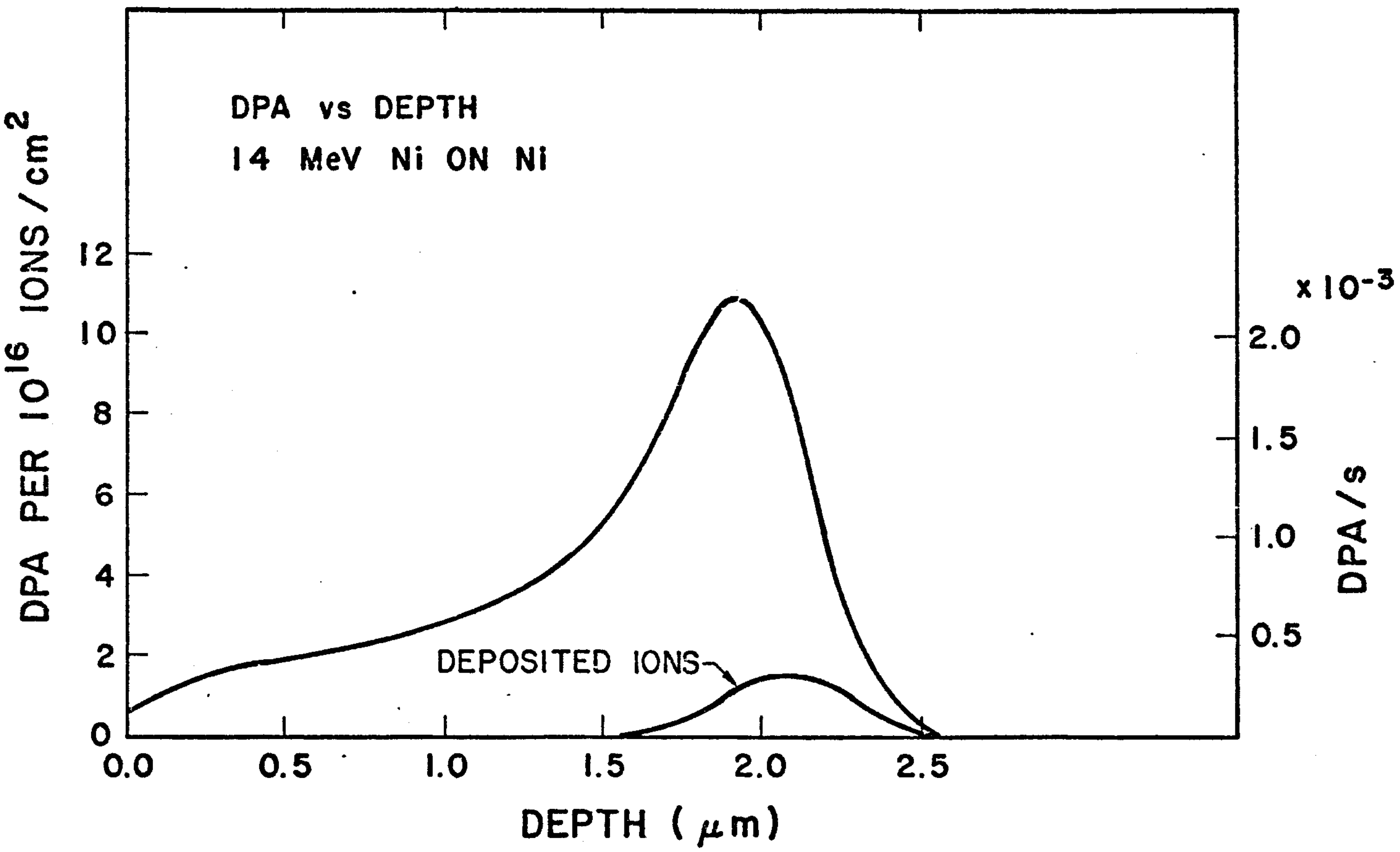

Figure 2. Displacement damage versus depth for 14 MeV nickel ions incident on nickel as given by Brice. The right hand axis gives the displacement rate for an ion flux typical of this study (2×10^{12} ions/cm^2/sec). The relative distribution of the deposited ions is also shown.

stopping is directly proportional to the ion velocity below an energy of approximately

$$Q = (27.211)\ M_1 Z_1^{1.376}\ (\mathrm{eV}) \qquad 21$$

This value for nickel is only 157. KeV. Above this energy, Robinson believes the electronic energy loss must increase faster than given by LSS. If this description is correct, then not only will the damage energy be lowered from the LSS value, but the spatial distribution of the damage will be altered. Experimental measurements of the electronic energy loss performed using helium and iodine incident on various targets have found oscillations in the stopping power with the Z of the target (134). These oscillations show a local minimum at a Z of 28 to 29 and if a similar behavior holds for all incident ions, it would indicate a lower energy loss rate into nickel and hence a longer range. A final answer to this question must await further experimental measurements of the electronic energy loss.

The other assumptions inherent in calculating the curve of Figure 2 are: 1) the electronic excitation does not contribute to atomic displacements, and 2) the target density remains constant. The neglect of the electronic contributions is probably correct since the maximum energy transferred to the relatively light electron by a scatter with an ion is too small to displace lattice atoms. Since we are concerned with metals, any disturbance in the electronic configuration caused by the passing ion should recover rapidly and not affect the structure stability. The target density does change as voids are formed, and once the swelling has been measured, the energy loss equations can be corrected easily (48).

B. PKA Spectra and Collision Cascades

When correlating neutron irradiations to ion simulation results, the next refinement to the calculation of the gross number of defects produced (as was done in the previous section) would be an analysis of the spatial distribution of these defects and the determination of the number of defects surviving the initial cascade. Under neutron or ion irradiation, many of the lattice atoms displaced by interactions with the incident particle are given energies well in excess of E_d, and thus can travel through the lattice producing subsequent displacements. The energy of these primary knock-on atoms, or PKA's, is usually less than a few KeV. At these energies, the mean free path between displacement collisions for the PKA becomes the order of the lattice spacing (49,50). This dense collection of defects, called a collision cascade, may contain several hundred defects, and due to the small volume of the cascade, the final state of the defects (i.e., the fraction that either recombine or cluster) would be expected to be quite different from a case where the same number of defects were produced uniformly throughout the lattice.

In a qualitative sense, a collision cascade might be expected to consist of a vacancy rich core, called the depleted zone, surrounded by a shell with a high interstitial concentration. In a crystal, there are certain directions in the structure which are relatively open and can allow an energetic particle to channel through the crystal without causing displacements. If a particle is ejected in one of the crystals close packed directions, it can initiate a sequence of replacement collisions and form a dynamic crowdion. The dynamic crowdion (also called a focused replacement event) along with channeling, both tend to increase the distance traveled by an ejected atom. This increased separation of interstitials and vacancies will reduce the amount of cascade annealing that takes place and leave more defects free to migrate through the lattice. Various attempts to quantify the cascade details by computer simulations have been made (39,51). In these calculations, an energetic ion is introduced into a crystal and the ion energy allowed to dissipate by collision events. Spontaneous recombination of unlike defects is allowed if they come within next nearest neighbors lattice sites. It is the results of these types of calculations that led to the factor of $\kappa = 0.8$ used in the previous section to correct the displacement calculations for in-cascade recombination.

These calculational techniques have been expanded to take the cascade configurations and, by a Monte Carlo method, allow the defects to thermally diffuse and anneal. Doran (52) has developed such a code and he found that approximately 80% of the defects left at the end of the collision cascade event would be annihilated during a short term anneal at 800°K and of the defects that did survive, only 1/3 of the vacancies and 1/2 of the interstitials survived as isolated defects. The remainder of the defects clustered into groups containing up to eight defects.

These computer calculations suffer from the lack of an accurate atomic potential to describe a real system. For example, Norgett (53) has repeated the cascade generation and anneal stages allowing for the focused replacement events which were restricted by Beeler. Norgett found an upper limit of ~25% recombination for the short-term cascade anneal, which was in general agreement with the experimental results of Merkle and Averback (54). Merkle and Averback estimated the in-cascade annealing by measuring the size distribution of the defect clusters produced by the low energy self ion bombardment of gold and silver. They found that about 40% of the vacancies survived the cascade and formed visible defects, and in some cases, they observed almost 100% survival. These results imply very efficient transport of the interstitials away from the depleted zone by focusing or some other mechanism, while the resistivity recovery experiments of Blewitt et al. (55) in ordered Cu_3Au found only 10% of the vacancies surviving the cascade. These results may not be inconsistent since focusing is a structure sensitive phenomenon and may be limited in the Cu_3Au alloy. If this is the case, then calculations of the number of surviving defects in a material may depend both on the major alloy composition and on the impurity levels.

The PKA energy spectrum from heavy ion bombardment can be calculated in a straightforward manner using Equation 6 of LSS theory and the approximation of Equation 7 (56). These calculations were carried out for 14 MeV nickel ions incident on a nickel target and are shown in Figure 3. Also shown in this figure is the PKA spectrum for nickel bombarded with 14 MeV neutrons (57). Note that this calculation does not include the backscattered neutrons that would be present in any actual CTR or neutron production device. The heavy ion irradiation fails to reproduce the resonant behavior of the neutron spectrum, and also gives more low energy collisions.

Another important feature of the PKA spectra is the variation in the spectrum with both the mass and the energy (and therefore the depth of penetration) of the incoming heavy ion. In Figure 4 is shown the PKA energy spectra at two depths for a 14 MeV nickel ion, a 8.1 MeV aluminum ion and a 5 MeV carbon ion incident on a nickel target. Due to the inverse energy dependence of the cross section, it can be seen the density of cascades initiated by a given energy of PKA will be greater for the lower energy ion up to the maximum energy transfer possible by the ion. The high energy ion does create a few very high energy cascades. These cascades, however, will probably not affect the final damage structure since they will subdivide into several separate, lower energy cascades typical of a lower energy PKA instead of creating a large "super" cascades (58) with unique damage properties.

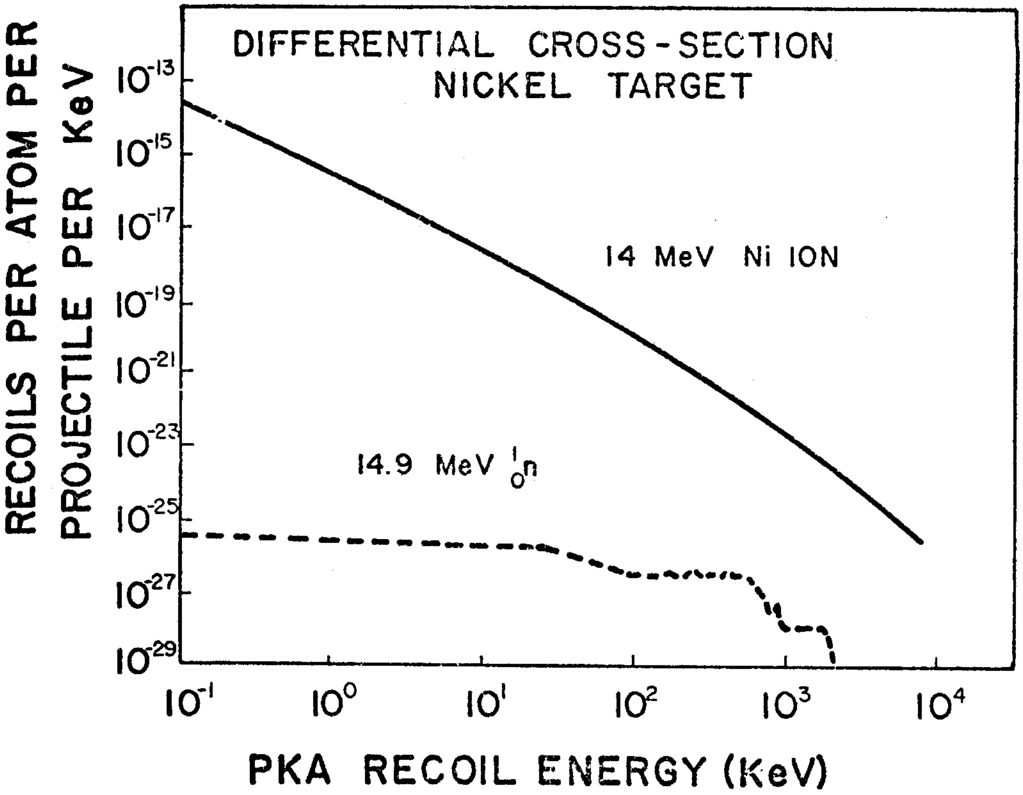

Figure 3. The differential displacement cross-section for a 14 MeV nickel ion (solid curve) and for a 14.9 MeV neutron (dashed curve) incident on a nickel target. The neutron curve was calculated by Avci (57).

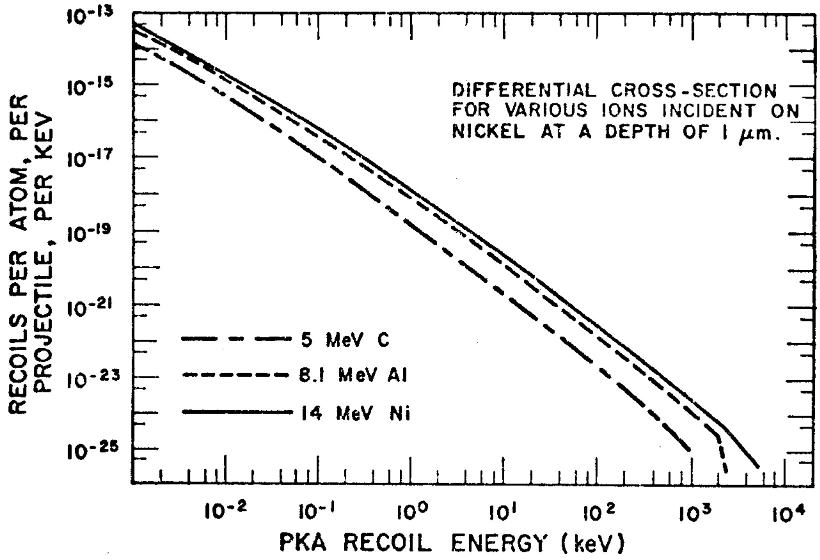

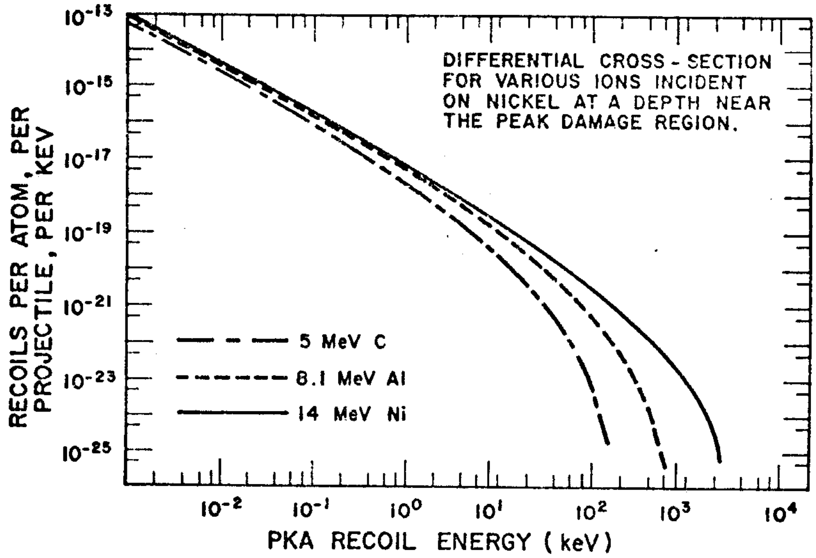

Figure 4. Differential cross-section for 14 MeV nickel ions, 8.1 MeV aluminum ions, and 5 MeV carbon ions incident on nickel at two depths into the target (Note that these ions all had a mean range of about 2 micrometers into nickel.

C. Cluster Formation

Defect clusters such as voids and loops form in materials due to the non-equilibrium density of defects created in the lattice by the irradiation. The degree of departure from equilibrium is given by the supersaturation

$$S_{i,v} = C_{i,v} / C_{i,v}^{eq} \qquad 22$$

where $C_{i,v}$ is the radiation induced concentrations of interstitials or vacancies and $C_{i,v}^{eq}$ is the concentration of defects in a crystal at equilibrium without irradiation. The calculation of $C_{i,v}$ involves the solution of a series of rate equations which balance the defect production and loss rates. These rate equations will be discussed in detail in the next section. Until then, the defect concentrations will be assumed to be known from appropriate calculations.

There are four general requirements necessary for void swelling to develop in a material. They are: 1) the crystal must have a vacancy supersaturation, 2) the vacancies must be mobile, 3) voids must nucleate, and 4) more vacancies than interstitials must enter the void. The first requirement places an upper limit on the temperature range of void formation since the thermal vacancy concentration C_v^{eq} is increasing exponetially while C_v is decreasing due to the increased vacancy mobility at higher temperatures. Hence the supersaturation S decreases rapidly above ~0.5 T_m (where T_m is the absolute melting temperature of the material). The second requirement, that of vacancy mobility, places a lower temperature limit on swelling. In most materials, vacancies start becoming mobile above approximately 0.2 T_m. The fourth requirement is necessary since a void, if it is to grow, must have a net flux of vacancies into it. This imbalance of point defect currents into the void can exist if there are other sinks in the system which preferentially attract interstitials. It is now generally accepted that dislocations play this role. Theoretically, this interaction can be estimated if the strain field due to the point defects is substituted into Ham's solution (59) for the diffusion of defects in the stress field of a dislocation. Due to the larger strain field of the interstitial, it has a preferential drift to the dislocation (see also ref. 60). Note that this analysis assumes the effectiveness of the dislocation as a sink is limited only by point defect diffusion to the sink, and not by point defect absorption at the dislocation. Even if the dislocation climb was absorption limited, the net effect would be the same if the absorption of an interstitial is easier than the absorption of a vacancy.

The third requirement of void nucleation is stated simply because of the experimental observation that not all metals form voids. For example, voids have not been observed in irradiated gold or zirconium, implying that even though a large vacancy supersaturation existed in the proper temperature range, the nucleation of stable voids was very difficult. Some of the current thought regarding the nucleation of both voids and loops will now be discussed.

The nucleation processes that are normally mentioned can be classified into two general categories, namely homogeneous or heterogeneous. In homogeneous nucleation, the small clusters form by chance encounters of individual defects undergoing random walks in the solid. These clusters may either grow by adding a like defect, or may shrink by emitting a like defect or by absorbing an opposite type defect. Above a certain critical size, the probability of a cluster absorbing a like defect and growing becomes larger than its probability of shrinking. The rate at which clusters achieve this critical size determines the nucleation rate.

Heterogeneous nucleation refers to the appearance of clusters on existing structural features of the material. For example, heterogeneous nucleation sites might include such things as dislocations, precipitate particles, and gas bubbles. The depleted zones created in a displacement cascade might also serve as a nucleation site, even though the nucleation of voids during electron bombardment, where no spikes are formed, indicates that these zones are not a requirement for void formation. The relative importance of homogeneous vs. heterogeneous nucleation has been discussed by several authors (2,61-63) and evidence exists for both mechanisms. The experimental observation that neither voids or loops nucleate on grain boundaries indicates the importance of a large defect supersaturation in driving nucleation since grain boundaries, which are favorable sites for void nucleation due to a lower surface energy barrier, also serve as point defect sinks and thus drastically reduce the defect concentration in the surrounding matrix.

All studies of void nucleation emphasize the importance of helium on void formation. Helium is formed during fast neutron irradiation in virtually all materials from various (n,α) type reactions. Various experiments have been performed where helium was implanted in the material prior to irradiation (2,64). In general, the increased helium content resulted in an increased void concentration, but not in increased swelling. The presence of helium is not a requirement for void formation, however, since voids can be formed in pure metals during ion irradiation without helium implanting. In the early stages of void studies, helium was thought to play an important role in stabilizing the small void embryos and prevent their collapse into vacancy loops (1). Bloom et al. (63) have reviewed the role of helium and conclude that the helium may also promote void formation by the enhanced formation of interstitial loops. They do not propose a mechanism to explain how helium would enhance loop formation, but their observation serves to emphasize the importance a proper understanding of the role the developing dislocation structure plays on void nucleation.

In most cases, void nucleation probably occurs by a combination of homogeneous and heterogeneous nucleation, with helium and other impurities assisting the nucleation process by precipitating out simultaneously with the vacancies. Attempts were made by Katz and

Wiedersich (65) and by Russell (66) fairly quickly after the discovery of voids to develop a theory for the homogeneous nucleation of voids in the absence of gas. The development of this theory was not a matter of simply modifying classical nucleation theory since a material under irradiation not only contains a vacancy supersaturation, but also a supersaturation of the vacancy anti-particle, the interstitial. In classical nucleation theory, a cluster can change size by the addition or loss of a monomer of a single species (see, for example, ref. 67). A void, however, can grow by either absorbing a vacancy or emitting an interstitial, and can shrink by emitting a vacancy or absorbing an interstitial. If helium or some other mobile impurity is allowed, the nucleation process will then involve three species and become quite complicated. It is possible to modify classical nucleation theory to include the effects of interstitials if one accounts for the destructive influence of interstitials on the void nuclei by defining an effective free energy for the voids. At a certain critical void size r_v^{crit}, the free energy of the void is a maximum. Above this critical void size, the void is more likely to grow than shrink. Hence, the nucleation rate, J, is the rate at which sub-critical clusters achieve this critical size and for a void of radius r_v^{crit}, containing n_v^{crit} vacancies and n_g gas atoms, it is given by (68)

$$J = ZD_vC_vN_o\exp\left[\frac{-\Delta G'(n_v^{crit}, n_g)}{kT}\right] \qquad 23$$

where $\Delta G'$ is the effective free energy of the critical cluster, C_v is the vacancy concentration, D_v the vacancy diffusion coefficient, N_o the number of possible nucleation sites, and Z the Zeldovich factor which is proportional to the curvature of the free energy vs. void size curve.

In classical nucleation theory, the critical cluster size and its free energy can be found by applying equilibrium thermodynamics. Under irradiation, the crystal is driven into a highly non-equilibrium state, and attempts to define an equilibrium distribution of voids are difficult (69). To overcome this problem, Wiedersich has proposed a generalized theory of void nucleation that does not require the assumptions and simplifications inherent in classical nucleation theory (70). The general rate equation describing the nucleation and growth of any second phase cluster can be obtained from the following reaction rate equation for a type j cluster of concentration C_j

$$\frac{dC_j}{dt} = \sum_k k_{k\to j}\, C_k - \sum_k k_{j\to k}\, C_j + K_j - L_j \qquad 24$$

$$j = 1,2,3,\ldots$$

where $k_{k\to j}$ is the rate constant that gives the probability a cluster of type k will be converted into a cluster of type j, K_j is the rate at which clusters of type j form directly (such as a vacancy cluster formed in a displacement spike), and L_j is the loss rate of clusters or defects to sinks other than the allowed clusters (for example, the loss of vacancies or di-vacancies to grain boundaries). In the case of void nucleation in the presence of helium, a type j cluster will contain m_j vacancies and n_j gas atoms. The rate constants for the steps in phase space must be derived from considering the appropriate models. For example, a void containing x vacancies can increase in size to x+1 vacancies by either absorbing a vacancy, or by emitting an interstitial. This process is represented by

$$k_{x \to x+1} = A(x)\ C_v \nu_v a_v + A(x)\ g_i(x) \qquad 25$$

where A(x) is the surface area of the void, ν_v the vacancy jump rate, a_v a geometric term (note that $C_v \nu_v a_v$ is the vacancy flux per unit area), and $g_i(x)$ the interstitial emission rate per unit area of void surface. Due to the large formation energy of interstitials, this last term is usually neglected. The rate constant for the inverse process, that of a void of size x+1 shrinking to size x is given by

$$k_{x+1 \to x} = A(x+1)\ C_i \nu_i a_i + A(x+1)\ g_v(x+1) \qquad 26$$

As was the case before, the first term gives the rate of interstitial absorption, while the second term is the rate of vacancy emission. The vacancy emission term is important and can be calculated by considering a detailed chemical balance (65). In this method, the void is considered to exist in a crystal at equilibrium containing a

Boltzman distribution of voids. By invoking detailed balancing, which requires the rate of vacancy emission (which is unknown) to equal the vacancy absorption rate (which is now known since the vacancy and sink concentrations are known), the vacancy emission can be shown to be

$$g_v(x+1) = C_v \nu_v a_v \exp\left[-\frac{\Delta F}{kT}\right] \qquad 27$$

where ΔF is the free energy change when a cluster shrinks by one vacancy and is given by (71)

$$\Delta F = kT\ell nS + \Delta(\text{surface energy}) + \Delta(\text{work on gas}) \qquad 28$$

The first term is the chemical potential of the vacancy, the second term the surface energy times the reduction in area due to shrinking, and the last term the work due to the compression of any insoluble gas contained in the void. For this last term to be significant, relatively high gas pressures are required and hence a proper equation of state must be used to calculate the pressure increase. These high pressures are also the reason why only insoluble gases (i.e., He, Ar, H_2O, etc.) contribute to this term. The soluble gases, such as hydrogen or oxygen, are probably more important in changing the surface energy of the void.

The other rate constants necessary to describe the system can be found in a similar manner. For example, the role of gas atoms and mobile di-vacancies could be easily included. Even though

Eq. 24 is completely general, it must be realized that the calculation of the various rate constants involves many inherent assumptions about the microscopic processes. For example, the rate constants derived for a void assumed the vacancy admission into a void was limited by the diffusion of vacancies to the void and not by the absorption of the vacancies. Likewise, the calculation of the vacancy emission term assumed the rate of vacancy emission during irradiation was equal to the vacancy emission rate under equilibrium conditions. If the vacancy emission depends on microscopic details such as the step density of the void surface, then the emission rate may increase with the vacancy supersaturation. It has also been assumed that the voids are unbiased sinks, i.e., they have no net attraction for either interstitials or vacancies. Recent calculations by Wolfer and Yoo (72) find that small voids may have a significant bias for interstitials. This bias, which is due to an image force interaction, leads to a drastic reduction in the predicted nucleation rate and they conclude that void nucleation is possible only if impurity segregation around the void reduces the interstitial bias. These effects, along with others as they are discovered, should be considered in a proper derivation of the rate constants.

Soluble impurities, such as hydrogen, can strongly affect void nucleation. The effects of a surface active impurity on void nucleation was calculated by Russell (69,73) who used a simple absorption model which assigned a lower energy, E_b, to the absorbed atoms giving a surface energy

$$\sigma(C_x) = \sigma(0) - n_s kT \ \ell n(1 + C_x \exp(\frac{E_b}{kT})) \qquad 29$$

where $\sigma(C_x)$ and $\sigma(0)$ are the interfacial energies with and without absorption, n_s the number of possible surface sites per unit area, and C_x the matrix solute concentration. Russell's calculations for $C_x = 10^{-3}$ found that the void nucleation rate would be increased substantially if $E_b \gtrsim 0.3$ eV. Wolfer and Yoo (72) also calculated void nucleation rates assuming various surface energies and found the nucleation rate to be very sensitive to the surface energy, with a 10% reduction in the surface energy leading to an increase in the nucleation rate of several orders of magnitude.

So far this discussion has centered on the nucleation of voids. Void nucleation, however, is preceded by the development of a dislocation structure, a structure which normally includes interstitial loops. The importance of these small interstitial loops on the point defect balances was shown by Wolfer et al. (72) who found that the interstitial bias of a small dislocation loop is much greater than the bias term for a straight edge dislocation. Thus, the presence of these small loops in the matrix will lead to a larger arrival rate of vacancies to the void nuclei, and hence make their growth more probable. The time dependent nucleation of interstitial loops was treated quantitatively by Hayns (74,75) who numerically solved Eq. 24. In deriving the rate constants, Hayns assumed the di-interstitial was stable and could not thermally dissociate. With this assumption, the problem is not actually one of nucleation since there is no free energy barrier to overcome to form a stable nuclei. Hayns also ignores vacancy emission by the loops and di-interstitial motion. Modifying these assumptions would probably have little effect on his final results, however, and he found the loop concentration to rise very quickly and saturate at a level determined by the preirradiation microstructure, the temperature, and the dose rate. This saturation level is given by Eyre (68) as

$$C_L^i = C_o^i K^{1/2} \exp\left[\frac{-E_m^i}{2kT}\right] \qquad 30$$

where K is the displacement rate, E_m^i the interstitial migration energy, C_o^i a geometric constant, and C_L^i the interstitial loop concentration.

In a pure metal under irradiation, none of the present theories allow the nucleation of vacancy loops due to the strong interstitial bias calculated for the small loop nuclei. In an alloy, or in the presence of impurities, it may be possible for segregation to relieve the strain field of the loop and reduce the interstitial bias, allowing vacancy loops to form. The athermal collapse of the depleted zone of a displacement cascade has also been proposed as a mechanism leading to vacancy loop formation (68). In this model, the interstitials are assumed to be transported out of the spike by focused collision events, and some of the resulting vacancies left in the core rearrange themselves into small loops. Unless the interstitial bias is reduced, these loops will eventually be destroyed by the net interstitial flux into them.

As a final note on defect formation, it is important to realize that the microstructure is in a state of constant evolution during the initial stages of the irradiation, and as such, any steady state calculation of the nucleation rates will probably not be valid over long time periods. As the radiation induced cluster population grows, the number of sinks available for the point defects increases, leading to a reduction in the supersaturation. Eventually, this supersaturation will be reduced to a level incapable of nucleating new defects, and at this time, the microstructure will continue to develop and interact without adding appreciable numbers of new defect clusters. From this analysis, one would expect the final defect density at saturation to be dependent on the dose rate, an effect very important for simulation studies and one that has only recently been treated theoretically (76).

D. Void Growth

Once the initial distribution of supercritical clusters is determined, the next step to calculate the swelling is to find the defect growth rate. There have been two approaches to the void growth problem, namely the cellular model of Bullough and Perrin (77) and the rate theory models of Harkness and Li (78), Wiedersich (79), and Brailsford and Bullough (80). These two approaches are similar and differ basically in the details of the sink strength calculations. The following discussion will center on the rate theory model of Brailsford and Bullough (BB) (80) since it is mathematically simplier and more physically correct.

The basic assumption of rate theory is that a discrete, random array of sinks can be approximated by an appropriate continuum of sinks. This replacement of a set of discrete sinks with a continum means that the derived rate equations will contain an implied spatial averaging over distances greater than the average sink spacing and an average over a time interval greater than the average cascade lifetime (81). The essential hypothesis of the analysis will be that voids grow because another sink exists (assumed to be dislocations) which has a slight preference for interstitials. Since the irradiation produces the same number of free vacancies and interstitials (except for certain cases which will be discussed later), this depletion of interstitials will lead to a net flow of vacancies to the unbiased sinks (i.e., voids) and hence to void growth. For our purposes, the production rate of free defects will be assumed to be equal to the displacement rate. In practice, this production rate will depend on the details of the displacement cascade.

The basic equations relating the loss rate of vacancies and interstitials in the medium to their production rate are

$$\frac{dC_i}{dt} = \nabla D_i \nabla C_i + K_i - D_i C_i k_i^2 - \alpha C_v C_i \qquad 31$$

and

$$\frac{dC_v}{dt} = \nabla D_v \nabla C_v + K_v - D_v C_v k_v^2 - \alpha C_v C_i \qquad 32$$

where $K_{i,v}$ is the effective production rate of point defects and includes those produced by the irradiation plus the defects emitted by sinks, C_i and C_v are the average fractional interstitial and vacancy concentrations, the D's are diffusion coefficients, and α is a homogeneous recombination coefficient. The quantity DCk^2 is the loss rate of defects to all sinks, where k^{-1} is the mean free distance a defect travels before entering a sink. The k's must be determined by referring to an appropriate model.

The method used to determine the strength of each sink (i.e., its k_n) was to consider the flow of defects to the sink with the sink approximated by a sphere of radius r_{s1}, surrounded by a sink free region of radius R_1, with this region enclosed in an infinite medium containing a homogeneous distribution of the sinks of the system. This method has the desirable feature of linking the correct local environment (that is, that sinks do not usually lie immediately next to each other) with the continuum approximation. Neglecting recombination, the steady state concentrations of defects are described by the equations:

$$D\,\nabla^2 C + K = 0 \quad \text{for} \quad r_{s1} \leq r \leq R_1 \qquad 33$$

and

$$D\,\nabla^2 C + K - DCk^2 = 0 \quad \text{for} \quad r > R_1 \qquad 34$$

The boundary condition at the sink interface ($r = r_{s1}$) is given by

$$D\,\frac{dC}{dr} = \overline{K}\,(C - \overline{C}_1) \qquad 35$$

Here, $\overline{K}$ is the transfer velocity of the defects across the interface. The analysis of BB assumes this transfer rate is the same as the defect motion in the lattice, that is, that $\overline{K} = D/b$. If the absorption of the defect by the sink occurs with an activation enthalpy of ΔE_m, then $\overline{K}$ would have the form (82)

$$\overline{K} = \frac{D}{b}\,\exp\left[-\frac{\Delta E_m}{kT}\right] \qquad 36$$

The term $\overline{KC}_1$ represents the jump rate of defects out of the sink per available site (i.e., thermal emission), where

$$\overline{C}_1 = C^{eq}\,\exp\left[\frac{\Delta E}{kT}\right] \qquad 37$$

with C^{eq} the thermal equilibrium concentration of defects and ΔE the change in energy of the sink when the defect is emitted. For voids, $\overline{C}_1$ will depend on such things as the surface energy and the internal gas pressure, while for dislocation loops the term will depend on the stacking fault energy and the change in dislocation line length by an emission. For all metals of practical interest, the formation energy for interstitials is so high that their thermal emission can be neglected.

The final boundary conditions on Eq. 33 and 34 are that the defect concentration and its first derivative must be continuous at $r = R_1$. BB solved these equations assuming no surface reaction energy and found

$$k^2_{\text{void}} = 4\pi\, r_s C_s \qquad 38$$

and

$$k^{2\ i,v}_{\text{dislocation}} = Z_{i,v}\, \rho_d \qquad 39$$

where ρ_d is the total dislocation density and C_s the concentration of voids. For finite surface transfer kinetics, the void sink term is given by (82)

$$k^2_{\text{void}} = \frac{4\pi\, r_s C_s}{(1 + \frac{D}{\bar{K} r_s})} \qquad 40$$

Note that this case contains a term proportional to the void surface area. To account for the existence of biased sinks in the system, the radius of that sink is increased by a factor $Z_{i,v}$ such that this effective sink radius will correctly describe the defect flux to the sink. The absolute magnitude of Z_i and Z_v is difficult to calculate, but is really not needed since the important term is

$(Z_i - Z_v)$. This term, which is the net drift rate of interstitials to the biased sink, is usually taken as 0.01 - 0.02. Some recent studies (72,83) have used values of $(Z_i - Z_v)$ as large as 0.25. With the sink strengths known, Equations 31 and 32 can be solved to give the defect concentrations in the matrix. The swelling rate can now be found directly by finding the net flow of defects into the void sinks, given by

$$\frac{d}{dt}\left(\frac{\Delta V}{V}\right) = (D_v C_v - D_i C_i - D_v \bar{C}_i)\, 4\pi\, r_s C_s \qquad 41$$

Brailsford and Bullough solved Equation 41 for various cases and found that the peak of the swelling versus temperature curve would shift to higher temperatures when the dose rate was increased. This shift of the temperature dependence of swelling to higher temperatures under high displacement rates has been observed experimentally and can be visualized by the following process. At a given temperature and low displacement rate, a certain fraction of the defects recombine and the rest are partitioned among the various sinks. If an identical system at a higher displacement rate is studied, the fraction that recombine will have increased due to the increase in C_v and C_i. A similar increase in recombination could be achieved by lowering the temperature of the low dose rate case. If the ratio of the number of defects entering a sink to the number recombining is the important parameter, the high dose rate microstructure will be indicative of a lower "effective" temperature when compared to a low dose rate structure. Using this type of reasoning, an estimate of this shift in temperature can be derived by BB theory in the following manner (84). For this case, let us assume a lower temperature regime where thermal emmission of defects is negligible. Solving Equations 31 and 32 in steady state gives

$$C_v \simeq \frac{D_i k_i^2 C_i}{D_v k_v^2} \qquad 42$$

At low temperatures, recombination dominates; hence

$$K - \alpha C_i C_v \simeq 0$$

or

$$C_i \simeq \left[\frac{K D_v k_v^2}{\alpha D_i k_i^2}\right]^{1/2} \qquad 43$$

Now define ξ as the ratio of the rate of vacancy loss to sinks divided by the rate of vacancy loss to recombination, i.e.,

$$\xi = \frac{D_v k_v^2 C_v}{\alpha C_i C_v} = \frac{D_v k_v^2}{\alpha C_i} \qquad 44$$

Substituting expressions for $D_{i,v}$ and α gives

$$\xi = \text{constant} \times \left[\frac{k_i^2 k_v^2 \exp\left(-E_v^m/k_B T\right)}{K}\right]^{1/2} \qquad 45$$

The relationship that gives the temperatures necessary to keep ξ a constant when the dose rate changes from K_1 to K_2 is

$$\frac{1}{T_1} = \frac{1}{T_2} - \left(\frac{k_B}{E_v^m}\right) \ln \left[\left(\frac{k^2_{i,2}}{k^2_{i,1}}\right) \left(\frac{k^2_{v,2}}{k^2_{i,1}}\right) \left(\frac{K_1}{K_2}\right) \right] \qquad 46$$

where E_v^m is the vacancy migration energy, k_B the Boltzman constant, and the subscripts 1 and 2 refer to the two irradiation conditions being compared. Similar expressions have been derived for the lower and upper swelling cutoff temperatures (84). For $T_1 = 500°C$, $k^2_{1,v} = k^2_{2,v}$, and $K_1/K_2 = 10$, this equation gives a temperature shift of 53°C.

Before concluding this section on void growth, some of the recent advances in rate theory should be mentioned. One major assumption of the theory as described to this point has been that the defects were produced homogeneously throughout the lattice. During irradiation with neutrons or heavy ions, a different situation results. In this case the PKA's will generate displacement cascades and, if the interstitials are transported away from the cascade center by a focused collision process, a region of very high vacancy concentration will result. Eyre has observed small vacancy loops in a number of materials after heavy ion irradiation and suggests that these loops form by the collapse of the vacancy rich cascade cores (85). The implications of these clusters on swelling theory have been discussed by Straalsund (86) and Bullough (83). Bullough accounts for the cluster formation by assuming a certain fraction (ε) of the radiation induced vacancies form loops. These loops are then added to the other dislocation sinks of the system. The vacancy loops will shrink by the emission of vacancies and by the preferential absorption of interstitials. After some incubation time, the concentration of vacancy loops will reach a steady state value determined by the loop lifetime. The importance of these loops on the swelling behavior of a material arises from the temperature dependence of the loop lifetime. At high temperatures, the loop lifetime will be short due to its rapid thermal emission of vacancies. Hence, the steady state concentration of vacancy loops will be low and they will not substantially affect the swelling behavior of the material. At low temperatures, thermal emission of vacancies will be negligible, and the vacancy loops will shrink primarily by the absorption of interstitials. Thus, their steady state concentration will be high and they will serve to reduce the fraction of vacancies free to migrate to voids. With this model, Bullough (83) has had reasonable success in correlating HVEM irradiation studies, which have no displacement spikes and begin swelling at low temperatures, to heavy ion irradiated samples, which have large numbers of spikes and begin swelling at higher temperatures. The next important refinement to this theory will be a study of the effects of material parameters, such as impurity levels, on the spike collapse mechanism to see if this theory can help explain the swelling behavior of some of the poorly understood alloy systems.

Wolfer et al. (81) have recently shown that the rate equations governing void and loop growth can be condensed into Fokker-Planck equations. These equations have both nucleation and growth properly incorporated into a unified formalism. Briefly, these equations are derived by rewriting Equation 24 with the void size variable x treated as a continuous variable. For large void sizes, the size functions f(x,t) are expanded using a Taylor series, giving

$$\frac{\partial f(x,t)}{\partial t} = - \frac{\partial}{\partial x} [F(x) - \frac{\partial}{\partial x} D(x)] f(x,t) \qquad 47$$

This Fokker-Planck equation for the evolution of a size distribution has the form of a generalized diffusion equation, with D(x) a space-dependent diffusion coefficient and F(x) a drift force. F(x) is the familiar term describing the void growth rate (Equation 41) and gives the rate of growth of the average void size of the distribution. The diffusion coefficient D(x) describes the rate at which the void size distribution increases its width in size space as the average size increases. Wolfer et al. show that this diffusion term must be included in a description of void growth if the result is to be anything except a constant swelling rate.

E. Effects of Impurities on Void Swelling

As would be expected, the major alloying elements of materials play an important role in determining the swelling behavior of a system. It was discovered relatively quickly, however, that small additions of various "impurity" elements could also strongly affect a material swelling behavior. This sensitivity to small impurity levels is an indication of the rather delicate point defect balances that lead to void nucleation and growth. It may even be that a certain amount of impurities are necessary to allow voids to nucleate at all (72). While the importance of impurities on void swelling is easily seen, the actual mechanism (or mechanisms) by which they affect swelling are not.

When irradiating with heavy ions, it is always necessary to allow the incident ions to stop within the target material since the ion range is so short. For an irradiation using self ions, this will lead to the introduction of excess interstitials near the ion end of range. In most cases, these ions will represent only a small fraction of the irradiation produced damage and are not expected to significantly alter the response of the material except under low swelling rate conditions. If the irradiating ion is not the same species as the target material, the irradiation will lead to a buildup of impurities in the material. These buildups can become significant. For example, if the irradiation indicated by Figure 2 had used copper ions instead of nickel, and assuming the Gaussian distribution of the implanted ions is correct, an irradiation does of 10^{16} ions/cm^2 would lead to a maximum copper concentration of ~0.2% in the deposition region (if diffusion of the copper is neglected). The possible effects of these impurities on swelling will now be discussed briefly.

Several of the effects of alloying impurities have been previously discussed. For example, the introduction of impurities could tend to decrease the length of focused collision events occurring during a displacement spike and thus reduce the separation of the vacancies and interstitials, leading to greater in-spike recombination. The introduction of impurities could also change the surface and stacking fault energies of the material and hence affect both void and loop nucleation and growth. The additional elements could also serve to tie up impurities already present in the material, such as hydrogen, oxygen, or helium, and thus prevent their taking part in void or loop nucleation. The segregation of impurities around either voids or dislocations could modify the point defect interaction energy and affect the bias terms. Norris (87) proposes a mechanism where over-size solute atoms (such as copper in nickel) tend to form atmospheres around dislocations in such a way as to reduce the interstitial bias. The effect of impurity segregation on void growth has been discussed by Brailsford (88), and by Wolfer et al. (72), and Wolfer suggests that impurity segregation may be necessary to reduce the interstitial bias of small voids before voids can form at all.

The introduction of impurities could also lead to a decrease in swelling if the impurities had a significant binding energy to either type of point defect and if the impurity-defect complex was immobile. Under these conditions, the impurities would serve as trapping centers and lead to increased recombination in the matrix. Note that these trapped defects could also serve as heterogeneous nucleation sites. For interstitial trapping, this could lead to a high density of small interstitial loops and therefore to a larger interstitial sink strength which would increase swelling. Smidt and Sprague (89) postulate a vacancy trapping mechanism and show that a binding energy 0.5 eV is sufficient to drastically reduce void nucleation.

Experimentally, there have been many studies of the effects of impurities on swelling, but of particular interest are those involving 1 - 2% additions of copper to nickel (90,91,92). Both Brimhall and Kissinger (92) and Mazey and Menzinger (91) found the 2% copper alloy to swell less than the pure nickel control, while Smidt and Sprague (90) found a 1% copper alloy to swell more than a pure nickel control. The trend observed was for alloying to decrease the void density and increase the void size. Brimhall and Kissinger also observed a higher density of prismatic loops in the alloy system, indicating a possible reduction in the stacking fault energy in the alloy.

The effect of carbon impurities on void formation in nickel was studied by Sorensen and Chen (93,94) who doped nickel with carbon up to ~600 wt. ppm. before irradiating with neutrons at 500°C. They found the void density decreased with increasing carbon concentration while the void size increased. The net result was a reduction in swelling as the carbon level increased, and they attributed this behavior to the trapping of divacancies by the mobile carbon atoms. Void formation was completely suppressed in the ~600 wt. ppm. sample. At 500°C, the solubility of carbon in nickel is ~155 wt. ppm., and hence the pre-irradiated nickel-600 wt. ppm. C sample contained precipitates of Ni-C. After irradiation, these precipitates had dissolved from the matrix, and the primary defects observed were dislocations decorated with precipitates. Ryan[43] irradiated initially high purity nickel with carbon ions and examined the damage in the end of range region. He observed no precipitation and found the void size to be larger and the void number density lower than the corresponding nickel ion irradiated specimen. A double peak in the swelling versus temperature curve was found and attributed to an interaction with the implanted carbon ions.

III. REVIEW OF VOID STUDIES ON NICKEL

A. Neutron Irradiations

Voids, which were first observed in stainless steel, were soon observed in neutron irradiated high purity nickel by Mastel and Brimhall (96). They found that voids formed in pure nickel at total neutron fluences over two orders of magnitude less than the fluence required to form voids in stainless steel and thus illustrated the importance of material parameters on void formation. This study has been followed by numerous other neutron irradiations (21,93-105), and these results are summarized in Table 2. As a word of caution in studying these results, it must be realized that the measure of the total integrated fluence of high energy neutrons is not a direct measure of the total displacement damage since the damage produced is a function of the neutron energy spectrum at the sample position. These experiments were performed in different reactors and in different areas of a given reactor, and any comparison of data based on neutron fluence values must be made cautiously. Besides affecting the amount of displacement damage occurring, the neutron energy spectrum is also important in determining the transmutation rates in the material. This is especially true for studies on nickel due to the ^{58}Ni (n,γ) ^{59}Ni reaction followed by a thermal (n,α) reaction

TABLE 2

NEUTRON IRRADIATED NICKEL

Nickel Purity**	Fluence E > .1 Mev	Temperature (°C)	N_v (x 10^{14}) (cm^{-3})	$\bar{d}$ (Å)	$\frac{\Delta V}{V}$(%)	Comments	Ref.
4N7	$5 \times 10^{19} cm^{-2}$	380	40.	100	0.2	octahedron shape	96
	4×10^{19}	425	20.	100	0.1		
3N8	1.4×10^{20}	385	-	110	-		98
3N8	1×10^{21}	425	-	-	.25	saw little effect of 20% cold work	99
	3.5×10^{21}	425	-	-	.85		
2N6	1×10^{21}	425	-	-	0		
	3.5×10^{21}	425	-	-	0.1		
4N7	5×10^{19}	380	40.	83	.11		97
	1.2×10^{20}	260	400.	55	.30		
4N7	4×10^{19}	50	0	0	0	formed SFT on annealing	100
	1.2×10^{20}	260	200.	60	.21		
	5.7×10^{19}	380	40.	83	.11		

TABLE 2 (Cont.)

Nickel Purity**	Fluence E > .01 MeV	Temperature (°C)	N_v(x 10^{14} cm^{-3})	$\overline{d}$ (Å)	$\frac{\Delta V}{V}$(%)	Comments	Ref.
	5.7×10^{19}	500	8.0	165	.16		
	6.2×10^{19}	575	2.5	245	.17		
4N7	5.2×10^{19}	640	0.8	270	.07		101
	5.2×10^{19}	750	~.001	400	<.001		
3N8	1.4×10^{20}	385	2.9	126	.05	cubic voids	102
3N8	1.4×10^{20}	410	3.2	133	.07	cubic voids	102
	"	440	2.0	151	.06		
	"	470	3.2	160	.08	octahedral voids	
	"	525	2.4	-	-	elongated voids	
	1.1×10^{18}	370	1.2	<60	-	cubic voids	
	3.2×10^{19}	370	2.9	103	-		
	1.5×10^{22}	470	1.0	>300	-		

TABLE 2 (Cont.)

Nickel Purity**	Fluence E > .1 MeV	Temperature (°C)	N_v (x 10^{14}) (cm^{-3})	$\overline{d}$ (Å)	$\frac{\Delta V}{V}$(%)	Comments	Ref.
4N	5.5×10^{18}	285	0.7	50	.00043		92
	1.3×10^{19}	285	1.5	70	.0025		
	2.4×10^{19}	285	3.6	105	0.2		
3N5	2.3×10^{20}	300	40.	90	.18	cold work increased swelling	102
	"	400	8.5	160	0.2		
	"	500	5.8	200	.23		
	"	600	5.0	270	.07		
4N8	2.5×10^{19}	350	1.2	210	.06	studied 3 purities of nickel	104
	"	400	0.5	280	.05		
	"	450	0.4	340	.07		
2N4	2.5×10^{19}	350	Inhomogeneous	-	-		104
	"	400	"	<90	-		
	"	450	"	90	<.01		

TABLE 2 (Cont.)

Nickel Purity**	Fluence E > .1 MeV	Temperature (°C)	$N_V(\times 10^{14}$ $cm^{-3})$	$\bar{d}$ (Å)	$\frac{\Delta V}{V}$ (%)	Comments	Ref.
4N5	2×10^{17}	400	0	0	0		95
	5×10^{17}	"	0.1	-	.0001	cubic voids at	
	1×10^{18}	"	0.2	-	.001	low fluences	
	5×10^{18}	"	1.1	-	.004		
	1×10^{19}	"	2.	-	.02	octahedron voids	
	1×10^{20}	"	20.	-	.3	" "	
4N	4×10^{18}	500	0.2	146	.006	studied effects of C impurity additions	93, 94
	5.3×10^{19}	500	2.5	198	.19		
4N5	5.4×10^{20}	300	11.	93	0.044		21
	5.4×10^{20}	350	12.	186	0.42		
	6.3×10^{20}	400	3.4	293	0.44		
	6.2×10^{20}	450	7.8	203	0.34		
	6.2×10^{20}	500	2.0	265	0.197		

TABLE 2 (Cont.)

Nickel Purity**	Fluence E > .1 MeV	Temperature (°C)	N_v (x 10^{14}) (cm^{-3})	$\overline{d}$ (Å)	$\frac{\Delta V}{V}$ (%)	Comments	Ref.
	69.5×10^{20}	550	0.78	237	0.056		
	6.9×10^{20}	750	0.044	323	0.007		
	10.4×10^{20}	850	0.022	425	0.0086		

**4N7 = 99.99%, 3N8 = 99.98%, etc.

in the ^{59}Ni (105). This reaction chain leads to generation of large amounts of helium in nickel by the thermal neutron flux, and hence the amount of thermal flux in a reactor can strongly affect the swelling behavior without significantly contributing to the displacement damage. Note also that the sample materials are of varying grades of purity, a feature that by itself can strongly affect the swelling behavior.

Voids have been observed in neutron irradiated nickel at temperatures from 260°C to 850°C, and above a neutron fluence of 5×10^{17} n/cm^2. (As a crude estimate of damage, 10^{22} n/cm^2 corresponds to ~5 dpa in EBR-II (43).) The void shapes were either cubic or octahedron, with cubic voids seemingly favored at low temperatures (102) and low fluences (95). At 525°C, Steigler and Bloom (102) observed about one-third of the voids to be elongated in <110> directions with a length to width ratio of 5:1. They also observed a heterogeneous distribution of voids. The maximum swelling temperature was 400-500"C, and cold working had either little effect (99) or led to increased swelling (103).

During irradiation, the dislocation structure developed by the formation of rather homogeneously distributed dislocation loops, followed by a gradual increase in the dislocation density as the loops grew and impinged on each other. The structure was denuded around grain boundaries (100,102) and coarsened with increasing irradiation temperature (102,21). When irradiated at temperatures below 50°C and then given a high temperature anneal, the primary vacancy cluster was found to be stacking fault tetrahedron (104).

Two other interesting results from neutron irradiated nickel were discussed by Levy (106). In the first experiment, a sample of nickel enriched in the Ni-62 isotope was irradiated and compared to a natural isotopic nickel sample irradiated under identical conditions. The post-irradiation microstructure of the Ni-62 sample consisted of a smaller void density and a larger void size than the natural nickel, an observation consistent with the decreased rate of helium production in the enriched sample. The second experiment compared nickel samples irradiated at two different neutron flux levels, the high flux sample seeing about five times the flux level of the other sample. At 250°C, the low flux (i.e., low displacement rate) sample formed voids, while the high flux sample formed regular arrays of vacancy loops and no voids. Apparently the effective temperature of the high dose rate sample was below the lower cutoff temperature for void formation. This experiment emphasizes the importance a proper understanding of dose rate effects has on correlating results, even when comparing neutron irradiated samples.

B. Simulation Studies

Nickel has been extensively studied using both high energy ions (43,84,90,107-116), and the High Voltage Electron Microscope (HVEM, with energies >650 KeV) (117-125). Some of the important results from the ion bombardment studies are given in Table 3. In general, voids were observed in these studies at temperatures ranging from 300°C under proton irradiation (110) up to 725°C under intense Ni ion bombardment (113) with the peak swelling temperature ranging from about 550 to 625°C, depending on the displacement rate. The lowest dose at which voids were reported visible was .06 dpa (116).

Since practically all the experimental and material parameters varied greatly between different experimenters, it is difficult to draw any definite conclusions from a detailed comparison of this data. However, several general observations are important. One of the most interesting features of the irradiation of nickel is the development of regular arrays of defects. At high temperatures, the void structure that is often formed is such that the voids take the atom position of a large fcc superlattice with a lattice spacing of several hundred angstroms. Kulcinski et al. observed a void lattice in nickel after bombardment at 525°C with 6 MeV Se ions (109) and with 6 MeV Ni ions (107) to doses greater than 100 dpa. At low temperatures and low doses, aligned arrays of loops were observed which formed similar superlattices (84,113,115,127). The temperature range for this loop structure was rather narrow, ranging from 300 to 400°C. The formation of ordered defect structures has been observed in many other materials, such as Mo, Nb, W, and Ta, but the process is not well understood theoretically (127,128). Malen and Bullough (129)

TABLE 3

HEAVY ION IRRADIATED NICKEL

Purity	He (appm)	Ion	dpa/s	dpa	Temperature (°C)	$N_v \times 10^{14}$ (cm^{-3})	$\overline{d}$(Å)	$\frac{\Delta V}{V}$(%)	Comments	Ref.
High	0	4 MeV-H	6×10^{-6}	1	450	6.0	250	-	faulted interstitial loops	108
3N	0	6-11MeV Se	3×10^{-2}	.47	525	3.0	90	.0012		109
				2.0	"	17.	80	.1		
				2.3	"	27.	120	.24		
				12.	"	36.	210	1.7		
				47	"	40.	270	4.1		
				95	"	76.	220	4.2		
				400	"	140.	180	4.4	void lattice, d = 660Å	
4N7	.3	1.4MeV-H	2×10^{-4}	1	300	5.0	40	.001	formed no voids without He	110
	"			"	400	85.	80	.28		
	"			"	500	9.0	110	.10		

TABLE 3 (Cont.)

Purity	He (appm)	Ion	dpa/s	dpa	Temperature (°C)	$N_v \times 10^{14}$ (cm^{-3})	$\overline{d}$(Å)	$\frac{\Delta V}{V}$(%)	Comments	Ref.
4N7	7.	1.4MeV-Ni	2×10^{-4}	1	400	50.	65	.10		110
	28.			"	400	150.	55	.12		
High	10	20MeV-C	-	1	525	18.	-	.2		111
				10	"	30.	-	2.		
4N	15	5MeV-Ni	2×10^{-2}	140	625	19.	465	12		112
4N5	0	6MeV-Ni	2×10^{-2}	.43	525	3.8	135	.048		107
	"			1.3	"	10.	140	.14		
	"			6.	"	34.	140	.49		
	"			44	"	41.	265	3.95		
	3			1	"	11.	90	.07		
	"			4.4	"	20.	150	.19		
	"			6.5	"	29.	145	.46		
	"			10	"	32.	155	.61		
	"			25	"	35.	210	1.7		

TABLE 3 (Cont.)

Purity	He (appm)	Ion	dpa/s	dpa	Temperature (°C)	$N_v \times 10^{14}$ (cm^{-3})	$\overline{d}$(Å)	$\frac{\Delta V}{V}$(%)	Comments	Ref.
4N5	3	6MeV-Ni	2×10^{-2}	58	"	33.	250	2.7		107
	"			67	"	27.	305	4.0		
	"			360	"	42.	250	3.4	void lattice	
	"			480	"	40.	260	3.7		
4N5	0	2.8MeV-Ni	7×10^{-2}	13	325	0	0	0		113
				"	375,425	0	0	0	aligned loops	
				"	475	0	0	0	a few voids	
				"	525	76.	100	.48		
				"	575	69.	130	.90		
				"	625	18.	225	1.2		
				"	675	0.3	725	.62		
				"	725	0.14	800	.40		
4N	0	2.8MeV-Ni	7×10^{-2}	13	625	5.0	370	1.3		90

TABLE 3 (Cont.)

Purity	He (appm)	Ion	dpa/s	dpa	Temperature (°C)	$N_v \times 10^{14}$ (cm^{-3})	$\overline{d}$(Å)	$\frac{\Delta V}{V}$(%)	Comments	Ref.
4N5	0	2.8MeV-Ni	7×10^{-2}	1.3	575	47.	85	.16		114
				4	575	110.	75	.28		
				40	575	55.	150	1.23		
				80	575	20.	255	2.4		
				130	575	6.6	380	2.2		
				1.3	625	10.	125	.13		
				4	625	7.0	230	.50		
				40	625	2.7	550	2.6		
4N5	0	2.8MeV-Ni	7×10^{-4}	13	300	0	0	0	dense loops	84
				"	350	0	0	0	aligned loops	
				"	400	0	0	0		
				"	425	61.	80	.2		
				"	450	16.	200	.73		
				"	500	7.7	290	1.1		

TABLE 3 (Cont.)

Purity	He (appm)	Ion	dpa/s	dpa	Temperature (°C)	$N_v \times 10^{14}$ (cm^{-3})	$\overline{d}$(Å)	$\frac{\Delta V}{V}$(%)	Comments	Ref.
4N5	0	2.8MeV-Ni	7×10^{-4}	13	550	8.3	365	2.4		84
				"	600	0.9	550	.8		
				"	625	.07	320	.015		
4N5	0	5MeV-Ni	1×10^{-2}	10	185	0	0	0	dense loops	115
				"	280	"	"	"	aligned loops	
				"	370	"	"	"	55-120 Å dia.	
				"	435	"	"	"	λ = 700 - 900 Å	
4N5	1[a]	5MeV-Ni	6×10^{-3}	.06	575	.07	41	.0025		116
	2			.16	"	.02	93	.008		
	8			.27	"	.17	82	.054		
	32			2.2	"	.08	189	.32		
4N7	0	2.8MeV-Ni	2.5×10^{-3}	2	525	8.0	180	.5		43
				5	"	13.	260	1.5		
				10	"	10.	300	2.0		

TABLE 3 (Cont.)

Purity	He (appm)	Ion	dpa/s	dpa	Temperature (°C)	$N_v \times 10^{14}$ (cm^{-3})	$\overline{d}$(Å)	$\frac{\Delta V}{V}$(%)	Comments	Ref.
4N7	0	2.8MeV-Ni	$2.5x10^{-3}$	30	525	15.	320	3.5		43
				47	"	10.	410	4.6		
				60	"	4.	600	6.0		
	0	1 MeV-C	$2.5x10^{-3}$	8	475	21.	280	2.9		
				"	525	6.0	520	4.0		
				"	575	3.2	660	3.4	double peak in swelling vs. temp. curve	
				"	625	2.0	730	3.1		
				"	700	1.0	900	3.9		
				1	525	12.	140	.3		
				5	"	15.	325	2.5		
				10	"	12.	450	5.3		
				20	"	7.0	710	12.		

TABLE 3 (Cont.)

Purity	He (appm)	Ion	dpa/s	dpa	Temperature (°C)	$N_v \times 10^{14}$ (cm^{-3})	$\bar{d}$(Å)	$\frac{\Delta V}{V}$(%)	Comments	Ref.
4N5[a]	0	4.0MeV-Ni	3 c 10^{-3}	1	500	0.2	149	0.0032		21
	22[a]			1	"	2.7	139	0.36		
	22[b]			1	"	5.0	74	0.011		
4N5[a]	0			1	550	2.7	302	0.33		21
	22[a,c]			1	"	4.1	295	0.28		
	22			1	"	9.9	204	0.44		
4N5[a]	0[c]			1	600	3.0	335	0.56		21
	22[a]			1	"	2.1	421	0.75		
	22[b]			1	"	21.	156	0.42		
4N5[a]	0[c]			1	650	0.3	670	0.37		21
	22[a]			1	"	0.64	483	0.37		
	22[b]			1	"	12.	170	0.33		

TABLE 3 (Cont.)

Purity	He (appm)	Ion	dpa/s	dpa	Temperature (°C)	$N_v \times 10^{14}$ (cm^{-3})	$\bar{d}$(Å)	$\frac{\Delta V}{V}$(%)	Comments	Ref.
4N5[a]	0[c]	4.0MeV-Ni	3×10^{-3}	0.6	700	0.01	680	0.019		21
	22[a]			1	"	0.093	820	0.28		
	22[b]			1	"	1.5	390	0.47		
4N5	100[b]	5MeV-Ni	5×10^{-3}	1	625	50-90	85-125	0.3-0.5		126
	16[a]			0.35	"	3-10	120-240	0.12-0.28		
	100[b]			1	525	50-90	60	0.05-0.1		
	16[a]			0.35	"	20	80-150	0.05-0.4		
	6[b]			1.2	575	60	100	0.5		
	10[a]			1.1	"	2.	210	0.1		
	67[b]			2.0	"	8.	190	0.3		

[a] Simultaneous He injection.

[b] He preinjected.

[c] Average values from several samples.

attribute the void lattice to the elastic anisotropy of the material, with the interaction probably tending to enhance vacancy emission from voids not on a void lattice site. The structure of aligned loops is very similar in nature to the void lattice, but it may be due to a different mechanism. The loops are believed to be either vacancy loops, or perhaps small stacking fault tetrahedra in some cases (115). The defects may form randomly and then climb to the lower strain energy configuration of the defect lattice. Another possibility stated by Foreman (128) accounts for the defect lattice formation by the directional migration of the interstitial along the close packed directions. This theory has not yet gained acceptance, however, since it does not completely explain the experimental observations.

The void shapes were octahedral except at very high doses where cubic voids were observed (107). The void shapes produced under 100 KeV Ni ion bombardment of nickel were carefully studied by Chen (130). He found void shapes varying from octahedron to truncated cubic, with the surfaces of the voids always confined to the {111} and {100} planes. By varying the irradiation and sample preparation treatment, he could induce large changes in the degree of truncation of the octahedral voids, an effect he attributed to the absorption of impurities on the void surfaces. He also observed voids elongated in the <100> direction which he believed due mainly to the enhanced growth of certain voids in that direction, and to a lesser degree due to the coalescence of two voids.

The role of gaseous impurities on void formation was not clear from these studies. Voids were formed without preinjected helium in several cases, with only the proton irradiated nickel (110) failing to form voids without helium injection. When helium was not injected, or was injected in small amounts, the controlling influence on void nucleation was probably from the residual gaseous impurities in the material such as oxygen or hydrogen. Lanore et al. (131) found that void formation could be completely suppressed in nickel and in copper by thoroughly outgassing the samples prior to bombardment. Buswell et al. (132) found that the electropolishing conditions used in the final specimen preparation prior to irradiation to be very important in determining the void structure in steel, an effect apparently due to the pickup of hydrogen during the electropolishing. The effects of trace gaseous impurities on void formation are not yet well understood, but the experimental evidence indicates that these impurities can strongly affect the final damage state. It is important that the effect of these residual gases on void formation be understood, both to facilitate the comparison of different experiments and to judge the desirability of giving a reactor core element a certain type of treatment prior to its use in a reactor system.

One rather complete and systematic study of ion irradiated nickel was done by Ryan (43) using the facilities of ANL. His bombarding ions included Ni, C, Ne, and Cl. Under similar irradiating conditions, he found the carbon ions to be more efficient in producing damage than nickel ions, a result he attributed to the lower mass (and therefore a less dense collision cascade) of the carbon ion compared to nickel ions. Under the carbon ion irradiation, a double peak in the swelling vs. temperature curve was found, with the first peak occurring at a temperature about 75°C lower than the peak observed by nickel ion bombardment. Since this double peak occurred only at doses where the implanted carbon ion concentration was significant, he assumed the double peak was an artifact of the increased carbon content in the observed damage region. Under Ne or Cl ion irradiation, Ryan observed very rapid void nucleation in the end of range region due to the presence of the implanted gas, but the total swelling in this region was smaller because of the very high void concentration.

The most interesting observations made from the HVEM studies on nickel involve the growth of voids in the presence of local perturbations in the microstructure. Norris (121) studied the growth of voids near dislocations and found that voids were stable defects only in the presence of dislocations. If the dislocations were to climb away from a growing void, the void would cease to grow and actually start shrinking. This implies that in an otherwise perfect crystal under these conditions, a void will preferentially attract interstitials; if the crystal contains both types of defects, the dislocation will have the stronger bias. Urban (124) also concluded that dislocations had a strong preference for interstitials when he found that vacancy loops could grow if they were in the presence of straight edge dislocations, and Harbottle (125) found that voids could grow only if the dislocation density was greater than $\sim 10^9 \mathrm{cm}^{-2}$. All of these experiments indicate that the dislocation has a stronger preference for interstitials than does a void and thus serves as the biased sink necessary for void growth.

C. Review of Full Range Viewing of Ion Bombarded Samples

The procedure for viewing in the electron microscope the cross section of a thin specimen was first developed for the studies of deformed metal specimens (135,136) and for various semiconductor materials (137). The cross section of an ion irradiated foil was first prepared by Spurling and Rhodes (138) who examined proton irradiated stainless steel. Similar procedures have since been applied to heavy ion irradiated nickel (139-141), copper (142), molybdenum (143), and vanadium (156). In addition to these methods in which the damage region can be viewed directly in cross section, the depth distribution of the damage region in ion bombarded samples has been viewed by optical microscopy (144), by a scanning electron microscope (145) by the use of stereo microscopy in a TEM foil prepared in the plane of the foil surface (146-148), and by performing successive thinning operations on a foil to section through the damage region (149). The pertinent results of these studies will now be briefly discussed.

Keefer and Pard (150) applied the method developed by Spurling and Rhodes (138) to the study of the formation of voids in 316 stainless steel irradiated at 500°C with 1 MeV protons. They observed voids at depths into the foils that were ~15% greater than the proton range given by the tables of Janni. They believed the discrepancy in range to be due to an underestimation of the proton range by Janni and not due to any structural feature (such as channelling) or to experimental error. Narayan et al. (139,151) used the cross sectioning technique to study the room temperature damage formed after bombardment of a copper target with nickel and helium ions, and the bombardment of a nickel target with 4 MeV nickel ions. In both these cases, they observed loops at depths beyond the predicted ion range. For the irradiations using nickel ions, LSS theory was found to give good agreement for 58 MeV nickel ions incident on copper, but poor agreement for 4 MeV nickel ions incident on either copper or nickel. For these low energy nickel ions, good agreement could be achieved if the electronic stopping parameter k was reduced from the LSS value of 0.162 to a value of 0.126 for the nickel target and from 0.167 to 0.120 for the copper target. These low values of the stopping power are believed to be due to oscillations of the stopping power as a function of the target atomic number. These oscillations are related to the electronic charge distributions of the interacting species and hence are more pronounced at lower energies.

Henager et al. (143) used the cross sectioning technique to study molybdenum irradiated with nickel ions. They observed damage at a depth greater than the calculated ion range and attributed this behavior to the diffusion of the point defects into this undamaged region. They also observed a dip in the swelling curve in the end of range region, an effect they believe due to an interaction with the deposited nickel ions.

The studies using stereomicroscopy or repeated thinning of the foil are more indirect and subject to larger experimental error than is the cross sectioning technique. Using stereomicroscopy, Chen (146) observed voids in nickel irradiated with 100 KeV nickel ions at depths almost twice the predicted ion range, while Diamond et al (147) found little discrepancy between the depth at which voids were observed and the predicted ion range for a Fe-Ni-Cr alloy irradiated with 3.5 MeV nickel ions. Johnston et al. (148) used the successive thinning technique to study several steel alloys irradiated with 5 MeV nickel ions. They found the damage to extend slightly beyond the predicted range. They also observed a region of enhanced swelling near the front surface, an effect they attributed to the segregation of a major alloying element in this region.

While there has not yet been a large number of these types of studies, the cross sectioning technique has shown to be an extremely powerful method of studying heavy ion irradiated nickel or copper, with its primary drawback that of poorer statistics due to the small region of the TEM foil that contains the damage. The other techniques, while having better counting statistics on the defect structure, have other uncertainties and limitations that make these methods difficult. So far, none of these studies have contained any great surprises as far as our understanding of void theory is concerned. There is a general indication, however, that LSS theory overestimates the electronic energy loss for nickel ions incident on nickel or copper, while giving reasonable results for other materials.

IV. EXPERIMENTAL APPARATUS AND PROCEDURE

A. Irradiation Facilities

The high energy ion beams used in this study are provided by the University of Wisconsin tandem Van de Graaff accelerator (H.V.E.C. model EN). The schematic of this facility shown in Figure 5 gives the relative location of the main components of the system. The critical requirement for use of a tandem accelerator for heavy ion irradiations is the development of a source capable of producing the required intensity beam of the desired negative ions. A Sputter Penning Ionization Gauge Source (SPIGS) developed by Smith and Richards (25) uses cesium assisted sputtering of the cathodes to produce several microampere negative ion beams of copper, nickel, carbon, and aluminum.

The negative ions from the source were injected into the accelerator and achieved an energy equal to the dome voltage upon reaching the high voltage terminal. In the terminal, the negative ions passed through a nitrogen gas stripper canal where several electrons were stripped off. The final charge state (q) of the ions leaving the stripper was a function of several variables such as the dome voltage (V) and the gas pressure in the stripper canal. A typical charge state for copper or nickel ions entering the dome at 4 million volts was predominantly 4+. The final ion energy on leaving the

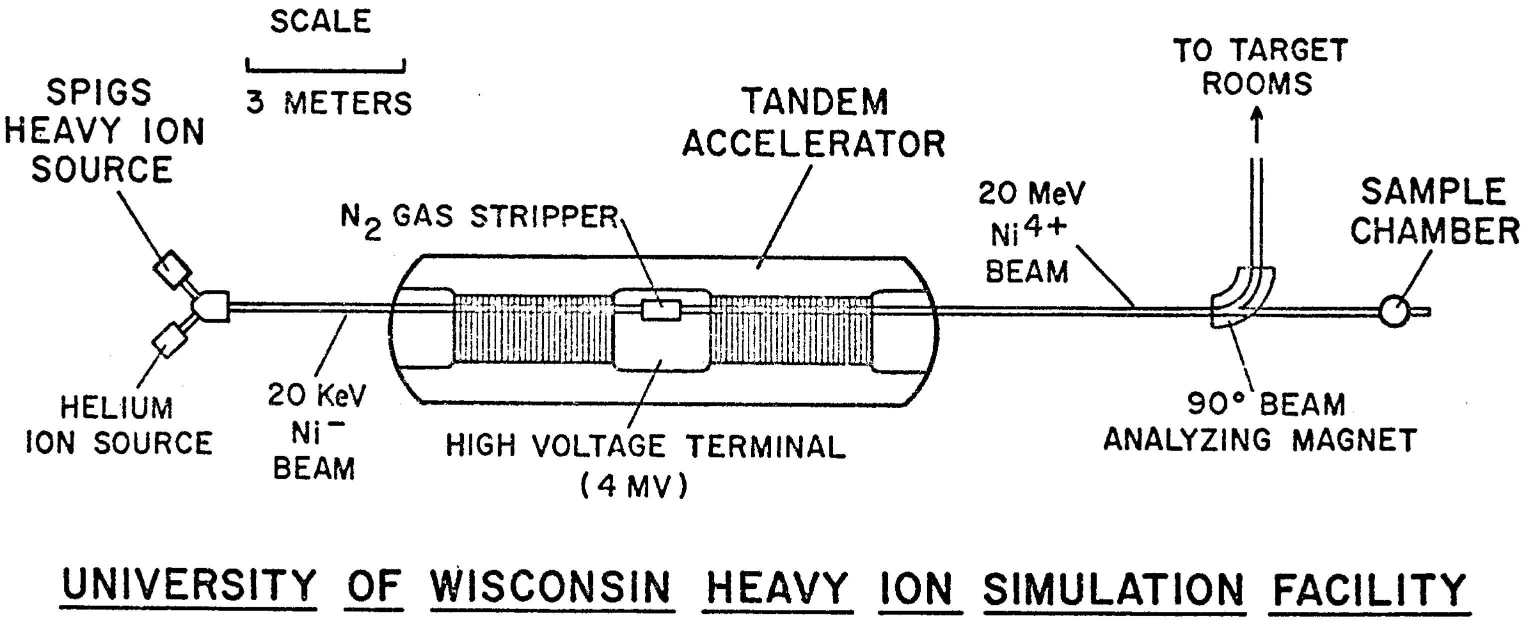

Figure 5. A schematic representation of the heavy ion irradiation facility showing the relative positions of the major componets.

accelerator is then given by

$$E = (q + 1)V \qquad 48$$

The dome voltage was measured using a digital voltmeter calibrated by magnetically analyzing a beam of known energy and charge state.

The 90° analyzing magnet was not capable of bending the high energy heavy ion beams used in this study into the target rooms. This required the sample chamber to be placed near the tandem axis. The various undesired beams exiting the accelerator were separated from the desired beam using the focal properties of the quadropole lens and the 1/4° bend in passing through the 90° magnet. The final beam charge state and purity were determined by recording in a solid state detector the energies of ions scattered through 90° by a thin gold foil (152,153). The arrangement of this system, along with the other beam diagnostics, is illustrated in Figure 6. A typical energy spectrum obtained from the charge state device when analyzing a copper beam is shown in Figure 7. The magnetic analysis was sufficient to separate the beams such that about 95% of the ions are Cu^{4+} and approximately 5% Cu^{2+}. The other beam impurities such as nitrogen are less than 0.2% of the total beam.

An ultra-high vacuum specimen environment was produced by using a system of three differentially pumped stages (152,153). The first stage (Figure 8) was pumped by a liquid nitrogen trapped diffusion pump and achieves a pressure of typically 2×10^{-6} torr. The

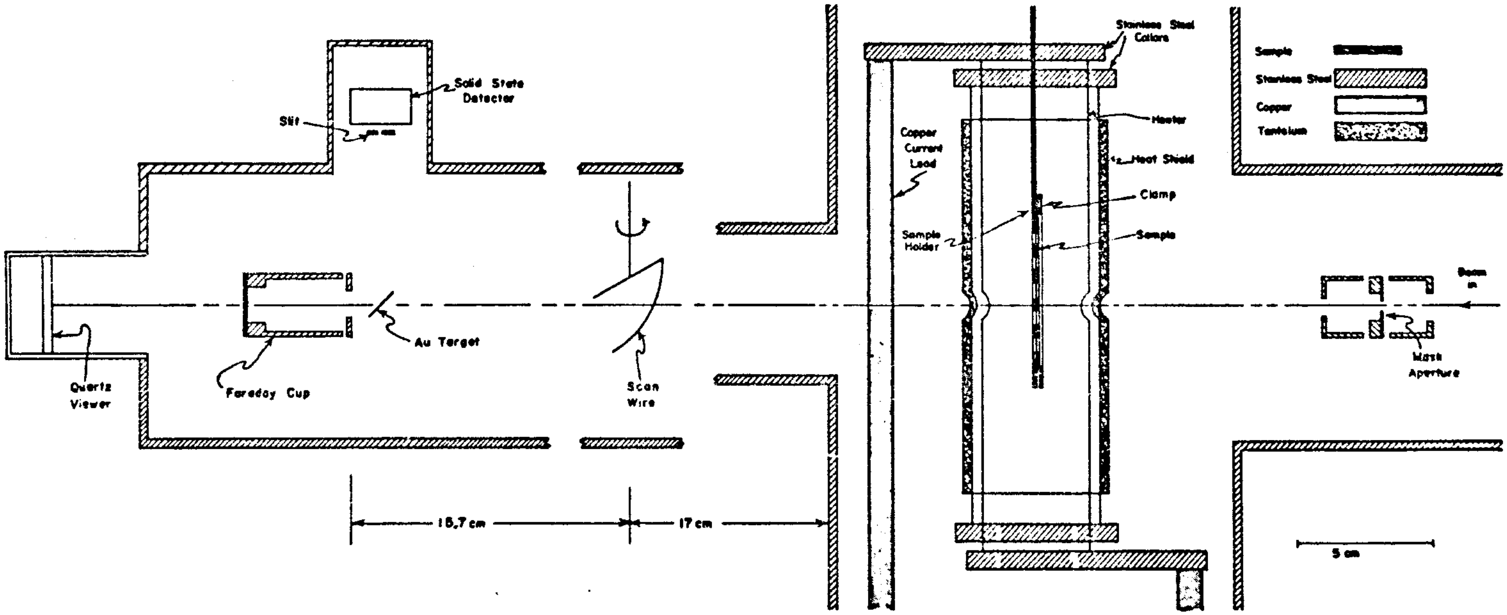

Figure 6. The radiation damage target area showing the sample holder and heater along with the various beam diagnostics.

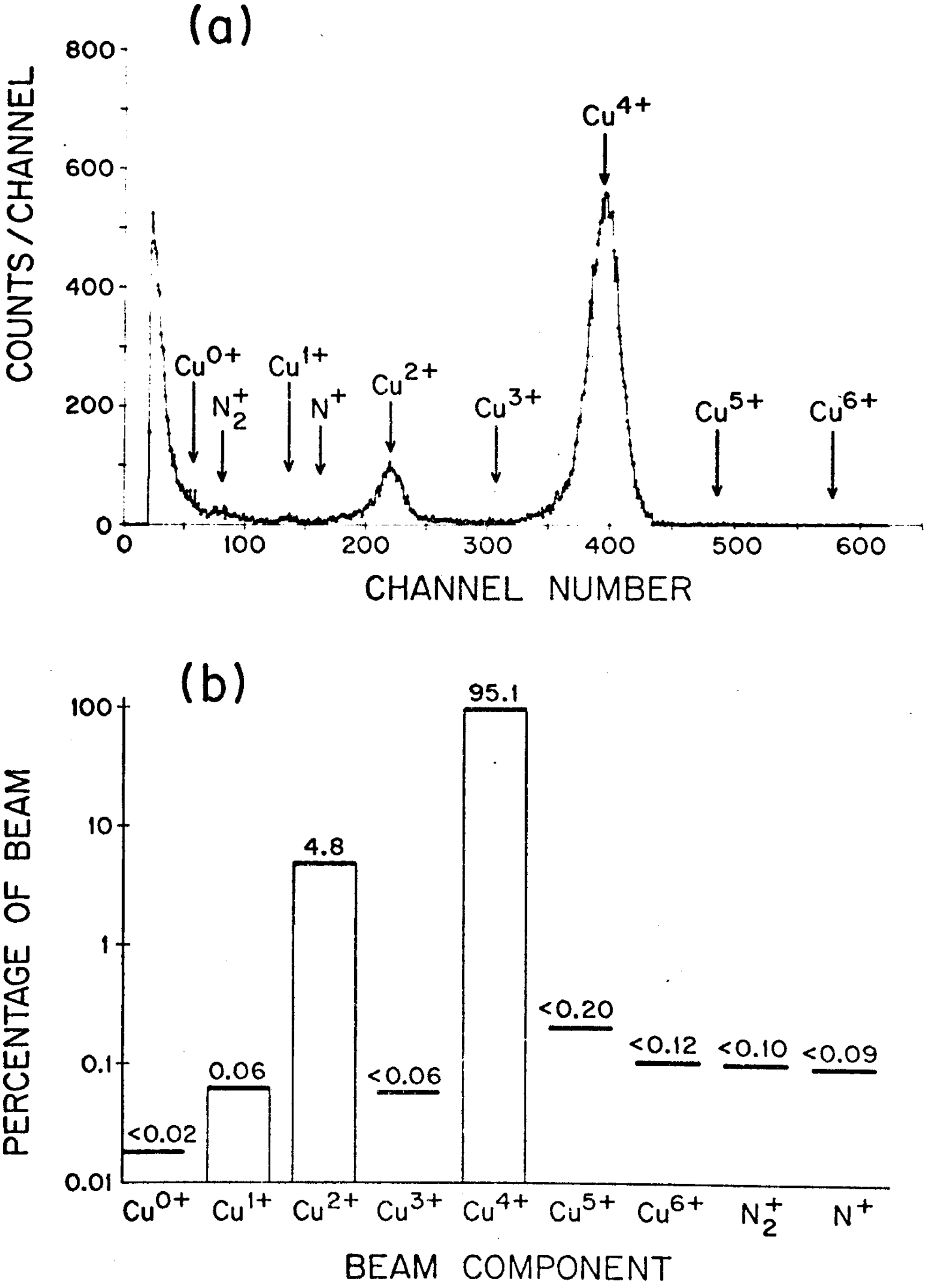

Figure 7. A typical charge state analysis with copper ions at a dome voltage of 4 MV. The top curve is the raw data, while the bottom curve has corrected this data for detector efficiency and different scattering cross-sections at different energies.

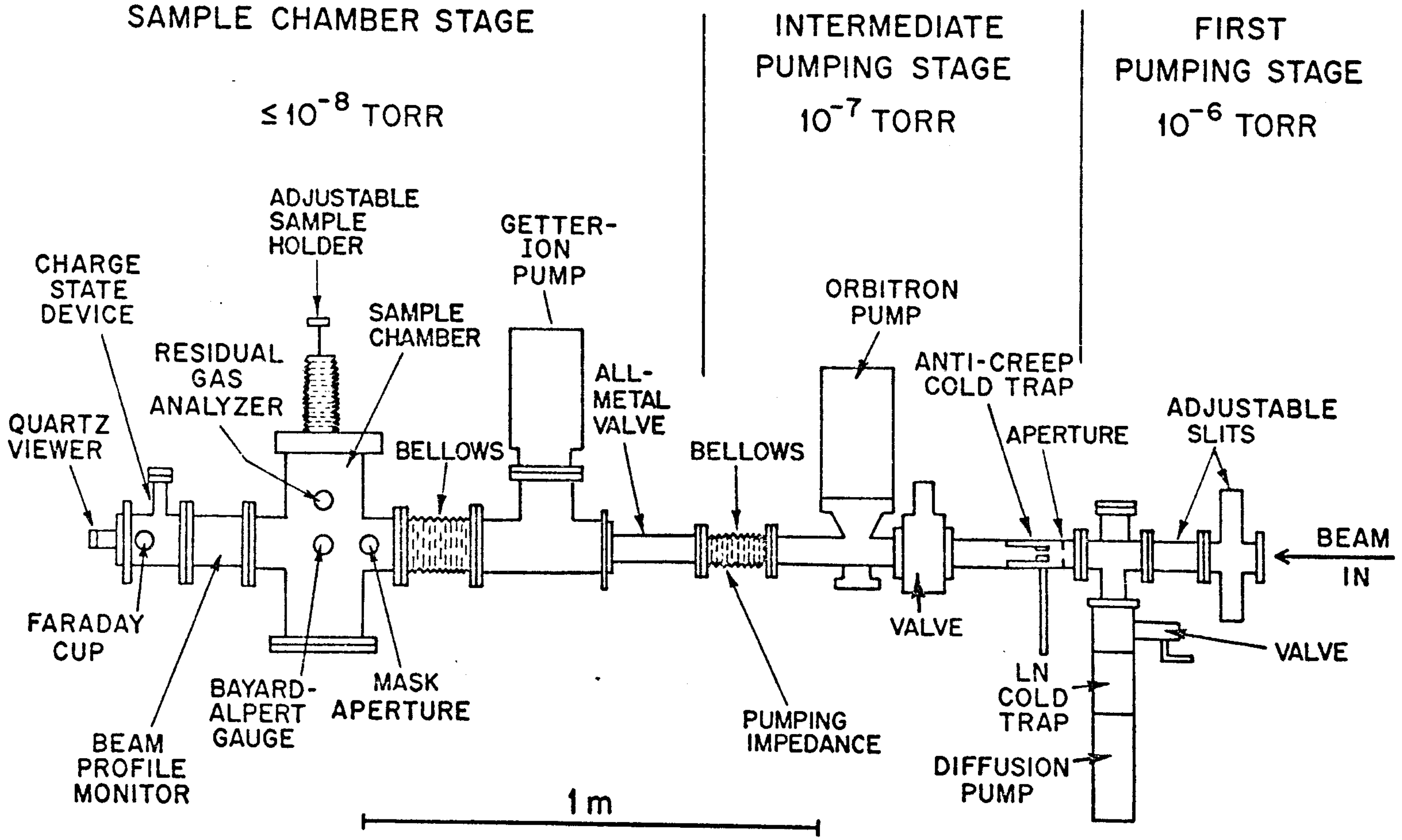

Figure 8. The radiation damage target stand showing the three differentially pumped stages. The ion beam enters from the right traveling to the left.

intermediate pumping region was isolated from the first pumping stage by a liquid nitrogen cooled cold trap and a 9.5 mm aperture, and was pumped by a 400 liter/sec orbitron pump. This stage was isolated from the final sample chamber region by a series of 15 6.5 mm apertures which have a very low conductance and virtually eliminate gas streaming down the beam line. The sample chamber environment was produced by a 1000 liter/sec getter ion pump. The base pressure of this system as measured on a Bayard-Alpert gauge was ~1×10^{-9} torr with the walls cold, and less than 5×10^{-8} torr with the samples heated to 1000°C. A residual gas analyzer (RGA) was an integral part of this system and was available to characterize the partial pressure composition of the different gas species in the chamber.

The samples were heated by a 4 cm diameter cylindrical thermal radiation heater (see Fig. 6). The heater was constructed of 0.025 mm tantalum sheet and was surrounded by a 15 layer, spirally wound heat shield used to reduce the power input requirements. The hot zone of the heater was approximately 9 cm long. At a sample temperature of 1000°C, the total power input to the heater was ~400 watts. The vacuum chamber walls in the heater region were water cooled to reduce outgassing during the irradiation.

The samples were placed in a tantalum sample holder and suspended in the center of the heater. The sample holder used to irradiate 3 mm disc is shown in Figure 9. The adjustable bellows from which the sample holder was suspended allows eight samples to be

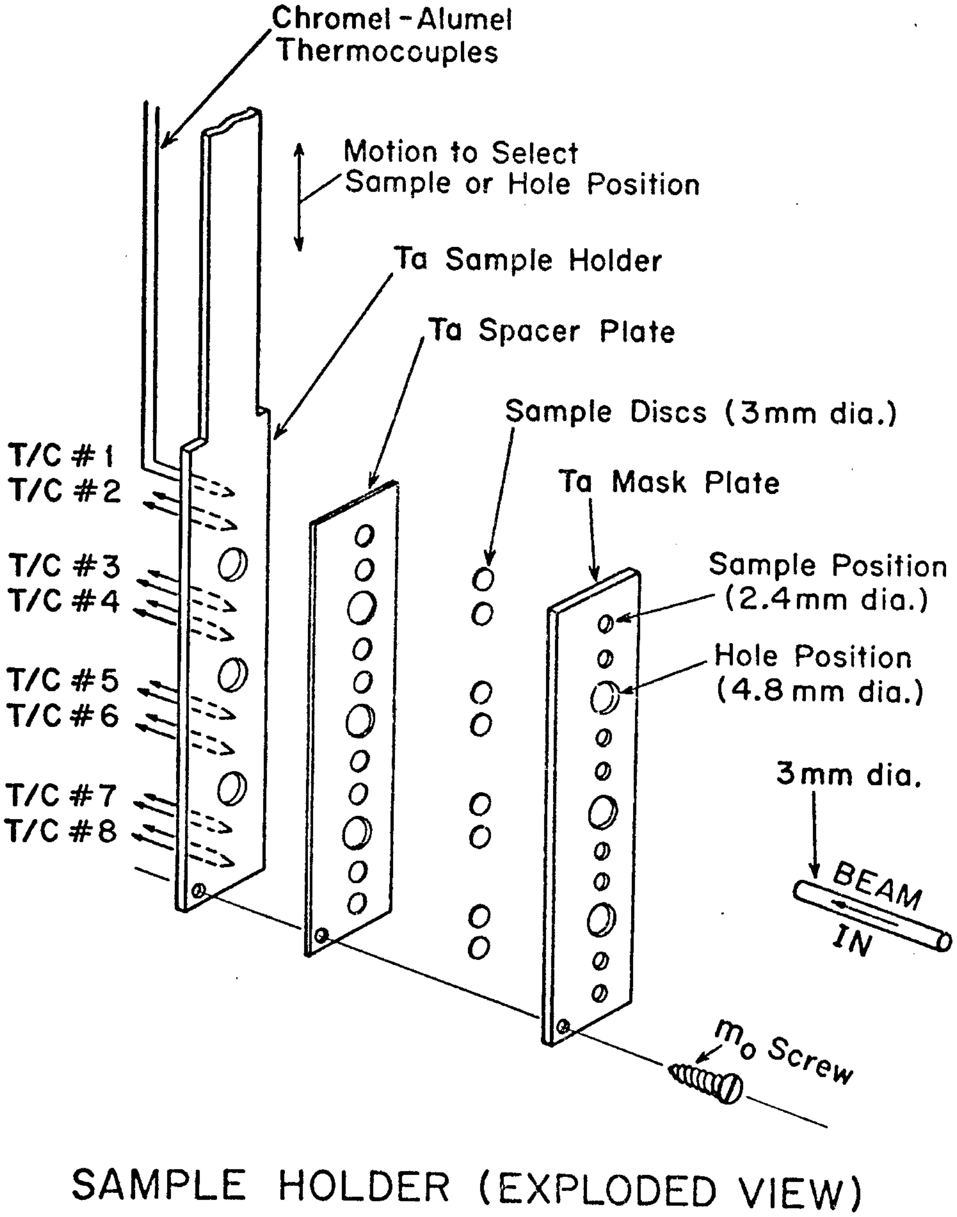

Figure 9. The sample holder used during heavy ion bombardment. The holder is constructed entirely out of tantalum.

irradiated without breaking the chamber vacuum. Chromel-alumel thermocouples were placed behind each sample position to allow accurate temperature measurement at all times. The three holes in the holder were used to align the holder and to allow beam diagnostics downstream from the holder. The sample holder, which was constructed entirely from refractory metals, was easily converted to accommodate 1 x 1.2 cm sample strips which were irradiated when the post-irradiation examination was by the cross sectioning technique. The primary limitation of the sample heater system was the difficulty of accurate temperature control at low temperatures due to beam heating and the instabilities of radiation heating. However, the system did work quite well down to temperatures of ~200°C.

The ion flux striking the sample was measured by first determining the ion charge state in the manner described previously, and then measuring the charge current striking the samples. Since the sample holder, heater, and heat shield were all electrically isolated, they could be shorted together to form a faraday cup arrangement which trapped the secondary electrons emitted when the beam strikes the samples. This allowed the true beam current to be measured directly. With the beam size defined by the entry aperture, the ion flux could be measured and integrated with an accuracy of ±10%.

B. Post Irradiation Examination

As has been mentioned several times previously, the unique aspect of this study on nickel was the preparation of the foils such that the damage region can be viewed in cross section. The preparation procedure is shown schematically in Figure 10. After being irradiated, the thin foils were removed from the target chamber and placed in a nickel electroplating solution where from 1 to 1.5 mm of nickel was plated onto each side of the foil. The sample was then removed from the solution, mounted in epoxy, and sliced perpendicular to the foil surface using a diamond saw. The slice was then thinned for TEM in the conventional manner (155).

To achieve good bonding of the plated nickel, the surface of the foil had to be as clean as possible before electroplating. Since any cleaning or other surface preparation after irradiating was undesirable, the samples were electropolished prior to irradiation in a solution of 60% sulfuric acid and 40% water, and stored in methyl alcohol at all times the samples were not under vacuum. Before electroplating, the samples were mounted in stainless steel tweezers and the edges covered with stopoff lacquer to reduce the undesired buildup of nickel on the edges. The samples were then given an activation treatment in a solution of Woods' nickel (154) by making the sample anodic for 20 seconds at a current density of 25 mA/cm^2. This step, which did remove material from the foil surface, was necessary to dissolve the metal oxide layer and assure a good bond.

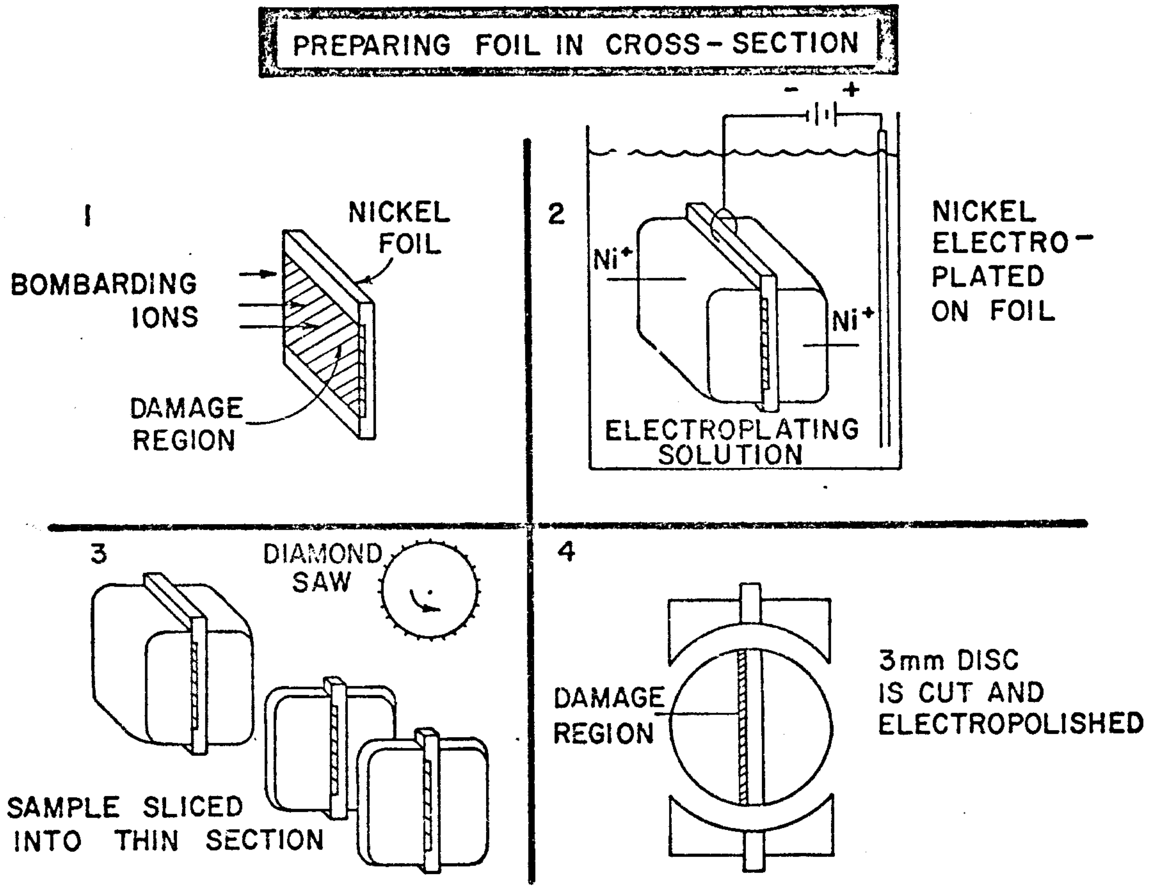

Figure 10. A schematic representation of the steps involved in preparing a sample for cross-sectional viewing in a transmission electron microscope.

The maximum amount of material removed in this step was estimated by interference microscopy to be less than 500Å. After activation, the current was reversed in this same solution and a thin nickel strike applied without removing the sample from the solution. The sample was then transferred directly to a high chlorine nickel plating solution containing 150 g nickel sulphate, 150 g nickel chloride, and 50 g boric acid in 1000 ml of water. Plating for ~24 hours in this solution at 50°C and a current density of 300 mA/cm^2 resulted in a final thickness greater than 2 mm. During the electroplating, the solution was agitated by flowing a small stream of air bubbles over the samples. The nickel plating stand shown in Figure 11 supplies filtered air, has current regulation and switching circuitry, temperature control and pH measurement.

The samples were sliced in cross section using a low speed saw (~100 rpm) with a 0.15 mm thick diamond wafering blade. By cutting slices about 0.25 mm thick at a very slow speed, the deformation damage to the sample was kept to a minimum. A 3 mm disc was then punched from this strip. The equipment used in sample preparation is shown in Figure 12. The final polishing was carried out in a twin jet electropolishing unit using a solution of 33% nitric acid and 67% methyl alcohol. With careful alignment of the polishing jets, a suitable electron transparent region usually occurred at the proper foil surface.

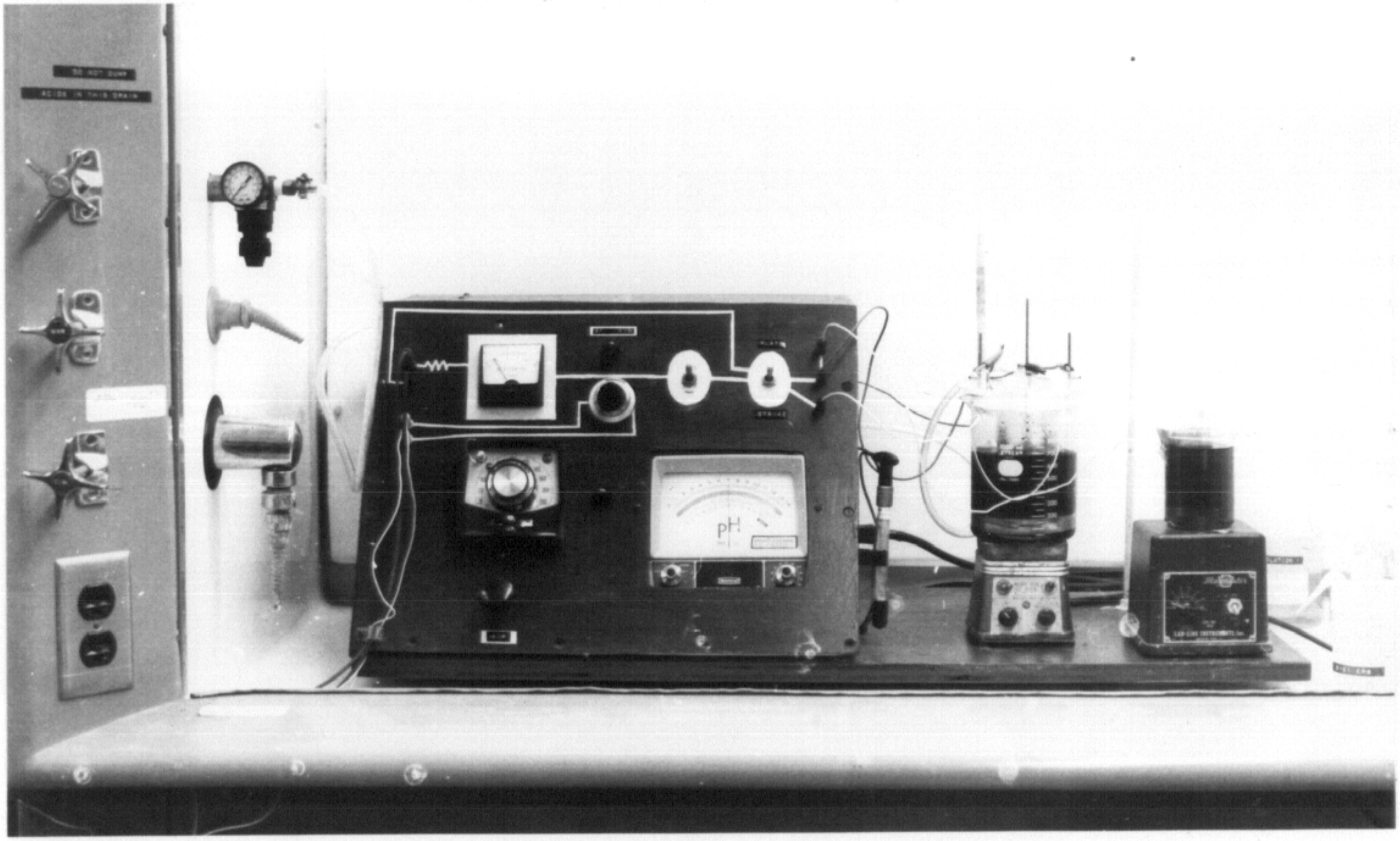

Figure 11. The stand used for nickel electroplating.

Figure 12. Some of the equipment and steps involved in sample preparation. a) 1 x 1.2 x 0.05 cm nickel foil. Two three millimeter spots are irradiated on each foil; b) sample holder for heavy ion irradiation; c) mold for epoxy mounts; d) nickel foil after plating; e) low speed saw; f) sliced sample; g) three millimeter punch; h) punched samples ready for electropolishing (arrows). (figure on following page)

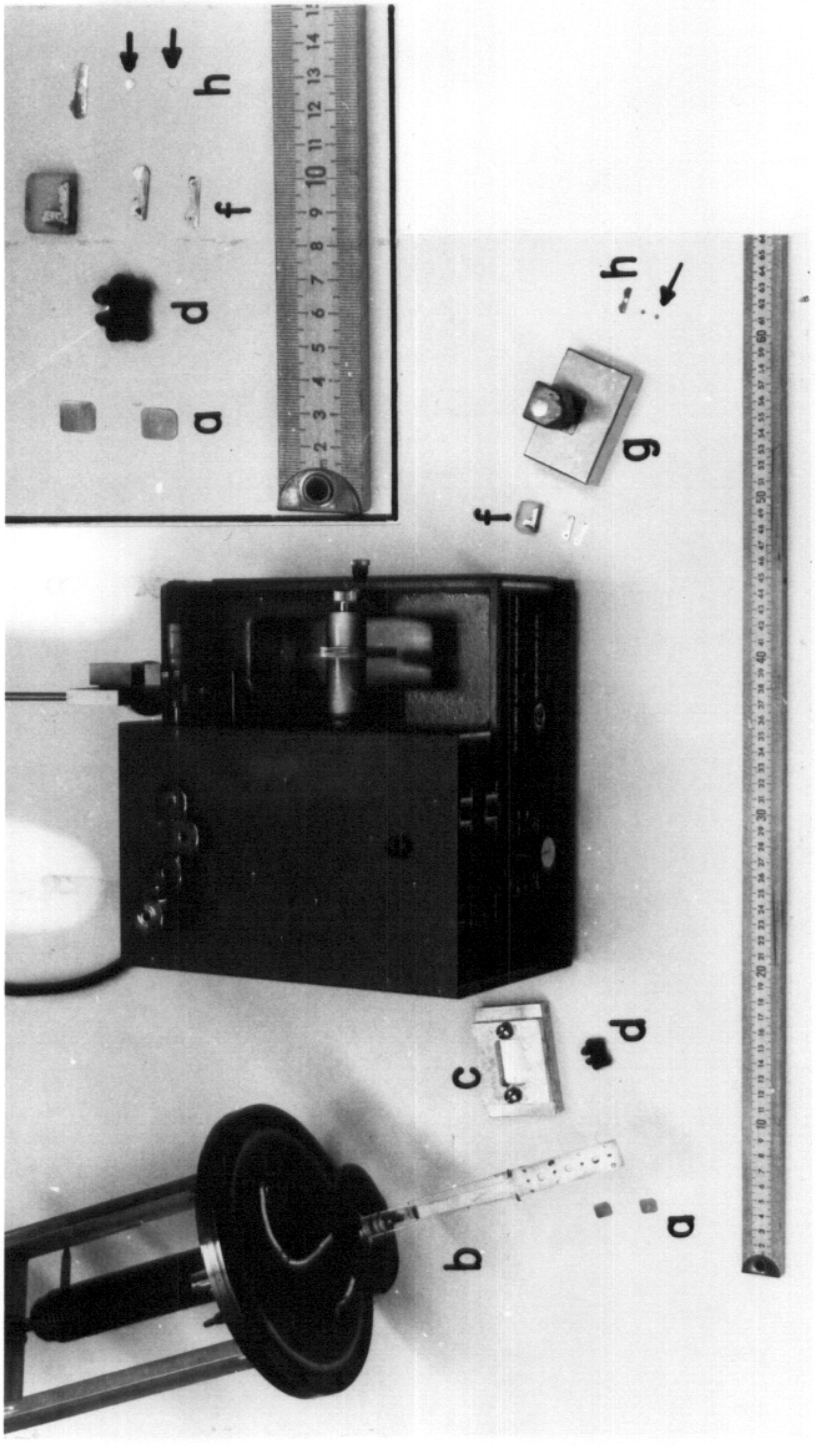

Figure 12.

The TEM analysis was carried out on a JEM 100 B electron microscope operating at 125 KV. For quantitative analysis, the foil thickness was determined using a stereo pair technique where the image parallax was measured using a Hilgar Watts stereoviewer. The foil thickness t was then given (in angstroms) by

$$t = \frac{p \times 10^7}{2M \sin(\frac{\theta}{2})} \qquad 49$$

where p was the image parallax in mm measured from features on opposite foil surfaces, M was the magnification of the print being analyzed, and θ was the total tilt angle between the prints. For most samples, the foil surfaces were marked with small contamination spots placed on the foil using the scanning transmission mode of microscope operation. The void size distribution was measured using a Zeiss comparator which records the void sizes into i classes. The number of voids in a class size was corrected for the fraction that would intersect the foil surface using

$$n_i' = [\frac{t}{(t-d_i)}] \; n_i \qquad 50$$

where d_i was the void diameter of size class i (measured to the middle of the image fringe), n_i the uncorrected void count, and n_i' the corrected void count for that class. The average void size $\overline{d}$ was given by

$$\overline{d} = \frac{1}{N} \Sigma \, n_i' d_i \qquad 51$$

where $N = \Sigma n_i'$. The standard deviation of the void size distribution was defined as

$$\sigma = \left\{ \frac{1}{N} \Sigma n_i (d_i - \overline{d})^2 \right\}^{1/2} \qquad 52$$

and finally, the swelling was given by

$$\frac{\Delta V}{V} = \frac{\pi}{6} \frac{1}{V'} \Sigma n_i' d_i^3 \qquad 53$$

where V' is the foil volume analyzed.

V. RESULTS

In this study, thirty samples of high purity nickel were irradiated with heavy ions under various conditions and analyzed using the cross sectioning technique. The material used in this study was MARZ grade nickel (<0.005% total impurities) obtained from Materials Research Corporation. The results of bulk analysis for several important impurities is given in Table 4. A complete listing of the irradiations performed and the irradiation conditions is given in Table 5. In this section, the results from specimens irradiated with nickel ions will be compared to those irradiated with copper ions. Next, the effect of pre-irradiation treatment on the resultant microstructure will be presented. The third part will compare the microstructure after irradiation with nickel, copper, aluminum, and carbon ions under similar irradiation conditions. The results of a high dose scan using nickel ions will be presented next, and lastly the effect of varying the irradiation temperature will be discussed.

A. Comparison of Nickel and Copper Ion Irradiations

The specimens for these irradiations were cleaned and given a recrystallization anneal at 1000°C for one hour in an inert gas atmosphere and furnace cooled. The samples were then electropolished in a solution of 60% sulfuric acid and 40% water prior to loading into the target chamber for irradiation. After the samples were

TABLE 4

MATERIAL ANALYSIS FOR MARZ GRADE NICKEL

Impurity Element	Content (wt-ppm)
O	<10.0
C	10.0
H	< 1.0
N	10.0
Fe	20.0
Cu	3.0
Ge	6.0
All Others	< 5.0

heated to 700°C, they were irradiated at 525°C with either 14-19 MeV copper ions or 14 MeV nickel ions. The displacement damage curve for 19 MeV copper ions is similar in shape to the curve of Figure 2, except that the peak of the damage curve occurs at a depth of 2.4 micrometers instead of 1.9 micrometers.

The primary purpose of this study was a comparison of samples irradiated at 525°C to different fluence levels using ions that differed chemically but had similar masses. A typical micrograph obtained from a sample irradiated with 19 MeV copper ions to a fluence of 5×10^{15} ions/cm^2 and prepared in cross section is shown in Figure 13. Voids were observed to form quite readily in all samples even without prior helium injection. The original foil surface is visible

TABLE 5

SAMPLES AND IRRADIATION CONDITIONS

Run Number	Sample Designation	Ion	Energy (MeV)	Temperature (°C)	Fluence Ions/cm^2 (x10^{16})	Average** Ion Flux Ions/cm^2/s (x10^{12})
1	T-20-00-01	Cu	19	525	1.0	1.5
	T-20-00-02	Cu	19	525	0.5	1.5
	T-20-00-03	Cu	19	525	0.3	1.5
2	T-20-00-04*	Ni	18	625	0.43	1.5
	T-20-00-05*	Ni	18	575	0.43	1.5
	T-20-00-06*	Ni	18	525	0.43	1.5
3	T-20-00-07*	Cu	14	625	0.67	1.5
	T-20-00-08*	Cu	14	525	1.3	1.5
	T-20-00-09	Cu	14	525	1.3	1.5
	T-20-00-10*	Ni	14	525	1.3	1.5
	T-20-00-11*	Ni	14	525	1.3	1.5
	T-20-00-12*	Ni	14	400	0.67	1.5
	T-20-00-13*	Ni	14	300	0.67	1.5
	T-20-00-14*	Ni	14	200	0.67	1.5
4	T-20-00-15	Ni	14	625	1.0	2.0
	T-20-00-16	Ni	14	525	14.	2.0
	T-20-00-17	Ni	14	525	7.5	2.0
	T-20-00-18	Ni	14	525	4.0	2.0
	T-20-00-19	Ni	14	525	2.0	2.0
	T-20-00-20	Ni	14	525	1.0	2.0
	T-20-00-21	Ni	14	525	0.5	2.0
	T-20-00-22	Ni	14	525	0.2	2.0
5	T-20-00-23	Al	8.1	525	2.1	0.8
	T-20-00-24	Al	8.1	525	1.2	0.8
	T-20-00-25	Al	8.1	525	0.7	0.8
	T-20-00-26	Al	8.1	525	0.4	0.8
	T-20-00-27	C	5	525	9.2	4.
	T-20-00-28	C	5	525	1.5	4.
6	T-20-00-29	Cu	14	525	1.0	2.7
	T-20-00-30	Cu	14	400	10.	5.8

*Outgassed samples

**Average flux ± 20%

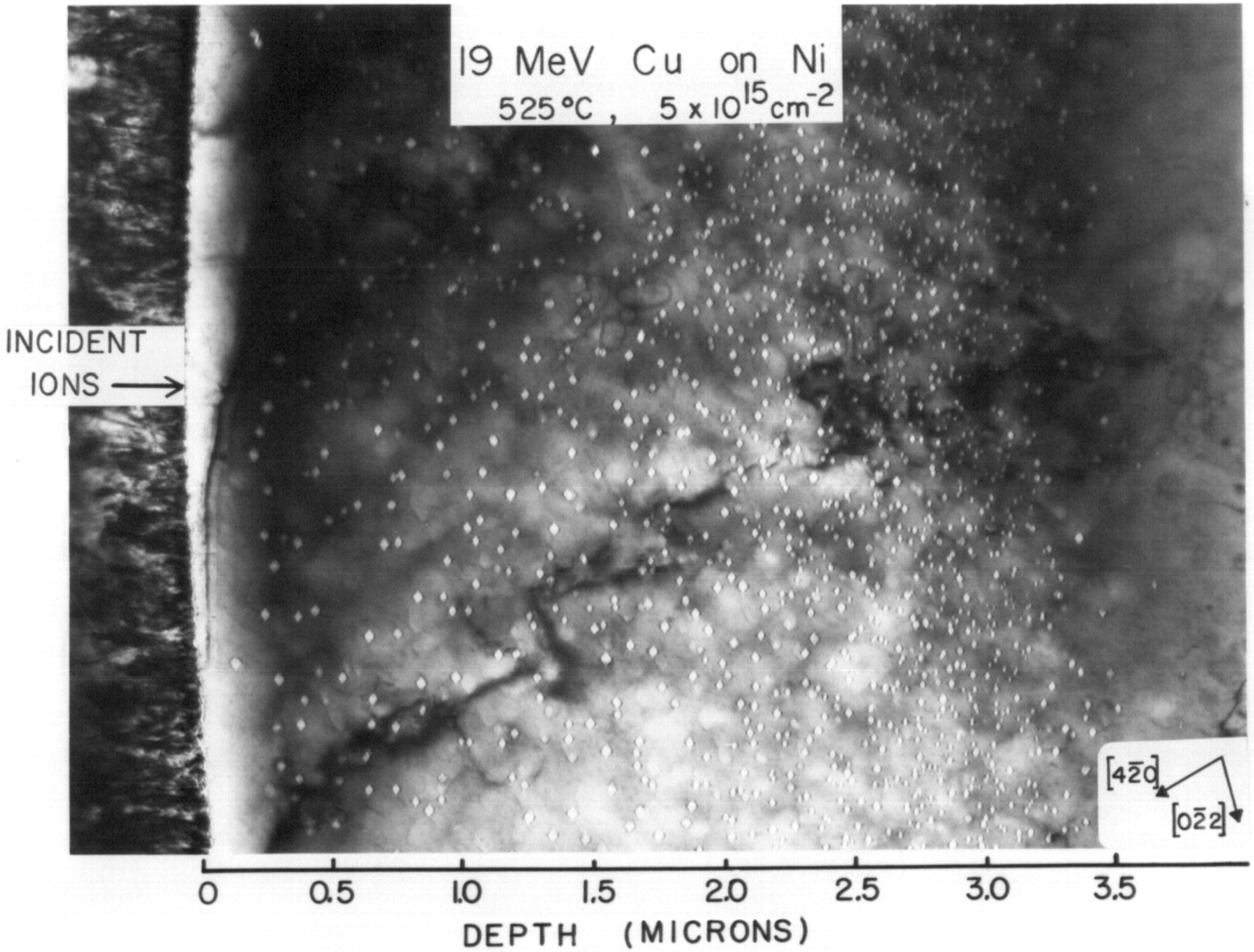

Figure 13. The depth dependent microstructure in nickel after irradiation at 525^oC with 19 MeV copper ions to a fluence of $5x10^{15}$ ions/cm^2.

at the left-hand-side of the micrograph, with the incident ions having travelled from left to right. There is a definite denuded region at the front surface with very few voids observed closer than ≈100 nm from the surface. This denuded area was followed by a region ≈150 nm wide of unusually large voids. Over the next micrometer, the void density rises while void size drops. The voids throughout the damage region were truncated <111> octahedra with the degree of truncation increasing slightly with depth. Near the end-of-range the void density drops rapidly. In all samples voids were observed at depths ≈15% greater than the range of damage predicted by Brice (44).

A limited dose scan with total ion fluence ranging from 3×10^{15} to 1×10^{16} ions/cm^2 was carried out at 525°C with 19 MeV copper ions. The micrographs of Figure 14 show the void microstructure development with dose. The void density in the end-of-range region is seen to increase with increasing dose, with relatively few voids seen at depth of 3.6 μm in the low dose sample. The high dose sample, however, has a significant number in this region defining a rather sharp end-of-range. The variation from sample to sample showed the expected behavior with void size and void density increasing with dose.

Figure 15 shows the depth dependence of the void number densities determined for these samples using a 0.25 μm wide depth interval. Note that this data would be most accurately presented as a histogram. To simplify the data curves, however, it is plotted as data points with each point shown at the center of its

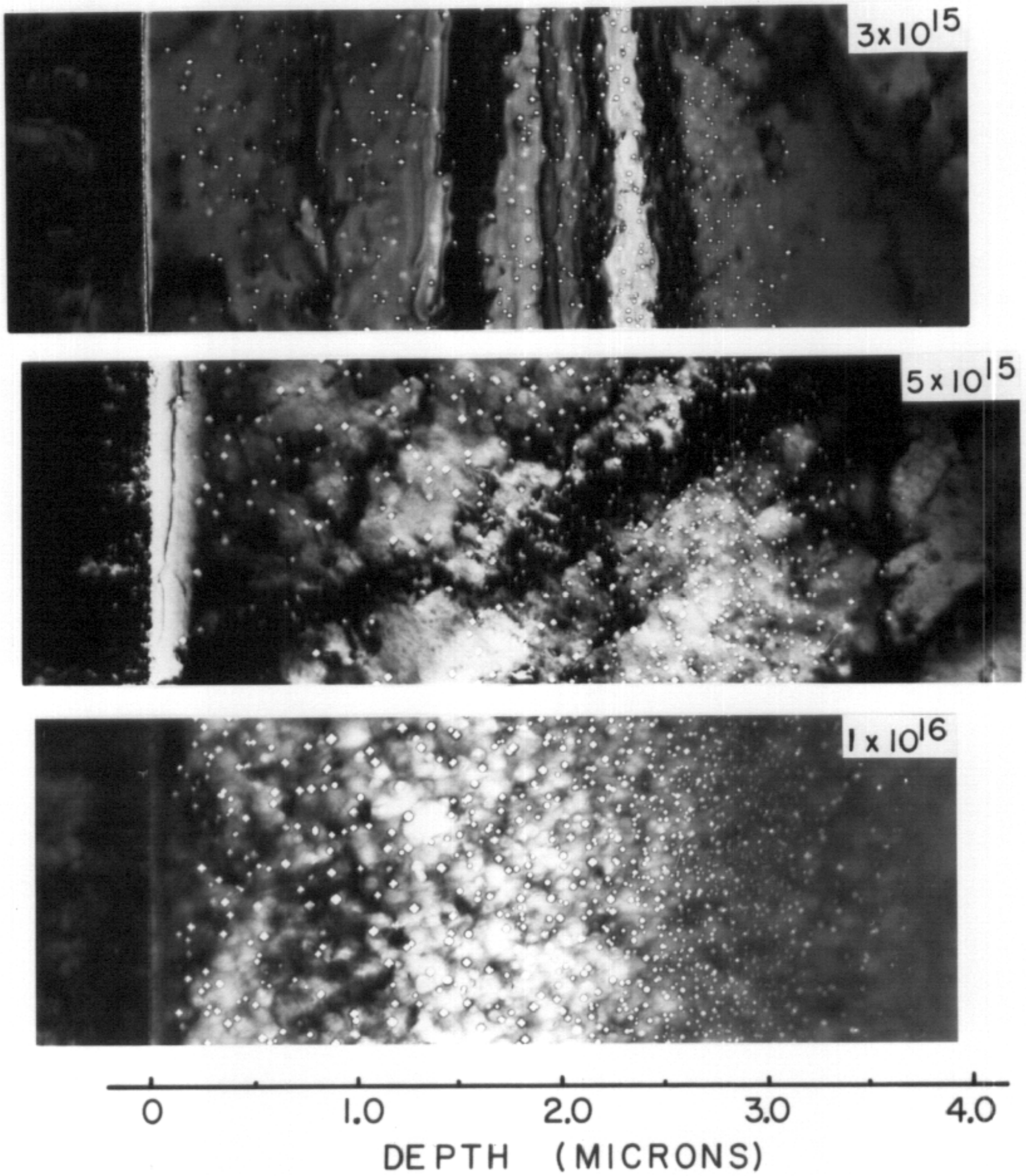

Figure 14. Nickel after irradiation at 525°C with 19 MeV copper ions to the three fluence levels (in ions/cm^2) marked on the micrographs.

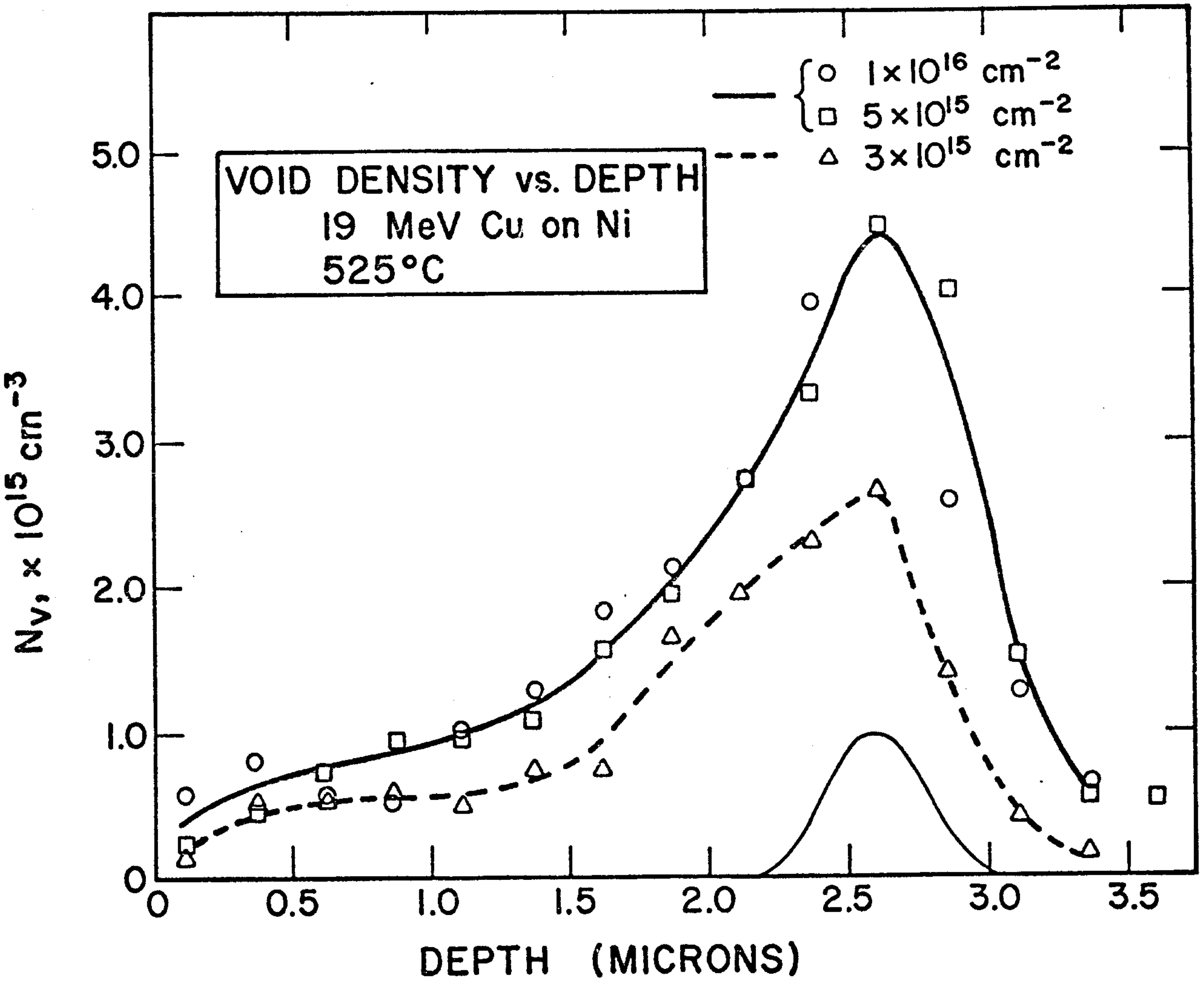

Figure 15. Void density vs. depth for three fluence levels of 19 MeV copper ions incident on nickel at 525°C. Each data point is the value measured for a 0.25 micrometer wide depth interval, and the curves are drawn to aid the eye. The deposited ion curve is also shown.

respective depth interval. Curves are then drawn through the points to serve as aids to the eye in following data trends. In general, the void density curve follows the shape of the displacement curve rather closely. This result is not unexpected since the void nucleation rate is dose rate dependent. The void densities for the two high dose samples are the same within the experimental error indicating that the void density has saturated. This implies that the final void density at the end of nucleation is determined by the dose rate and not only by the total damage state.

To study the effects of irradiating with copper ions in the end-of-range region, irradiations were performed on samples given identical pre-irradiation treatments, and then irradiated at 525°C with either 14 MeV nickel ions or 14 MeV copper ions to a fluence of 1.3×10^{16} ions/cm^2 (i.e., ≈15 dpa at the peak). The void size, void number density and the void volume fraction measured from these samples as a function of depth are shown in Figures 16 and 17. In general, there were no drastic differences observed between the two microstructures. The copper ion irradiated sample has a slightly lower void density and void size in the end-of-range region and this may be an indication of point defect interactions with the implanted copper ions. The magnitude of the reduction is rather small, however, indicating that the interaction, if any, is weak at these copper concentrations (≈2000 appm copper).

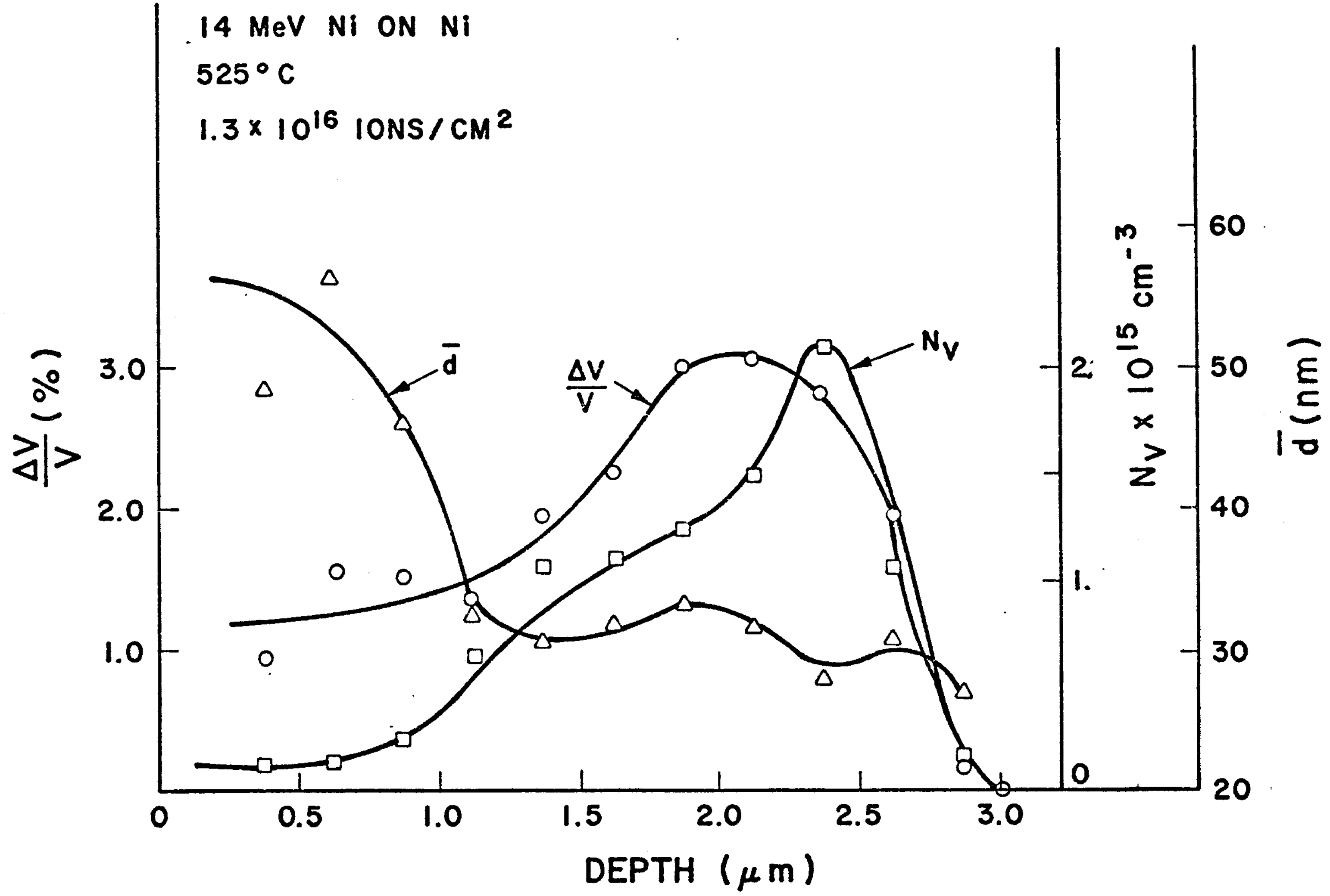

Figure 16. Void volume, density, and size as a function of depth in nickel irradiated with 14 MeV nickel ions at 525^{o}C to a fluence of $1.3x10^{16}$ ions/cm^2.

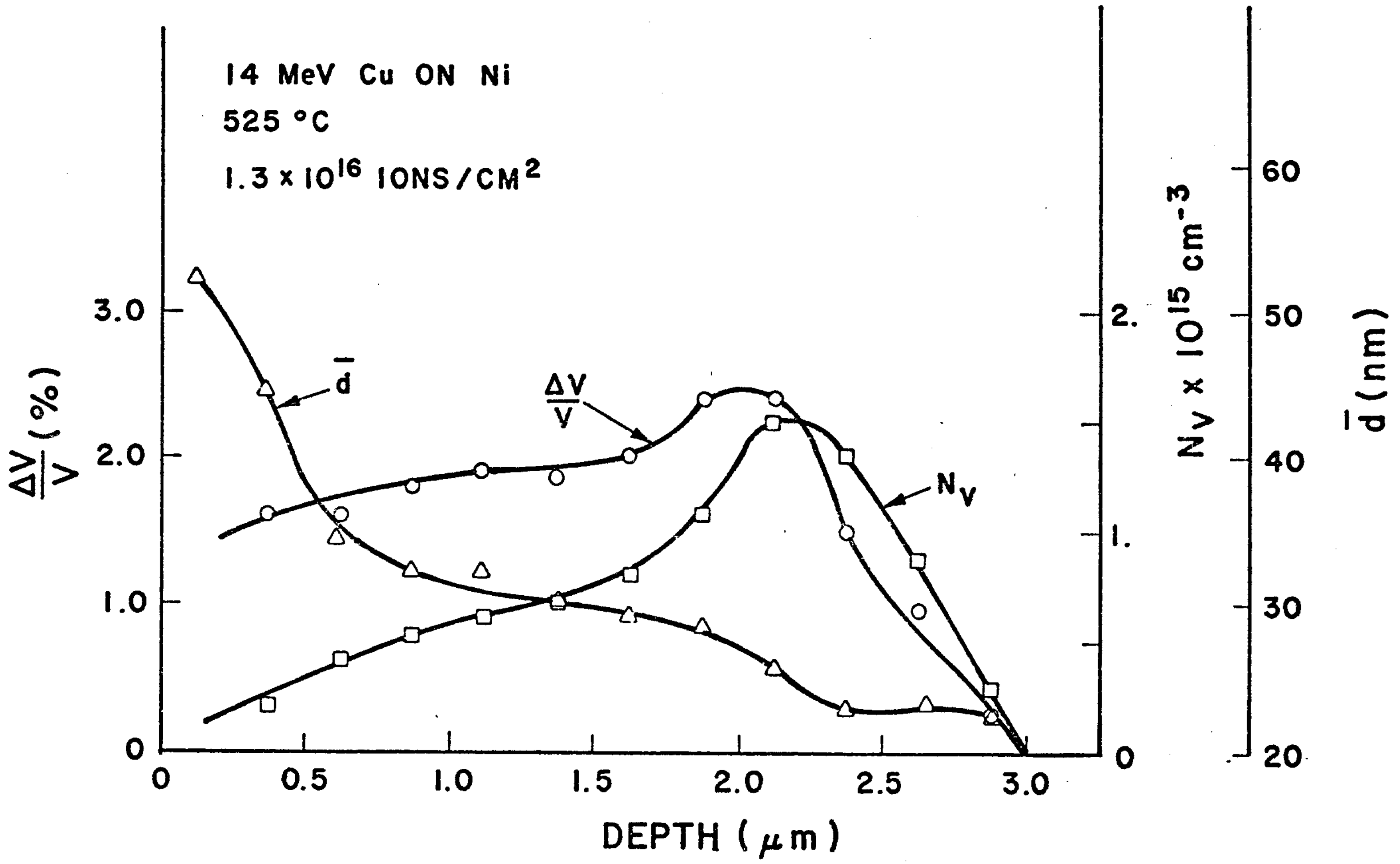

Figure 17. Void volume, void density, and void size as a function of depth in nickel irradiated at 525°C with 14 MeV copper ions to a fluence of 1.3x10^{16}ions/cm^2.

In Figure 18, the swelling curves of Figures 16 and 17 are shown plotted along with the displacement curve of Figure 2. The end-of-range swelling values and the variations from mid-range to peak for the copper irradiated sample are lower than the values from the nickel irradiated sample. Note, however, that the variation in the swelling curve for the nickel irradiated sample is much smaller than the variation in the displacement curve in the equivalent depth range, indicating that even for self-ion irradiations, the final swelling profile is not always directly related to the total damage level.

The dislocation density developed with depth as is shown in Figure 19. The structure consisted of well developed dislocation cells with the tangled cells walls often connecting voids. Very few loops were observed in these samples. The dislocation density varied from about 5×10^9 cm/cm^3 to about 1×10^{10} cm/cm^3. The typical dislocation structure that developed in the end-of-range is shown in Figure 20.

B. Effect of Different Sample Preparation

In preparing samples for irradiation, the final step prior to loading the samples into the target chamber was to electropolish. This step was done to obtain the cleanest possible surfaces on the foils and hence improve the bonding of the electroplated nickel. These samples were then normally heated to temperatures from 650 to

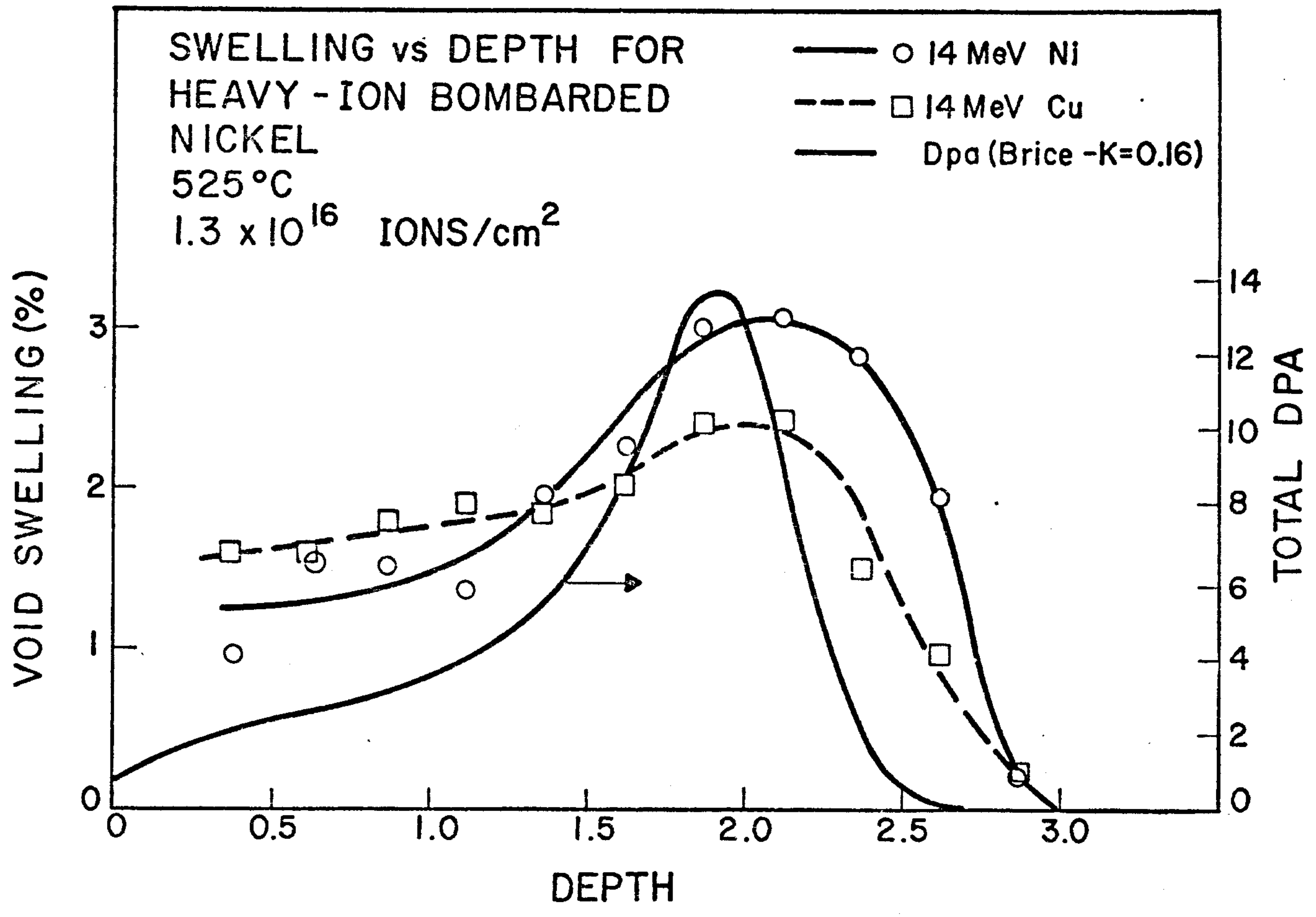

Figure 18. Swelling vs. depth for nickel irradiated at 525°C with 14 MeV nickel ions (from figure 16) and with 14 MeV copper ions (from figure 17). The displacement curve of figure 2 is also shown, where the right hand axis gives the total dose.

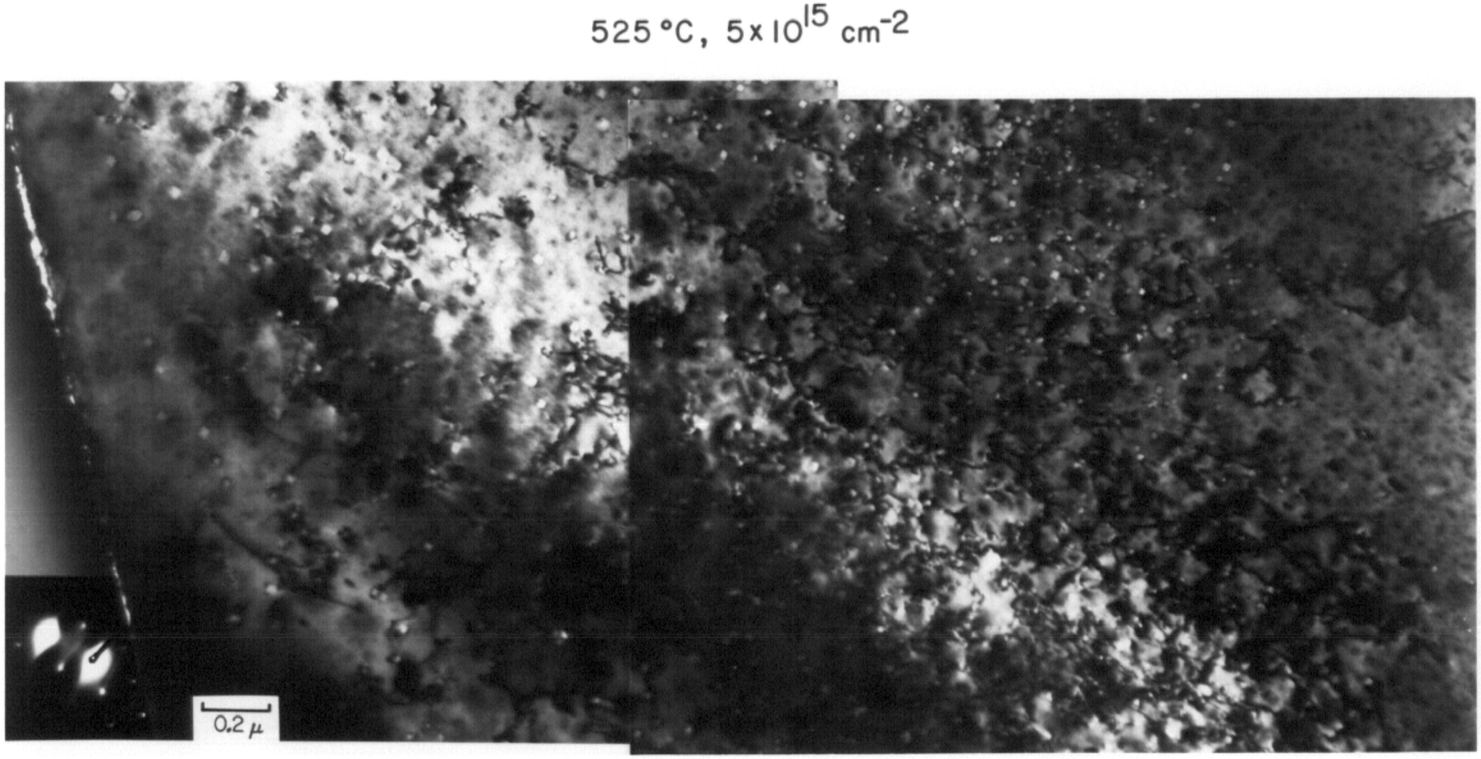

Figure 19. The dislocation structure in nickel after irradiation at 525°C with 19 MeV copper ions to a fluence of 5×10^{15} ions/cm^2.

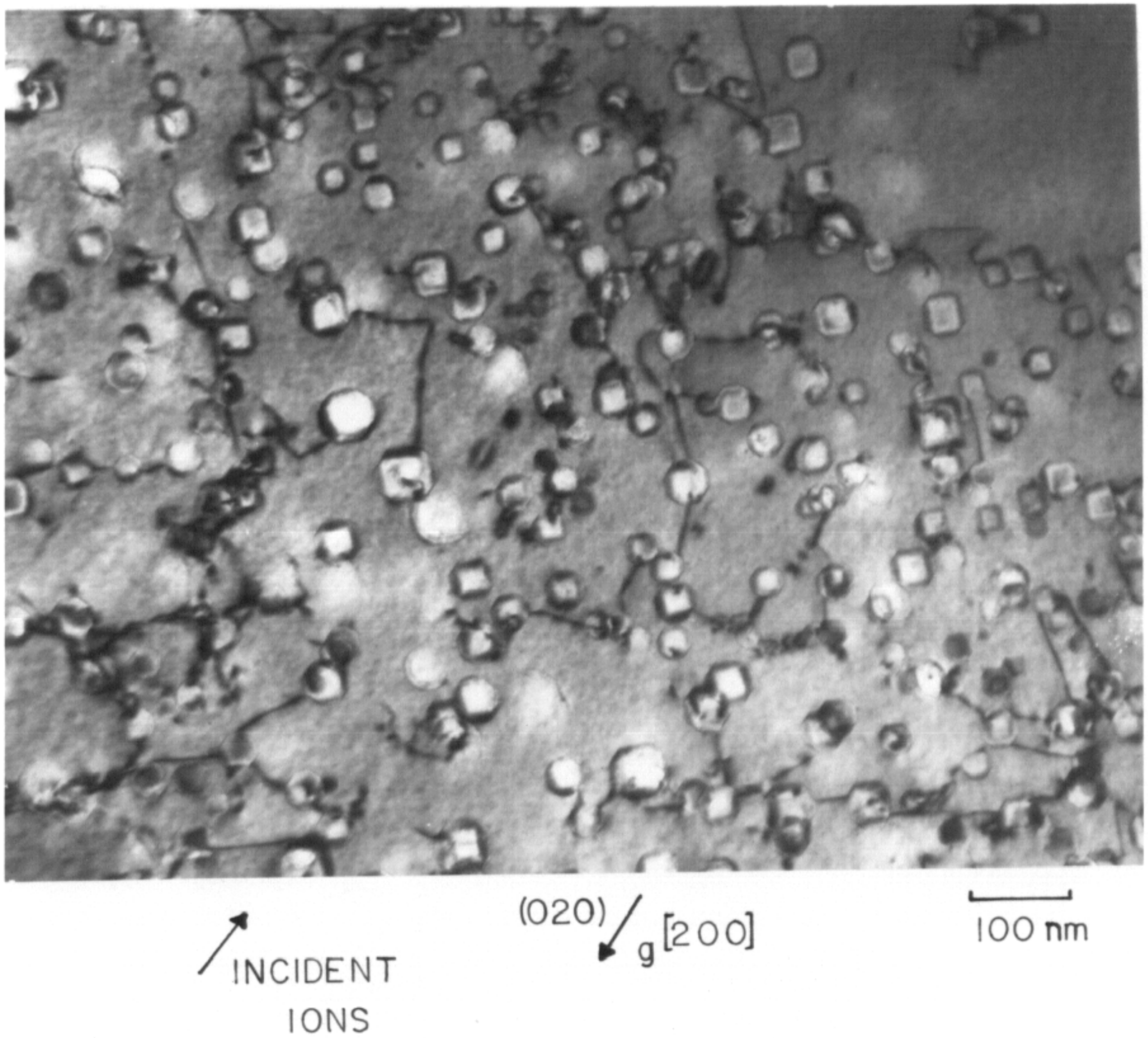

Figure 20. The dislocation structure near the ion end-of-range in a sample irradiated at 525°C with 14 MeV nickel ions to a fluence of $1.3\text{x}10^{16}$ ions/cm^2.

700°C prior to the start of the irradiation. In one run, the normal procedure was followed except that the samples were outgassed at a temperature of 900°C for several hours while some molybdenum samples were being irradiated. The temperature was then lowered and the nickel samples irradiated at 625, 575, and 525°C with 18 MeV nickel ions.

The typical microstructure that developed in these samples is shown in Figure 21. This microstructure is compared to the previously observed microstructure in Figure 22 and as can be seen, there was a drastic reduction in the void nucleation rate in the latter samples. In these outgassed foils, voids were observed mainly near the peak damage region and at a density over two orders of magnitude lower than the previous foils as is shown in the density curves of Figure 23. The observed damage structure consisted mainly of small, unfaulted loops. The loop structure is better seen in the micrograph of Figure 24 which was taken near the end of ion range. The loop density increased with depth, reaching a peak density of about 10^{15} /cm^{3} with loop diameters of approximately 30 to 50 nm. Void diameters were very large, ranging from about 80 nm at 525°C to over 200 nm at 625°C. Void data from the 575°C sample was taken using a depth interval of 0.75 μm and is shown in Figure 25. These values must be viewed with caution, however, since the very low void densities made void counting very difficult, leading to errors of about a factor of 2. Note that the peak swelling value of

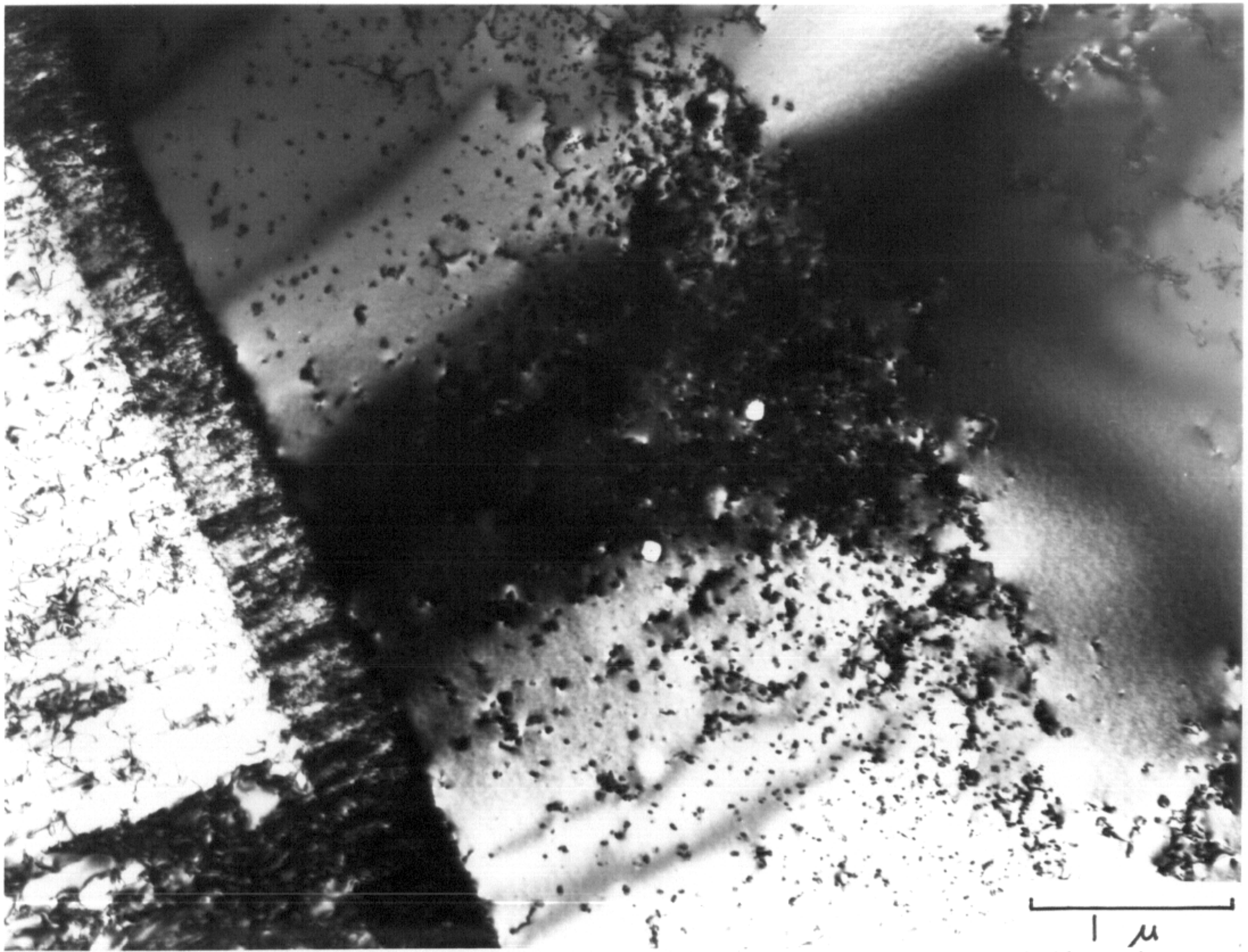

Figure 21. The microstructure observed in an outgassed sample after irradiation at 525^{o}C with 18 MeV nickel ions to a fluence of $4.3x10^{15}$ ions/cm^2.

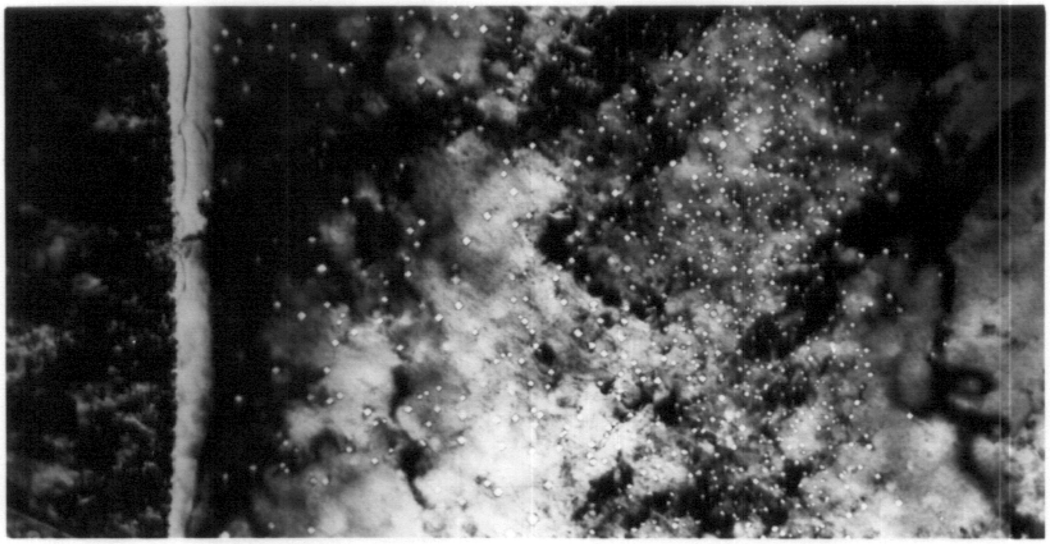

a) 19 MeV Cu

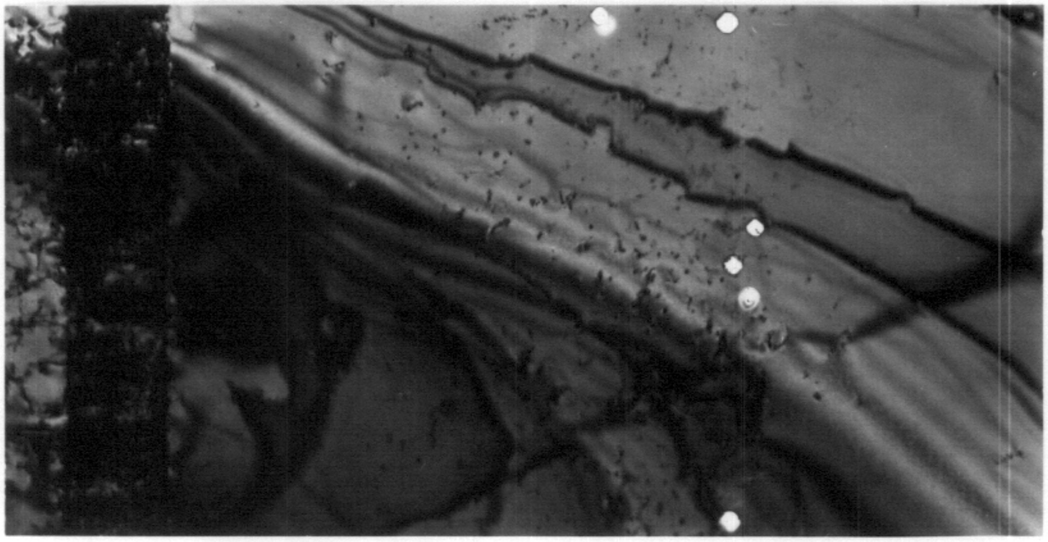

b) 18 MeV Ni, OUTGASSED

Figure 22. A comparison of the void microstructures of an electropolished (a) and an outgassed (b) sample after irradiation at 525°C.

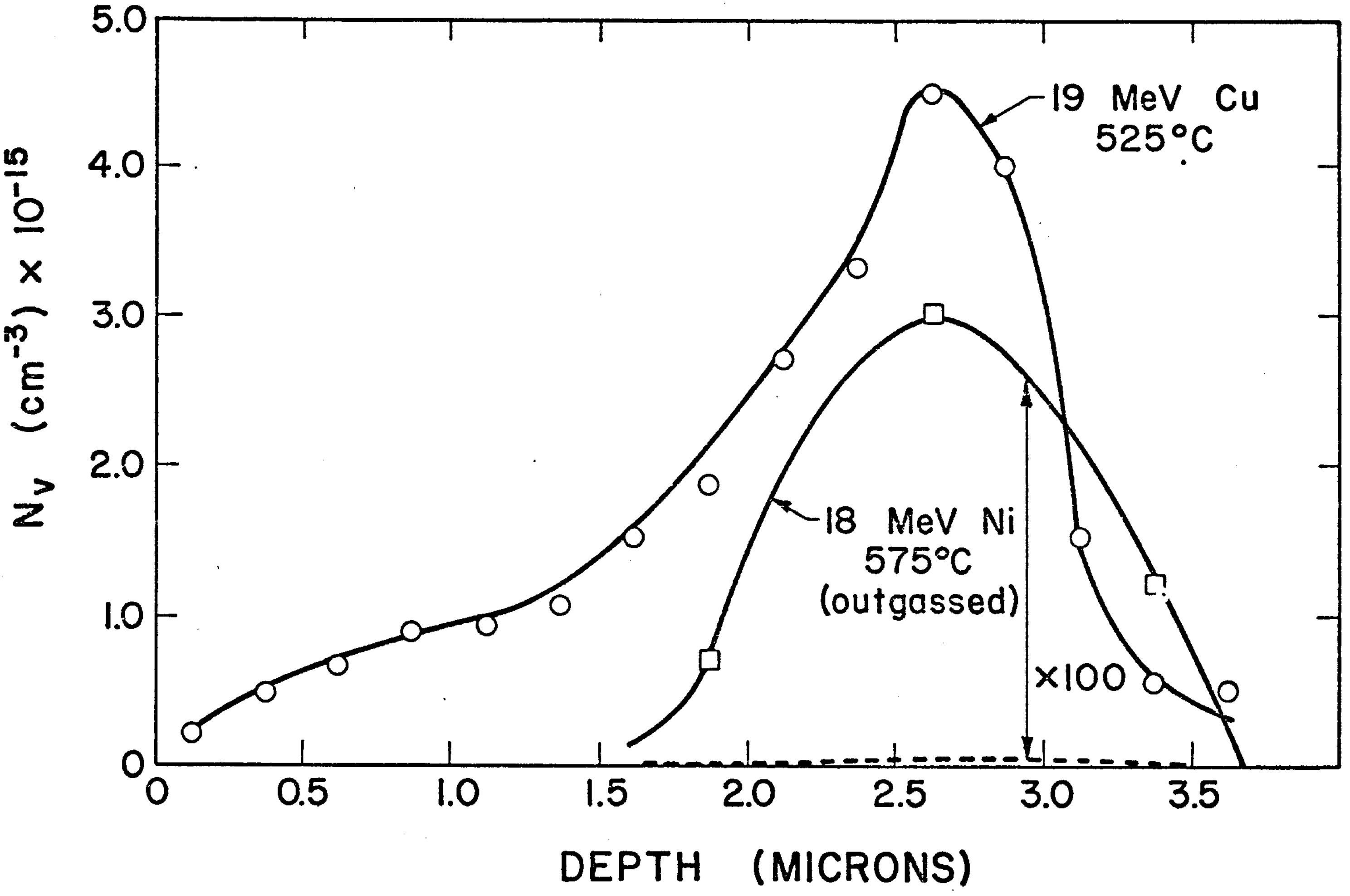

Figure 23. A comparison of void densities between electropolished and outgassed samples. Note the change of scale for the outgassed curve.

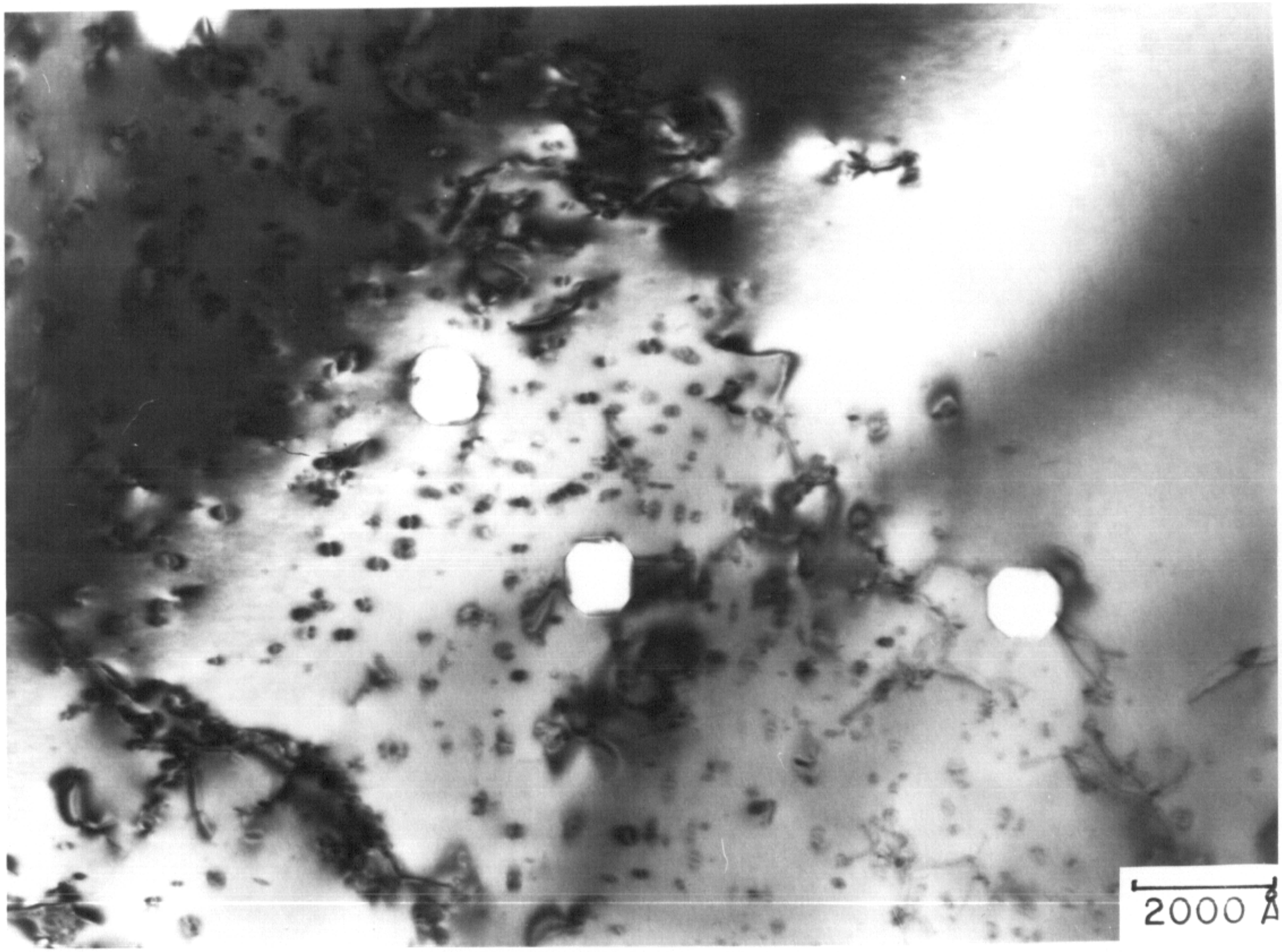

Figure 24. The end-of-range region of an outgassed nickel sample after irradiation at 525°C with 18 MeV nickel ions to a fluence of 4.3×10^{15} ions/cm^2.

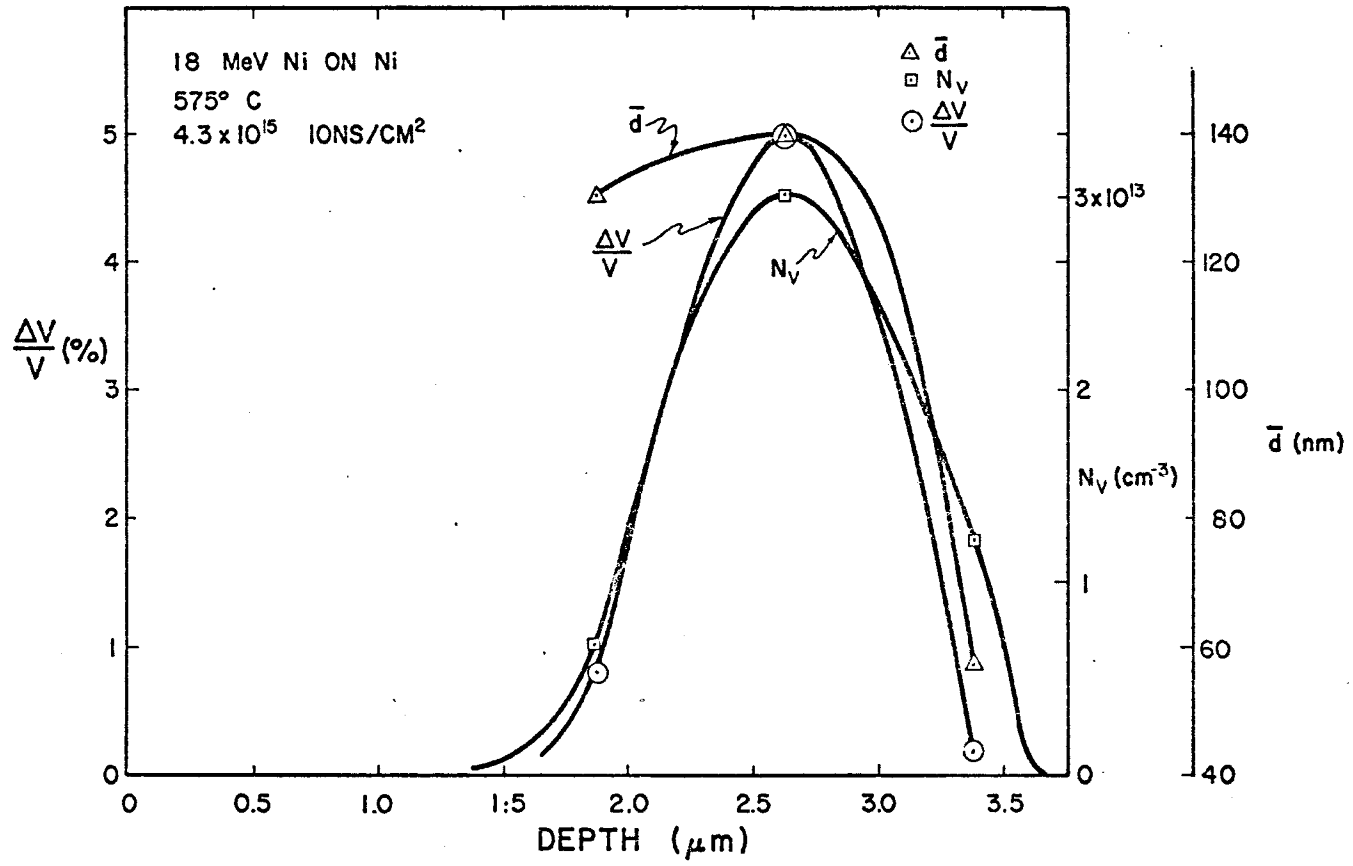

Figure 25. Void volume, void density, and void size for an outgassed nickel sample irradiated with 18 MeV nickel ions.

this sample is within a factor of two of the previous non-outgassed samples (Figure 17).

To confirm this outgassing effect, the experiment was repeated by outgassing a series of samples in a separate ultra-high vacuum furnace and loading part of the samples directly into the target chamber while giving the rest the standard electropolishing treatment before loading. After irradiating both types of samples under identical conditions, the outgassed samples had a void size and density distribution very similar to that of Figure 25, while the electropolished sample data is shown in Figure 26. There is no apparent difference between annealing in an inert gas atmosphere plus electropolishing and annealing in an ultra-high vacuum plus electropolishing, but there is approximately a two order of magnitude reduction in the void density if the sample is outgassed and not electropolished. Summarizing the results of these outgassing studies, we observed the nucleating agent in these samples was picked up during the electropolish and not during the inert gas anneal or other handling procedures. The nucleating agent did not outgas at temperatures below 700°C in times of several hours, and the nucleating agent did outgas if taken above 900°C in a ultra-high vacuum environment.

These results are consistent with previous studies of outgassed nickel and copper (131) and electropolishing has been previously observed to enhance void formation in metals, presumably by

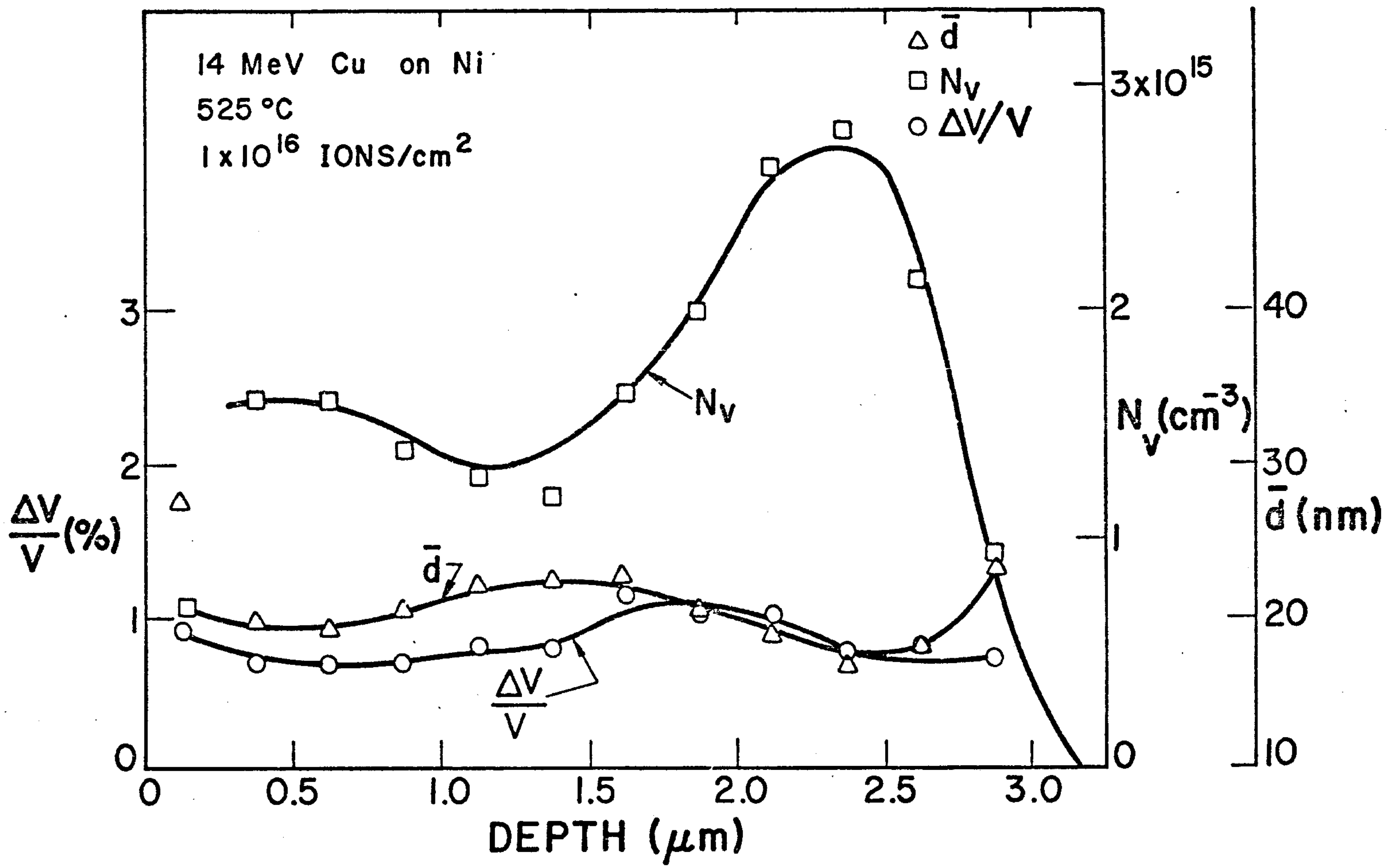

Figure 26. Void volume, void density, and void size as a function of depth in a sample annealed in an ultra-high vacuum and then electropolished prior to irradiation with 14 MeV copper ions.

introducing hydrogen into the samples (132). In this study, hydrogen pickup during electropolishing seems the most likely explanation for the behavior observed. Since the effect proved to be quite reproducable, the electropolishing step was kept in the procedure to assist void nucleation and allow studies of void behavior without the need to introduce helium into the specimens.

C. Comparison of Nickel, Aluminum and Carbon Ion Irradiation

To investigate the effect of irradiating with ions of lower mass than nickel and to further study the possible effects of implanted impurity ions, irradiations were performed using 8.1 MeV aluminum ions and 5 MeV carbon ions (158). The displacement curves for these ions are shown in Figure 27. The ion energies were chosen such that their ranges into nickel would be similar. Their displacement efficiencies are quite different, however, as is shown by the different axis for the ions. Basically, it takes two aluminum or ten carbon ions to produce the same peak damage level as one nickel ion. The PKA spectra for these ions also vary as is shown by Figure 4.

1) Aluminum Ion Irradiations

Nickel samples were irradiated at 525°C (798°K) with 8.1 MeV aluminum ions with fluences ranging from 4×10^{15} ions/cm^2 to 2.1×10^{16} ions/cm^2. The ions flux used was typically 8×10^{11} ions/cm^{2}s ($\approx 4 \times 10^{-4}$ dpa/s at the peak). The development of the

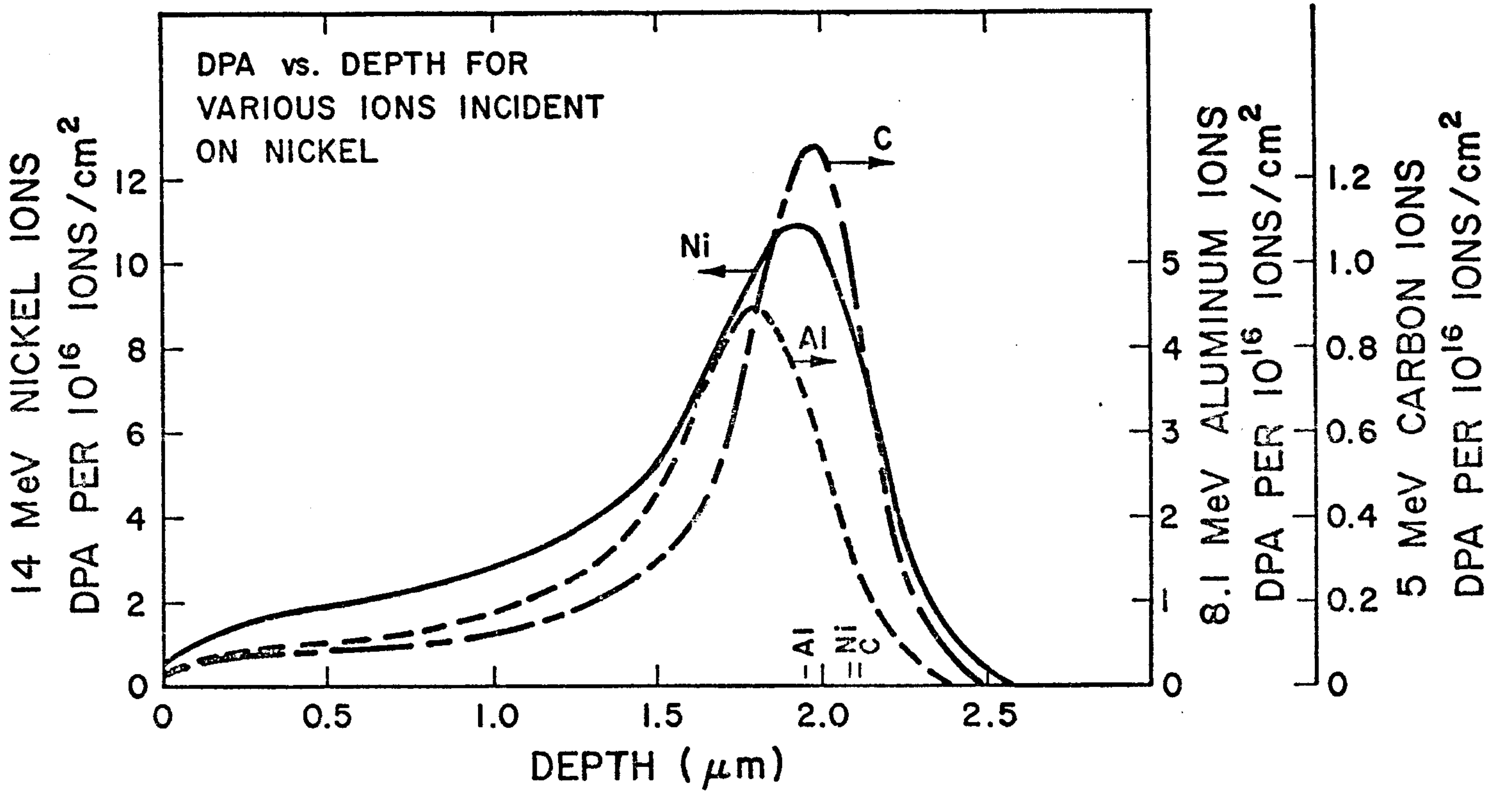

Figure 27. Displacement damage vs. depth for 14 MeV nickel, 8.1 MeV aluminum, and 5 MeV carbon ions incident on nickel. Note the different scale values for the different ions. Also shown near the base of the curves are the mean ion ranges.

depth dependent microstructure is shown in the micrographs of Figure 28. The left-hand-side of each micrograph shows the original foil surface. The incident ions have traveled from left to right and come to rest in the area near the right-hand-side of each micrograph. Voids nucleated quite readily in this material and were observed at all damage levels. The voids were always observed in these samples up to depths of 2.75 μm, with a few voids observed at even greater depths. There was no deviation in the void microstructure in the implanted range region that could be attributed to point defect interaction with aluminum ions. The voids were truncated octahedra throughout the damage region.

Void data was obtained from these specimens by dividing each into depth intervals 0.25 μm wide parallel to the foil surface. Average void diameter, void density, and void volume fraction were then measured within each interval. Figures 29-32 show the data obtained for the four fluence levels. The data points for each interval are plotted as points and not as histograms, with the curves drawn to aid the eye in following the depth variation in void parameters. At low fluences (Figure 29) the void density curve has the same general shape as the displacement curve. At high fluences, however, the void density has dropped significantly and shows much less variation in magnitude from the front surface to the end-of-range than at low fluences. Except for the near surface region where larger voids are observed, the average void size throughout the damage

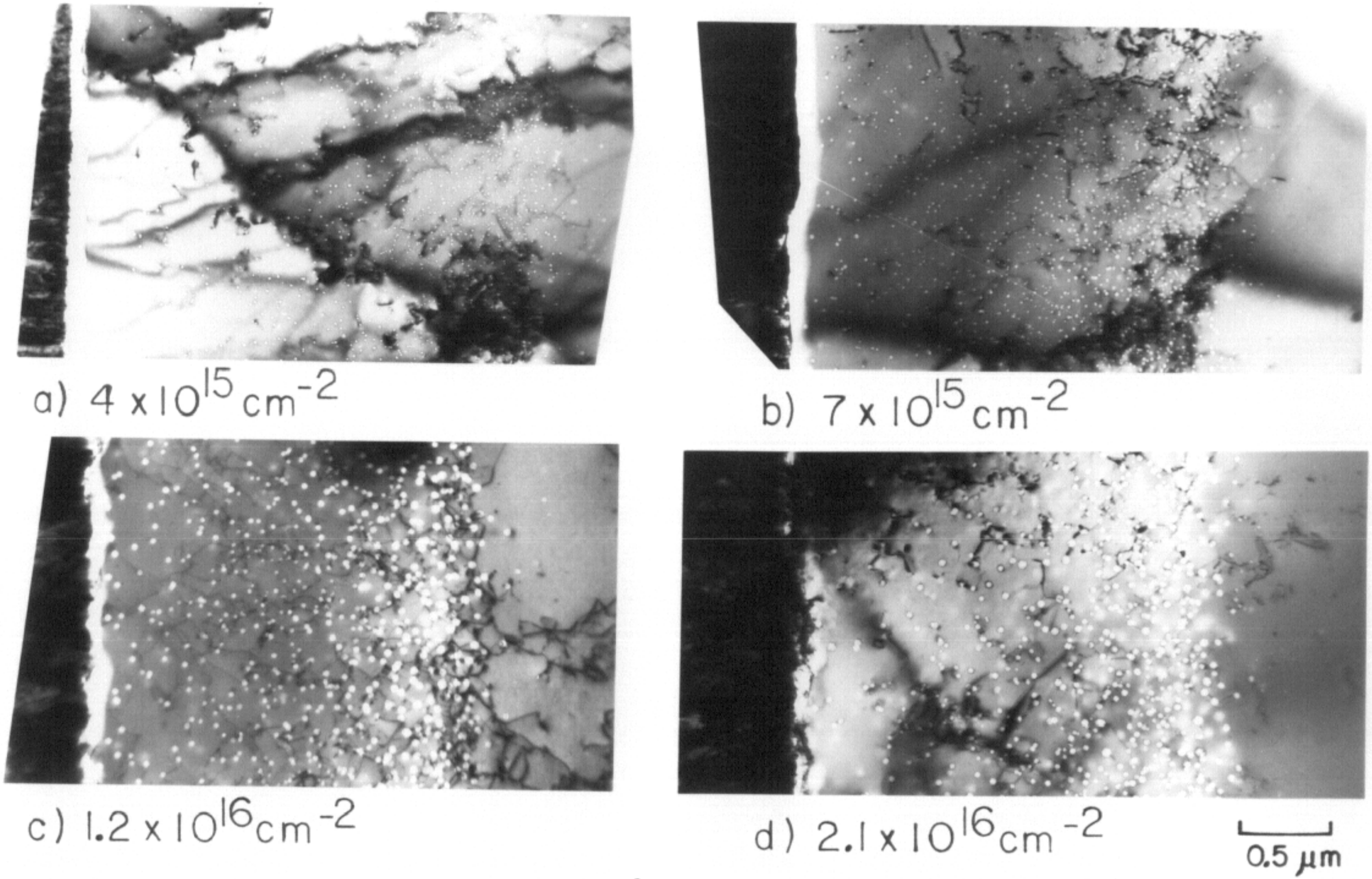
a) 4×10^{15} cm^{-2}
b) 7×10^{15} cm^{-2}
c) 1.2×10^{16} cm^{-2}
d) 2.1×10^{16} cm^{-2}

Figure 28. Nickel after irradiation at 525°C with 8.1 MeV aluminum ions to the fluence levels shown.

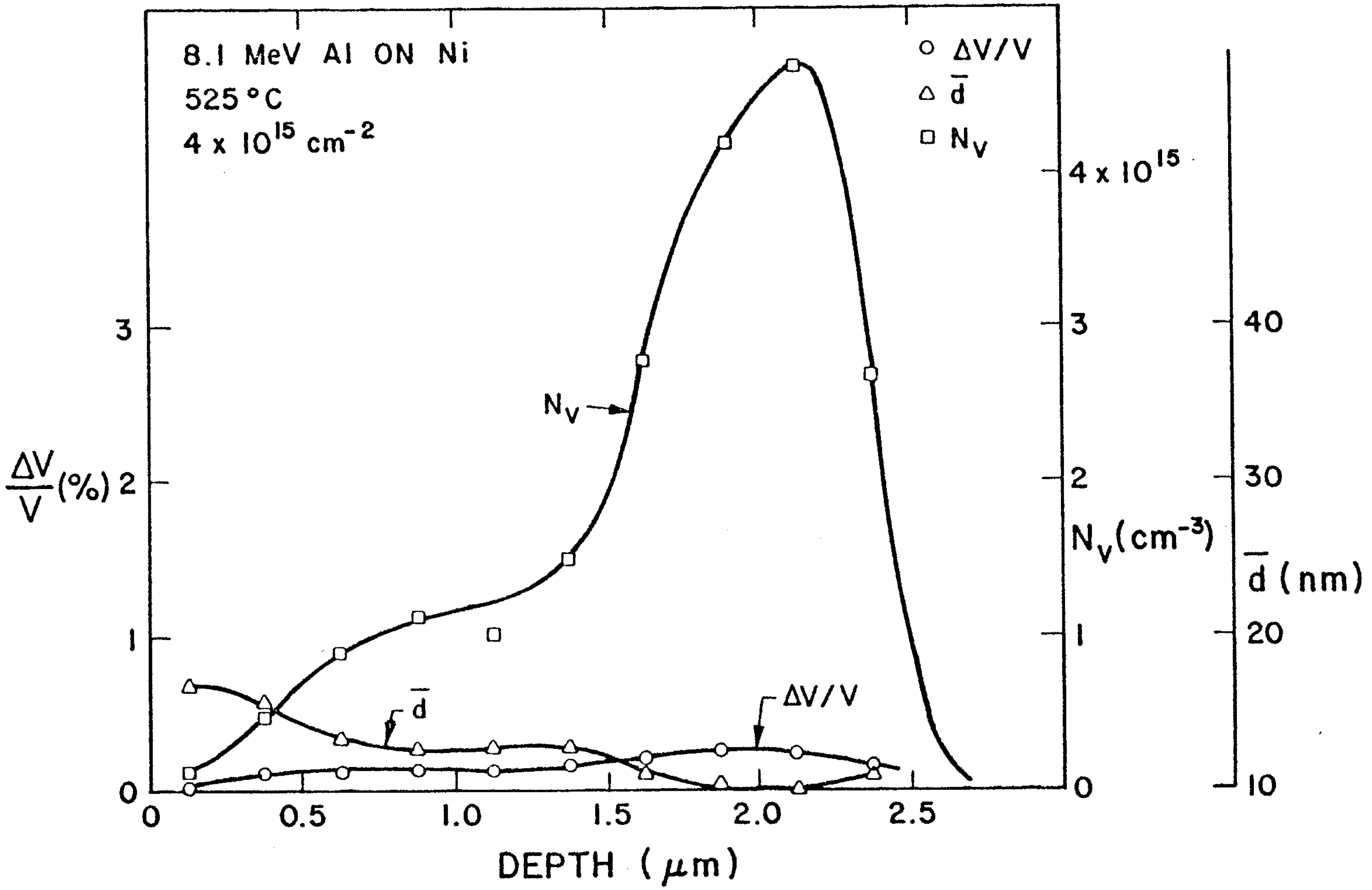

Figure 29. Void volume, void density, and void size as a function of depth in nickel irradiated with 8.1 MeV aluminum ions to a fluence of $4x10^{15}$ions/cm^2.

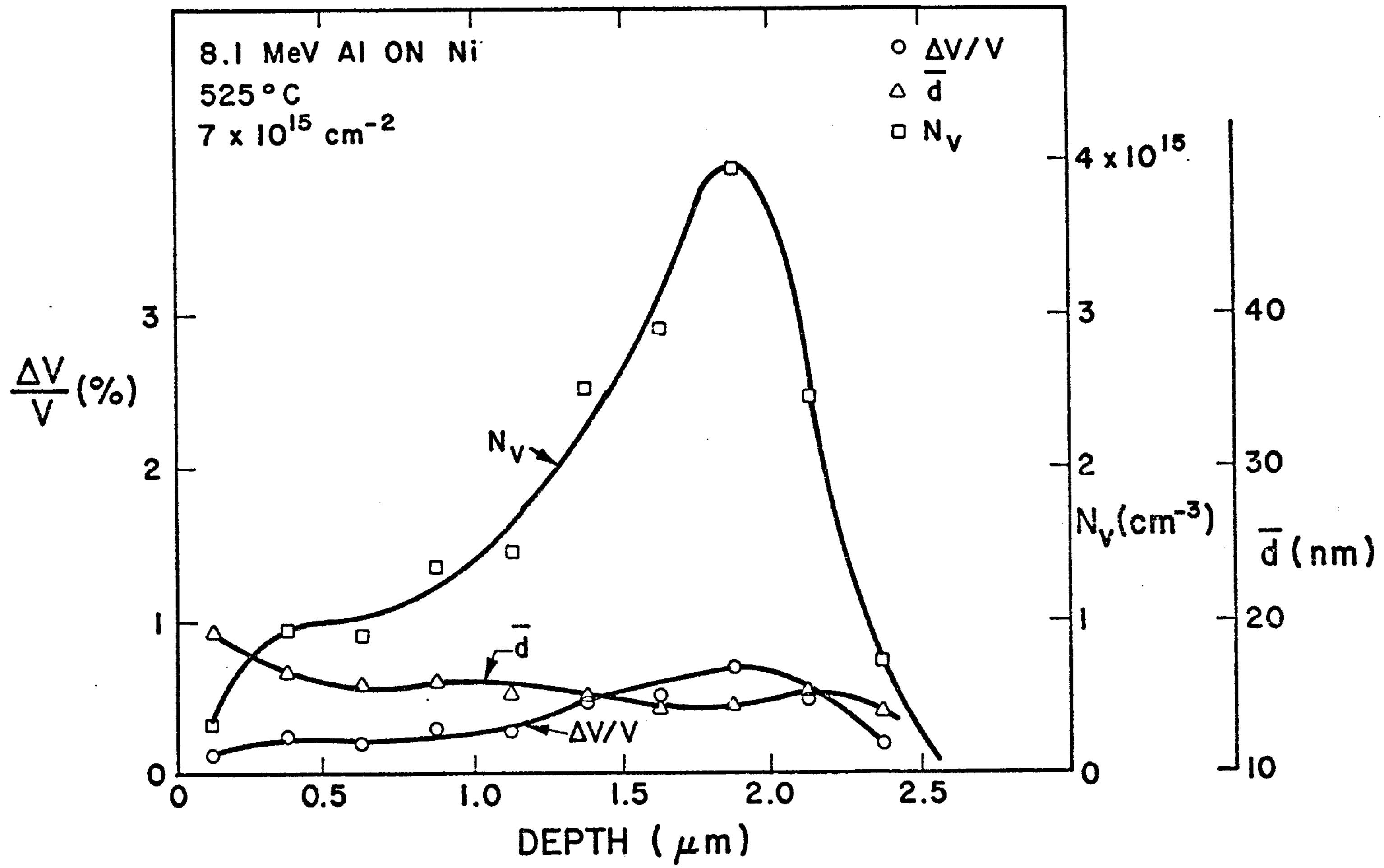

Figure 30. Void volume, void density, and void size for nickel irradiated with 8.1 MeV aluminum ions to a fluence of 7×10^{15} ions/cm^2.

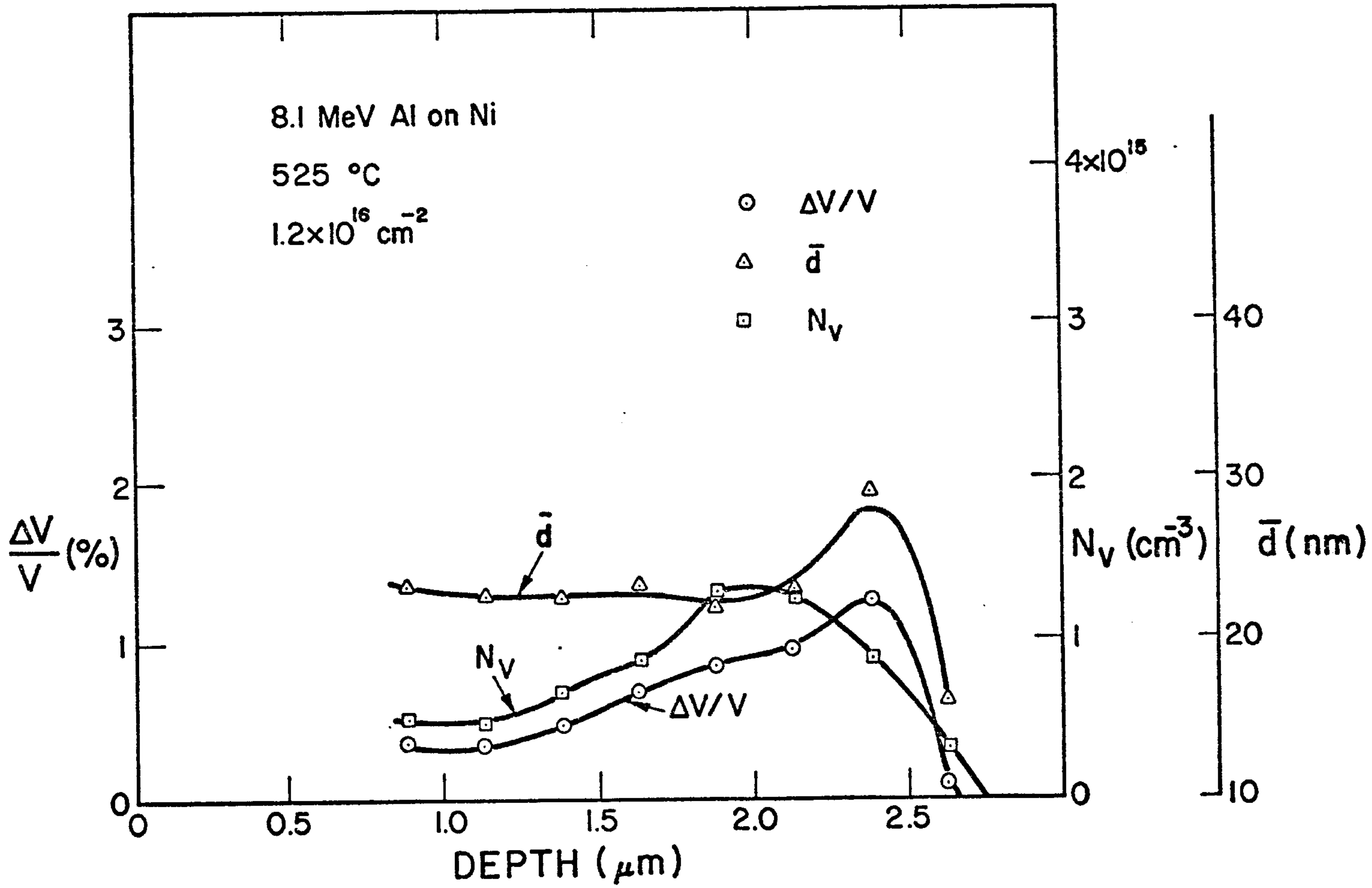

Figure 31. Void volume, void density, and void size vs. depth in nickel irradiated with 8.1 MeV aluminum ions to a fluence of 1.2×10^{16} ions/cm^2.

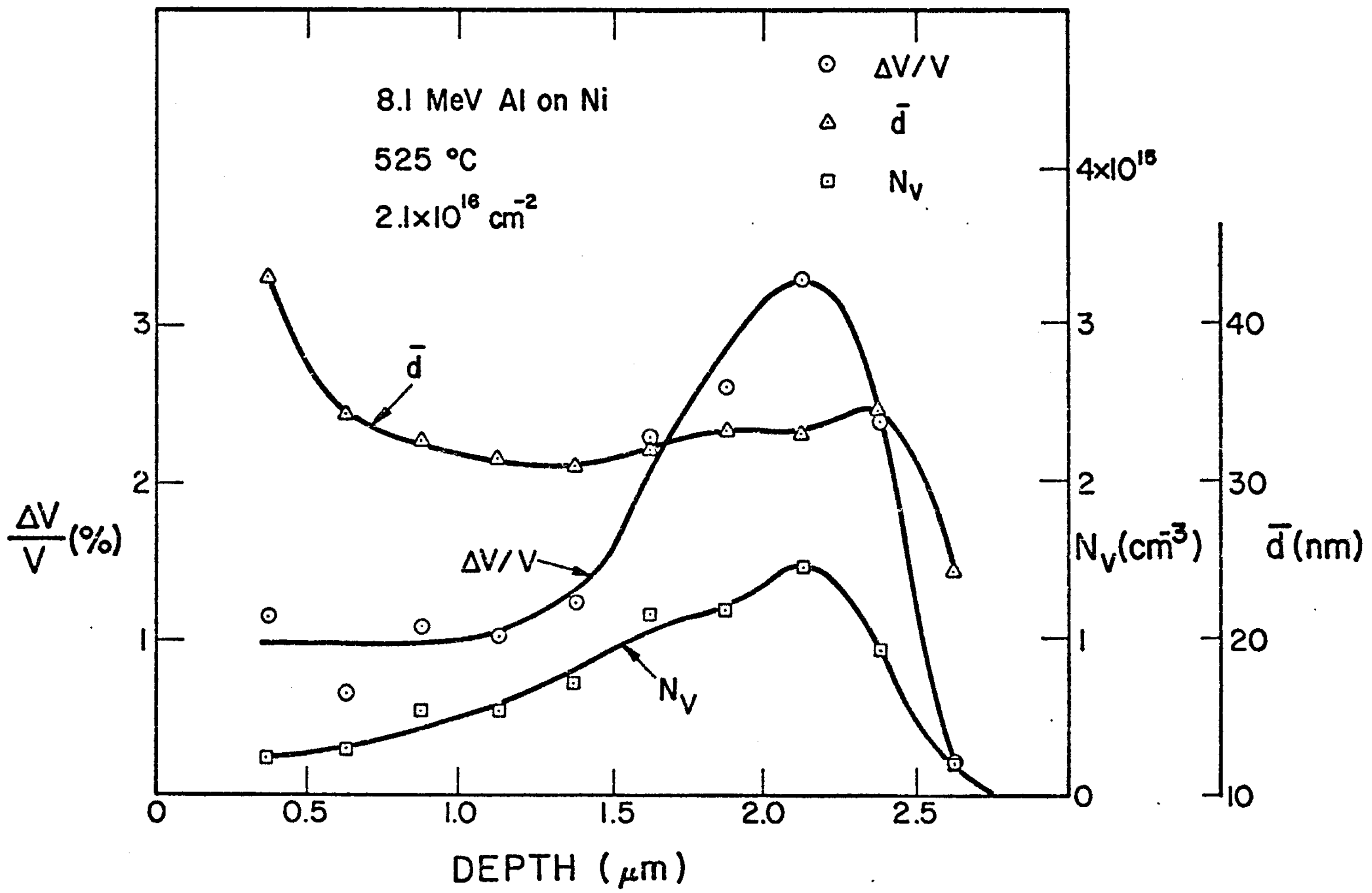

Figure 32. Void volume, void density, and void size vs. depth in nickel irradiated with 8.1 MeV aluminum ions to a fluence of 2.1×10^{16} ions/cm^2.

region does not vary significantly. The void size distribution as a function of dose at two different depths is shown by the histograms of Figure 33. The width of the void size distribution is narrower in the midrange region than in the end-of-range region, even though the average void sizes in the high dose case are not significantly different. The region of peak void swelling occurs at about 2.1 μm reaching a value of 3.3%. The theoretical peak damage level in this sample occurred at 1.8 μm reaching a value of 9.5 dpa.

2. Carbon Ion Irradiation

The carbon ion irradiations were carried out on specimens prepared identically to those for the aluminum irradiation and the irradiation was conducted at 525°C (798°K). The carbon ion flux was 4×10^{12} ions/$\text{cm}^2 \cdot \text{s}$ (5×10^{-4} dpa/s at the peak) and the ion fluences were 1.5×10^{16} ions/cm^2 and 9.3×10^{16} ions/cm^2. The void structures developed from these irradiations are shown in Figure 34, where again the original foil surface is shown on the left-hand-side of the micrographs. Voids were once more observed throughout the entire damage region, (even down to 0.2 dpa) indicating the ease with which voids could nucleate in these samples. Most voids were observed in these samples at depths less than 2.85 μm, with a few voids seen at depths up to 3.2 μm. There is a slight increase in the void size at the end-of-range. Void shapes were again truncated octahedra.

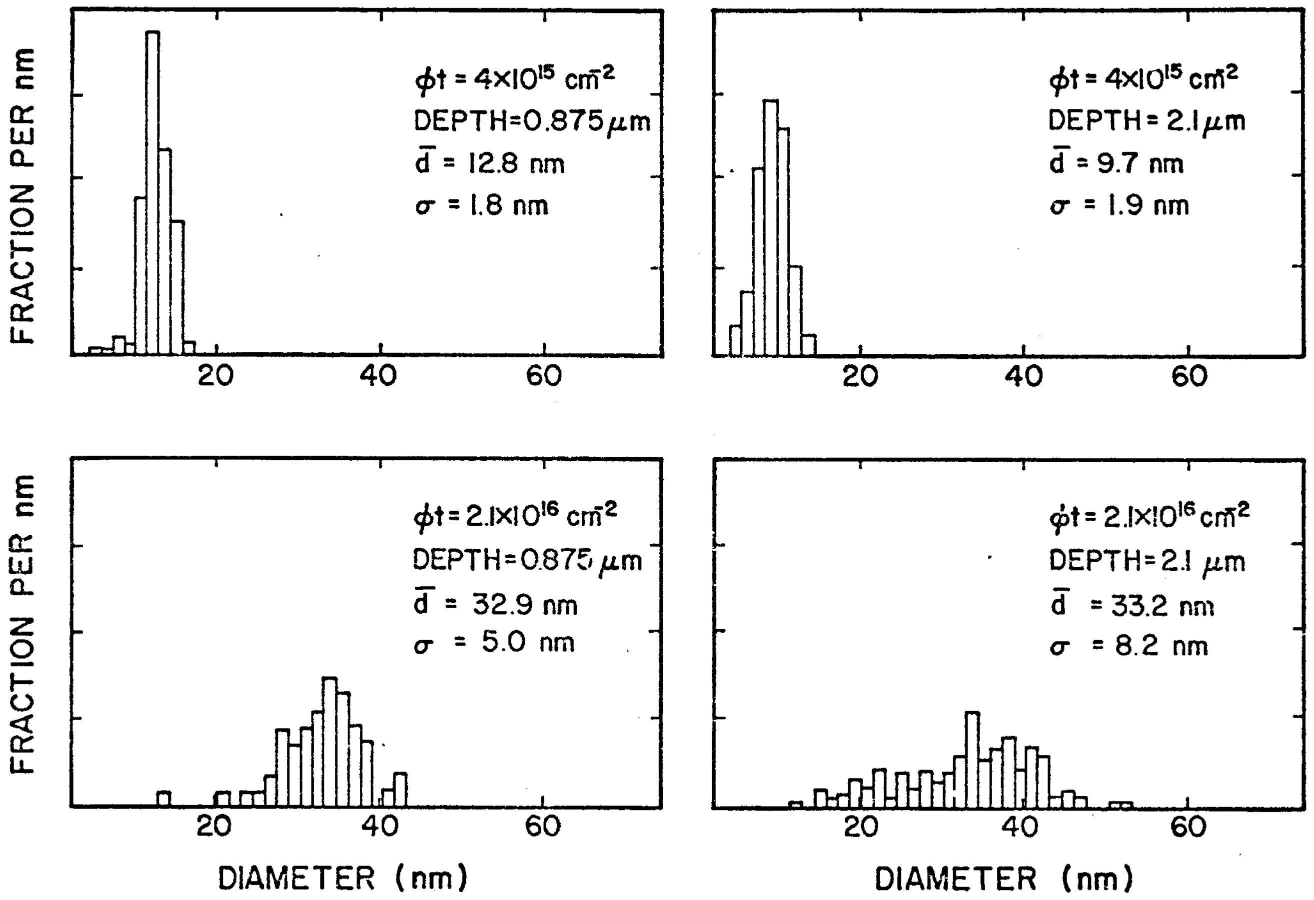

Figure 33. Void size distributions in nickel irradiated with 8.1 MeV aluminum ions at a temperature of 525°C. The data is taken from two depths in samples irradiated at fluences of 4×10^{15} and 2.1×10^{16} ions/cm^2.

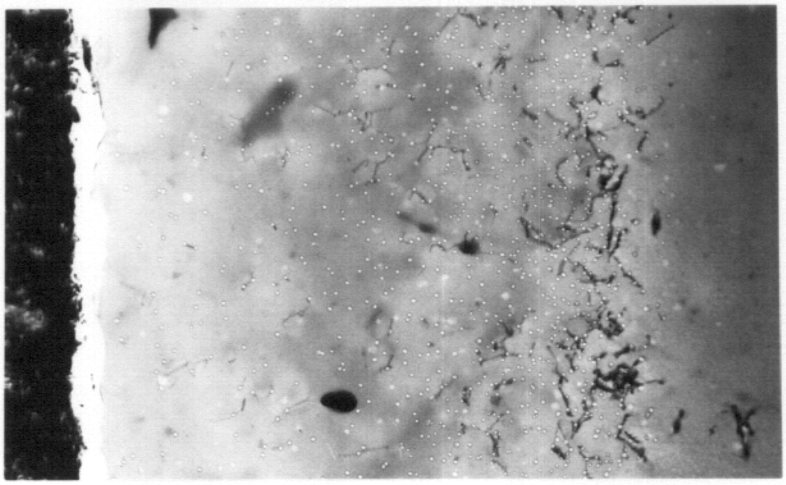

a) $1.5 \times 10^{16} cm^{-2}$

b) $9.2 \times 10^{16} cm^{-2}$

Figure 34. Nickel after irradiation at 525°C with 5 MeV carbon ions.

The plots of void density, void size and void volume fraction for the two carbon ion fluences are shown in Figures 35 and 36. The void density curve is noticeably broader than the displacement curve in this case. The void density does not drop as rapidly with dose as in the aluminum ion irradiation, nor does the void size vary strongly with depth except for the surface region and the end-of-range region where it is larger than average. The peak void swelling in the carbon irradiated samples occurred at 2.4 µm with a value of 2.6%. The theoretical damage peak of 12 dpa occurs at a depth of 2.0 µm.

3. Dislocation Structure Development

The dislocation structure observed after irradiation with carbon ions is shown in Figure 37a. The structure consists mainly of network dislocations with a few scattered loops. The total dislocation density ranged from 10^{10} to 10^{11} cm/cm^3, and increased significantly in the end-of-range region.

The dislocation structure for the aluminum irradiated samples is shown for two fluence levels in Figures 37b and 37c. Here, at the low fluence, the dislocation structure consists of a dense network of dislocations interwoven among the high density of voids. This structure contains very few loops and is confined to the end-of-range region. At the highest fluence, the dislocation density has been reduced somewhat while at the same time extending to the near surface region.

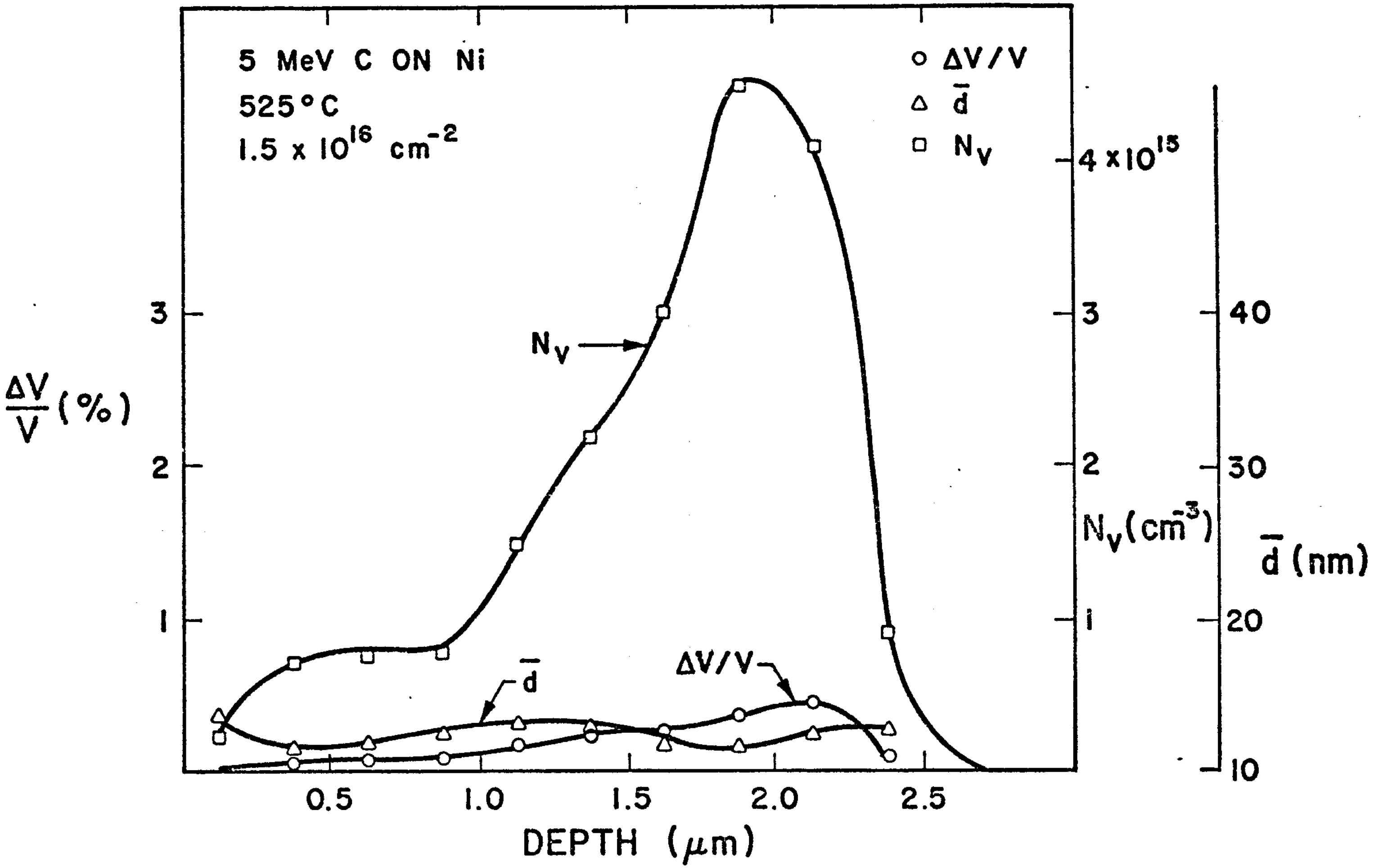

Figure 35. Void volume, void density, and void size in nickel irradiated at 525°C with 5 MeV carbon ions to a fluence of 1.5×10^{16} ions/cm^2.

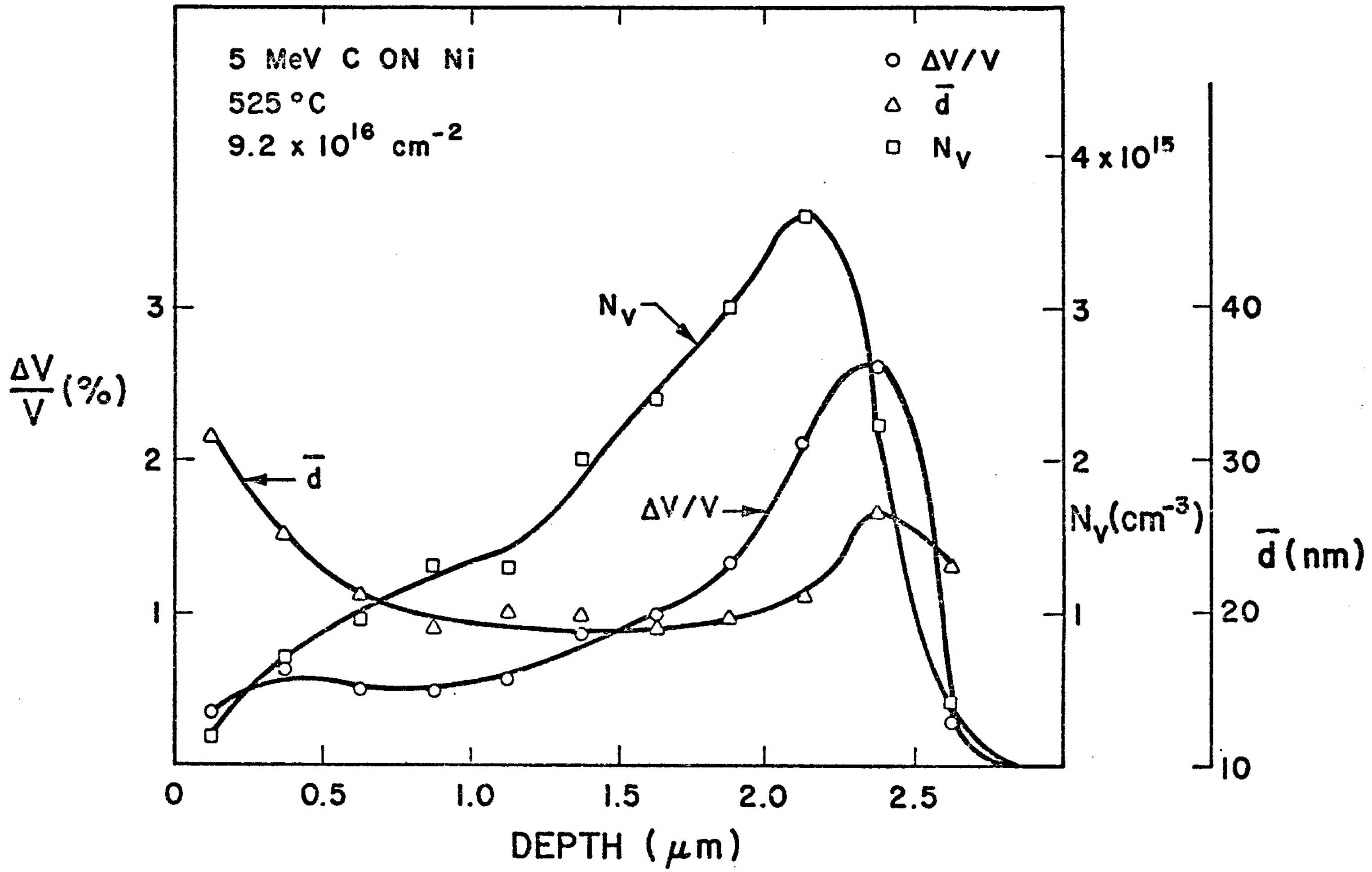

Figure 36. Void volume, void density, and void size in nickel irradiated at 525°C with 5 MeV carbon ions to a fluence of 9.2x10^{16} ions/cm^2.

a) 5 MeV C, 1.5×10^{16} cm^{-2}

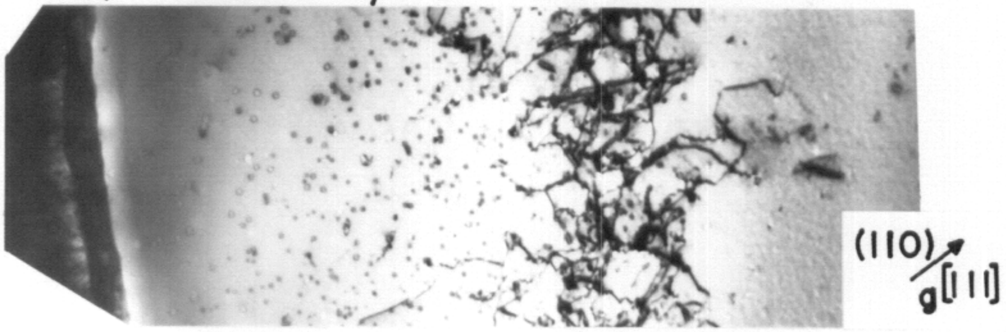

b) 8.1 MeV Al, 7×10^{15} cm^{-2}

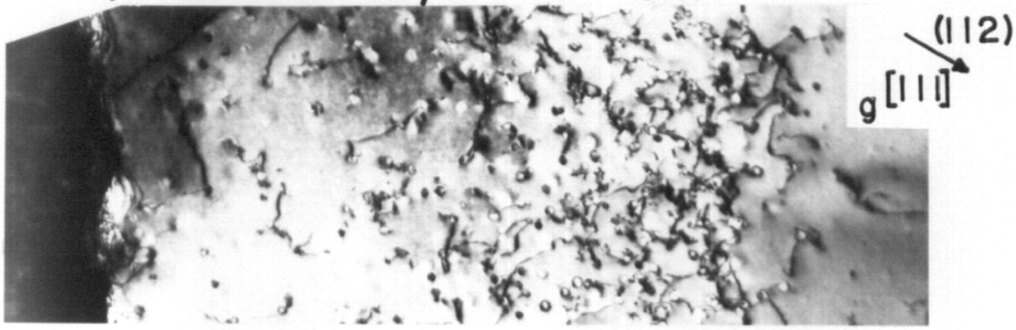

c) 8.1 MeV Al, 2.1×10^{16} cm^{-2}

Figure 37. Dislocation structure after irradiation at 525°C with carbon or aluminum ions.

4. Comparison to Self-Ion Irradiations of Identical Specimens

The carbon and aluminum irradiations were designed such that a relatively direct comparison could be made with a self-ion irradiated specimen. In Figure 38 such a comparison is shown where the ion fluences are such that the peak damage values vary form ~15 dpa for the nickel ion irradiated specimen, to ~10 dpa for the aluminum ion irradiated specimen. The void data obtained from the self-ion irradiated specimen is shown in Figure 16. The nickel ion sample was irradiated at a higher dose rate, however, with a nickel ion flux of 1.5×10^{12} ions/cm^2•s (1.6×10^{-3} dpa/s at the peak compared to 5×10^{-4} dpa/s for the carbon and aluminum irradiated specimens).

There were several differences in the void microstructure between the specimens irradiated with different ions. In the near surface region, the self-ion irradiated specimen had a much larger void size in the surface region than either the aluminum or carbon irradiated specimens. This increase in void diameter is similar to the increase seen next to grain boundaries in these specimens. The self-ion irradiated specimen showed a reduction in the void size in the end-of-range region which was not seen with the other ions. This reduction corresponds to the peak in the void density curve. After aluminum irradiation, there is little variation in the void density and this reduction in void size is not seen. The carbon ion irradiated sample fails to show a drop in void size with increasing void density, but does show an increase at the far end-of-range region.

a) 5 MeV C, 9.2×10^{16} cm^{-2}

b) 8.1 MeV Al, 2.1×10^{16} cm^{-2}

c) 14 MeV Ni, 1.3×10^{16} cm^{-2}

Figure 38. Nickel irradiated at 525°C with different ions to similar peak damage levels. The arrows mark the predicted maximum ion range.

All specimens contained voids at depths greater than the range of the damage curve. This is shown in Figure 38, where the arrows on the micrographs indicate the predicted maximum ion range. The nickel ion irradiated sample showed a rather sharp void density cutoff with very few voids found beyond this range. Both the carbon and the aluminum irradiated samples failed to show this sharp cutoff, with a few scattered voids as much as 200-300 nm beyond the general void containing area.

D. Results of 14 MeV Nickel Ion Irradiation

To aid in interpreting the depth dependent void growth rates, a series of seven samples were irradiated at 525°C with 14 MeV nickel ions to fluences ranging from 2×10^{15} to 1.4×10^{17} ions/cm^2. The samples were prepared for irradiation by annealing for one hour at 850°C in an inert atmosphere and then electropolishing. The development of the void structure as a function of ion fluence is shown in the micrographs of Figures 39 and 40. The original foil surface is visible near the left hand side of each micrograph with the incident ions having travelled from left to right.

Voids were again observed throughout the damage region at all fluence levels (down to 0.4 dpa). There was a denuded region at the front surface of 100 to 150 nm, with the voids adjacent to this denuded region being unusually large. The size of these voids increased with fluence until they became so large that they extended into the denuded zone and disappeared. Voids were observed up to depths of

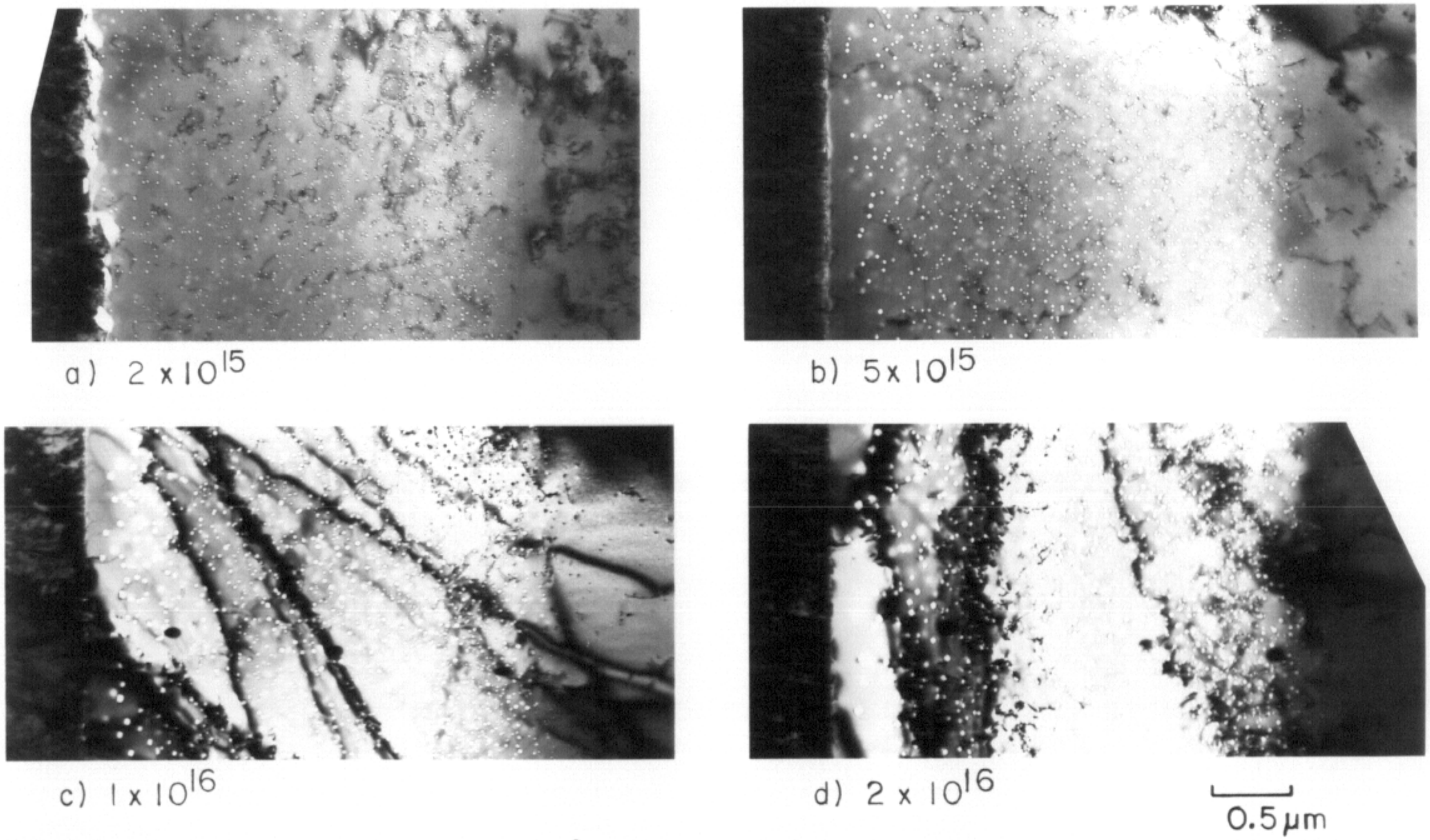
a) 2×10^{15}

b) 5×10^{15}

c) 1×10^{16}

d) 2×10^{16}

Figure 39. Nickel irradiated at 525°C with 14 MeV nickel ions to the fluence levels shown.

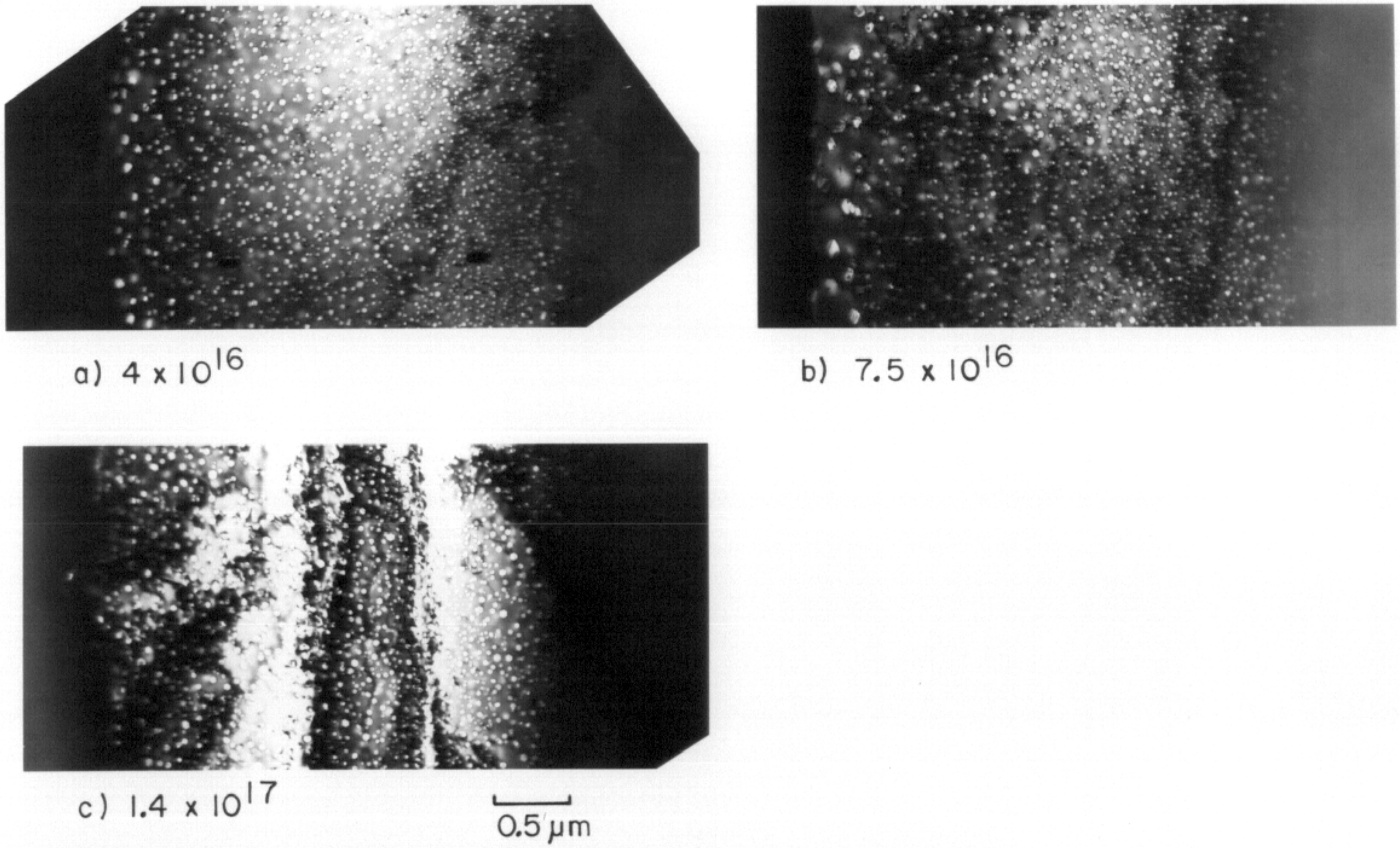

Figure 40. Nickel irradiated at 525°C with 14 MeV nickel ions to the fluence levels shown.

about 3.2 μm. At the highest fluence level (150 dpa at the peak), the voids show signs of partial ordering. This can be seen in the micrograph of Figure 41 where the foil normal was set very close to a (002) direction. This ordering is the early stages of a void lattice formation which has been previously observed in nickel (107). The void shapes were truncated octahedron except at the highest ion fluence, where the shapes were more cubic.

Void data was collected from these samples using 0.25 μm depth intervals and is presented in Figures 42-48. To assist in interpreting this data, it is replotted in Figures 49-51 by taking data from three depth intervals of each sample and plotting the data against the dpa value of each point as determined from the curve of Figure 2. Hence, the set of data points from a given depth will represent data where the main irradiation variable is the total ion fluence (that is, data that is typical of that taken by conventional sample preparation procedures). A comparison of data sets from different depths of the same sample will involve changes in dose rate, PKA spectrum, etc. From the void density curves of Figure 49, the void density is seen to saturate very early (<0.5 dpa). At a given dpa value, the void density increases with increasing depth, a result expected from the higher dose rate in these regions. The void size curve also shows the expected behavior of increasing void size with increasing dose, and decreasing void size with increasing dose rate (i.e., depth). Void sizes are either constant or drop slightly above 20 to 50 dpa (107).

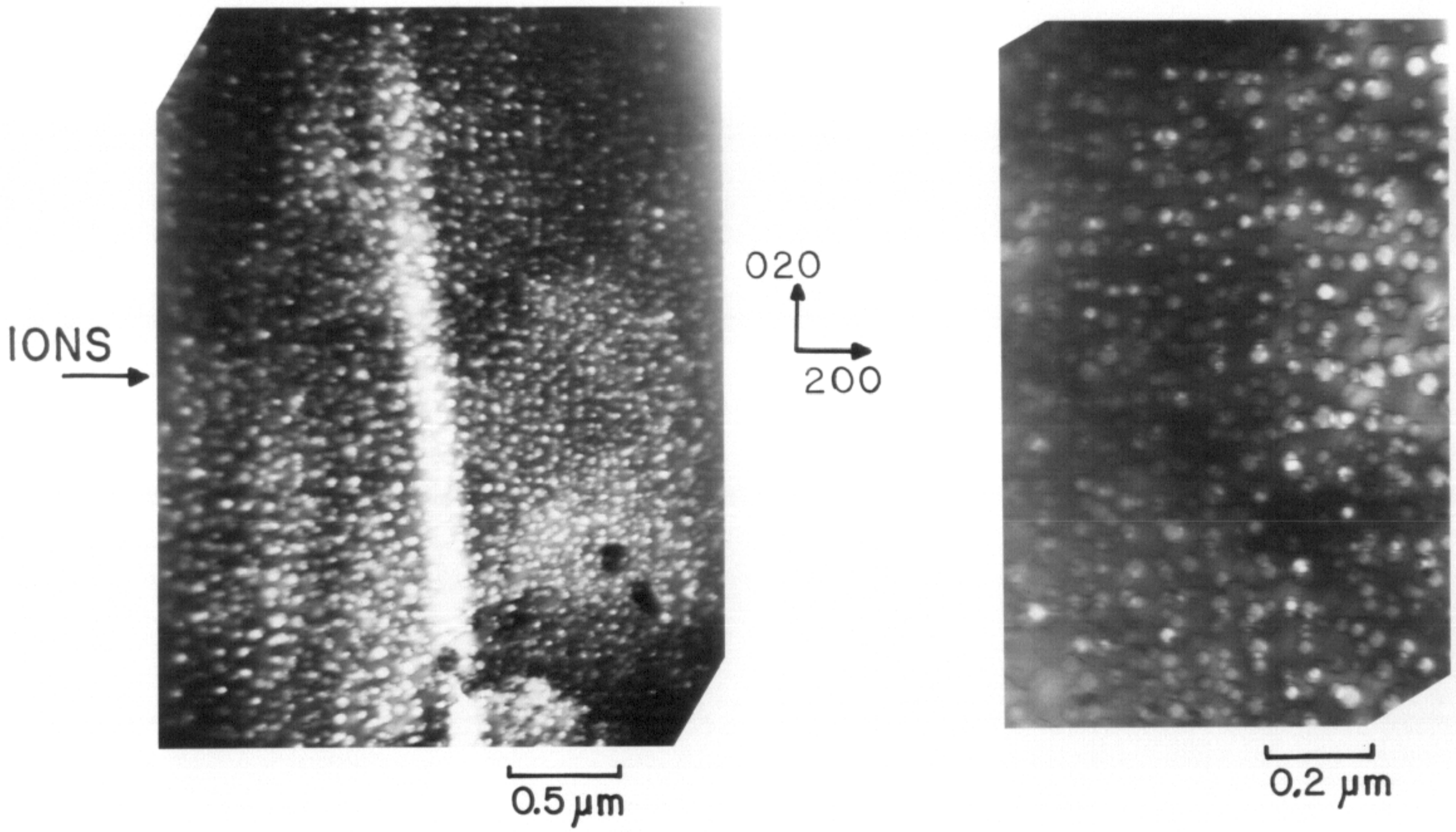

Figure 41. Void superlattice formation in nickel irradiated at 525°C with 14 MeV nickel ions to a fluence of 1.4×10^{17} ions/cm^2.

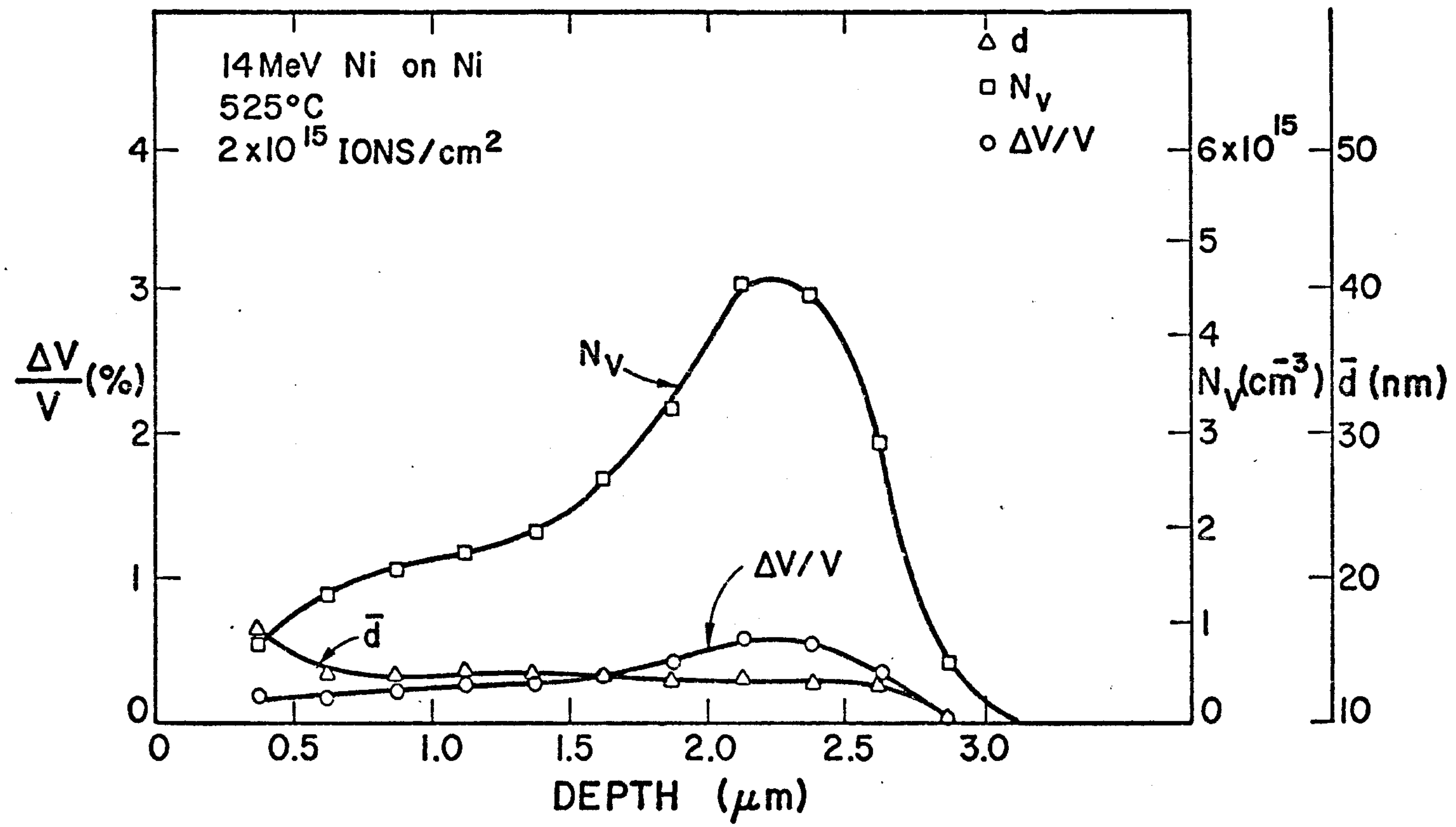

Figure 42. Void volume, void density, and void size as a function of depth in nickel irradiated at 525°C with 14 MeV nickel ions to a fluence of 2×10^{15} ions/cm^2.

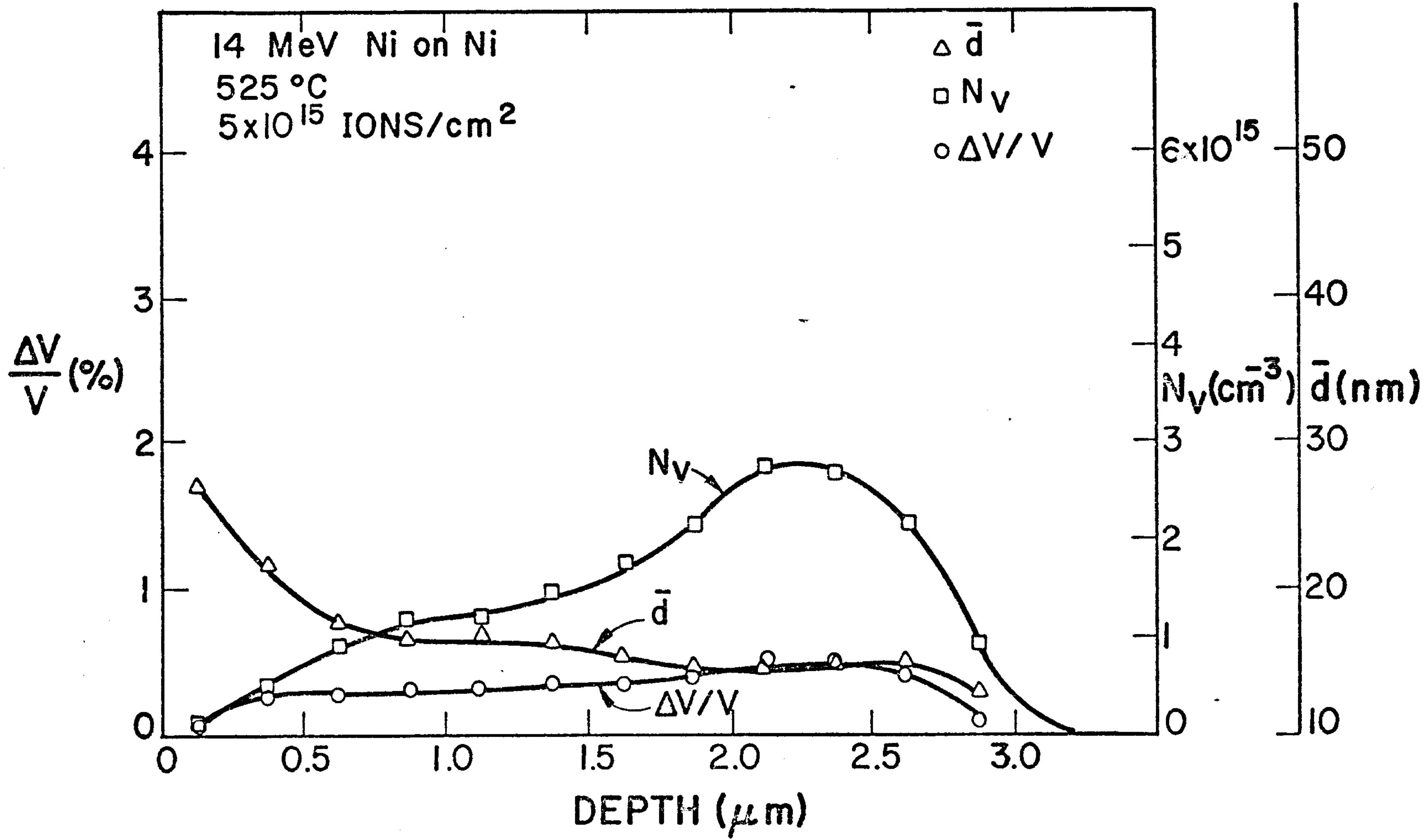

Figure 43. Void volume, void density, and void size for nickel irradiated at 525°C with 14 MeV nickel ions to a fluence of 5x10^{15} ions/cm^2.

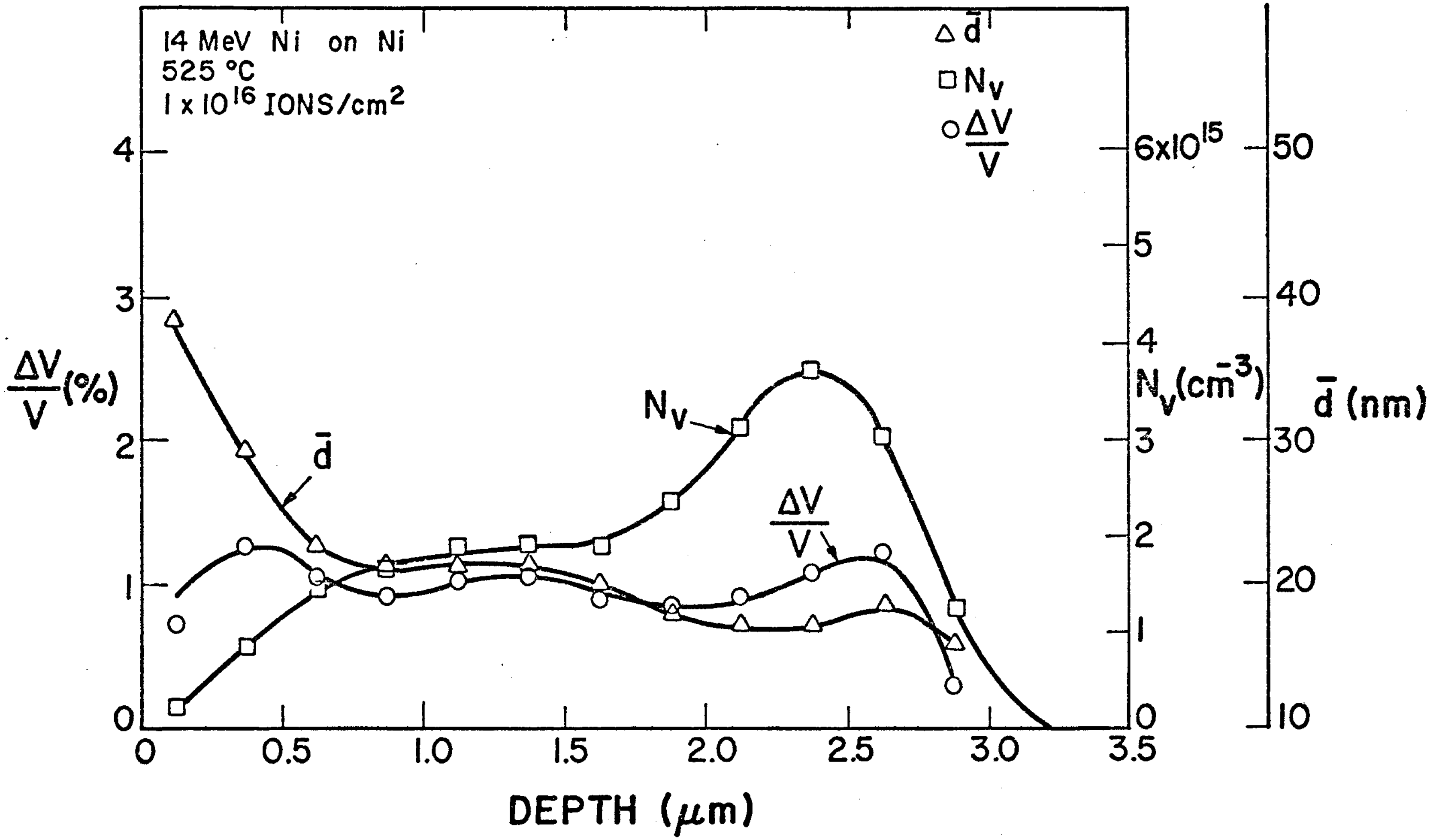

Figure 44. Void volume, void density, and void size in nickel irradiated at 525°C with 14 MeV nickel ions to a fluence of 1x10^{16} ions/cm^2.

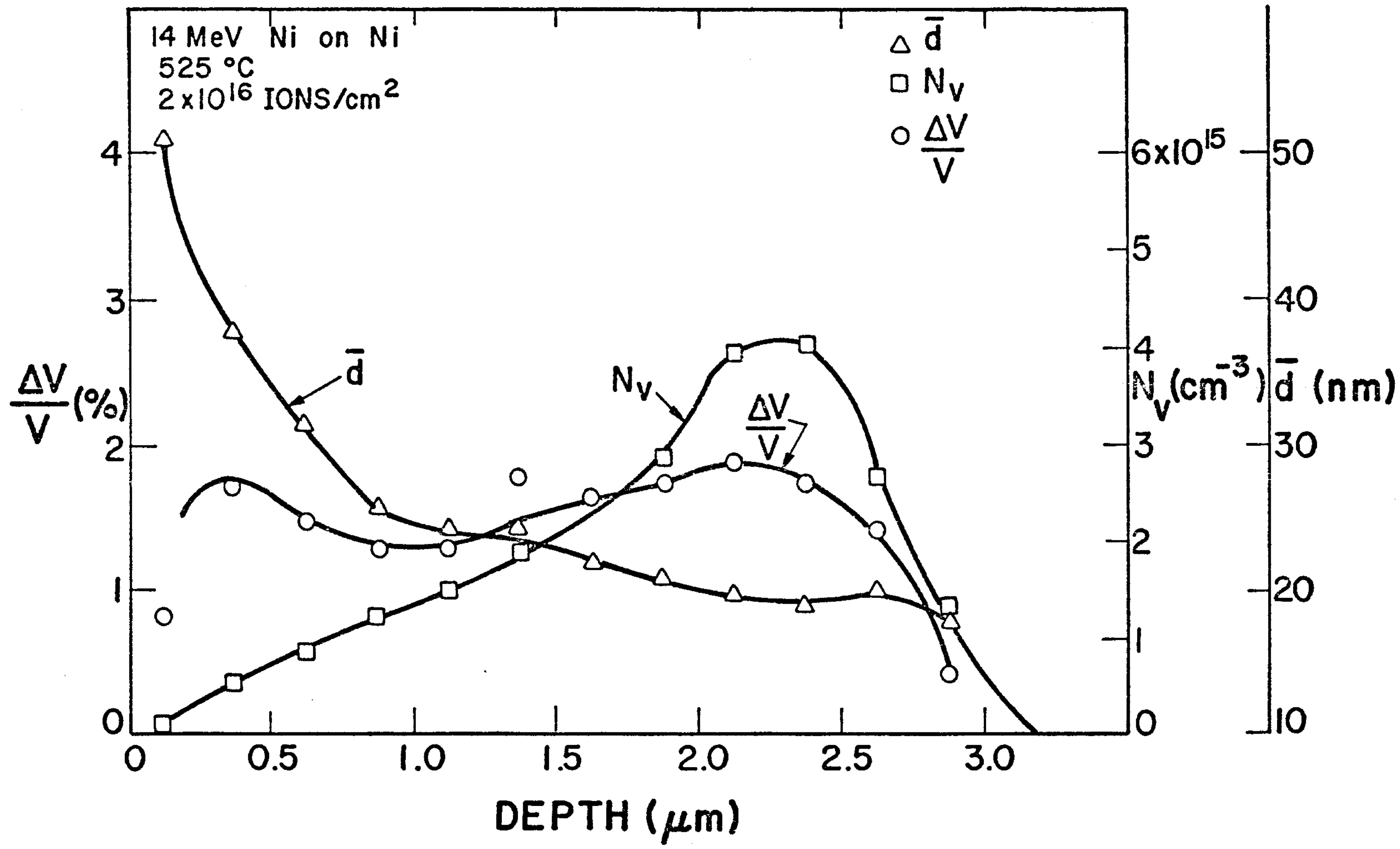

Figure 45. Void volume, void density, and void size as a function of depth in nickel irradiated at 525°C with 14 MeV nickel ions to a fluence of 2×10^{16} ions/cm^2.

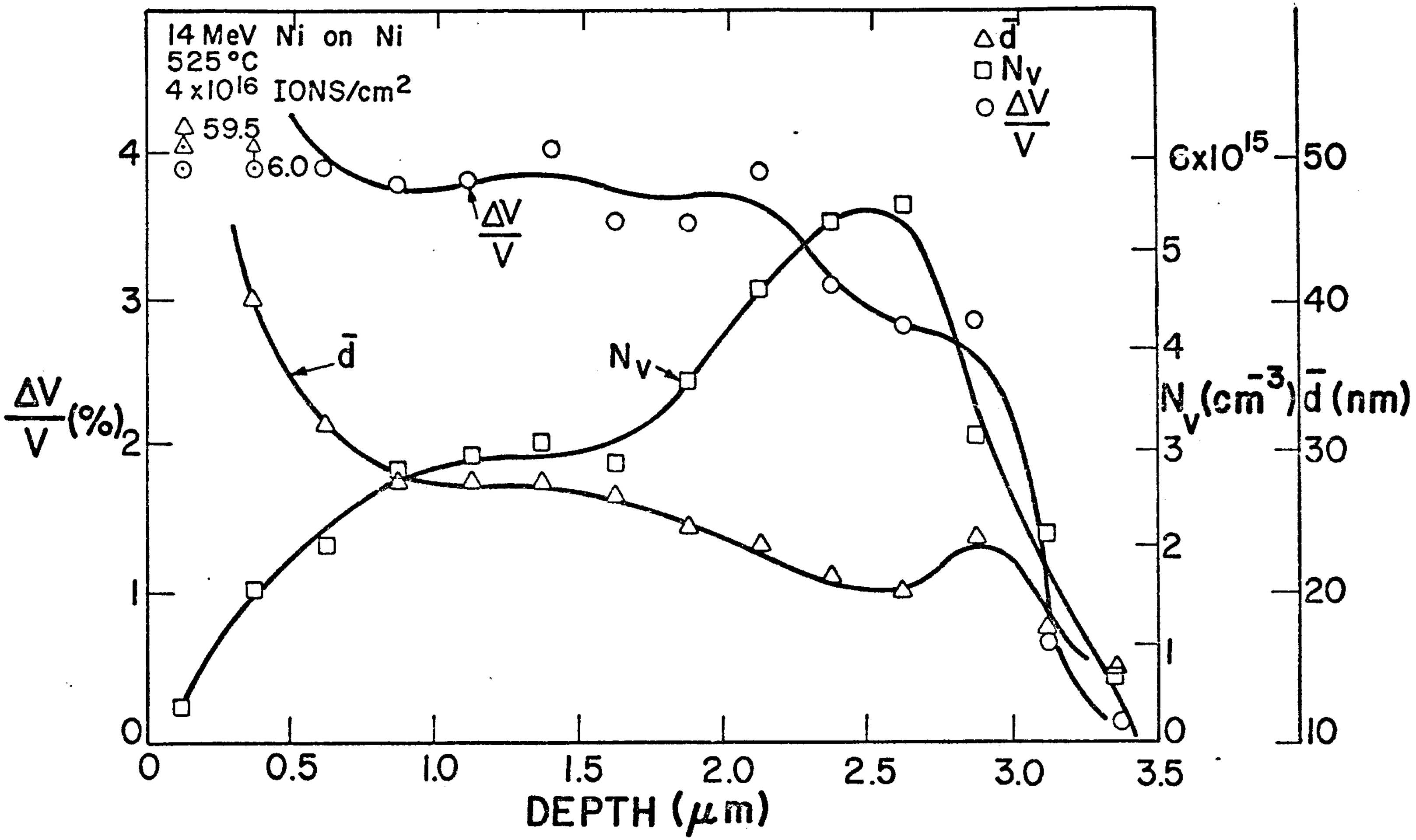

Figure 46. Void volume, void density, and void size in nickel irradiated at 525°C with 14 MeV nickel ions to a fluence of 4×10^{16} ions/cm^2.

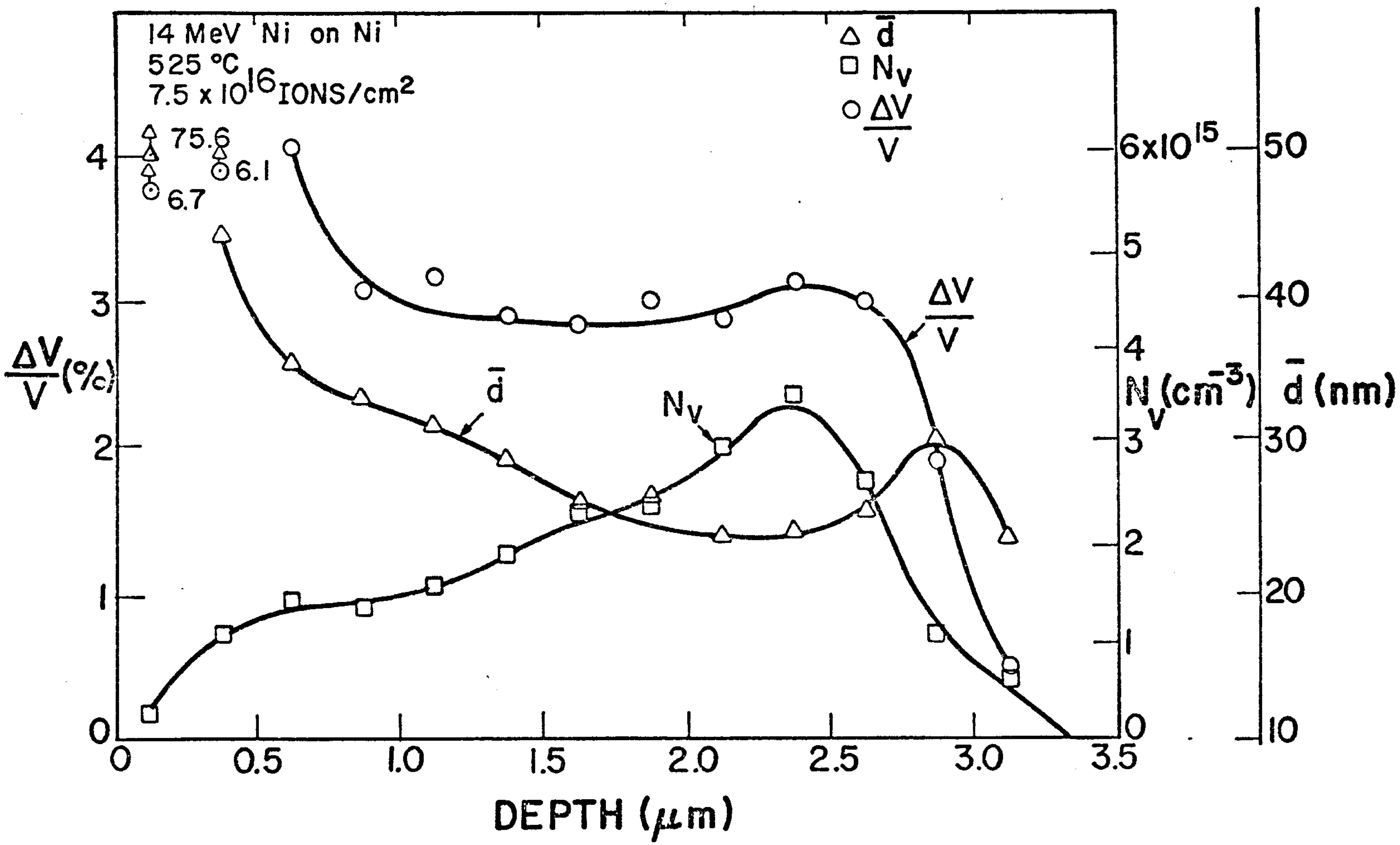

Figure 47. Void volume, void density, and void size in nickel irradiated at 525°C with 14 MeV nickel ions to a fluence of 7.5x10^{16} ions/cm^2.

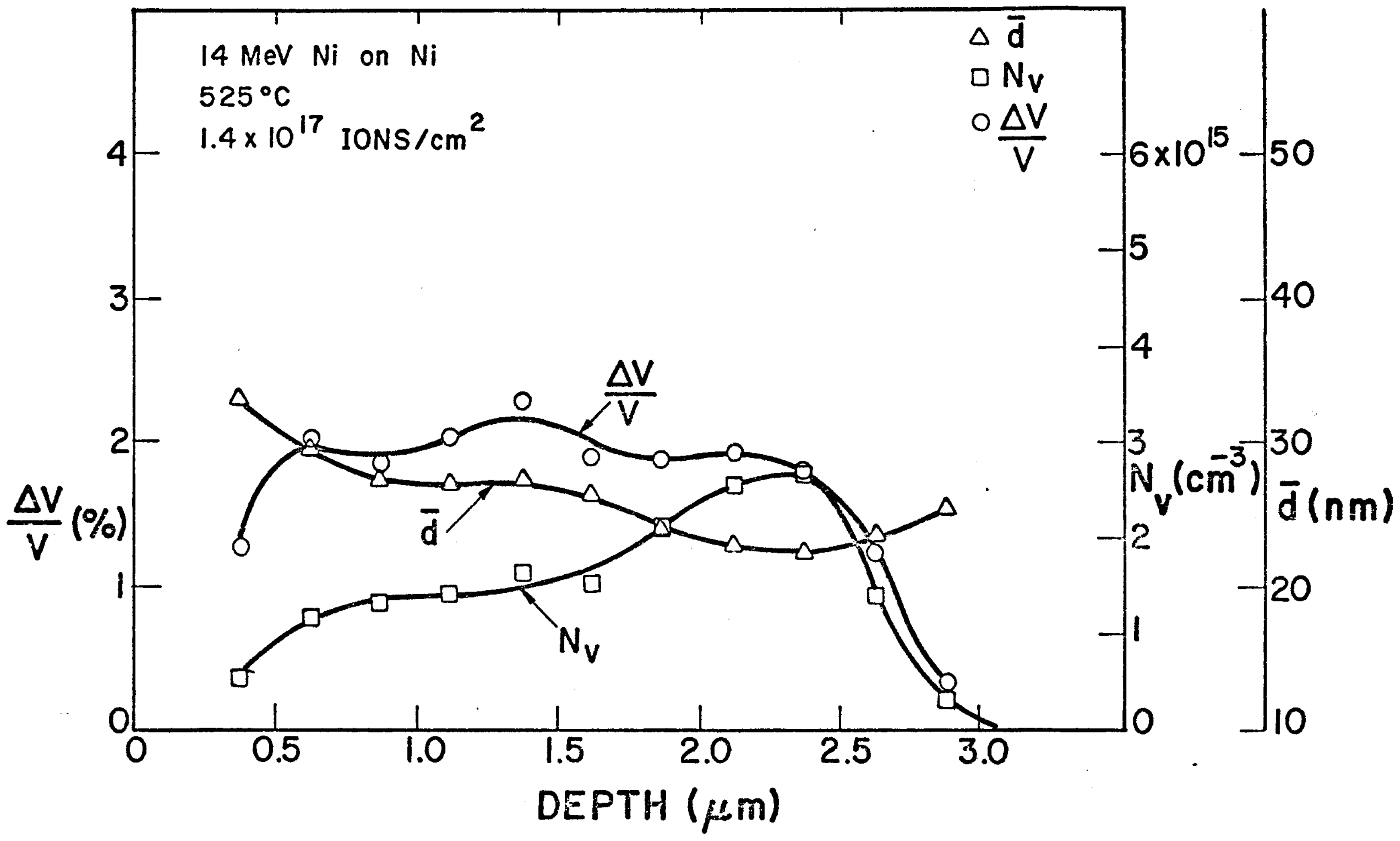

Figure 48. Void volume, void density, and void size in nickel irradiated at 525°C with 14 MeV nickel ions to a fluence of 1.4x10^{17} ions/cm^2.

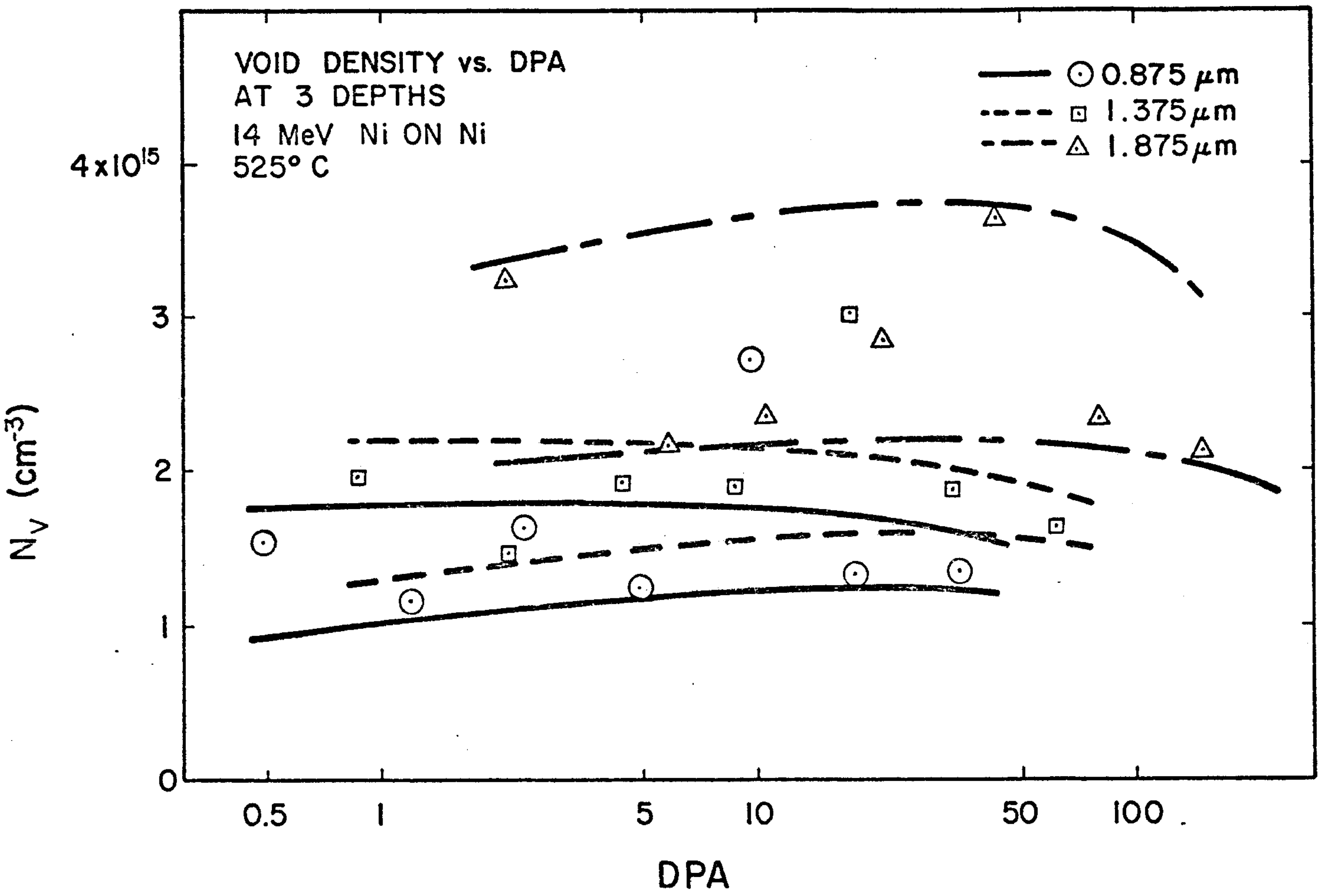

Figure 49. Void density versus displacement damage at three depths in nickel irradiated at 525°C with 14 MeV nickel ions to fluences of $2\text{x}10^{15}$ to $1.4\text{x}10^{17}$ ions/cm^2. The displacement values were taken from figure 2, and the density data from figures 42 through 48.

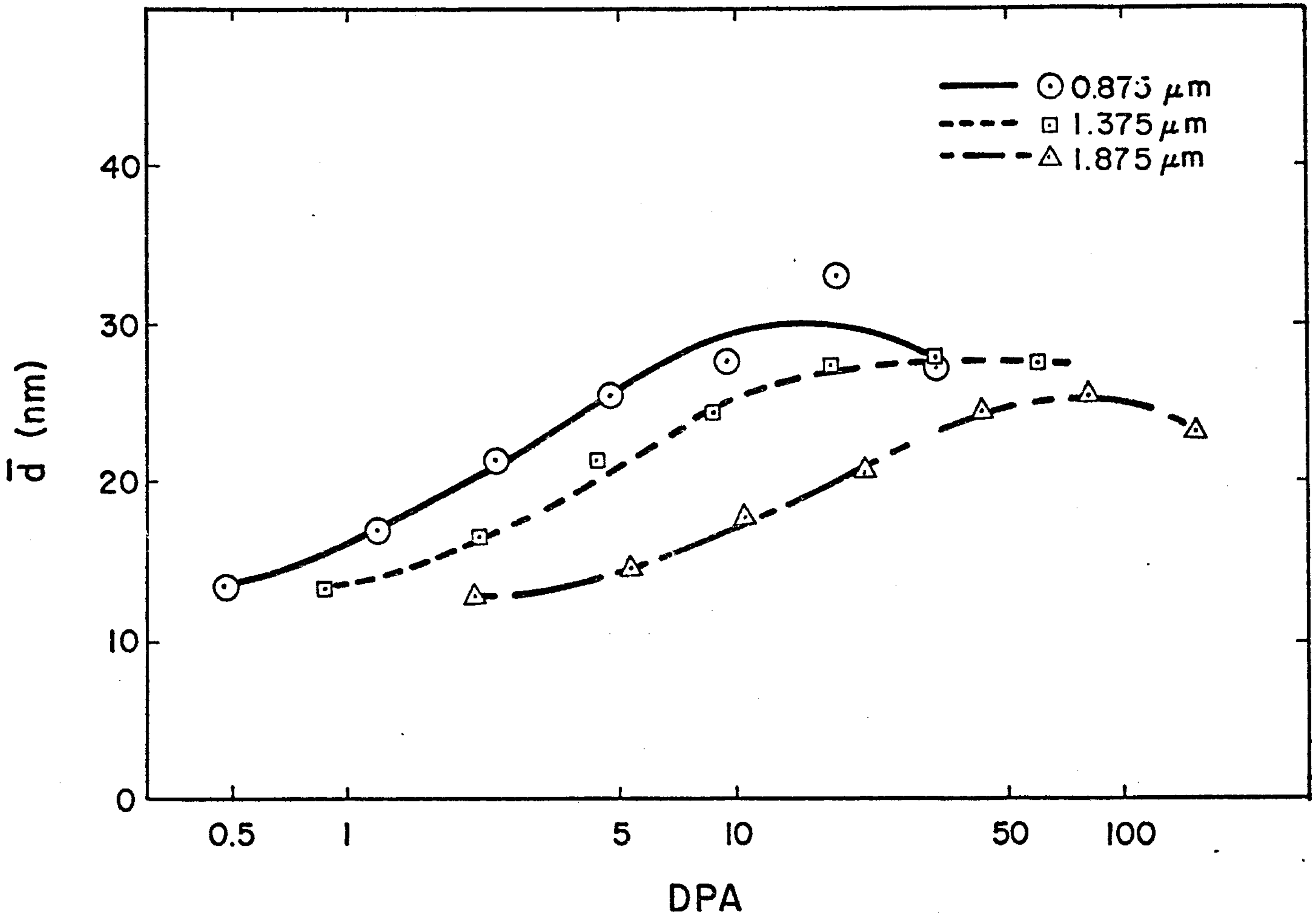

Figure 50. Average void diameters versus displacement damage in nickel irradiated at 525°C with 14 MeV nickel at fluences of 2×10^{15} to 1.4×10^{17} ions/cm^2.

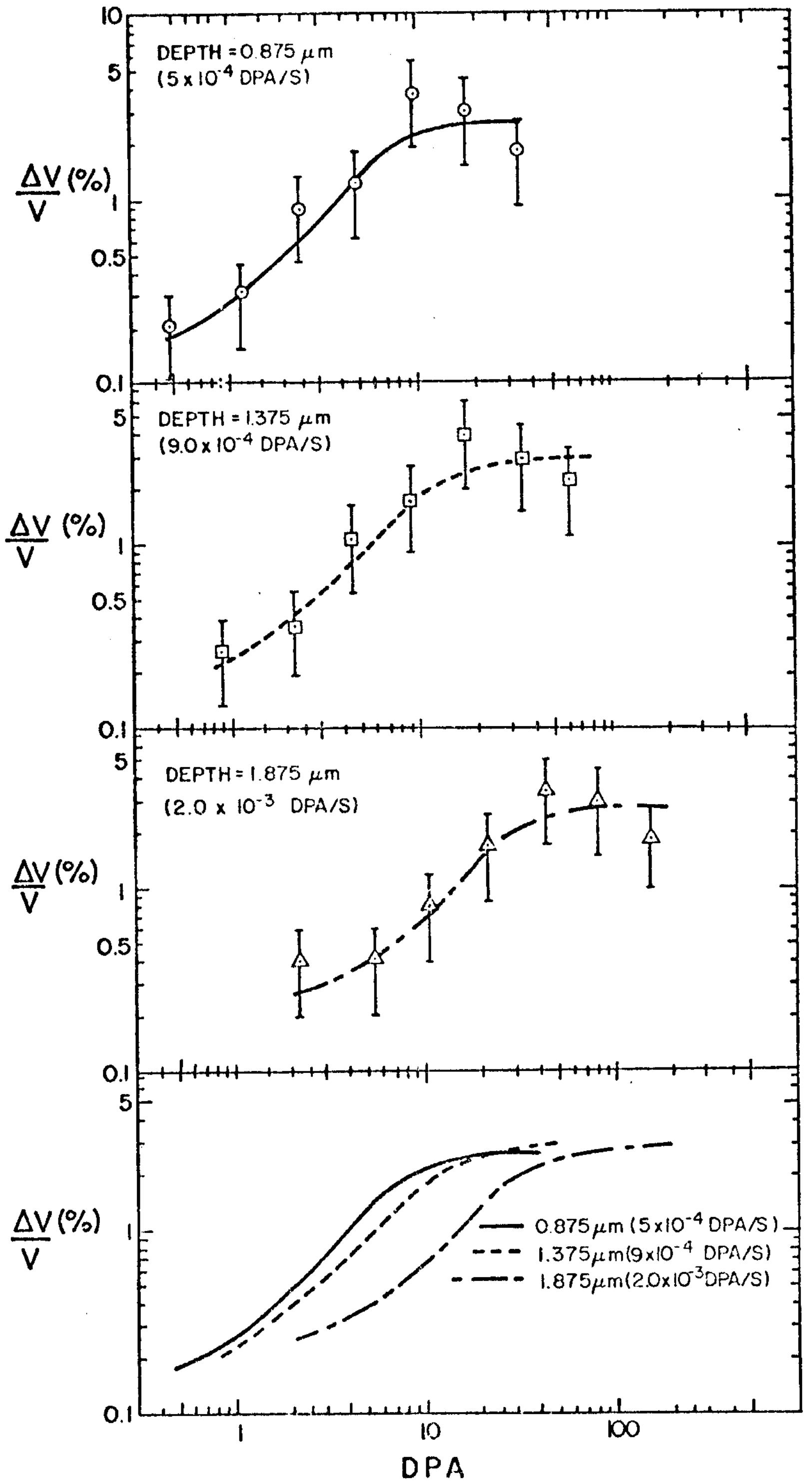

Figure 51. Void swelling versus displacement damage at three depths in nickel irradiated at 525°C with 14 MeV nickel ions at fluences from 2×10^{15} to 1.4×10^{17} ions/cm^2.

The swelling values from these specimens at the three depths are shown in Figure 51. In general, the swelling curves for each depth increase approximately linearly with dose up to about 20 to 50 dpa, at which time the swelling levels off at a value of 3%. At a given dpa value, swelling decreases with increasing depth (i.e., increasing dose rate). The slopes of the swelling curves are roughly equal. The swelling value saturates at a larger dpa value for the 1.875 μm case than it does for the other depths, but the final swelling values at saturation are about equal.

The dislocation structure at early doses in these samples is shown in Figure 52. Even at the lowest ion fluence, the structure contained few loops and consisted mainly of network dislocation. The dislocation density varied from 5×10^9 to 10^{10} cm/cm^3. The structure at higher ion fluences did not change appreciably from that shown in Figure 52.

E. Results of Varying the Irradiation Temperature

While most irradiations for this study were conducted at a temperature of 525°C and other irradiation parameters varied, several samples were irradiated at different temperatures with interesting results.

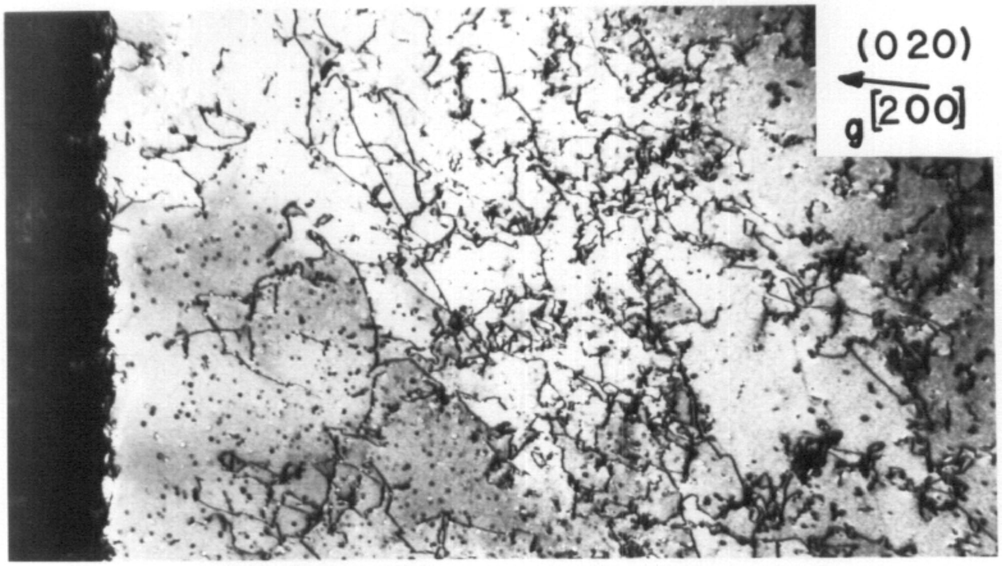

a) 2×10^{15} cm^{-2}

b) 5×10^{15} cm^{-2}

Figure 52. Dislocation structure in nickel irradiated at 525°C with 14 MeV nickel ions to the fluence levels shown.

1. Irradiation at 625°C

The void microstructure after irradiation with 14 MeV nickel ions at a temperature of 625°C was somewhat different than at 525°C. This microstructure is shown in Figure 53, where the foil surface is again at the left hand side of the micrograph. The surface denuded zone at this temperature is much larger than at 525°C, now extending back 0.5 μm. The void microstructures after irradiation at 525 and 625°C to identical ion fluences is shown in Figure 54. The higher temperature sample had larger void sizes and lower void densities throughout the damage region. There was one anamalous feature of the void microstructure in the end-of-range region at this sample. The void density is observed to drop off rather abruptly at about 2.8 μm, have a small gap with very few voids, and then end with a line of voids at a depth of about 3.1 μm. This type of behavior was only observed at this irradiation temperature.

Void data was collected from this sample using 0.25 μm depth intervals and is shown in Figure 55. The measured swelling values are similar to those observed at 525°C at this ion fluence. This indicates that the peak swelling temperature would probably lie between these two temperatures. The observed dislocation structure is shown in Figure 56. Total dislocation line lengths were lower than those observed at 525°C, ranging up to about 2×10^9 cm/cm^3.

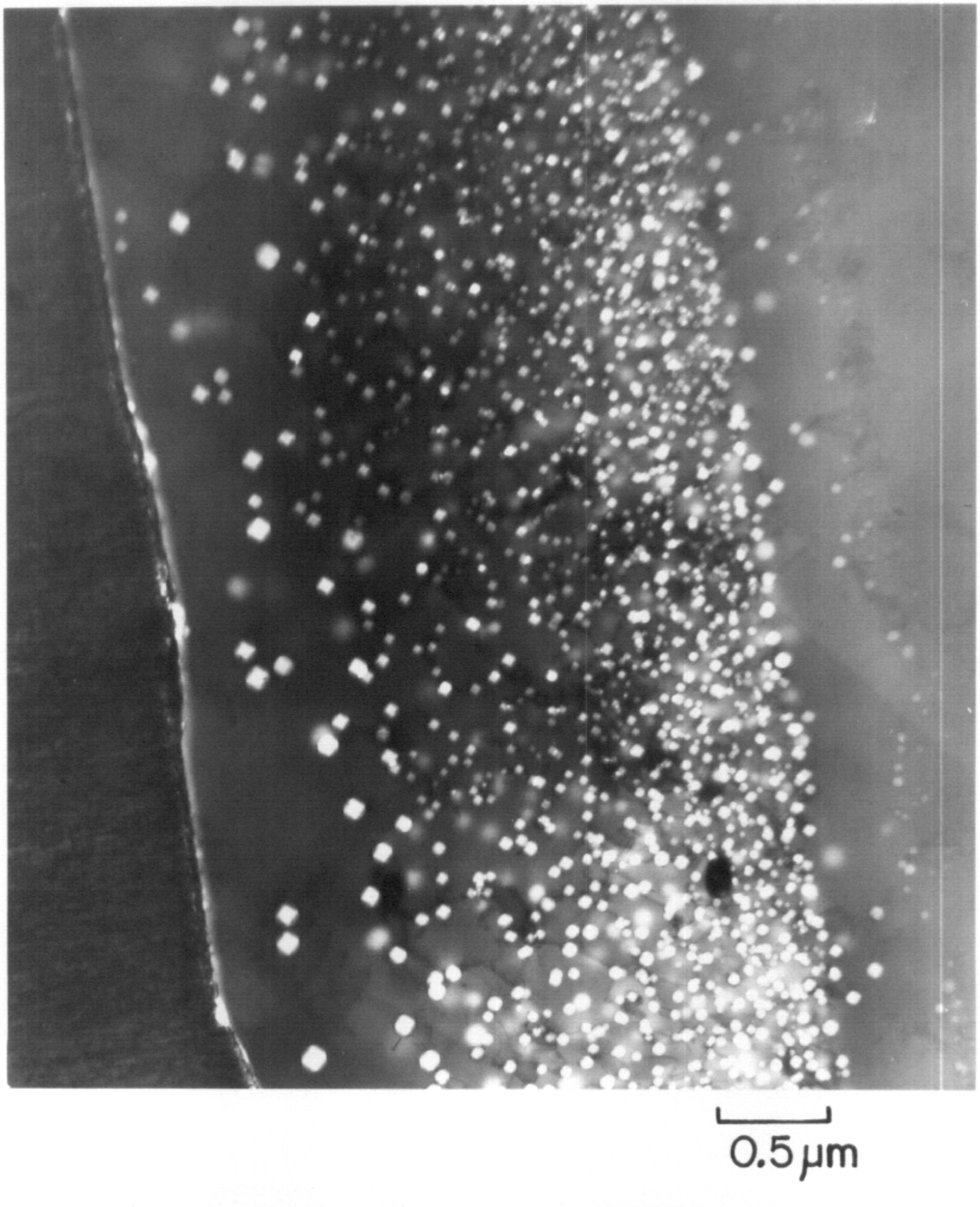

Figure 53. The void microstructure in nickel after irradiation at 625°C with 14 MeV nickel ions to a fluence of 1×10^{16} ions/cm^2.

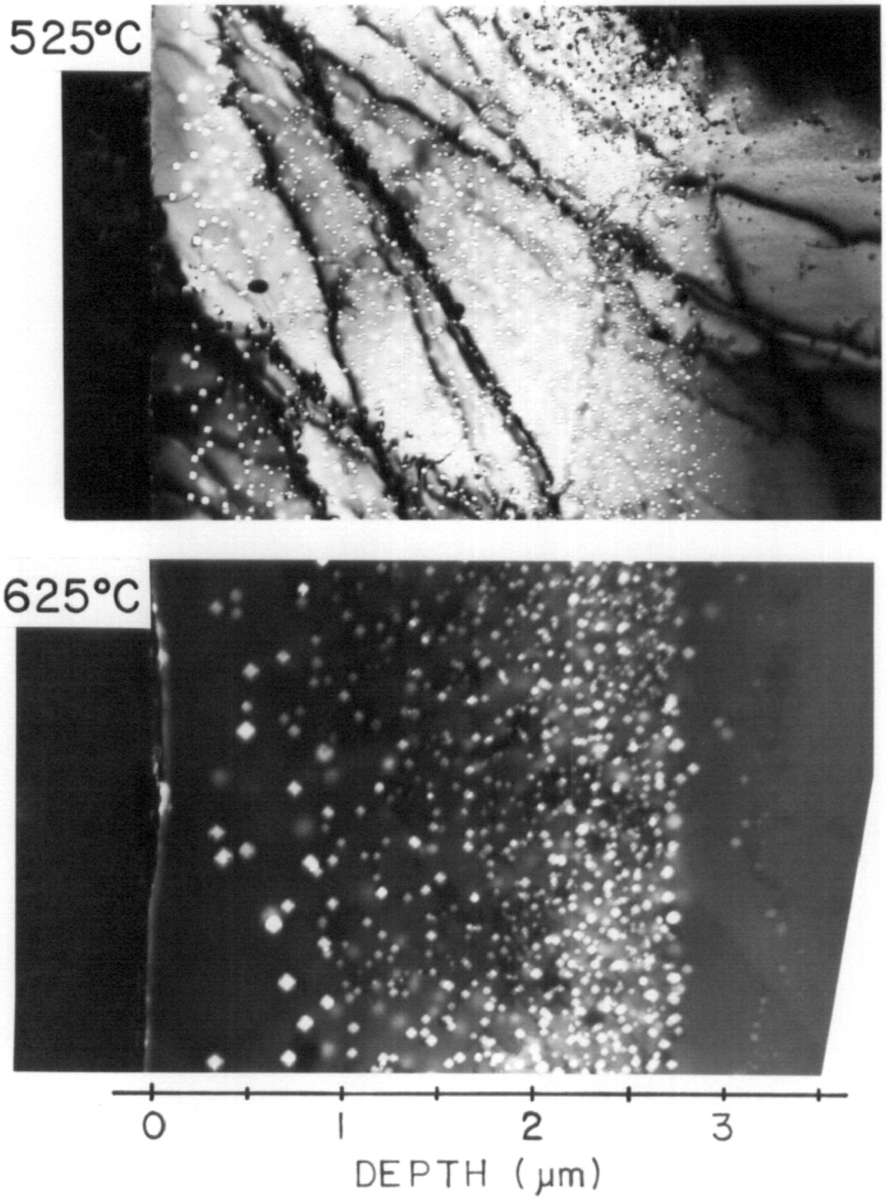

Figure 54. A comparison of the microstructure after irradiation at two temperatures with 14 MeV nickel ions to a fluence of 1×10^{16} ions/cm^2.

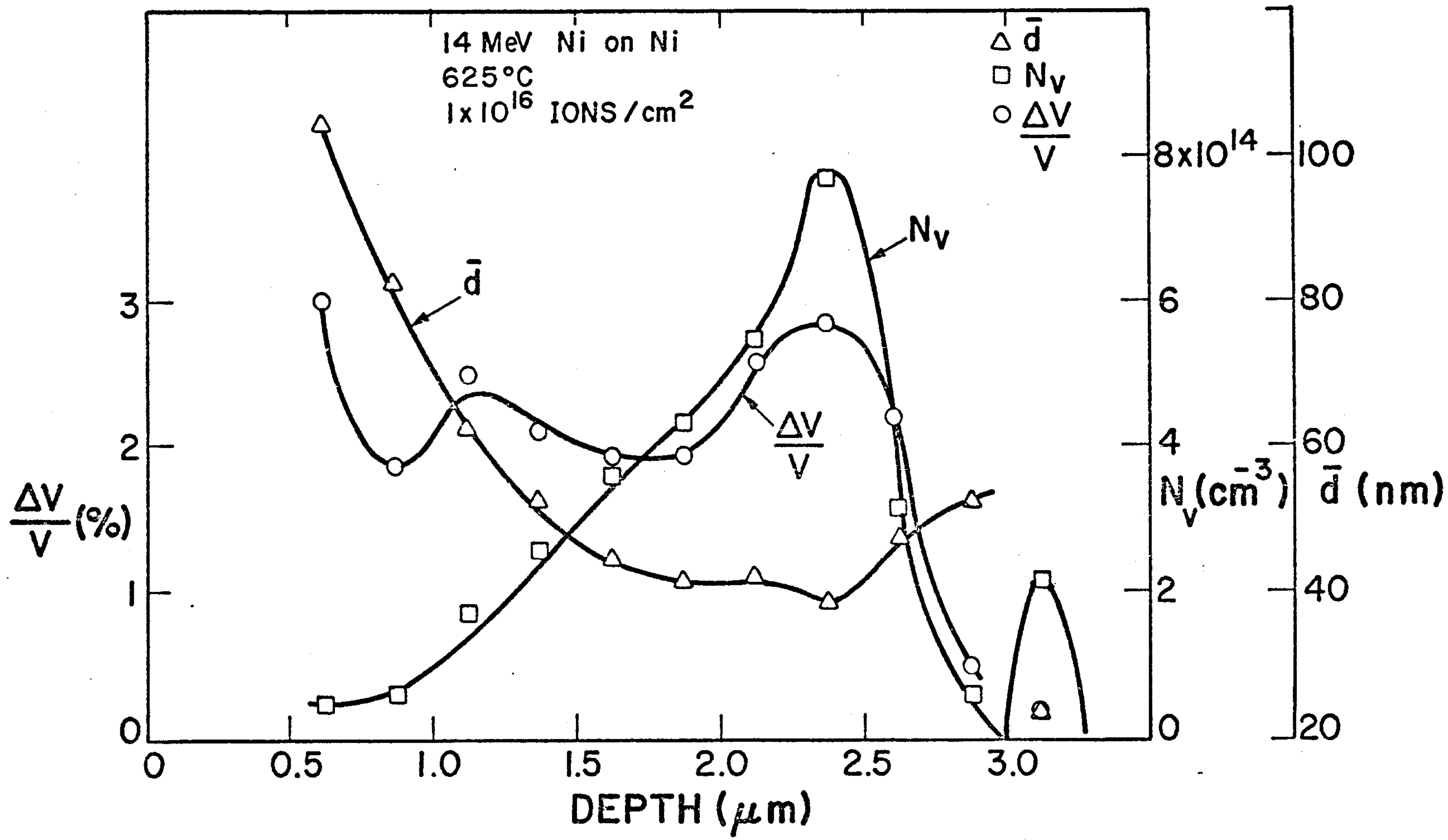

Figure 55. Void volume, void density, and void size versus depth in nickel irradiated at 625°C with 14 MeV nickel ions to a fluence of 1x10^{16} ions/cm^2.

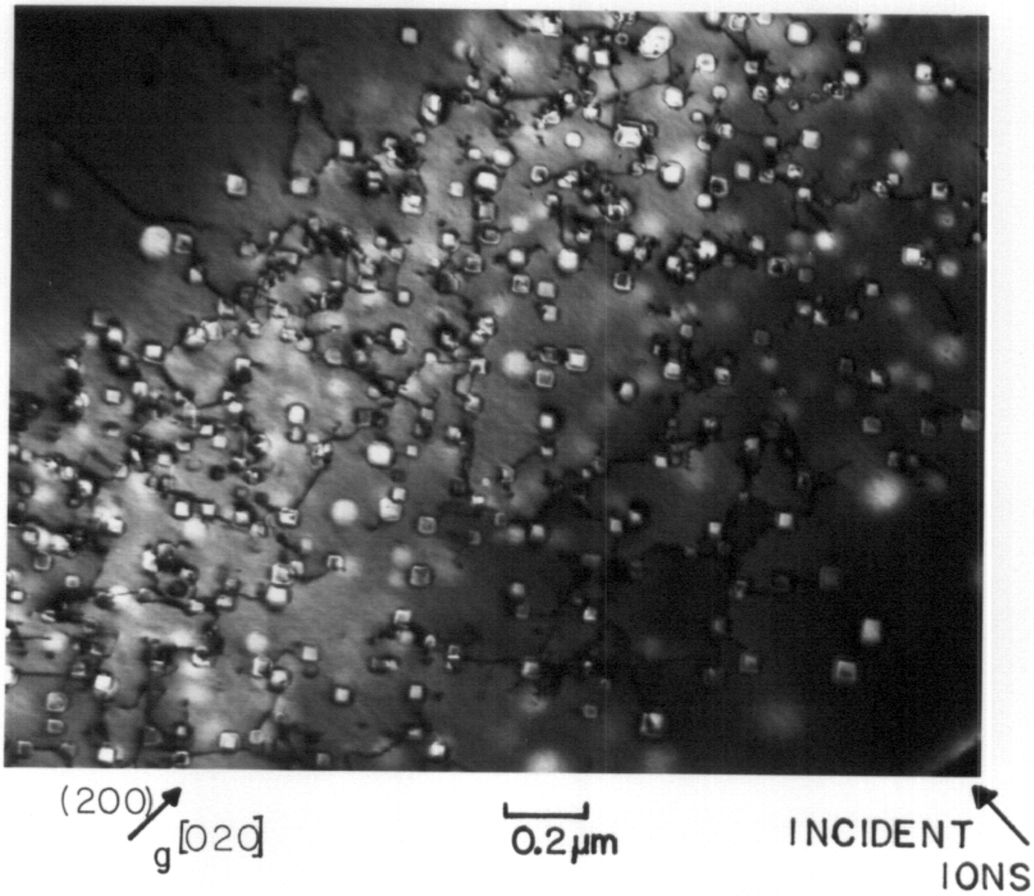

Figure 56. The end-of-range dislocation structure after irradiation at 625°C with 14 MeV nickel ions to a fluence of 1×10^{16} ions/cm^2.

2. Irradiation at 400 and 200°C

An irradiation was performed at a temperature of 400°C using 14 MeV copper ions to a fluence of 10^{17} ions/cm^2. To achieve this high fluence level, the beam from the accelerator was rather sharply focused on the sample and hence was not uniform in intensity. During the post-irradiation analysis, a very interesting microstructure was observed in a foil taken from the edge of the beam spot where the beam intensity was down by approximately a factor of two. In this sample, shown in Figure 57, the microstructure could be divided up into three distinct regions. In region a, which extended to a depth of about 0.5 μm, the microstructure consisted of random, relatively small voids. Region b, which extended to about 1.2 μm, consisted of voids and random loops. Region c contained an ordered loop lattice with a spacing of 41 nm and extended to 2.6 μm. The structure then reverted back to type b for about 0.2 μm, and ended with random voids to a total depth of 3.3 μm. Therefore, in this sample where all irradiating conditions stayed equal except for the variation in dose rate with depth, the microstructure has shifted from allowing voids to nucleate and grow to a region where only loops could form. This observation is evidence for a temperature shift as was proposed by Brailsford and Bullough (80) and specifically for an internal temperature shift as proposed by Garner and Guthrie (160).

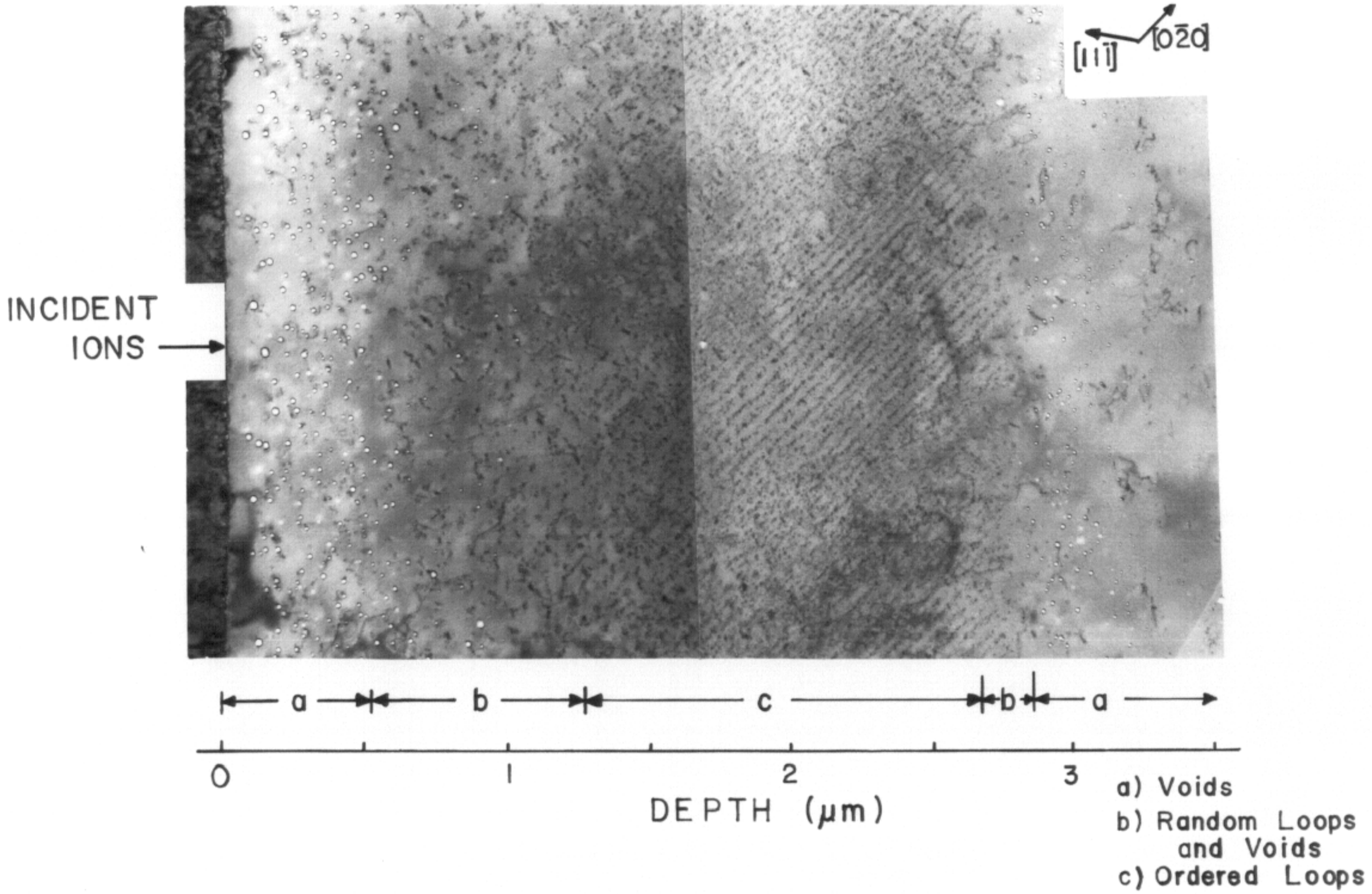

Figure 57. The void and loop microstructure observed in nickel after irradiation at 400°C with 14 MeV copper ions to a fluence of 5×10^{16} ions/cm^2.

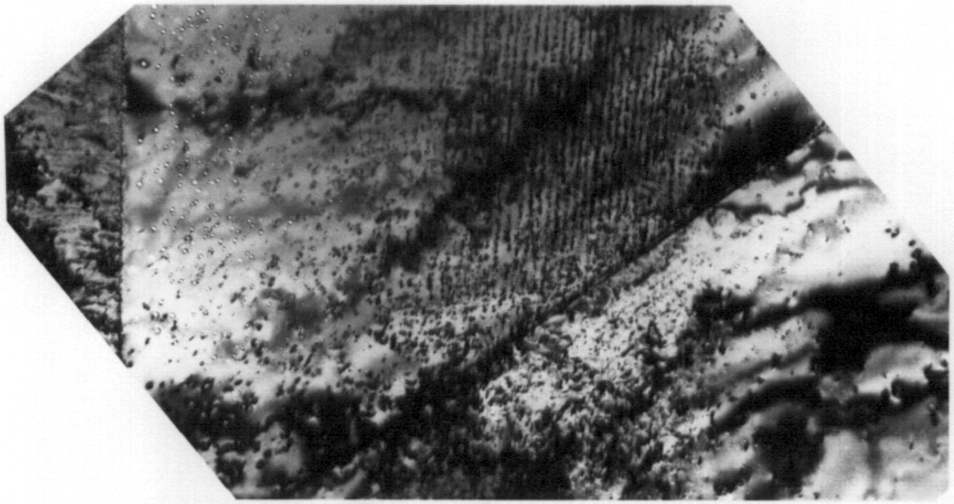

a) 5×10^{16} cm^{-2}

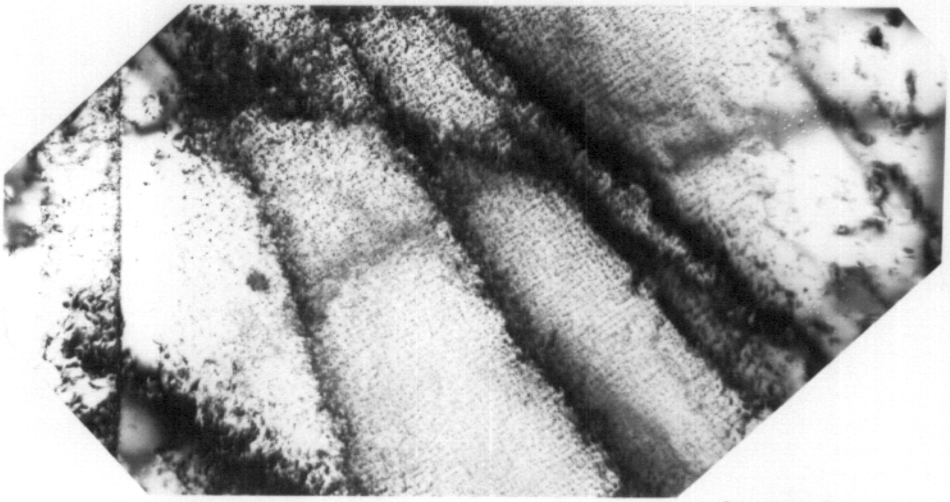

b) 1×10^{17} cm^{-2}

Figure 58. Nickel irradiated at 400°C with 14 MeV copper ions to two fluence levels at different dose rates.

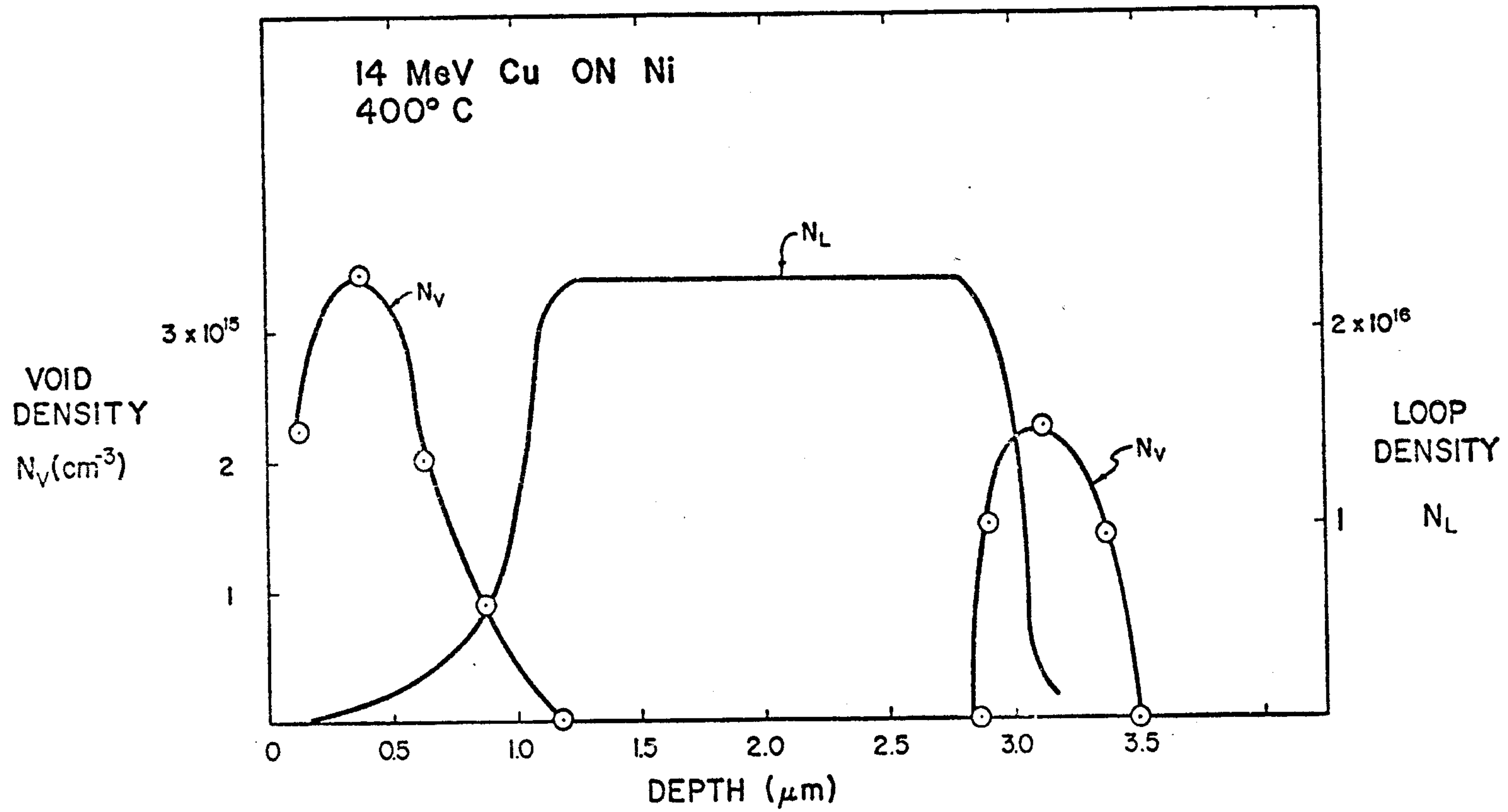

Figure 59. Void and loop density as a function of depth in nickel irradiated at 400°C with 14 MeV copper ions to a fluence of about $5\text{x}10^{16}$ ions/cm^2.

The microstructure from this sample is compared to a sample from the center of the beam spot in Figure 58. The higher dose rate of this latter specimen was sufficient to preclude void formation in the front surface region of this sample, but voids are still visible near the end of range. Void and loop counting was done in the previous sample and the results shown in Figure 59. Approximately 3 loops were observed per lattice site, a value close to that observed by Brimhall (115). This loop structure is shown more clearly in Figure 60. Analysis of this region using the 2-1/2 D quasi-stereo technique (161) indicated approximately half of the loops to be of the vacancy type.

An irradiation was also carried out at 200°C with 14 MeV nickel ions to study the development of the loop structure at low temperatures. A well-developed loop lattice formed along {100} directions with a spacing of ≈40 nm as is shown in Figure 61. This result is consistent with several other low temperature nickel irradiations (84,113,127) except that the lowest temperature at which an aligned structure had been previously observed was 280°C. The loop structure in this study extended all the way to the foil surface without disordering. The loop lattice also extends well beyond the area of peak damage, and can be observed at depths of 3 μm. The loop lattice spacing is approximately constant throughout the damage region and hence does not vary with the local dose rate.

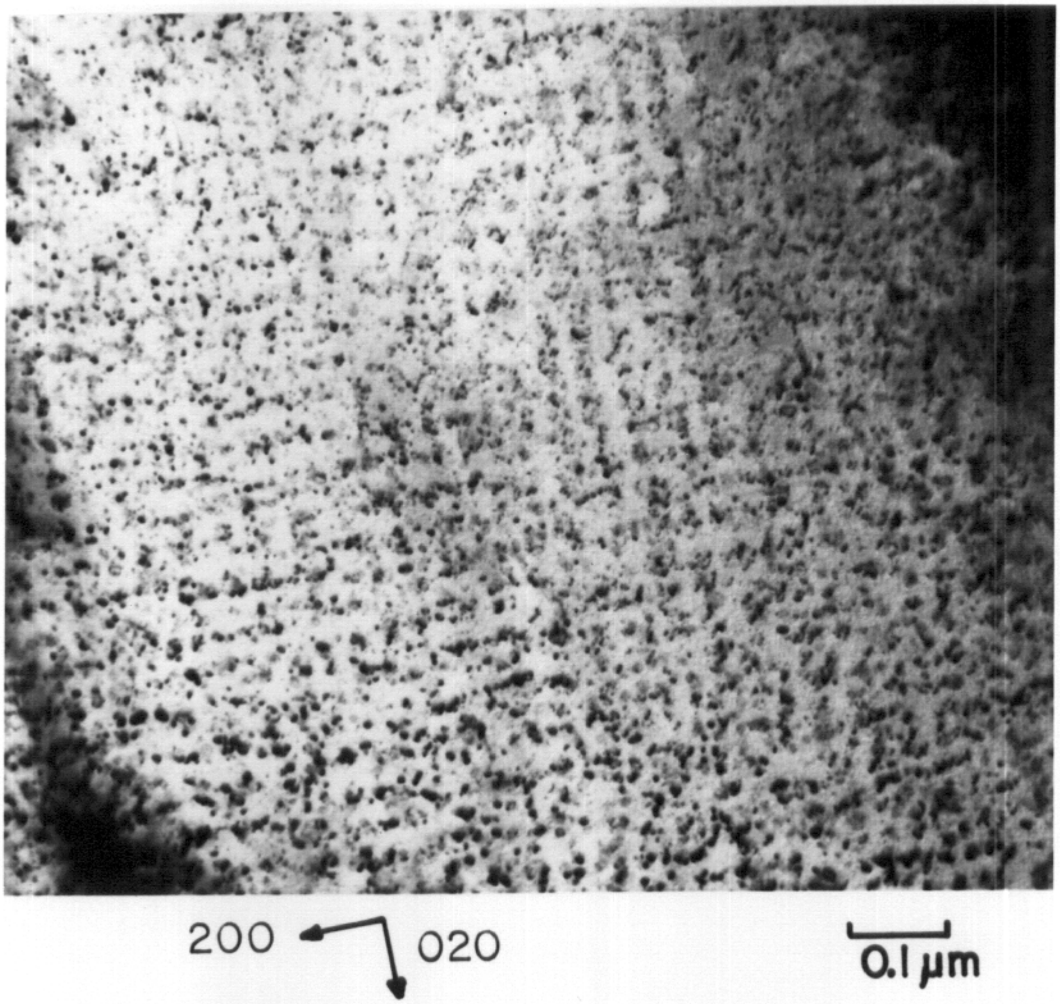

Figure 60. The end-of-range region of the loop lattice structure of figure 58b.

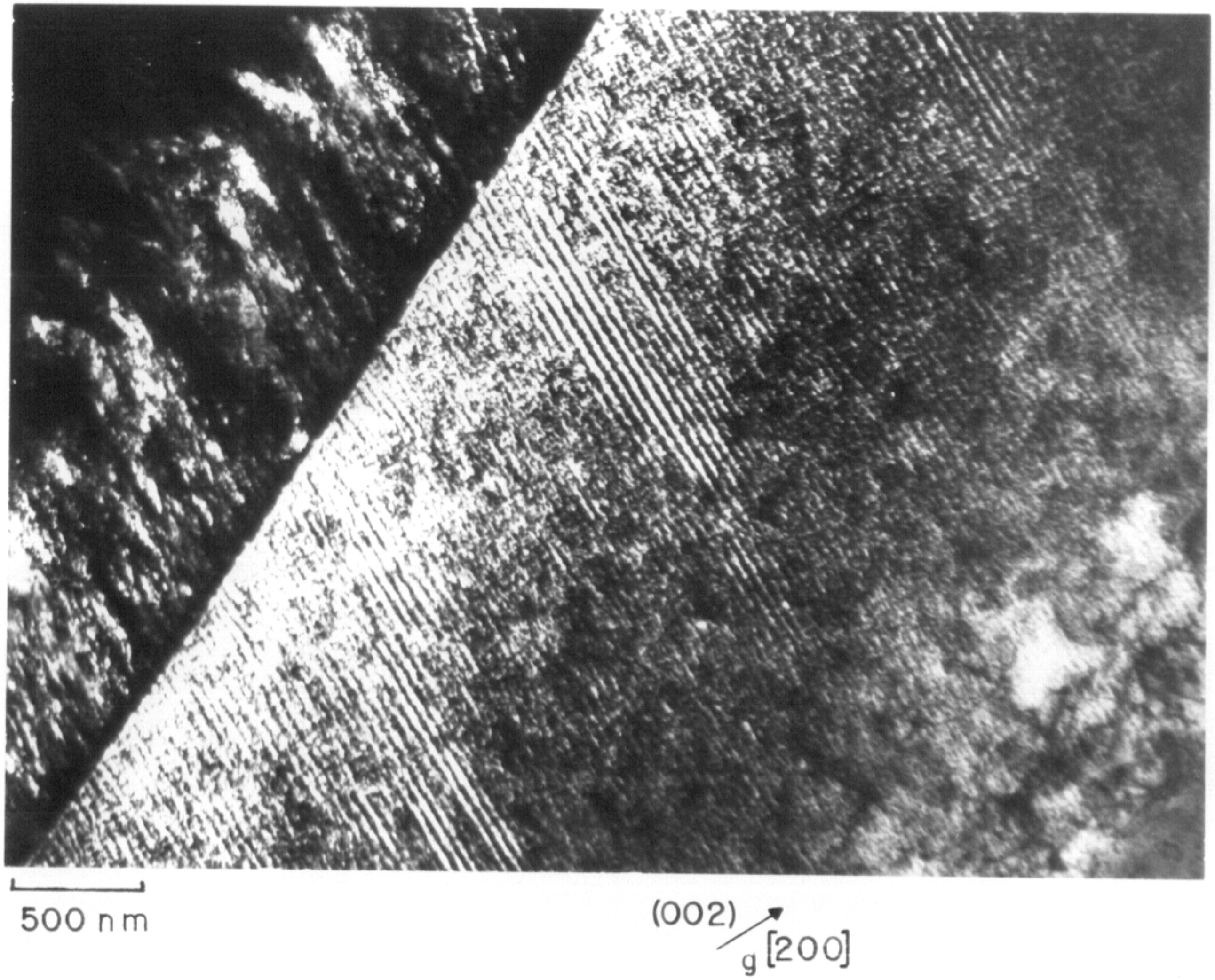

Figure 61. The loop lattice structure which formed after irradiation at 200°C with 14 MeV nickel ions to a fluence of 7×10^{15} ions/cm^2.

VI. DISCUSSION

A. Utility of Cross Sectioning Technique

Due to the large amount of data extracted by this sample preparation technique, it is important to understand its relative strengths and weaknesses. First, for a given sample, such variables as sample heat treatment history, handling, irradiation temperature, ion flux and ion fluence are all identical. While the absolute values of void statistics are no better with this technique than in conventional sample preparation, the relative error between intervals of a given sample is reduced since microscope magnification errors are eliminated and foil thickness errors are reduced. Absolute errors are estimated to be ±50%, while relative errors are estimated to be about 25%.

The interpretation of the observed structure is complicated, however, by the depth variation of features such as dose rate, total dose, impurity levels, internally generated stress levels, surface effects, and the changing primary-knock-on (PKA) spectrum. The changing differential nuclear scattering cross section for nickel on nickel is shown for two depths in Figure 4. As the ion slows down, cascades initiated by high energy PKA's are eliminated and the bulk of the displacement events are caused by lower energy, and hence smaller, cascades. Over 10 percent of the displacements at the surface are caused by recoils of energy greater than 1 MeV, while there are virtually no cascades of this size at a depth of 2 μm. Within our present understanding of the radiation damage process, it has not been possible to correlate this changing PKA spectrum with any microstructural features, even though the cascade size could be expected to affect the fraction of defects surviving immediate recombination in the cascade. It is also possible that the cascade size distribution could affect such mechanisms as cascade collapse into vacancy clusters (83).

To avoid smearing out microstructural data that may be affected by these rapidly varying features, it was necessary to restrict the depth interval size to the relatively small value of 0.25 μm. This restriction leads to the primary problem with this technique, namely that of counting statistics. In a sample or region of a sample that has a low defect density, it may be difficult to include enough defects within an interval to give an acceptable statistical uncertainty. In this study, most samples had high enough void densities to reduce this problem except in the first one or two depth intervals, but this technique would be very limited as a method of measuring the depth dependence of defects with densities below $\approx 5 \times 10^{13}$ cm^{-3}.

B. Defect Profile Calculations

To assist in the interpretation of the experimental results, it is useful to know not only the depth profile of the defect production rate, but also the depth profiles of the vacancy and interstitial concentrations. If the ion beam is not the same chemical species as the target material, it is also important to know the final concentration profile of the incident ions and their concentration levels. The steady-state rate equations that describe the point defect concentrations are given by Equations 31 and 32. Sink terms are calculated using Equations 38 and 39. Note that cascade collapse into vacancy loops is not included in this formulation. These equations were formulated in a one-dimensional manner similar to Myers, et al. (162) and solved using a modified Gauss-Siedel iterative technique (163). D_i, D_v and α were assumed not to vary with depth or with the local defect concentration. The defect production rates were taken from the Brice code (44) and if voids were present in the microstructure, the ion range and energy loss rates were modified in the manner of Odette (48). Figure 62 shows the vacancy and interstitial concentration obtained for the case of 14 MeV nickel ions incident on a nickel target using the parameters given in Table 6. Several features of the curves of Figure 62 are important in interpreting the depth dependent microstructure of heavy ion irradiated samples. First, the front surface is a perfect defect sink, and as such it reduces both the vacancy and interstitial concentrations in this

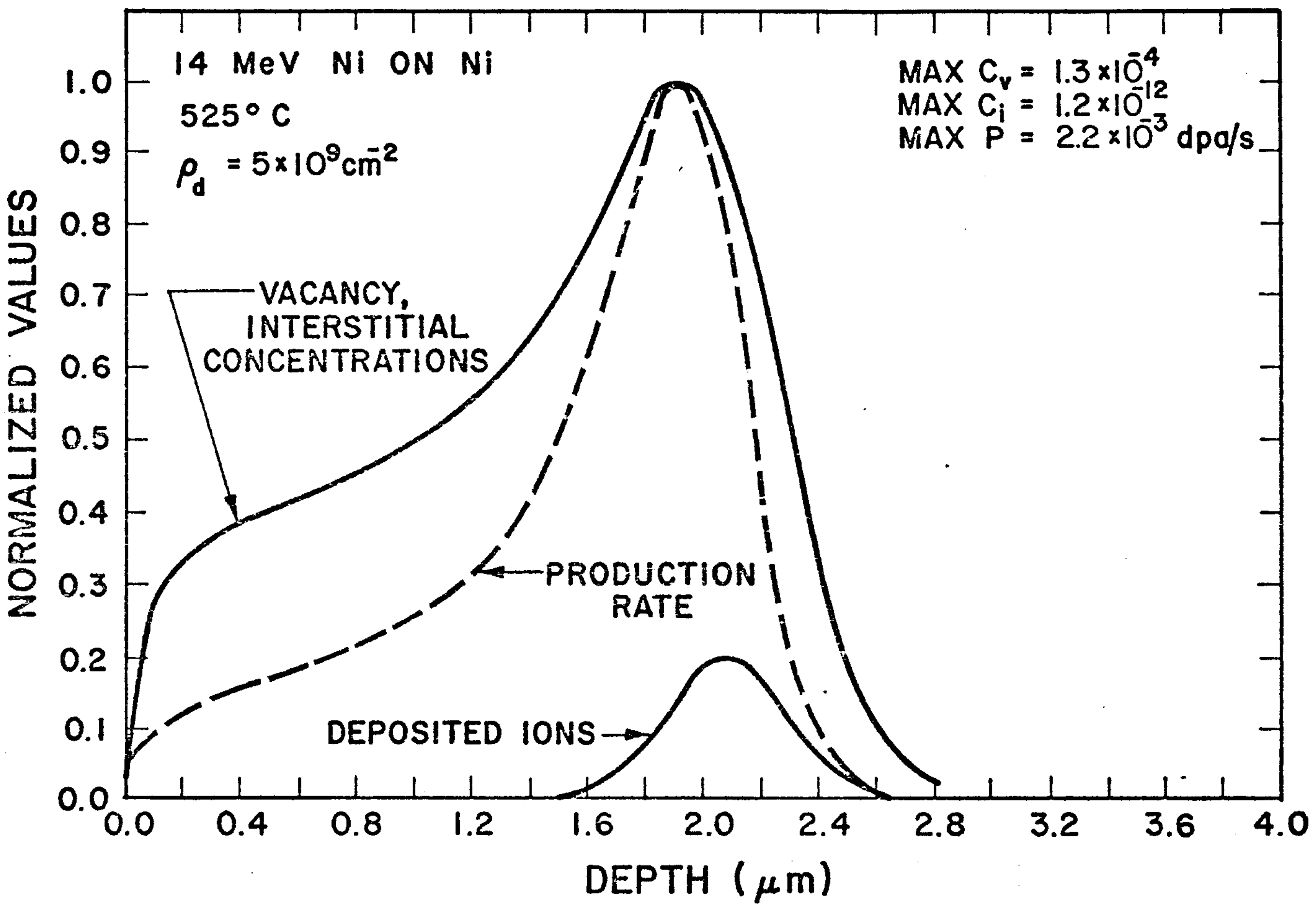

Figure 62. Calculated steady state point defect concentrations as a function of depth for a nickel foil bombarded at 525°C with 14 MeV nickel ions. A uniform dislocation density of 5×10^{9} cm/cm^{3} was assumed. All curves except the deposited ion curve are normalized to the peak values given in the figure.

TABLE 6

INPUT PARAMETERS USED IN SOVLING EQUATION 31 AND 32
(Most Material Parameters are from Ref. 10)

Temperature	525°C
Dislocation density	5×10^9 cm^{-2}
Surface energy	1000 mJ/m^2 (erg/cm^2)
Vacancy migration energy	1.38 eV
Interstitial migration energy	0.15 eV
Vacancy formation pre-exponential	4.48
Interstitial formation pre-exponential	5.0
Vacancy diffusion coefficient pre-exponential	0.062 cm^2/s
Interstitial diffusion coefficient pre-exponential	0.12 cm^2/s
Vacancy formation energy	1.39 eV
Interstitial formation energy	4.08 eV
Recombination factor, α/D_i	1×10^{15} cm^{-2}
Dislocation bias	2.0%
Ion flux	2×10^{12} ions/cm^2/s

region, altering both void nucleation and void growth rates. The width of this zone will be dependent both on temperature and sink density. The defect concentrations also show less variation in magnitude from the midrange to the peak region than does the defect production rate curve. This behavior is due to the non-linear response of the defect recombination rate which leads to a larger fraction of the defects recombining as the steady-state defect concentrations increase. This is illustrated by the defect rate curves of Figure 63, where the

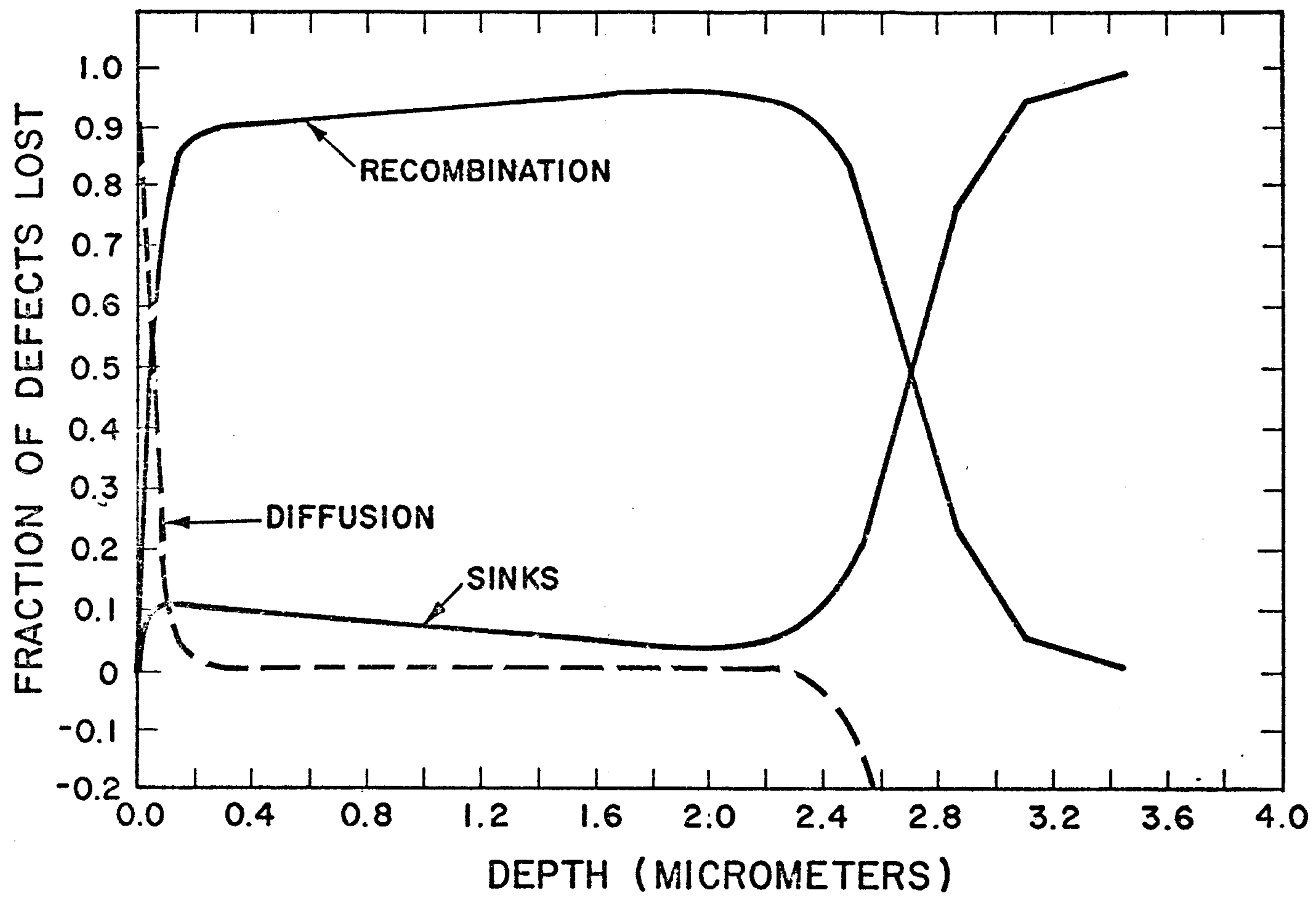

Figure 63. The fraction of defects in each depth interval which are lost by recombination, by absorption at sinks, and by diffusion from the interval. A negative diffusion fraction means that there is a net flux of defects into the interval. These results are from the calcullation of figure 62.

fractions of defects lost to sinks, recombination and by diffusion out of depth zones are shown for the curves of Figure 62. For the parameters used in this case, recombination dominates except near the front surface. Diffusion of defects beyond the production curve does give significant defect concentrations in this "undamaged" region. In this particular case the vacancy concentration at 3.0 μm was still about five orders of magnitude greater than the equilibrium value.

The code will also solve for the steady state defect concentrations in foils with depth dependent sink strengths. Figure 64 shows the calculation using the parameters of Table 6 except that the depth dependent void sink densities were taken from Figure 16. The increased sink density in the end-of-range region has lowered the peak defect concentrations and reduced the amount of diffusion beyond the peak. The calculated growth fluid for this case (where the growth fluid is defined as (160) $D_vC_v - D_iC_i - D_v\bar{C}_i$) is shown in Figure 65 assuming a radius of 1.0 nm for the test void.

In interpreting the end-of-range microstructure of the copper ion irradiated samples, it is important to know the resultant impurity distribution. The concentration of an impurity is described by

$$\frac{\partial C_A}{\partial t} = \nabla D_A \, \nabla C_A + S_A \qquad 54$$

where S_A is the source term for the impurity and will be depth dependent in this case. C_A is the concentration of the impurity A in

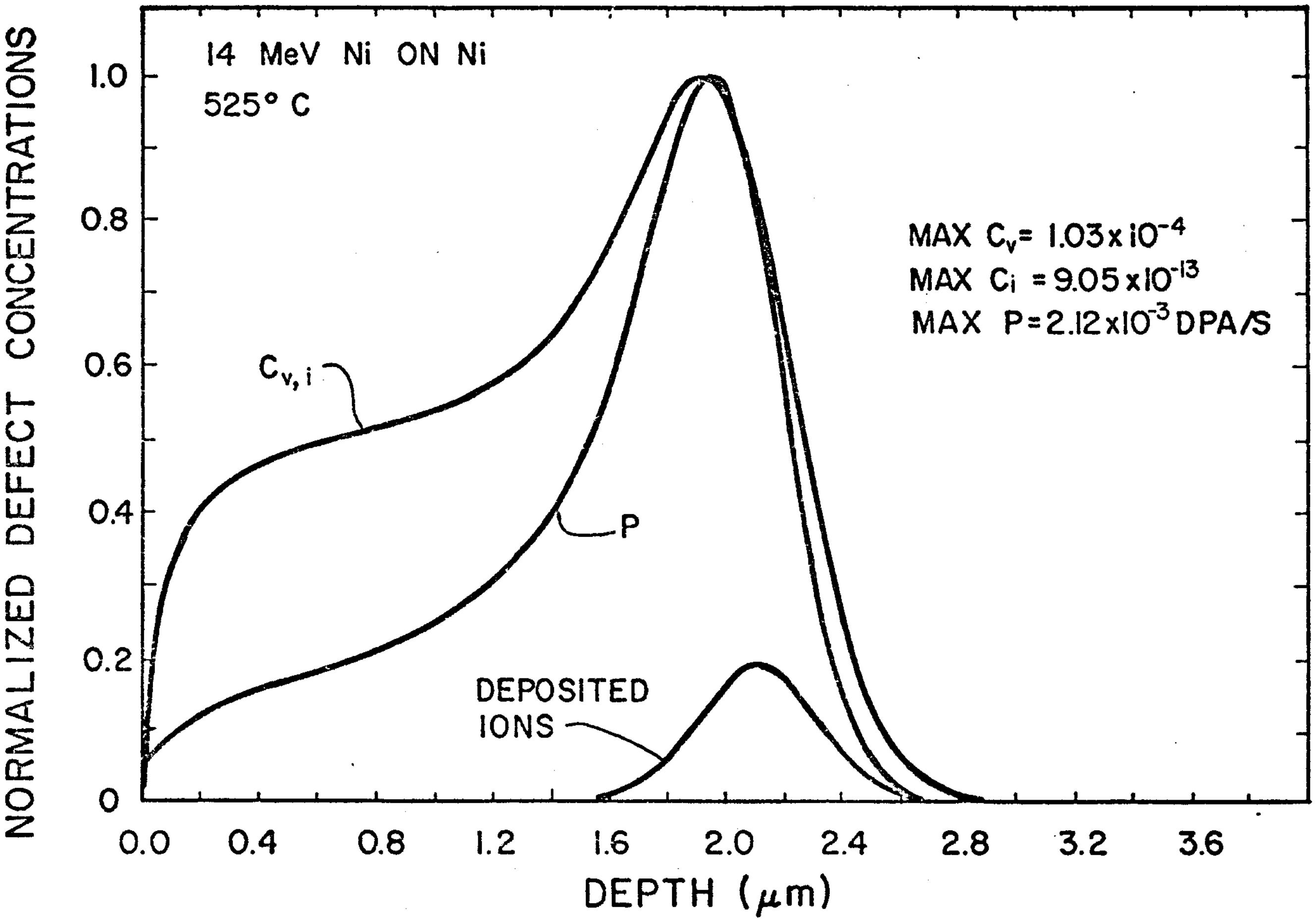

Figure 64. The vacancy and interstitial concentration profiles calculated using the experimentally measured depth dependent sink values of figure 16.

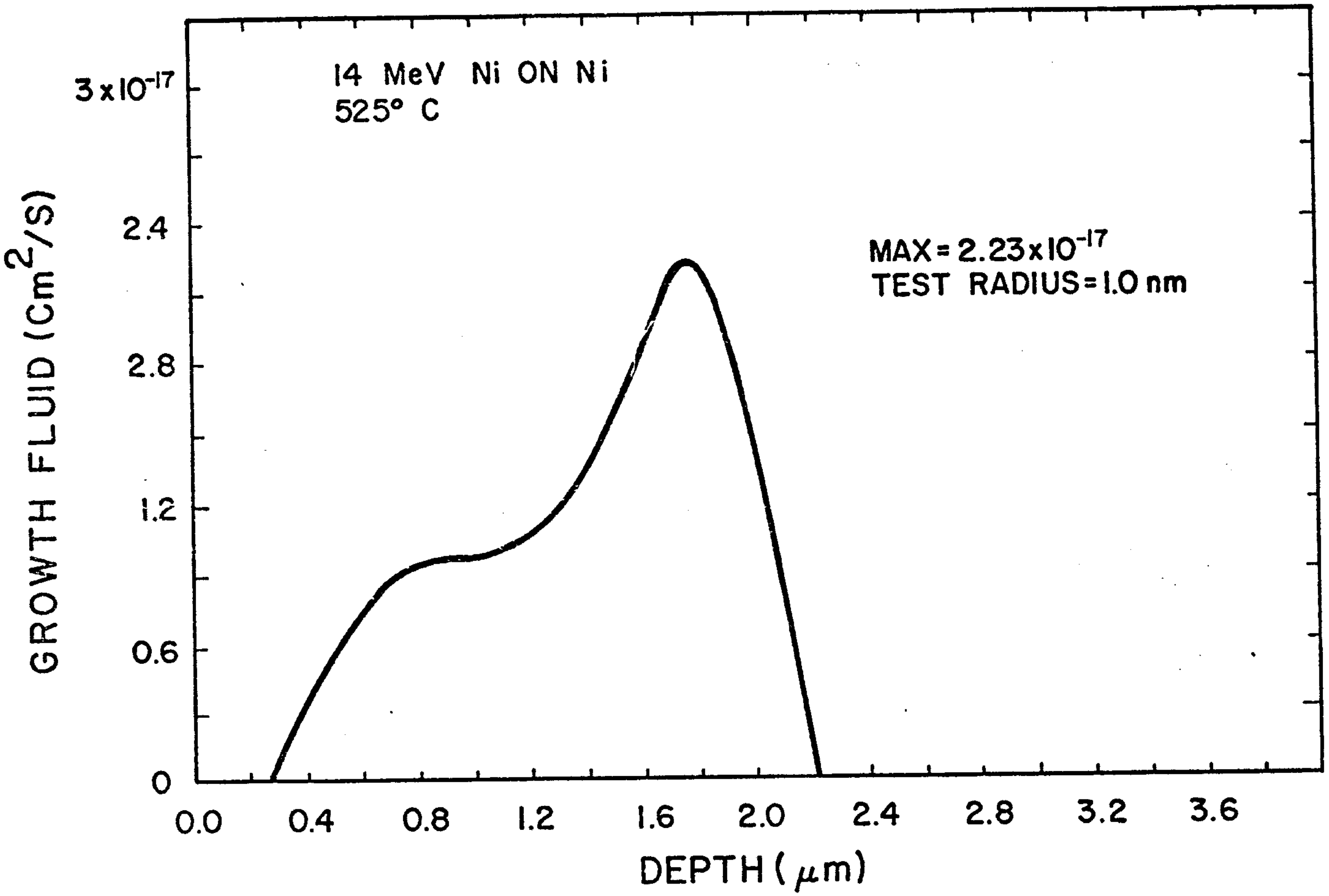

Figure 65. The growth fluid (defined as $D_vC_v-D_iC_i-D_vC_1$) for the depth dependent sink calculation of figure 64.

the matrix, and D_A its radiation enhanced diffusion coefficient assumed to be of the form (162)

$$D_A = \sum_K F_K D_K C_K \qquad 55$$

where the sum is over all mobile defects and defect clusters, and the F_K are correlation factors. Note that this model of radiation enhanced diffusion does not apply to interstitial impurities and neglects solute drag effects.

To model the ion irradiation case, the steady-state solutions for the vacancy and interstitial concentrations were found from the previous calculations and substituted into Equation 55 to give the depth dependent diffusion constant (note that mobile defect clusters such as di-vacancies were ignored in this solution). This diffusion constant was then used to solve Equation 54 in one dimension. The vacancy and interstitial correlation factors were taken as 0.78 and 0.4, respectively (164).

Results of this calculation for 14 MeV copper ions incident on nickel are shown in Figures 66 and 67. The radiation enhanced diffusion spreads the impurity predominately towards the front surface while lowering the peak concentration. At the low ion fluence typical of this study, the range of influence of the copper is still confined to the end-of-range region (Figure 66). Even in this case, however, the peak copper concentration exceeds 0.2 atomic percent.

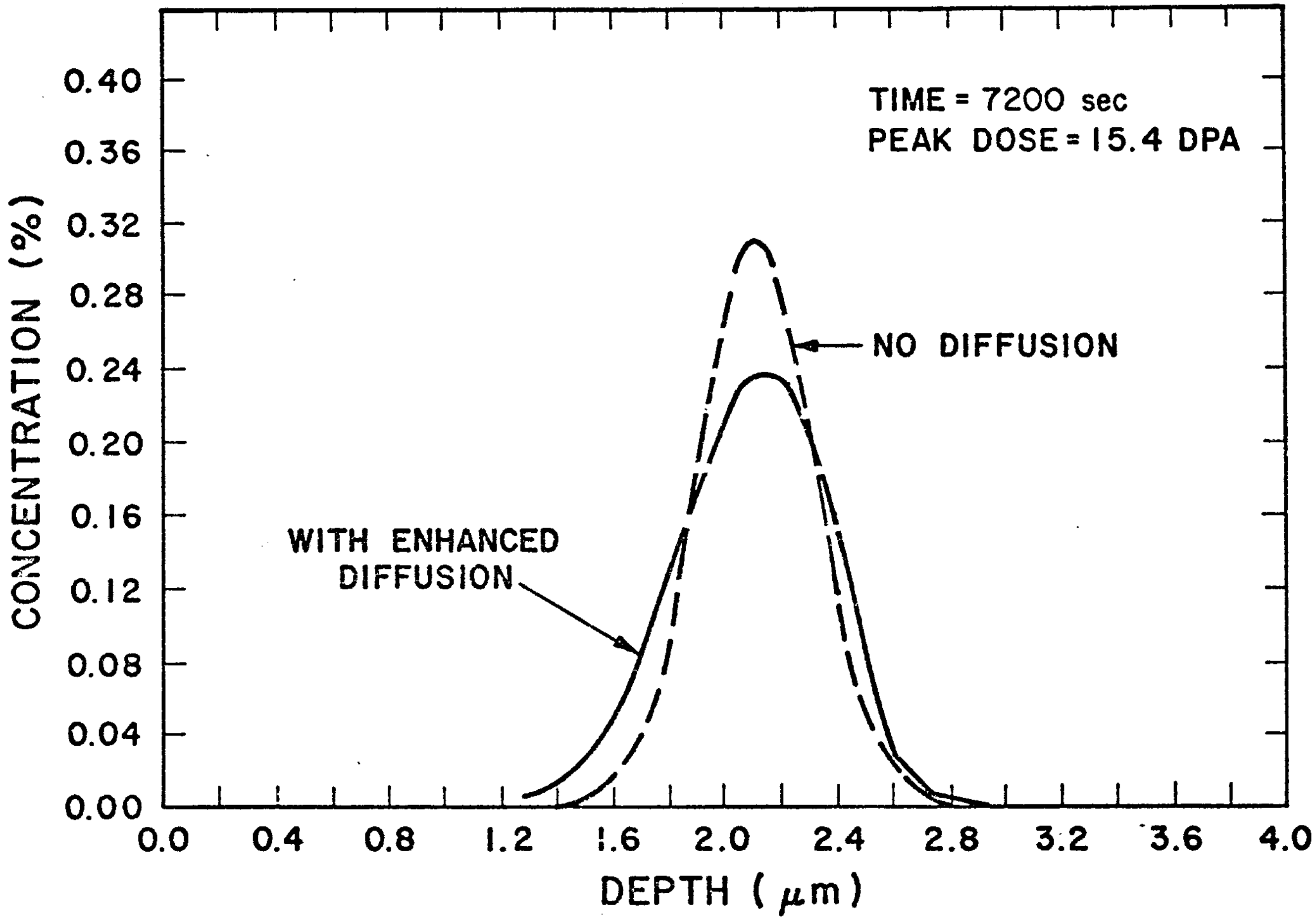

Figure 66. The deposited copper impurity profile after irradiation with 14 MeV copper ions with (solid curve) and without (dashed curve) radiation enhanced diffusion. The temperature was 525°C and the total ion fluence 1.4×10^{16} ions/cm^2.

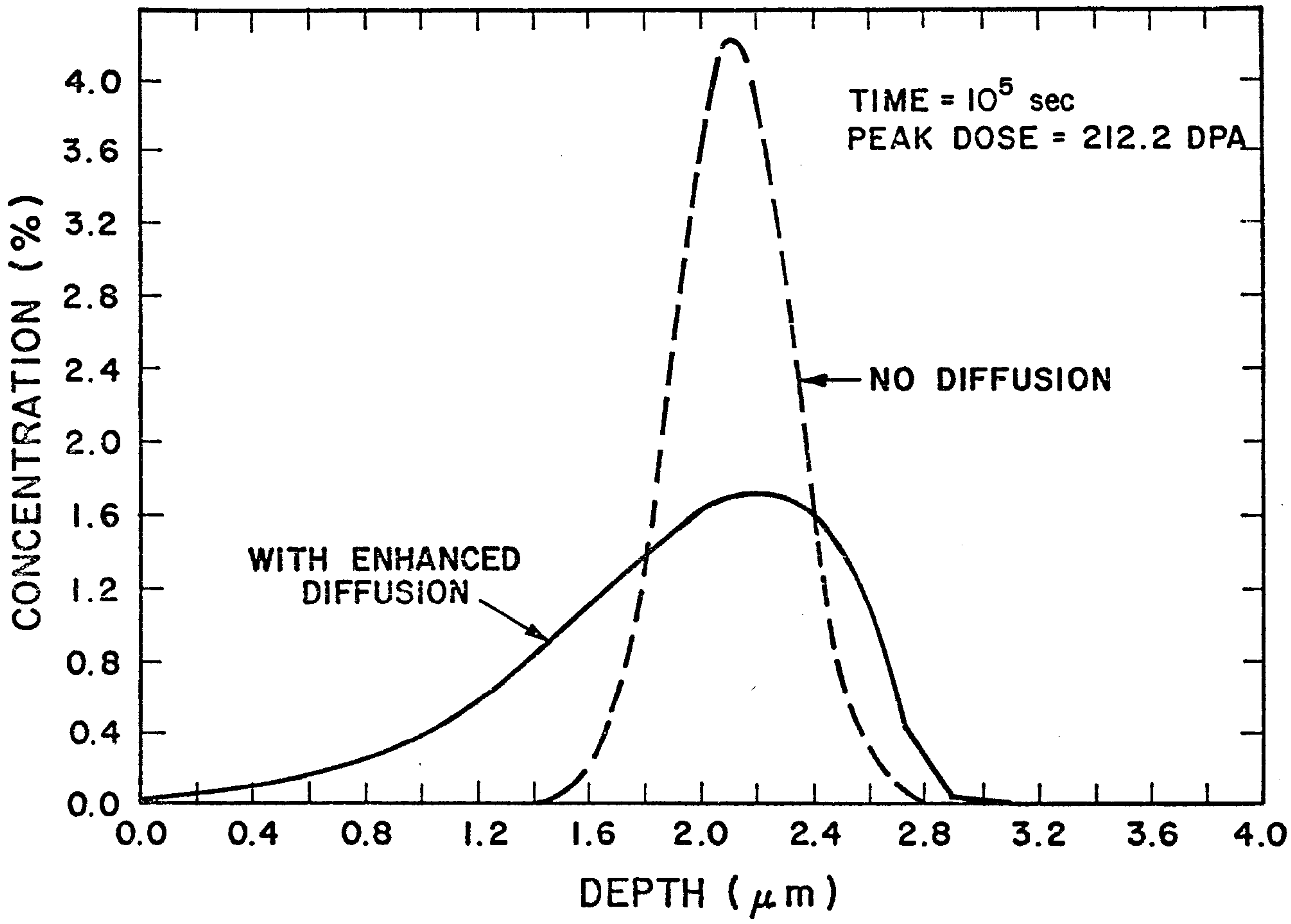

Figure 67. The implanted copper ion profile with and without radiation enhanced diffusion after a total ion fluence of $2\text{x}10^{17}$ ions/cm^2.

In the high fluence case (Figure 67) the copper has spread throughout the damage region of the sample and reached peak concentration values exceeding 1.5 atomic percent.

C. Outgassing Effects

In this study, electropolishing was definitely identified as a sample preparation procedure that was introducing an agent into the samples capable of aiding void nucleation. Electropolishing has been frequently observed to charge samples with hydrogen (132) when the polishing was carried out in anything except very low temperature baths (i.e., <-50°C). At higher temperatures, the hydrogen will diffuse into the samples faster than material is being removed and saturate the sample. Hydrogen would most probably enhance nucleation by absorbing onto the void surface and lowering the surface energy.

For the hydrogen introduced into the samples during the electropolish to aid void nucleation, it must not diffuse out of the specimen at irradiation temperatures. Calculations of hydrogen behavior in metals (165) have revealed hydrogen-vacancy binding energies of about 0.2 eV. It was also found that molecular hydrogen would not form in the metal lattice. If these calculations are correct, then the only way hydrogen could be kept in the samples during the heating to irradiation temperatures would be by trapping at other impurities. Carbon and oxygen are both present in small amounts (see Table 4) and could form hydrogen compounds that would effectively trap the hydrogen.

During irradiation, either the hydrogen would be freed from these traps and migrate to the void nuclei or the hydrogen compound would migrate to the void nuclei. At high temperatures (> 900°C), the hydrogen would be freed from the traps and diffuse from the samples. If this mechanism is valid, then the amount of hydrogen available to aid nucleation will depend only on the impurity concentration and on the introduction of sufficient hydrogen to saturate the available trapping sites. The exact sample handling procedure and the details of how the hydrogen was introduced (such as the polishing time) will not be important. In this study, electropolishing was found to give reproducable void densities and was used in lieu of helium injection.

D. Extended Range Observations

In all samples examined in this study, defect clusters were observed at depths from 10 to 20% beyond that predicted by Brice (44) of Manning and Mueller (36). In these calculations, Manning and Mueller used the standard LSS electronic stopping formula given by Equations 12 and 13. The Brice calculations used a three factor formula for electronic stopping with tabulated values used for these three constants (166). The peak defect density was also shifted back from the front surface, but generally by only about 10%. These results are not believed due to any experimental errors. The irradiation conditions were carefully characterized before and during each irradiation sequence to assure that no ions of energy higher than desired were striking the samples. Microscope magnification was also calibrated and checked by several users. Other errors such as the samples being tilted slightly while taking micrographs for range measurements would reduce the measured range and hence would not be in the direction of the experimental results.

These results are consistent with the observations of Narayan, et al (142,151) in heavy ion irradiated copper and nickel. They found better agreement between the observed defect density peak and the damage peak given by Manning and Mueller if the coefficient of the Lindhard electron energy loss term was reduced at low ion energies. By reducing the rate of electronic energy loss and correspondingly increasing the nuclear stopping power, the damage curve was shifted away from the front surface and the total number of displacements increased. There are at least three other possible explanations for the observed extension of damage. An error in the range straggling calculation would extend the damage region, as would channelling of either the incident ion or a high energy recoil atom. Channelling does not seem to be indicated since grain orientation was not observed to make any difference in the maximum defect cluster depth. The diffusion of vacancies into this region could lead to void formation without extending the damage curve as was shown in the calculations of Figure 62. No definite conclusion could be drawn as to the cause of the range deviation in this work, but the observation that the peak void density was shifted away from the front surface would indicate that the electronic stopping is underestimated somewhat, with the rest of the defect clusters being due to point defect diffusion into an "undamaged" region.

E. Effects Due to Disparate Incident Ions

There are two basic differences between irradiations with different ions that could be expected to affect the final damage state of the material. The first is the change in chemical composition by implantation while the second is the change in cascade structure. These will be discussed in turn.

1. Excess Interstitials and Impurity Effects

An important difference between irradiations performed with different ions are the end-of-range effects due to the incident ions coming to rest in the material. In the copper, aluminum and nickel ion irradiated samples, the incident ion behaves like a lattice atom and hence will represent an extra interstitial produced in these regions. Under low swelling rate conditions, (i.e., when defect loss by recombination or to unbiased sinks dominates) this small fraction of excess interstitials could significantly reduce the void swelling rate in the end-of-range region (167). This effect is not believed to be important for the high swelling rates observed in this study. In the case of copper, aluminum or carbon irradiations, the incident ion represents an impurity which gradually increases in concentration as the irradiation proceeds. Since impurities often affect swelling behavior quite strongly, the end-of-range region of ion irradiated samples may be suspect. In this study, however, no major differences in void microstructure were observed in the end-of-range region of any of the specimens. The relatively small increase in void size at the end-of-range in the carbon sample may be due to an impurity effect such as a lowering of the surface energy. The copper ion irradiated sample displayed a slightly lower swelling value than the self-ion irradiated sample, but these differences were not considered significant.

The computer calculations for the final copper concentration profile showed that for this study, the copper impurities were confined to the end-of-range region. This implies that any modifications in swelling behavior due to the presence of the copper will only occur in this region. This result will also apply to the aluminum ion irradiated specimens. Carbon diffuses interstitially in nickel and hence the radiation enhanced diffusion model used in these calculation does not apply. The effects of copper impurities on void swelling is somewhat uncertain. Brimhall and Kissinger (92) and Mazey and Menzinger (91) both found a 2% copper, 98% nickel alloy to swell less than a pure nickel control sample, while Smidt and Sprague (90) found of 1% copper alloy to swell more. All these workers did observe a decreased void density and an increased void size with alloying however. Brimhall and Kissinger also observed a higher density of prismatic loops in the alloy system, possibly indicating a reduction in the stacking fault energy with alloying. In contrast to these studies of nickel-copper alloys, the copper injected by the irradiating beam in this study seems to have lowered both the void density and the void size. In fact the different shapes of the swelling curves of Figures 16 and 17 show a reduced swelling rate in the end-of-range region of the copper irradiated sample. A more dramatic effect might be expected if the sample were irradiated to a higher damage level.

The swelling behavior of the self-ion irradiated samples (Figure 16) does not directly follow the displacement curve. Specifically, the variation from mid-range to the peak swelling value is much smaller than the corresponding variation in the damage curve. In Figure 68, this swelling curve is shown plotted along with the net flux of vacancies into a distribution of test voids calculated from the data of Figure 62. This "growth fluid" is a valuable aid in interpreting void growth data. (While these curves are not exactly equivalent in that the growth fluid is a swelling rate, the discrepancy is minor since the small incubation dose of pure materials allows one to approximate a swelling rate by a single swelling value.) The good qualitative agreement between these curves indicate that the reduced swelling value per dpa in the peak region can be at least partially explained by the enhanced recombination and the excess interstitials deposited in the end-of-range region. Note that

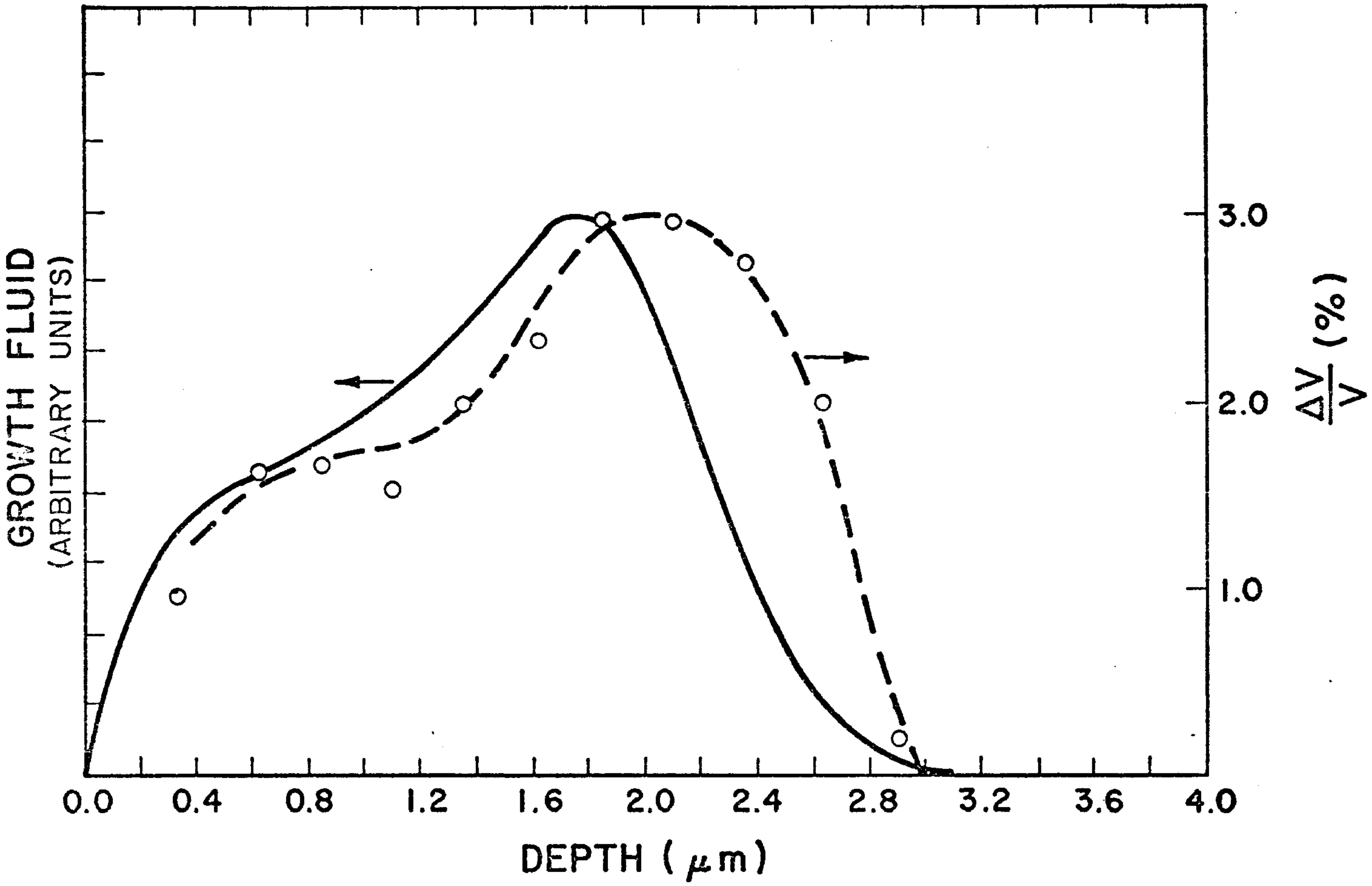

Figure 68. The normalized growth fluid from the calculations of figure 62 (void test radius of 1.0 nm) and the swelling values from the 14 MeV nickel ion irradiation of figure 16.

this result is similar to that obtained by the internal temperature shift at temperatures below the peaking swelling temperature as described by Garner and Guthrie (160). In calculating the growth fluid, however, a void distribution was assumed, while the experimental temperature shift includes the temperature and rate variations in void nucleation.

Previous studies of nickel containing carbon (43,44) and nickel containing aluminum (90) before irradiation showed significant decreases in swelling when compared to pure nickel specimens. The studies of carbon doped nickel of Sorenson and Chen (93,94) found that a carbon level of 0.3 atomic percent would completely suppress void formation. In the high dose sample of this study, carbon was injected to a level of at least ≈0.4 atomic percent (even if the carbon distributes itself uniformly throughout the damage region). In the previous studies, the impurity was present in significant amounts at the start of the irradiation and hence could play a significant role in the void and loop nucleation process. When the impurity is being introduced by the irradiating beam, it is still at very low concentration levels early in the irradiation sequence and hence cannot significantly alter the nucleation process in materials that nucleate voids as rapidly as the material used in this study. If an irradiation were to be continued to much higher fluence levels, it is possible that the effects of implanted impurities on the void <u>growth rate</u> would become evident. The major observation of this study was that the history of the irradiation-impurity level is important in determining what effects, if any, will be seen. This would be important in considering such studies as simultaneous gas implanation with ion bombardment and in considering what effects transmutation reaction products might have on materials subject to neutron irradiation.

2. Cascade Effects

The second effect examined in this study is the different displacement cascade structures produced by ions of different mass. Previous studies on irradiated stainless steel (168,169) have found protons to be over ten times more effective in producing swelling than an equivalent dpa irradiation using nickel ions. This difference was believed due to the lower mass of the proton. The differential scattering cross-sections for the three different ions at two different depths are shown in Figure 4. It can be seen that the primary knock-on (PKA) cross section, and hence the number of defects produced by a single incident ion, decreases with decreasing ion mass. With increasing depth, the cross section for producing low energy PKA's will increase while the maximum energy that can be transferred is decreasing. One would expect the smaller displacement cascade of the light ions to allow less in-cascade recombination and hence release a larger fraction of the radiation produced defects to diffuse into the matrix. The results presented here, however, show that within a factor of two, there are no significant differences in the void microstructure that can be attributed to the different cascade structures. Specifically, the lower mass carbon ion did not produce higher swelling values per calculated dpa levels than the nickel ions. As is shown in Figure 69, the carbon ion irradiation at 525°C produced even lower swelling rates than the heavier aluminum and nickel ions. Ryan (43) found a different temperature response when irradiating with carbon ions. A possible explanation for this result is that the "effective temperature" during the carbon irradiation is further from the peak swelling temperature than the aluminum and nickel irradiations. There has been no satisfactory explanation for the different peak swelling temperature when irradiating with carbon ions.

F. Dose Effects

Under the aluminum ion irradiation, the void number density was observed to be a maximum at the lowest ion fluence, and then to drop with increasing fluence. Similar behavior has been observed previously in nickel (43,114) and is not believed to be due to void impingement, but rather due to local changes in the microstructure (43). In the material prepared for this study, voids did nucleate quite easily. This apparently leads to such a high void density that continuing the irradiation beyond that necessary to nucleate the voids causes a subsequent change in the microstructure which allows some of the voids to continue to grow, with the rest shrinking and

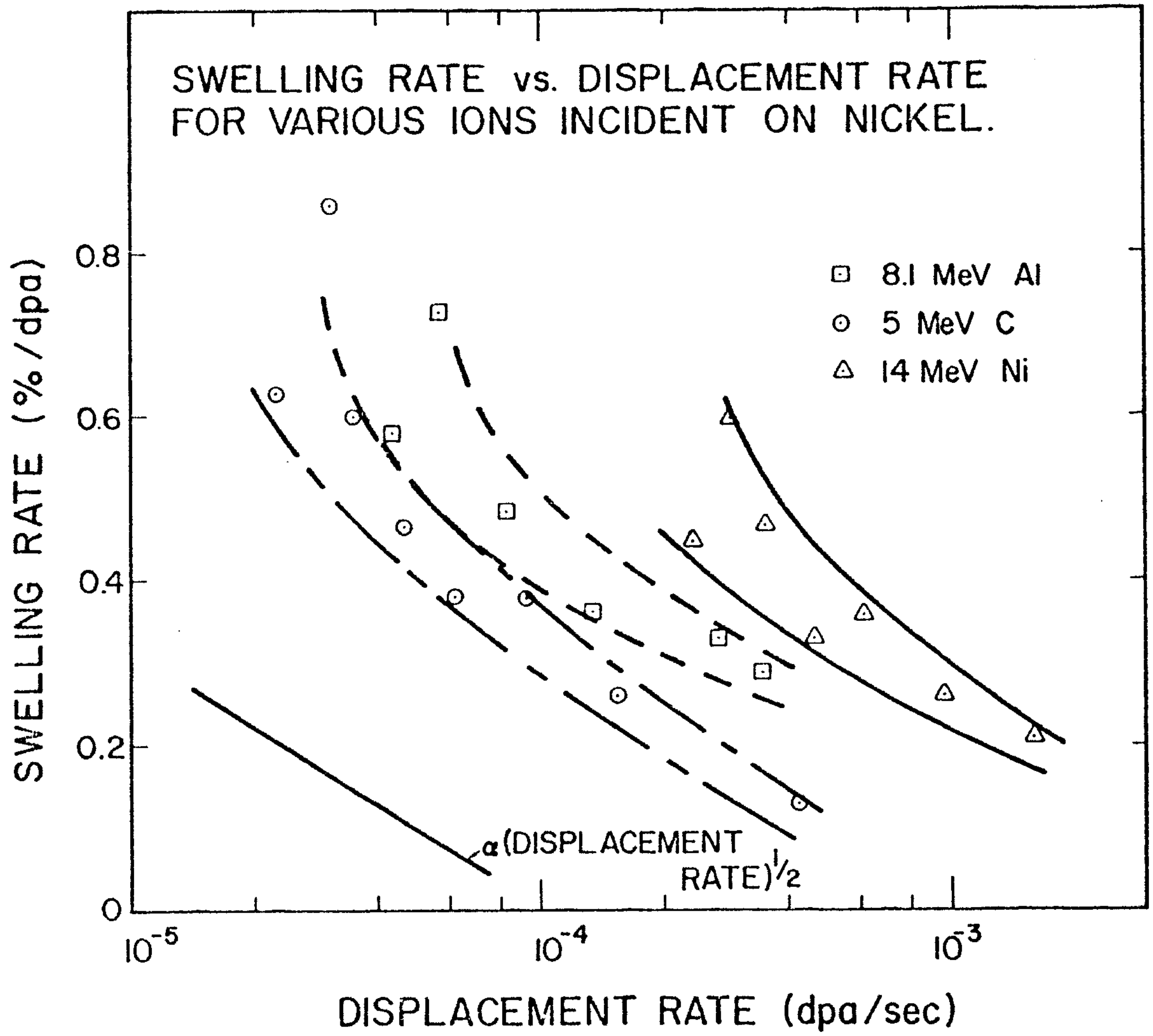

Figure 69. Swelling rate versus displacement rate for 14 MeV nickel, 8.1 MeV aluminum, and 5 MeV carbon ions incident on nickel at 525°C. The points for each different ion are all taken from a single sample.

disappearing. Possible causes for this behavior include: a) an increase in the void critical size, b) the dislocations connecting the voids leading to enhanced void coarsening, and c) the lower vacancy concentration due to the increasing sink density (170).

Under nickel ion irradiation, the void density saturated at very low doses (Figure 49). The void size and void volume fraction increased with dose up to 10-50 dpa and then saturates as well (see Figures 50 and 51). The dose at which this levelling occurred increased with increasing depth, and indicates it may be dose rate dependent. This saturation in swelling has been previously observed in nickel (107,109) and occurs when the voids start to order. Both the dose at which saturation occurs and the amount of swelling at saturation agree reasonably well with those observed previously (107). Several attempts at theoretical explanations for ordered defect structures have been made, but none have been completely successful (159).

G. Dose Rate Effects

One of the primary advantages of the cross sectioning technique is that it allows a study of dose rate effects with many other experimental uncertainties eliminated. The micrograph of Figure 57 is a dramatic illustration of the sensitivity of the observed microstructure to the dose rate. A change in dose rate of less than a factor of two changed the structure from one of voids to a loop lattice. This effect has to be due to dose rate variations since there are no other irradiation parameters varying in this sample that could cause this behavior. This sample illustrates that an increasing dose rate can shift the observed structure from the behavior expected at one temperature (that of void formation) to a structure indicative of a lower irradiation temperature (that of loop formation).

While the previous example is the most dramatic illustration of dose rate effects, there are other observations that can be explained by dose rate variations. The swelling rate versus displacement rate curves of Figure 69 show a decreasing swelling rate with increasing displacement rate (within a given sample). This behavior is consistent with the predictions of the temperature shift models of Equation 46 when the irradiation temperature is below the peak swelling temperature. This same behavior is illustrated somewhat differently in Figure 70 where swelling values at two different depths from the aluminum ion irradiation are plotted against the predicted displacement values for each point. The points from the deeper intervals show a lower swelling rate and a higher incubation dose than do the other points. Similar behavior is shown by the curves from the nickel ion fluence scan of Figures 49-51. The higher dose rate of the deeper intervals leads to increased void densities and decreased void size and swelling values at otherwise equal values of the total damage level.

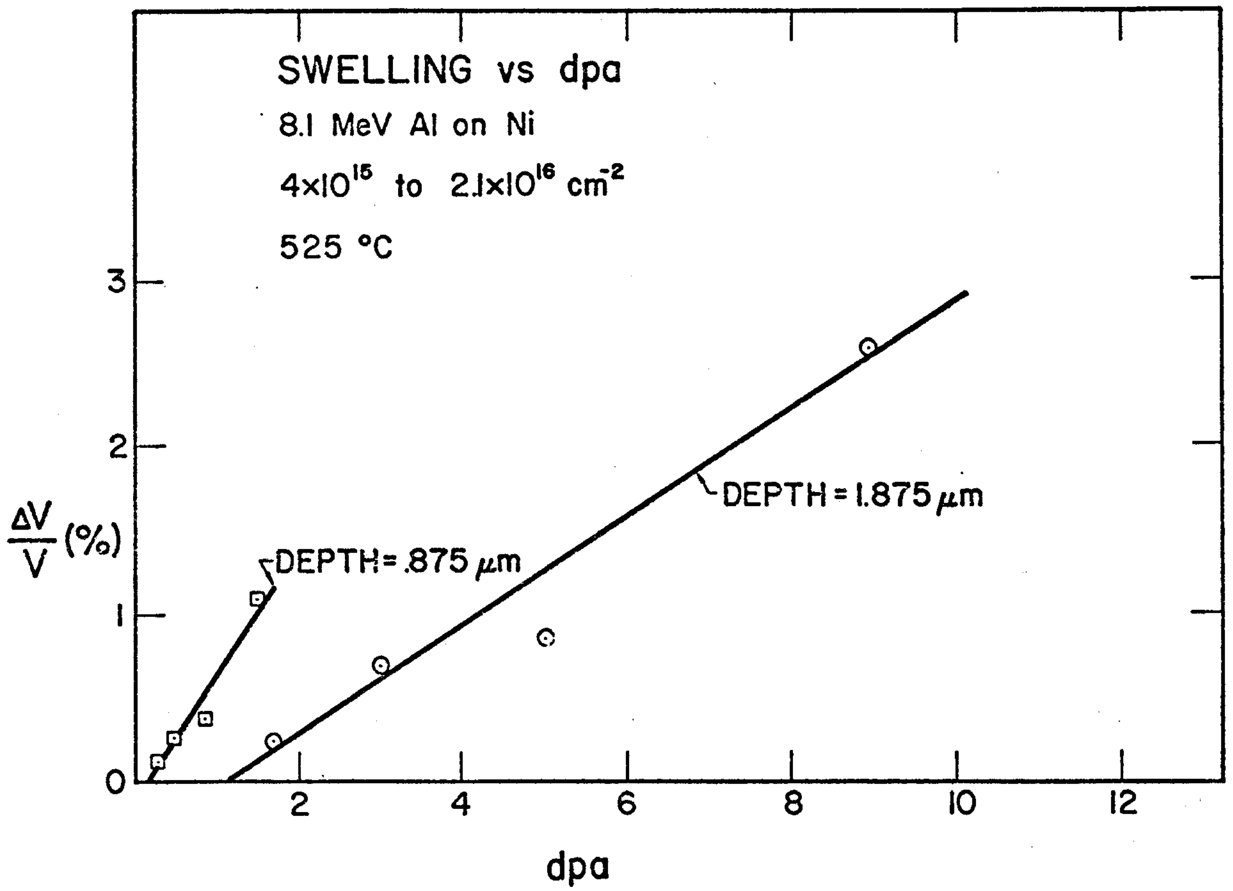

Figure 70. Swelling versus displacement damage at two depths in nickel irradiated at 525°C with 8.1 MeV aluminum ions. The swelling data was taken from figures 29-32 and the displacement data from figure 27.

This variation in dose rate is important in interpreting depth dependent void swelling data. The data of Figure 51 is replotted in Figure 71 to illustrate this point. The three data points are the swelling values at three depths within a single sample, namely the sample irradiated to a total ion fluence of 5×10^{15} ions/cm^2. The variation in swelling of these points with increasing dose is not indicative of the swelling rate expected by taking data from only one depth (i.e., dose rate) and increasing the total ion fluence. It is clear that data taken from different depths in a sample should not be used as a dose scan.

H. Grain Boundary and Surface Effects

The effect of the free surface on void formation is very important in ion irradiations using low energy ion or HVEM irradiation. The surface affected region is expected to be dose rate dependent, decreasing in extent with increasing dose rate (171). A typical surface denuded zone of samples irradiated at 525°C is shown in Figure 72. The denuded zone was typically 100-150 nm in width, and only a few voids were observed in these regions. Void sizes were larger next to this denuded zone. At very high fluences, these voids became so large that they grew into the void free zone and disappeared (see Figures 39, 40). Beyond the denuded zone, there was a zone where void sizes were larger than expected. At 525°C, the surface affected zone was ~0.5 μm, at 625°C, this zone was ~1.0 μm, and at 400°C, it was ~0.2 μm.

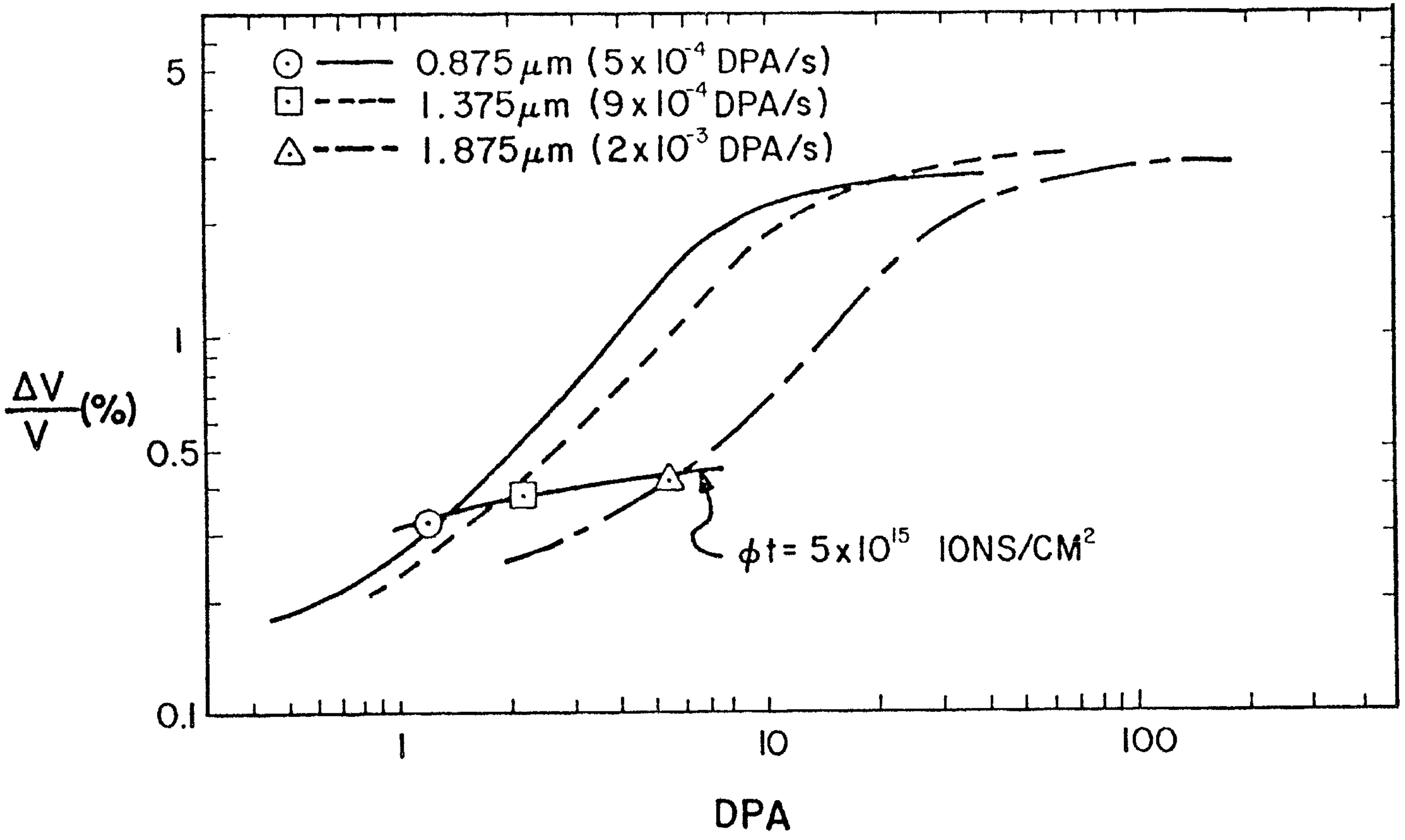

Figure 71. The swelling versus displacement curves of figure 51 showing the set of data points measured in a single sample (i.e., the sample with a total ion fluence of 5×10^{15} ions/cm^2).

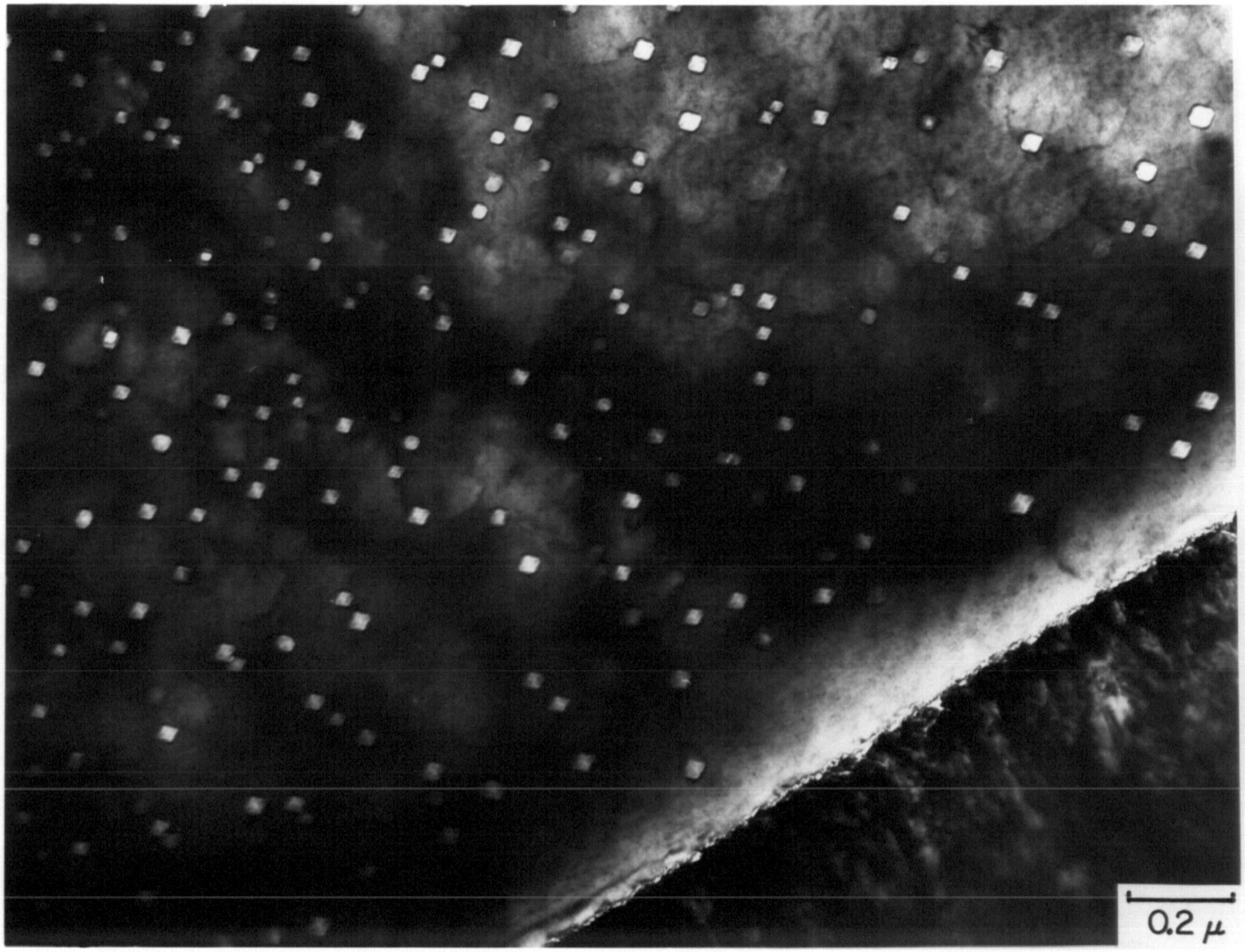

Figure 72. The surface region of a sample irradiated at 525°C with 19 MeV copper ions to a fluence of 5×10^{15} ions/cm^2.

Some of the typical grain boundaries observed in this study are shown in Figures 73 and 74. Most grain boundaries showed evidence of migration during the irradiation. The grain boundaries of Figure 73 have migrated large distances and as is evidenced by the low void densities, have cleaned the matrix of hydrogen behind them. The void size next to grain boundary denuded zones are generally larger than those next to the front surface, but this may simply be due to the higher doses further from the surface. The grain boundaries of Figure 74 have not migrated noticeably, and in these samples, there is little variation in the width of the grain boundary denuded zone with depth.

Grain boundary migration under irradiation has been observed before (43) and is not well understood. The sample irradiated at 400°C displayed interesting grain boundary behavior as is shown in Figure 75. In this sample, the grain boundary migrated in that part of the damage zone containing voids (marked by an arrow) and did not migrate elsewhere in the irradiated zone. Either the loop structure pinned the grain boundary or grain boundary migration requires the same irradiation conditions as void formation.

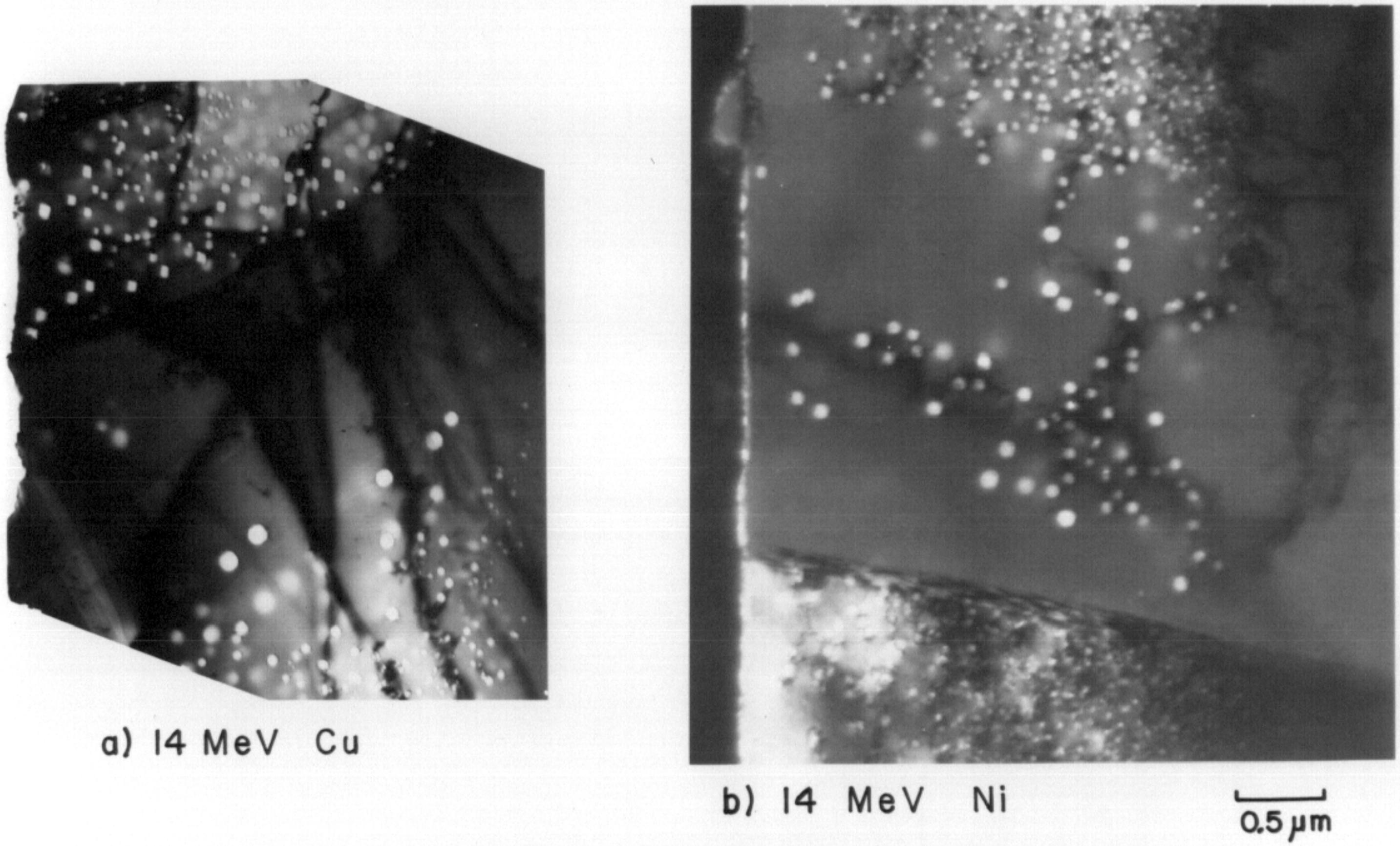
a) 14 MeV Cu

b) 14 MeV Ni

Figure 73. Grain boundaries in nickel irradiated at 525°C with the ions indicated.

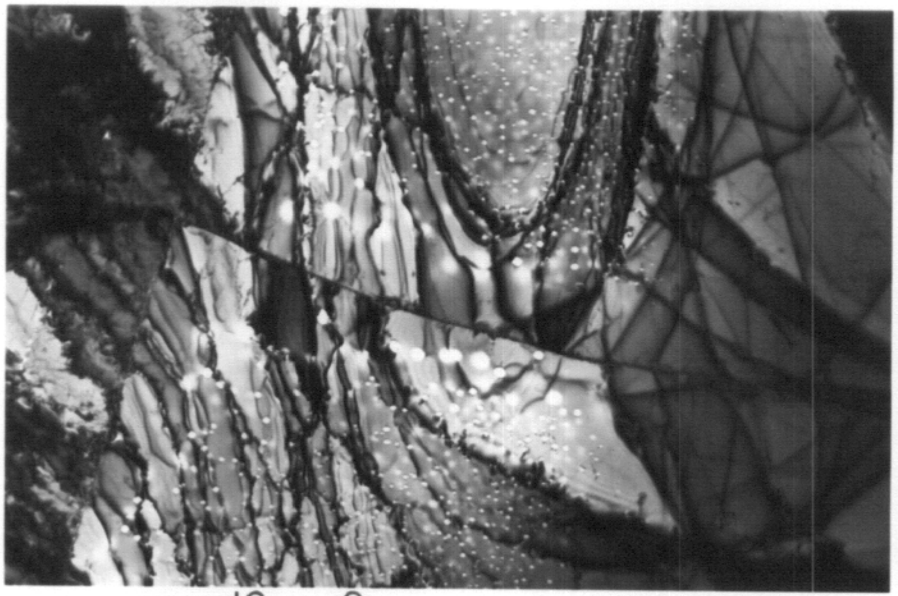

a) 1×10^{16} cm^{-2}

b) 4×10^{16} cm^{-2}

Figure 74. Grain boundaries in nickel irradiated at 525°C with 14 MeV nickel ions to the fluences indicated.

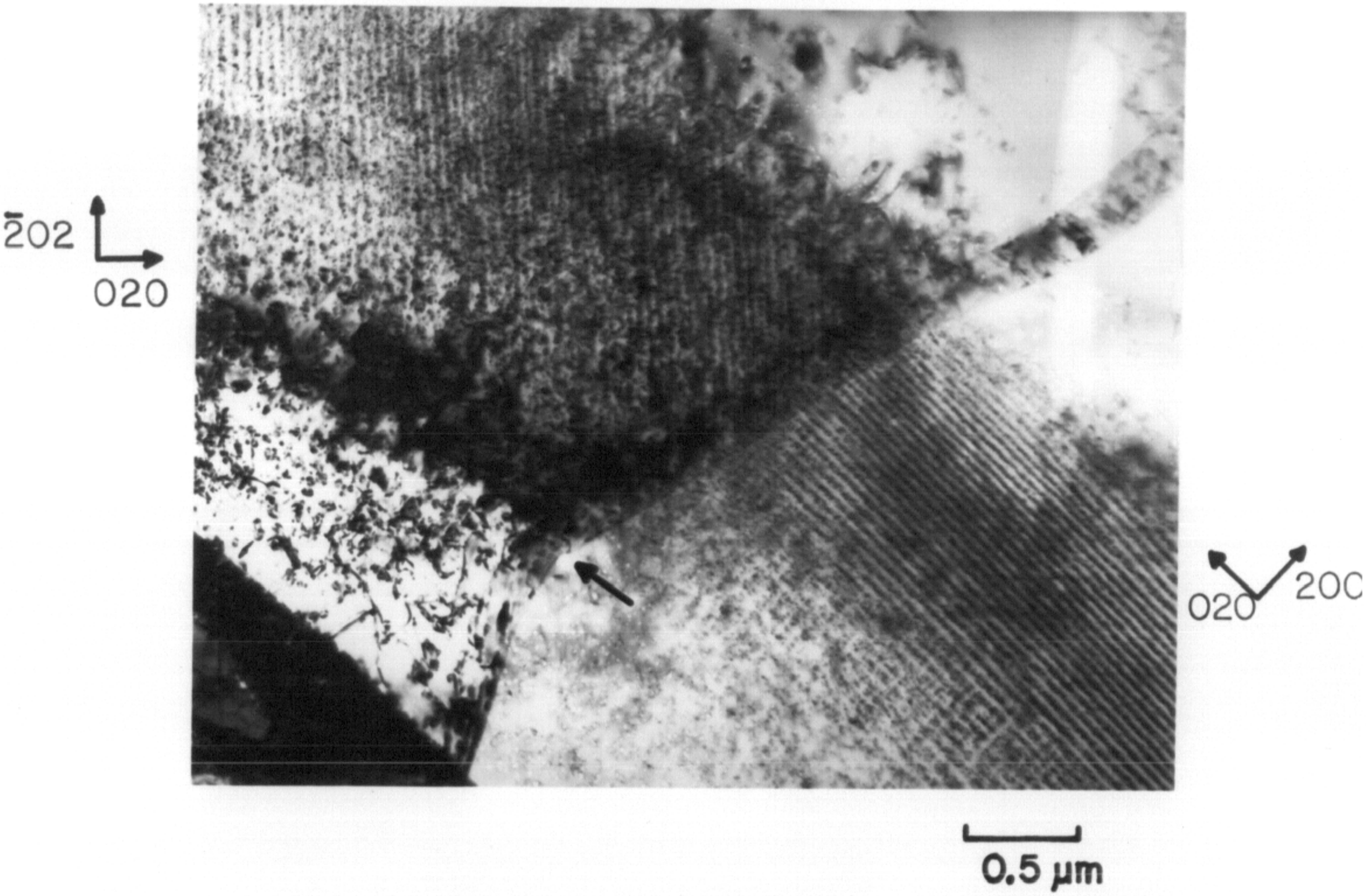

Figure 75. Grain boundary motion in nickel irradiated at 400°C with 14 MeV copper ions to a fluence of $5x10^{16}$ ions/cm^2. The arrow indicates the end of the void region.

VII. CONCLUSIONS

The cross sectioning method of post-irradiation sample preparation has been developed and applied to the study of heavy ion bombarded nickel. This technique has proven to be a valuable aid in understanding the microstructure produced by heavy ion irradiation, and was applied to the study of nickel irradiated with either nickel, copper, aluminum, or carbon ions at temperatures from 200 to 625°C and up to damage levels of 150 dpa. The steady state vacancy and interstitial concentration profiles were calculated for the general case of heavy ion irradiation, and a radiation enhanced diffusion model was then applied to predict the final concentration profile of impurities introduced by irradiating with ions other than nickel. Specific observations from this study are:

1. In thoroughly outgassed nickel, void nucleation was very difficult with observed void densities of the order of $10^{15}/cm^3$.

2. When sufficient hydrogen was introduced by electropolishing, void nucleation was enhanced, and void densities on the order of $10^{15}/cm^3$ were observed. Throughout this study, electropolishing was deliberately used to introduce hydrogen into the pre-irradiated specimens, thereby enhancing void nucleation and giving reproducible void densities.

3. The swelling rate per dpa in the end-of-range region was decreased significantly for all ion irradiations compared to the mid-range values. This is due mainly to the higher dose rate in this region.

4. Calculations of the steady-state defect concentrations predicted the observed decreased swelling rate at the end-of-range of the incident ions due to the higher recombination rate in these regions.

5. By modeling the radiation enhanced diffusion of the implanted copper ions, it was shown that, for the samples of this study, the copper was confined to the end-of-range region and should not diffuse significantly toward the front surface.

6. End-of-range effects of the irradiating ions on the nucleation and growth of voids are minimal. This demonstrates the importance of the impurity irradiation history, with impurities present in significant amounts at the start of the irradiation being much more important than impurities added during the irradiation.

7. The differences in the PKA spectra from carbon, aluminum, and nickel irradiations does not appear to have any major effect on the nucleation and growth of voids.

8. The void denstiy in nickel was a maximum at the lowest carbon and aluminum ion fluences (<2 dpa), and dropped with increasing ion fluence. It is thought that this is due to the increase in the critical void size for growth.

9. Under nickel ion irradiation at 525°C, the void density saturated at very low doses (< 2 dpa). Between 20 and 50 dpa, the void size and swelling saturated, with the swelling value at saturation of ~3%. In the highest dose sample (> 100 dpa) a void superlattice was beginning to form.

10. The damage level necessary for swelling to saturate increased with increasing depth (from 20 to 50 dpa). The swelling value at saturation did not depend on depth (i.e., dose rate).

11. Due to the change of many parameters with depth (such as dose rate, PKA spectrum, etc.) the variation in total dose in a given sample cannot be used to predict the behavior of increasing dose at a constant dose rate.

12. A void denuded region of 100-150 nm was observed at the front surface at temperatures of 525°C, with the total surface affected zone extending about 0.5 μm. At 625°C, the denuded zone was 0.5 μm and the surface affected zone about 1.0 μm.

13. Voids were observed at depths 15-20% beyond the predicted damage curve. This is believed due to an underestimation of the theoretical energy loss models and to the formation of voids by vacancies that have diffused into the "undamaged" region beyond the ion range.

14. After irradiation at 400°C, the first 0.5 μm consisted of voids, with the next 2 μm containing a loop lattice with a spacing of 40 nm. This structure is conclusive evidence that an increasing dose rate can shift the damage microstructure from that indicative of a "high" temperature (i.e., void formation) to that indicative of a "low" temperature (loop formation).

15. A loop lattice with a lattice spacing of 40 nm was observed after irradiation at 200°C, and the lattice spacing was not found to be dose rate or otherwise depth dependent.

VIII. BIBLIOGRAPHY

1. C. Cawthorne and E. J. Fulton, Nature 216, 575 (1967).

2. D. I. R. Norris, Rad. Eff. 14, 1; and Rad. Eff. 15, 1 (1972).

3. B. L. Eyre, Conf. on Fund. Aspects of Rad. Damage in Metals, Gatlinburg, Tenn., p. 729 (1975).

4. Radiation Damage in Reactor Materials, II, IAEA Symposium Proceedings, Vienna, June 1969, STI-PUB-230 (1969).

5. Proceedings of BNES European Conf. on Voids Formed By Irradiation of Reactor Materials, ed. S. F. Pugh, N. H. Loretto and D. I. R. Norris, Reading, U.K., March 1971.

6. Proceedings of the Int. Conf. on Radiation-Induced Voids in Metals, ed. J. W. Corbett and L. C. Ianniello, Albany, N.Y., June 1971, CONF-710601 (1972).

7. Proceedings of ASTM Conf. on Irradiation Effects on Structural Alloys for Nuclear Reactor Applications, Niagara Falls, N.Y., June 1970, ASTM-STP-484 (1971).

8. Proceedings of ASTM Conf. on Effects of Radiation on Substructural and Mechanical Properties of Metals and Alloys, Los Angeles, Calif. June 1972, ASTM-STP-529 (1973).

9. Proceedings of Eighth Int. ASTM Symp. on The Effects of Radiation on Structural Materials, St. Louis, Mo., May 1976.

10. Proceedings of 1973 Int. Conf. on Defects and Defect Clusters in BCC. Metals and Their Alloys, ed. R. J. Arsenault, Gaithersburg, Maryland (1973).

11. Consultant Symposium on The Physics of Irradiation Produced Voids, ed. R. S. Nelson, Harwell, Oxfordshire, U.K., Sept. 1974, AERE-R7934 (1975).

12. Proceedings of Int. Conf. on Radiation Effects and Tritium Technology for Fusion Reactors, Gatlinburg, Tenn. Oct. 1975, CONF 750989 (1976).

13. Proceedings of Int. Conf. on Fund. Aspects of Radiation Damage in Metals, Gatlinburg, Tenn., Oct. 1975, CONF 751006 (1976).

14. Proceedings of Applications of Ion Beams to Metals, ed. by Picraux, Eerllisse, and Vook, Plenum Press, N.Y., (1974).

15. Proceedings of Int. Conf. on Applications of Ion Beams to Materials, 1975, ed. by Carter, Colligon and Grant, Univ. of Warwick, Sept. 1975, Conf. Series No. 28.

16. Int. Conf. on Radiation Effects in Breeder Reactor Structural Materials, AIME, Scottsdale, Arizona, June, 1977.

17. P. R. Huebotter and T. Bump, Int. Conf. on Radiation-Induced Voids in Metals, ed. Corbett and Ianniello, Albany, N.Y., 1971, CONF-710601, p. 84 (1972).

18. R. S. Nelson, D. J. Mazey and J. A. Hudson, J. Nuc. Mat. 37 p. 1 (1971).

19. G. L. Kulcinski, Laidler and D. Doran, Rad. Eff. 7, p. 195 (1971).

20. D. W. Keefer, A. G. Pard and D. Kramer, Int. Conf. on Radiation-Induced Voids in Metals, ed. Corbett and Ianniello, Albany, N.Y., 1971, CONF-710601, p. 511 (1972).

21. N. H. Packan, K. Farrell, and J. Stiegler, "Correlation of Neutron and Heavy-Ion Damage", Accepted by Jour. of Nuc. Mat., 1978.

22. R. F. Decker and R. R. DeWitt, Jour. of Metals, Feb. 1965, p. 139.

23. G. P. Sabol and R. Stickler, Phys. Stat. Sol. 35, p. 11 (1969).

24. D. Raynor and Silcock, Metal Sci. Jour. 4, p. 121 (1970).

25. H. V. Smith, Jr., and H. T. Richards, Nuc. Inst. and Methods 125, 497 (1975).

26. B. T. Kelly, Irradiation Damage to Solids, Pergamon Press, N. Y. (1966).

27. D. S. Billington and J. H. Crawford, Radiation Damage in Solids, Princeton Univ. Press., N. J., (1961).

28. M. W. Thompson, Defects and Radiation Damage in Metals, Cambridge Univ. Press (1969).

29. D. R. Olander, Fundamental Aspects of Nuclear Reactor Fuel Elements, NTIS #TID-26711-P1 (1976).

30. B. Badger, Univ. of Wisc. memo, UWFDM 68 (1974).

31. D. R. Olander, Fundamental Aspects of Nuclear Reactor Fuel Elements, NTIS #TID-26711-P1, Chapter 17, (1976).

32. J. Lindhard, M. Scharff and H. E. Schiott, Mat. Fys. Medd. Dan. Vid. Selsk. 33, No. 14 (1963).

33. K. B. Winterbon, P. Sigmund and J. B. Sanders, Mat. Fys. Medd. Dan. Vid. Selsk. 37, No. 14 (1970).

34. J. Lindhard, V. Nielsen and M. Scharff, Mat. Fys. Medd. Dan. Vid. Selsk. 36, No. 10 (1968).

35. J. Lindhard and M. Scharff, Phys. Rev. 124, p. 128 (1961).

36. I. Manning and G. P. Mueller, Com. Phy. Comm. 7, p. 85 (1974).

37. J. Lindhard, V. Nielsen, M. Scharff and P. L. Thompson, Mat. Fys. Medd. Dan. Vid. Selsk. 33, No. 10 (1963).

38. M. T. Robinson, Nuclear Fusion Reactors, BNES, London, 1971, p. 410.

39. I. M. Torrens and M. T. Robinson, Int. Conf. on Radiation-Induced Voids in Metals, ed. Corbett and Ianneillo, Albany, N. Y., 1971, CONF-710601, p. 739 (1972).

40. M. J. Norgett, M. T. Robinson and I. M. Torrens, IAEA Specialists' Meeting on Radiation Damage Units for Ferritic and Stainless Steels, Seattle, Wash., Oct. 1972.

41. P. G. Lucasson and R. M. Walker, Phy. Rev. 127, p. 485 (1962).

42. G. L. Kulcinski, Univ. of Wisc. class notes, 1975.

43. T. D. Ryan, Ph.D. Thesis, Univ. of Michigan, 1975.

44. D. K. Brice, SAND7500622, Sandia Laboratories, Albuquerque, New Mexico, July 1977.

45. H. E. Schiott, Can. Jour. of Phy. 46, 449 (1968).

46. W. W. Bowman, F. M. Lazafame, C. K. Cline, Yu-Wen Yu and M. Blann, Phy. Rev. 165, #2, 485 (1968).

47. M. T. Robinson, Consultant Symposium on The Physics of Irradiation Produced Voids, ed. Nelson, Harwell, U.K., 1974, AERE-R7934, p. 18 (1975).

48. G. R. Odette, D. Schwartz and A. Ardell, Rad. Eff. 22, 217 (1974.

49. J. R. Beeler, Jr., Proceeding of Applications of Ion Beams to Metals, ed. Picraux, EerNisse, Vook, Plenum Press, N.Y., p. 651 (1974).

50. D. R. Olander, Fundamental Aspects of Nuclear Reactor Fuel Elements, NTIS #TID-26711-P1, p. 404 (1976).

51. J. R. Beeler, Jr., Int. Conf. on Radiation-Induced Voids in Metals, ed. Corbett and Ianniello, Albany, N.Y., 1971, CONF-710601, p. 684 (1972).

52. D. G. Doran, Rad. Eff. 2, 249 (1970).

53. M. J. Norgett, Consultant Symposium on The Physics of Irradiation Produced Voids, ed. Nelson, Harwell, U.K., 1974, AERE-R7934, p. 44 (1975).

54. K. L. Merkle and R. S. Averback, Int. Conf. on Fund. Aspects of Radiation Damage in Metals, Gatlinberg, Tenn., 1975, CONF-751006, p. 127 (1976).

55. T. H. Blewitt, A. Klank, T. Scott, W. Weber, Int. Conf. on Radiation-Induced Voids in Metals, ed. Corbett and Ianneillo, Albany, N.Y., 1971, CONF-710601, p. 757, (1972).

56. A. D. Marwick, J. Nuc. Mat. 55, p. 259 (1975).

57. H. I. Avci, Ph.D. Thesis, Univ. of Wisconsin, 1978.

58. J. R. Beeler, Jr., M. F. Beeler and C. V. Parks, Int. Conf. on Radiation Effects and Tritium Technology for Fusion Reactors, Gatlinburg, Tenn., 1975, CONF-750989, p. I-362, (1976).

59. F. S. Ham, J. App. Phy. 30, #6, 915 (1959).

60. W. G. Wolfer and M. Ashkin, *J. App. Phy*. *47*, #3, p. 791 (1976).

61. E. E. Bloom, Int. Conf. on *Radiation-Induced Voids in Metals*, ed. Corbett and Ianniello, Albany, N.Y., 1971, CONF-710601, p. 1, (1972).

62. J. O. Stiegler, Int. Conf. on *Radiation-Induced Voids in Metals*, ed. Corbett and Ianniello, Albany, N.Y., 1971, CONF-710601, p. 292, (1972).

63. E. E. Bloom, K. Farrell, M. H. Yoo and J. O. Stiegler, Consultant Symposium on *The Physics of Irradiation Produced Voids*, ed. Nelson, Harwell, N.K., 1974, AERE-R7934, p. 330, (1975).

64. E. E. Bloom and J. O. Stiegler, *J. Nuc. Mat*. *36*, p. 331 (1970).

65. J. L. Katz and H. Wiedersich, *Jour. Chem. Phy*. *55*, #3, p. 1414 (1971).

66. K. C. Russell, *Acta. Met*. *19*, p. 753 (1971).

67. H. I. Aaronson, *Lectures on the Theory of Phase Transformations*, AIME, 1975.

68. B. L. Eyre, Int. Conf. on *Fund. Aspects of Radiation Damage in Metals*, Gatlinburg, Tenn., 1975, CONF-751006, p. 729 (1976).

69. K. C. Russell, Consultant Symposium on *The Physics of Irradiation Produced Voids*, ed. Nelson, Harwell, U.K., 1974, AERE-R7934, p. 158, (1975).

70. H. Wiedersich, Consultant Symposium on *The Physics of Irradiation Produced Voids*, ed. Nelson, Harwell, U.K., 1974, AERE-R7934, p. 147, (1975).

71. J. L. Katz and H. Wiedersich, *J. Nuc. Mat*. *46*, p. 41 (1973).

72. W. G. Wolfer and M. H. Yoo, Int. Conf. on *Radiation Effects and Tritium Technology for Fusion Reactors*, Gatlinburg, Tenn., 1975, CONF-750989, p. II-458, (1976).

73. W. H. Choi and A. L. Bement, Int. Conf. on *Radiation Effects and Tritium Technology for Fusion Reactors*, Gatlinburg, Tenn., 1975, CONF-750889, p. II-1, (1976).

74. M. R. Hayns, *J. Nuc. Mat*. *56*, p. 267 (1975).

75. M. R. Hayns and R. C. Perrin, Consultant Symposium on *The Physics of Irradiation Produced Voids*, ed. Nelson, Harwell, U.K., 1974, AERE-R7934, p. 188, (1975).

76. J. A. Sprague, K. C. Russell and Y. H. Choi, Int. Conf. on *Fund. Aspects of Radiation Damage in Metals*, Gatlinburg, Tenn., 1975, CONF-751006, p. 181, (1976).

77. R. Bullough and R. C. Perrin, Int. Conf. on *Radiation-Induced Voids in Metals*, ed. Corbett and Ianniello, Albany, N.Y., 1971, CONF-710601, p. 769, (1972).

78. S. D. Harkness and Che-Yu Li, *Met. Trans.* *2*, p. 1457 (1971).

79. H. Wiedersich, *Rad. Eff.* *12*, p. 111 (1972).

80. A. D. Brailsford and R. Bullough, *J. Nuc. Mat.* *44*, p. 121 (1972).

81. W. G. Wolfer, L. K. Mansur and J. A. Sprague, *Rad. Eff. in Breeder Reactor Structural Materials*, Scottsdale, Arizona, p. 841 (1977).

82. E. P. Simonen and J. L. Brimhall, Int. Conf. on *Fund. Aspects of Radiation Damage in Metals*, Gatlinburg, Tenn., 1975, CONF-751006, p. 1196, (1976).

83. R. Bullough, Consultant Symposium on *The Physics of Irradiation Produced Voids*, ed. Nelson, Harwell, U.K., 1974, AERE-R7934, p. 275 (1975).

84. J. E. Westmoreland, J. A. Sprague, F. A. Smidt and Malmberg, *Rad. Eff.* *26*, p. 1 (1975).

85. B. L. Eyre, *Jour. Phys. F. Metal Phy.* *3*, 422 (1973).

86. J. L. Straalsund, *J. Nuc. Mat.* *51*, 302 (1974).

87. D. I. R. Norris, Consultant Symposium on *The Physics of Irradiation Produced Voids*, ed. Nelson, Harwell, U.K., 1974, AERE-R7934, p. 134, (1975).

88. A. D. Brailsford, *J. Nuc. Mat.* *56*, p. 7 (1975).

89. F. A. Smidt, Jr., and J. A. Sprague, *Scr. Met.* *7*, p. 495 (1973).

90. F. A. Smidt, Jr., and J. A. Sprague, NRL Memorandem Report 2998, Progress report May-Oct. 1974, p. 39 (1975).

91. D. J. Mazey and F. Menzinger, *J. Nuc. Mat.* *48*, p. 15 (1973).

92. J. L. Brimhall and H. E. Kissinger, *Rad. Eff.* *15*, p. 259 (1972).

93. S. M. Sorensen, Jr. and C. W. Chen. Int. Conf. on *Fund. Aspects of Radiation Damage in Metals*, Gatlinburg, Tenn., 1975, CONF-751006, p. 1213, (1976).

94. S. M. Sorensen, Jr. and C. W. Chen, *Rad. Eff.* *33*, p. 109, (1977).

95. J. E. Harbottle and S. M. Dickerson, *J. Nuc. Mat.* *44*, 313 (1972).

96. J. L. Brimhall and B. Mastel, *J. Nuc. Mat.* *28*, 115 (1968).

97. J. L. Brimhall and B. Mastel, *J. Nuc. Mat.* *29*, 123 (1969).

98. E. E. Bloom and J. O. Stiegler, *Am. Nuc. Soc. Trans.*, *12*, p. 116 (1969).

99. J. J. Holmes, *Am. Nuc. Soc. Trans.*, *12*, p. 117 (1969).

100. J. L. Brimhall and B. Mastel, *J. Nuc. Mat.* *33*, p. 186 (1969).

101. J. L. Brimhall and B. Mastel, *Scripta Met.* *4*, p. 51 (1970).

102. J. O. Stiegler and E. E. Bloom, *Rad. Eff.* *8*, p. 33 (1971).

103. Y. Adda, Int. Conf. on *Radiation-Induced Voids in Metals*, ed. Corbett and Ianniello, Albany, N.Y., 1971, CONF-710601, p. 31, (1972).

104. J. L. Brimhall, H. E. Kissinger and G. L. Kulcinski, Int. Conf. on *Radiation-Induced Voids in Metals*, ed. Corbett and Ianniello, Albany, N.Y., 1971, CONF-710601, p. 338, (1972).

105. W. N. McElroy and H. Farrar, Int. Conf. on *Radiation-Induced Voids in Metals*, ed. Corbett and Ianniello, Albany, N.Y., 1971, CONF-710601, p. 187, (1972).

106. V. Levy, Consultant Symposium on *The Physics of Irradiation Produced Voids*, ed. Nelson, Harwell, U.K., 1974, AERE-R7934, p. 50, (1975).

107. G. L. Kulcinski, J. Brimhall and H. Kissinger, Int. Conf. on *Radiation-Induced Voids in Metals*, ed. Corbett and Ianniello, Albany, N.Y., 1971, CONF-710601, p. 449 (1972).

108. D. J. Mazey and J. A. Hudson, *J. Nuc. Mat.* *37*, p. 13 (1970).

109. G. L. Kulcinski, J. L. Brimhall and H. E. Kissinger, *J. Nuc. Mat.* *40*, p. 166 (1971).

110. H. H. Neely and K. Herschbach, *Rad. Eff.* *7*, p. 187 (1971).

111. J. A. Hudson, D. J. Mazey and R. S. Nelson, BNES Conf. on *Voids Formed by Irradiation of Reactor Materials*, ed. Pugh, Loretto and Norris, Reading, U.K., 1971, p. 213, (1971).

112. W. G. Johnston, J. Rosolowski and A. Turkalo, *J. Nuc. Mat.* *54*, p. 24 (1974).

113. J. A. Sprague, J. E. Westmoreland, F. A. Smidt, Jr., and P. R. Malmburg, *J. Nuc. Mat.* *54*, p. 286 (1974).

114. J. A. Sprague, J. E. Westmoreland, F. A. Smidt, Jr. and P. R. Malmberg, Consultant Symposium on *The Physics of Irradiation Produced Voids*, ed. Nelson, Harwell, U.K., 1974, AERE-R7934, p. 263, (1975).

115. J. L. Brimhall, BNWL-1839, UC-25, July, 1974. (ERDA report).

116. J. L. Brimhall and E. P. Simonen, BNWL01939 3, UC-20, p. 24 (April 1976).

117. D. I. R. Norris, *J. Nuc. Mat.* *40*, 66 (1971).

118. D. I. R. Norris, *Nature* *227*, p. 830 (1970).

119. K. Urban, *Phys. Stat. Sol. (a)* *3*, p. K167 (1970).

120. D. I. R. Norris, *Phil. Mag.* *22*, p. 1273 (1970).

121. D. I. R. Norris, *Phil. Mag.* *23*, No. 181, p. 135 (1971).

122. K. Urban and M. Wilkens, *Phys. Stat. Sol. (a)* *6*, p. 173 (1971).

123. D. I. R. Norris, BNES Conf. on *Voids Formed by Irradiation of Reactor Materials*, ed. Pugh, Loretto and Norris, Reading, U.K., 1971, p. 247, (1971).

124. K. Urban, BNES Conf. on *Voids Formed by Irradiation of Reactor Materials*, ed. Pugh, Loretto and Norris, Reading, U.K., 1971, p. 275, (1971).

125. J. E. Harbottle, *Phil. Mag.* *27*, p. 147 (1973).

126. J. L. Brimhall and E. P. Simonen, *J. Nuc. Mat.* *68*, p. 235 (1977).

127. G. L. Kulcinski and J. L. Brimhall, ASTM Conf. on *Effects of Radiation on Substructural and Mechanical Properties of Metals and Alloys*, Los Angeles, Calf, 1972, ASTM-STP-529, p. 258 (1973).

128. A. M. Stoneham, Consultant Symposium on *The Physics of Irradiation Produced Voids*, ed. Nelson, Harwell, Y.K., 1974, AERE-R7934, p. 319, (1975).

129. K. Malen and R. Bullough, BNES Conf. on *Voids Formed by Irradiation of Reactor Materials*, ed. Pugh, Loretto and Norris, Reading, U.K., 1971, p. 109, (1971).

130. C. W. Chen, *Phy. Stat. Sol. (a)* *16*, p. 197 (1973).

131. J. M. Lanore, L. Glowinski, A. Risbet, P. Regnier, J. Flament, and Y. Choi, Int. Conf. on *Fund. Aspects of Radiation Damage in Metals*, Gatlinburg, Tenn., 1975, CONF-751006, p. 1169 (1976).

132. J. R. Buswell, S. B. Fisher, J. E. Harbottle and D. I. R. Norris, *Physical Metallurgy of Reactor Fuel Elements*, ed. by J. E. Harris and E. C. Sykes, Berkeley, Sept., 1973, p. 170.

133. J. L. Brimhall, Consultant Symposium on *The Physics of Irradiation Produced Voids*, ed. Nelson, Harwell, U.K., 1974, AERE-R7934, p. 197, (1975).

134. P. Sigmond, *Rad. Damage Processes in Materials*, ed. Dupuy, Noordhoff, Leyden, 1975, p. 3, (1975).

135. J. V. Sharp, *Rad. Eff.* *14*, p. 71 (1972).

136. P. R. Swann, *Acta Metal.* *14*, p. 900 (1966).

137. M. S. Abrahams and C. Buiocchi, *J. App. Phy.* *45*, #8, p. 3315 (1974).

138. R. A. Spurling and C. Rhodes, J. Nuc. Mat. 44, p. 341 (1972).

139. J. Narayan and O. S. Oen, ORNL-5135, UC-25, p. 78 (May, 1976).

140. J. B. Whitley, P. Wilkes and G. L. Kulcinski, UWFDM 159, (1976).

141. G. Fenske, S. K. Das, M. Kaminsky and G. H. Miley, Trans. of Am. Nuc. Soc., June, 1978.

142. O. S. Oen, J. Narayan and T. S. Noggle, Proceedings of Applications of Ion Beams to Metals, ed. by Picraux, Eerllisse and Vook, Plenum Press, N.Y., p. 639, (1974).

143. C. H. Henager, Jr., J. L. Brimhall and E. P. Simonen, Rad. Eff. 36, p. 49 (1978).

144. J. S. Armijo and T. Lauritzen, Int. Conf. on Radiation-Induced Voids in Metals, ed. Corbett and Ianniello, Albany, N.Y., 1971, CONF-710601, p. 479, (1972).

145. W. G. Johnston and J. H. Rosolowske, Int. Conf. on Applications of Ion Beams to Materials, 1975, ed. by Carter, Colligon and Grant, Univ. of Warwick, Conf. Series #28, p. 228 (1975).

146. C. W. Chen, A. Mastenbroek and J. D. Elen, Rad. Eff. 16, p. 127 (1972).

147. S. Diamond, I. M. Baron, M. L. Blieberg, R. Bajaj and R. W. Chichering, Int. Conf. on Radiation Effects and Tritium Technology for Fusion Reactors, Gatlinburg, Tenn., 1975, CONF-750989, p. I-207, (1976).

148. W. G. Johnston, J. H. Rosolowski, A. M. Turkalo and T. Lauritzen, Consultant Symposium on The Physics of Irradiation Produced Voids, ed. Nelson, Harwell, U.K., 1974, AERE-R7934, p. 101, (1975).

149. W. G. Johnston, T. Lauritze, J. Rosolowski and A. Turkalo, G. E. Report, 4/30/76, Schenectady, N.Y.

150. D. W. Keefer and A. G. Pard, Rad. Eff. 22, p. 181 (1975).

151. J. Narayan, T. S. Noggle and O. S. Oen, Int. Conf. on Fund. Aspects of Radiation Damage in Metals, Gatlinburg, Tenn., 1975, CONF-751006, p. 90, (1976).

152. R. G. Lott and H. V. Smith, Jr., *Exp. Methods for Charged Part. Irrad.*, Gatlinburg, Tenn., CONF-750947, p. 82 (1975).

153. H. V. Smith, Jr., and R. G. Lott, *Nuc. Inst. and Methods*, *143*, p. 125 (1977).

154. T. M. Rodgers, *Handbook of Practical Electroplating*, p. 225.

155. J. B. Whitley, P. Wilkes and G. L. Kulcinski, *Trans. Am. Nuc. Soc*. *23*, p. 136 (1976).

156. R. G. Lott, Univ. of Wisconsin, unpublished data (1978).

157. J. B. Whitley, G. L. Kulcinski, P. Wilkes and H. V. Smith, Jr,, "Void Swelling Profiles in Nickel Irradiated with Copper or Nickel Ions", accepted by *J. Nuc. Mat.*, 1978.

158. J. B. Whitley, G. L. Kulcinski, H. V. Smith, Jr. and P. Wilkes, Presented at *Ninth Int. Sym. on the Effect of Radiation on Structural Materials*, Richland, Wash., 1978, (ASTM).

159. G. L. Kulcinski and J. L. Brimhall, *Effects of Rad. on Substructure and Mechanical Properties of Metals and Alloys*, ASTM-STP-529, ASTM, p. 258, (1973).

160. F. A. Garner and G. L. Guthrie, Int. Conf. on *Rad. Effects and Tritium Technology for Fusion Reactors*, CONF-750989, p. I-491 (1976).

161. W. L. Bell, *J. Applied Physics 47*, #4, p. 1676, (1976).

162. S. M. Myers, D. E. Amos, D. K. Brice, *J. App. Physics*, No. 5, p. 1812 (1976).

163. J. B. Whitley, G. L. Kulcinski, UWFDM-241, Nuc. Engr. Dept., Madison, Wis. (1978).

164. Y. Adda, M. Beyeler, and G. Brebec, *Thin Solid Films*, *25*, p. 107 (1975).

165. W. D. Wilson, Sandia Laboratories, Livermore, personal communication (1978).

166. D. K. Brice, *Ion Implantation Range and Energy Deposition Distributions*, Plenum Data Co., N.Y., (1975).

167. A. D. Brailsford and L. K. Mansur, *J. Nuc. Mat*. *71*, p. 110, (1977).

168. G. L. Kulcinski, *Applications of Ion Beams to Metals*, Plenum Corporation, N.Y., pp. 613-637, (1974).

169. D. W. Keefer and A. G. Pard, *Journal of Nuclear Materials*, *47*, p. 97, (1973).

170. N. Ghoniem and G. L. Kulcinski, *Journal of Nuclear Materials*, *69, 70*, pp. 816-820, (1978).

171. J. T. Buswell, S. B. Fisher, J. E. Harbottle, D. I. R. Norris and K. R. Williams, Int. Conf. on *Radiation-Induced Voids in Metals*, ed. Corbett and L. C. Ianniello, Albany, N.Y., 1971, CONF-710601, p. 533 (1972).